CFD Modelling of Transient Two-phase Flows for High Pressure Pipeline Decompression

By

Hongen Jie

Supervised by: Prof. Jennifer X. Wen

Dr Siaka Dembele

Dr Baopeng Xu

Thesis submitted in partial fulfilment of the requirements of Kingston University for the Degree of Doctor of Philosophy

Faculty of Science, Engineering and Computing

Kingston University, London

October 2013

Acknowledgements

I would like to give a big thanks to my supervisor Prof. Jennifer X. Wen. She provides me a great chance to do the research closely related to Carbon Capture and Storage. She guides me through all the research period and sponsors me the scholarship.

Also, co-supervisor Dr. Siaka Dembele is acknowledged. He provides me a great support to complete my dissertation in my most difficult time. His nice smile and patience ease my tense mood.

My co-supervisor Dr. Baopeng Xu is indispensably acknowledged for his precious support and expertise in various aspects of the project.

I also would like to thank especially my previous supervisor, Professor Xiaofang Wang and Associate Professor Rong Xie at Dalian University of Technology in China for their encouragements and supports.

I wish to thank the China Scholarship Council for awarding a scholarship under the State Scholarship Fund to purse my study abroad for first two years. Without the scholarship, I would not have studied aboard to explore my research.

Thanks are also due to my colleagues, Hamed Aghajani, Madhav Rao Vendra, especially Dr. Zhibin Chen and Dr. Changjian Wang for taking time to discuss some issues.

I thank Research Coordinator of Faculty Jackie Deacon for her supports and helps during my PhD study.

I have benefitted from technical discussions with Russell Cooper and Julian Barnett of National Grid, David Jones from Pipeline Integrity Engineers Ltd and Andrew Cosham from Atkins Boreas during the development of the work. Financial support from National Grid for related work is also gratefully acknowledged.

Last but not least, I would like to thank my wife Ruiping Zhang and also my lovely daughter Gracie Jie and also my family. Without their patience, encouragement and support from the spirit, it would not have been possible to achieve this.

The dissertation is dedicated to all the people. Thank you very much for all your great support.

Abstract

A CFD model has been developed with the aim to predict transient two-phase flows for pipeline decompression. The arbitrary Lagrangian-Eulerian method was introduced to solve separately the convection terms from the other terms in a sub-cycled explicit manner using a sub-timestep that is only a fraction of the main computational timestep, which can significantly simplify solution procedures and improve computational efficiency.

The homogeneous equilibrium model (HEM) and homogeneous relaxation model (HRM) were employed to treat multi-component two phases as a continuous mixture based on the basic assumption of homogeneous flow. HEM assumes that the two phases are not only in thermodynamic equilibrium but also in mechanical equilibrium, namely the two phases share identical velocity, temperature and pressure and the rate of phase change is rapidly enough so that equilibrium is reached. However, the rate at which the phase change took place depends on interphase heat transfer and non-equilibrium effects. For the rapid pipeline decompression, the rates of interphase heat transfer are a limiting factor for phase change. In order to examine the non-equilibrium effect, the rate equation is introduced to evaluate the non-equilibrium generation of vapour or liquid phase by an approach of relaxation. HRM is proposed to deal with two-phase flows involved during pipeline decompression, and is extended for the multi-component dense fluid.

The use of CFD allows the effect of pipe wall heat transfer and friction to be quantified. The wall heat transfer is considered through the implementation of a conjugate heat transfer model while the wall friction is computed using established empirical correlations. The Peng-Robinson-Stryjek-Vera equation

of state (EOS), which is capable of predicting the real gas thermodynamic behaviour of mixture, has been implemented in addition to the Peng-Robinson EOS and Span-Wagner EOS, and the latter is used as a reference specifically for pure CO_2. GERG-2004 is also employed for CO_2-rich mixture. Additionally, the liquid-vapour phase equilibrium of a multi-component two-phase mixture is determined by flash calculation.

The current code with HEM is validated for natural gas, rich gas, liquefied petroleum gas, gaseous and dense phase CO_2 decompression against the available data of shock tube test. The decompression curve, which describes the propagation of the expansion wave immediately following a rupture, is obtained to be treated as the key input to the Battelle two-curve method which often used to determine the toughness required to arrest a running ductile fracture in a pipeline. Furthermore, the predictions of pressure and temperature time traces are compared with the results of British Gas shock tube tests, Botros's rich gas experiments, Isle of Grain full-scale experiments. The predictions show reasonably good agreement with the experimental data.

Finally, CO_2 shock tube decompression is examined with the current model. Gaseous and dense phase CO_2 and CO_2-rich mixture shock tube tests are predicted. Predictions are compared with the available experimental data. The results show good agreement for CO_2 tests. The decompression behaviours of high pressure CO_2 pipeline are studied and discussed. The effect of initial conditions and impurities on the decompression behaviour is investigated. Additionally, the effects of friction and heat transfer are evaluated for the gaseous and dense tests. Lastly, the non-equilibrium effect on the decompression behaviour is also evaluated for dense tests by employing the approach of HRM.

Content

List of Abbreviations and Acronyms

ALE	arbitrary Lagrangian-Eulerian
BGC	British Gas cases
BTCM	Battelle two-curve method
BWRS	Benedict-Webb-Rubin-Starling
CCS	carbon capture and storage
CFD	computational fluid dynamic
CFL	Courant–Friedrichs–Lewy
CO_2	carbon dioxide
EOR	enhanced oil recovery
EOS	equation of state
FDM	finite difference methods
FV	finite volume
GERG	Groupe Européen de Recherches Gaziéres
HEM	homogeneous equilibrium model
HRM	homogeneous relaxation model
LPG	liquefied petroleum gas
ML	metastable liquid
MOC	method of characteristics
NS	Navier-Stokes
PDC	partial donor cell
PR EOS	Peng-Robinson equation of state
PRSV EOS	Peng-Robinson-Stryjek-Vera equation of state
QRA	quantitative risk assessment
QSOU	quasi-second-order upwind
SIMPLE	semi implicit method for pressure linked equation
SRK EOS	Soave-Redlich-Kwong equation of state

SW EOS	Span-Wagner equation of state

Nomenclature

Roman Symbols

Symbol	Description
A	Cross-sectional area of pipeline
a, b	Parameter for PR EOS
C	Specific heat, speed of sound, fanning friction factor with subscripts f
D	Diffusion coefficient, $\frac{\mu}{\rho \mathrm{Sc}}$,pipeline inner diameter
g	Gravity vector
h	heat transfer coefficient
I	Specific internal energy
I	Unit dyadic
i, j, k	Unit vector in the x, y, z directions
J	contributions of heat conduction and enthalpy diffusion
K	Diffusion/transport coefficient, $\mu C_p/\mathrm{Pr}$
M	Mass of fluid
N	Number of components in the mixture
P	Fluid pressure
Pr	Prandtl number
Q	Heat transfer per unit volume
R	Universal gas constant
Re	Reynolds number
s	Specific entropy of bulk fluid

Sc	Schmidt number
T	Fluid temperature
t	Time
$\mathbf{u}$	Velocity vector
u, v, w	Components of velocity in the x, y, z directions
W	decompression wave speed
w	Molecular weight
x	mole fraction of the component
$\mathbf{x}$	Spatial position vector
x, y, z	Spatial dimension
Y	Mass fraction
Z	Mole fraction using in PR EOS

Greek Symbols

Symbol	Description
α	Void fraction of vapour/gas phase
Γ	Mass transfer source term
Δ	Difference
δ	Reduced density
ε	Residual, Nikuradse sand-grain roughness
ζ	Thermodynamic properties of two phase mixture
Θ	Relaxation time
θ	Angle of inclination of the pipeline to horizontal
κ	Parameter at PR EOS
μ	Viscosity
ρ	mass density
$\boldsymbol{\sigma}$	Viscous stress tensor
τ	Inverse reduced temperature, frictional force term

υ	Mole volume
ϕ	Dimensionless Helmholtz energy
ψ, φ	Non-dimensional parameter of pressure difference
ω	Acentric factor
∇	vector operator

Subscripts

Symbol	Description
Q_0, Q_1	Parameter for substance using in PRSV EOS
Q_c	Q at critical condition
Q_f	Q of fluid
Q_{GR}	Q related to vapour/gas
Q_i, Q_j	Q of specie i, j
Q_{ij}	Binary specific parameter
Q_{ijk}	Q of at the point (i, j, k)
Q_{in}	Q at the initial condition
Q_l, Q_v	Q of liquid, vapour phase
Q_m	Q of specie m
Q_{ML}	Q of metastable liquid
Q_p	Q at constant pressure
Q_{qv}	Q of quality of dryness fraction of fluid
Q_R	Reduced parameter
Q_r	Q of mixture

$Q_{s,HRM}$	$\boldsymbol{Q}$ calculated with HRM
Q_s	$\boldsymbol{Q}$ related to speed of sound, saturation parameters
Q_{sv}, Q_{sl}	$\boldsymbol{Q}$ of saturated vapour and saturated liquid
Q_w	$\boldsymbol{Q}$ of pipeline wall

Superscripts

Symbol	Description
Q^*	$\boldsymbol{Q}$ at the isentropic condition
$Q^{(n)}$	$\boldsymbol{Q}$ at the iteration time n
Q^0	Part of $\boldsymbol{Q}$ dependent on the ideal-gas behaviour
Q^G	$\boldsymbol{Q}$ at the Eulerian phase
Q^L	$\boldsymbol{Q}$ at the Lagrangian phase
Q^r	Part of $\boldsymbol{Q}$ taking into account the residual fluid behaviour

List of Figures

List of Tables

Chapter 1 Introduction

1.1. Background

Carbon capture and storage (CCS) is considered as an effective and feasible means to mitigate the contribution of greenhouse gas carbon dioxide (CO_2) emissions to global warming. Such a technology inevitably involves the transport of CO_2 from source to storage sites. Pipeline is the most effective way to transport large quantities of CO_2 over long distances.

Considerable industry experiences exist on the transport of CO_2 via pipelines. For example, there are long distance transport pipelines with a total length of over 6000km in the USA and Canada [1], which operate for enhanced oil recovery (EOR) projects. There also exist other CO_2 pipelines operating in Europe, for example Snøhvit pipeline which is the world's first offshore CO_2 pipeline [2]. Additionally, CCS demonstration projects [3] are also being carried out, such as FutureGen 2.0 in the USA [4], Compostilla Oxy CFB 300 in Europe [5] and GreenGen and Shenhua CtL in China [6].

Fracture control is one of the most important issues in designing CO_2 pipelines [7]. The aim of fracture control is to prevent or minimize the length of long running fracture. Running fracture is a typical brittle one caused at lower energy inputs [8]. When decompression response is slower than the spread of fracture [9], the fracture will propagates along the pressurized transportation pipeline further resulting in potential catastrophic failures.

Fracture control can be achieved by specifying appropriate toughness for the transmission pipelines [7]. Toughness is a critical property of transmission pipelines and is directly related to the safe operation of pipelines. Sufficient

toughness for pipeline design is determined by evaluating the required fracture toughness of the pipeline steel with a critical crack size. Because it is often impossible to construct pipelines with a sufficiently high toughness, some pipelines are installed with mechanical crack arrestors at regular intervals along the length of pipelines [10] in order to arrest the running fractures. However the installation of crack arrestors is quite expensive and leads to a considerable increase in the cost of pipeline construction and hence should be avoided [11].

The Battelle two-curve method (BTCM) [12] is widely used in fracture propagation control studies to determine the toughness required to arrest the running fracture in a pipeline. It describes the resistance and driving force with respect to the relationship between fracture and fluid decompression wave speeds. Under the local pressure condition, if the fluid decompression wave speed is larger than the fracture speed, the fracture tip stress will decrease and the fracture can finally be arrested due to the fact that the fracture tip stress is less than the arrest stress of pipeline, otherwise the fracture will inevitably propagate along the length of pipeline. Figure 1.1 shows the application of BTCM [7]. Two kinds of curves are presented in the figure: decompression curves and pipeline fracture curves. They describe variation of decompression wave speed and fracture velocity with the local pressure, respectively. Moreover, the decompression curve indicates the propagation of decompression wave immediately following a rupture. The decompression curves for methane and CO_2 are demonstrated here.

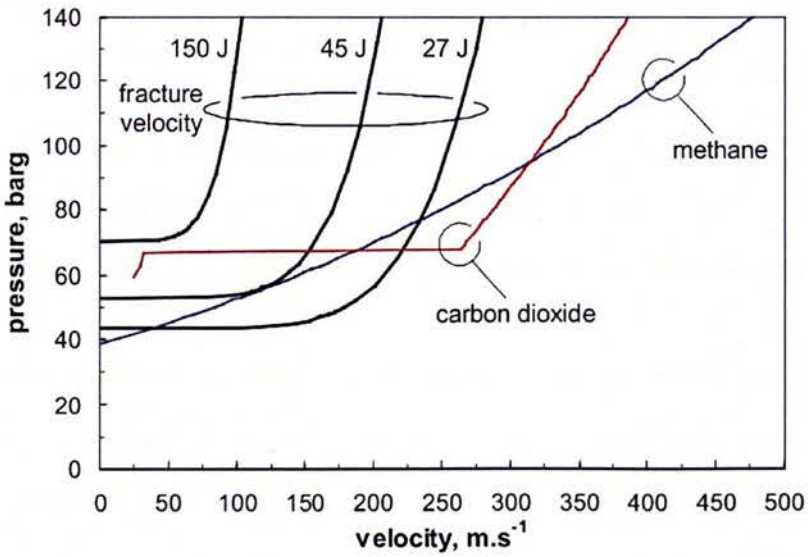

Figure 1.1 Illustration of the BTCM [7]

Some studies [13], [14] claimed that CO_2 pipelines are more susceptible to ductile fracture propagation than the hydrocarbon pipelines. As demonstrated in Figure 1.1, the decompression curve of CO_2 is greatly different from methane. There exists an apparent plateau for the decompression curve of CO_2. Hence CO_2 pipeline may require higher toughness in comparison with the hydrocarbon pipeline due to its higher decompression pressure. Depending on the initial fluid pressure and temperature, phase transition may result in a uniquely prolonged decompression process, and further affect the profile of decompression curve. Although commercial codes, such as GASDECOM [15], are available to predict the decompression curves for natural gas pipelines, it is questionable that some of these codes without modifications have been directly used for CO_2 pipelines neglecting the complex thermodynamic properties such as phase transition.

Decompression is a complicated process describing the expansion of the high-pressure fluid to the condition of low-pressure (for example, the atmospheric pressure), or describing the rapid escape and release of pressurized

fluid from containing pipelines. Accurately predicting the variation of flow parameters such as pressure, temperature and void fraction, is quite important to determine decompression curve, and to further investigate the characteristics of decompression. Moreover, the local distributions of flow parameters inside pipelines may significantly benefit the pipeline design and operation [16].

In summary, it is vital to study the decompression behaviours of high pressure pipelines, particularly when phase transition is involved. Due to possibility of involving the complicated two-phase flow, depending on the initial fluid pressure and temperature, the decompression process of high pressure CO_2 pipeline is further complicated.

1.2. Pipeline Decompression

The decompression phenomenon is an extremely important issue in the chemical and oil/gas industries. In the chemical industries, decompression of pressurized pipelines or vessels can be a dangerous operation due to the very low temperature caused by the rapid decrease of pressure of pressurized fluid [17]. For the oil/gas industries, controlled decompression of transportation pipelines is frequently required in order to perform normal maintenance. Additionally, the low temperature caused during decompression process may lead to the formation of hydrates blocking the transport of pipeline if free water is present.

For the CCS technology, captured CO_2 should be transmitted via high-pressure pipelines in gaseous or dense phases. In the thesis dense phase specifies liquid phase CO_2. If a pipeline ruptures, a rapid decompression wave is initiated at the rupture plane and propagates into the undisturbed regions at the local speed of sound of the transported fluid. The speed represents the rate of a perturb

passing the local position. In the context of the pressure-enthalpy phase diagram (see Figure 1.2), the decompression path may meet the dome-shaped phase boundary depending on the initial condition. When the path intersects with the phase boundary, the decompressed CO_2 may become metastable, i.e. supersaturated if the decompression rate is fast and then undergoes phase transition. If the decompression path meets the right-hand side of the phase dome, i.e. point B, phase transition occurs in the form of liquid condensation from gaseous phase, i.e. the new phase emerges as tiny liquid particles subject to further growth due to exchanges of mass and energy with the gaseous phase. Accompanying the condensation process, an amount of latent heat is released and the metastable CO_2 tends to restore back to an equilibrium condition. While in the case of the decompression path intersecting with the left-hand side of the phase dome, i.e. point A, phase transition occurs in the form of gas vaporization, i.e. the new phase appears as nucleated vapour bubbles which are also subject to further growth due to exchanges of mass and energy with the liquid phase. The process of rapid appearance of vapour bubbles in the liquid fluid due to fast decompression is often referred to as flashing. After the inception of nucleated bubbles, different two-phase flow regimes e.g. bubble, slug, annular, stratified flows may develop along the pipeline depending on flow geometries, fluid properties and flow conditions. The existence of different flow regimes greatly complicates the numerical analysis due to highly inhomogeneous and non-equilibrium nature of the flows compared to the condensation of the two-phase flow. In both cases, the resulting flow is most likely two-phase and choked at the rupture plane. The depressurized CO_2 might fall below the triple point near the rupture plane and form solid, which is also called dry ice. The appearance of dry ice can further complicate the analysis of the decompression process.

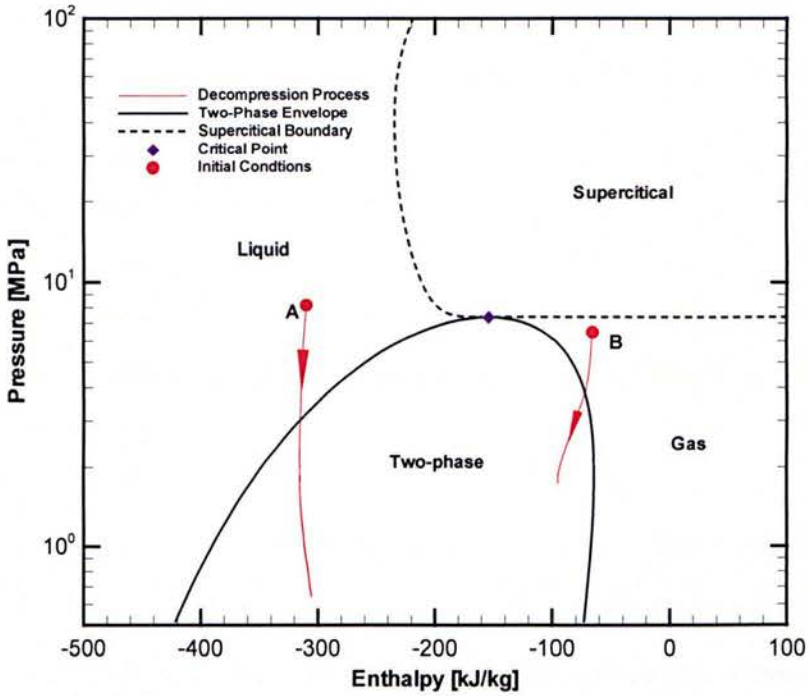

Figure 1.2 Pressure-Enthalpy diagram of CO_2 decompression processes

Therefore, during the decompression process of CO_2 pipeline, the risk is caused not only because of the low temperature in the pipe wall but also because of the large outflow rate resulting from the high pressure and large inventory of long pipelines. Eldevik et al. [18] claimed that rapid decompression following the failure of pressurized CO_2 pipeline may result in quick decrease of temperature below the triple point, and the low temperature could cause some problems relating to the operation and structure of CO_2 pipeline. The deposition of solid CO_2 on pipelines may make the local temperature as low as -78°C [19]. This can have a severe effect on the toughness or resistance of pipelines.

In summary, the study on decompression behaviours of pressurized CO_2 pipeline is important in the assessment of safety practices and procedures to prevent or minimise the consequences of CO_2 pipeline failures. The information on decompression behaviours of pressurized CO_2 pipeline is helpful to predict the probability of pipeline ductile fracture propagation. Most

notably, the two-phase flow involved during decompression process should be taken into consideration to evaluate the decompression behaviours.

1.3. Objectives of Study

The main goal of the study is to develop a CFD model of transient two-phase flows for high pressure pipeline decompression. The main objectives of the study are as follows:

- Development of a computational fluid dynamic solution technique for two-phase model applicable to simulation of highly transient two-phase flow. The new developed model should ensure the computational efficiency and numerical stability.

- Implementation of Equation of State to calculate the thermodynamic properties of real fluid.

- Determination of suitable physical models to deal with the two-phase flow. Such models take into account the effects of wall friction and heat transfer.

- Implementation of arbitrary Lagrangian-Eulerian method to discretize the governing equations by dividing the time solution into Lagrangian phase and Eulerian phase.

- Validation of the model against the current existing experimental data for natural gas, rich gas and liquefied petroleum gas (LPG) obtained from the published papers.

- Validation studies with the experimental data for CO_2 provided by National Grid and additional data obtained from other sources.

- Predictions of the decompression characteristics of gaseous and dense phase CO_2 pipeline. The decompression flow of CO_2 pipeline is carefully studied.

1.4. Organization of Dissertation

The dissertation consists of six chapters. The first chapter gives a brief introduction to the research, and objectives of the present study are briefly described and the organization of dissertation is also presented.

Chapter 2 firstly provides an overview of previous studies on two-phase flow models. Next the popular mathematical models for decompression flow are particularly reviewed. Then the mathematical methods to model transient two-phase flows for pipeline decompression are described in more detail. In this chapter, the Navier-Stokes (NS) equations are represented for unsteady three-dimensional compressible flow. Some assumptions are made to deal with the transient two-phase decompression flow. The Homogeneous Equilibrium Model (HEM) is described to deal with the two-phase flow. Some important issues are addressed, such as equations of state and boundary conditions. The former is used to calculate the thermodynamic properties of real fluid, and the calculation of speed of sound is given in more detail. Wall friction and heat transfer are specified as boundary conditions to define the interaction between the wall and fluid. In addition, Homogeneous Relaxation Model (HRM) is also incorporated to take account of the non-equilibrium effects for decompression flow. The volumetric vapour generation rate is specified to close the conservation equations of HRM. The definitions of thermodynamic properties

for two-phase fluid with HRM are determined. The calculation of the metastable liquid is specified. The thermodynamic properties of two-phase fluid are determined with HEM and HRM.

Chapter 3 describes the processes of numerical methods and discretization. The methods of temporal and spatial difference schemes are demonstrated. arbitrary Lagrangian-Eulerian (ALE) method is particularly applied to discretize the governing equations. The time solution of the governing equations is divided into two phases: Lagrangian phase and Eulerian phase.

Chapter 4 investigates the decompression behaviour of shock tube containing natural gas, rich gas and LPG. Decompression wave speed, one of key characteristics of decompression process, is firstly defined. Several shock tube cases are calculated to validate the model against the existing experimental data. Comparisons of flow parameters and decompression wave curves are made between experiments and predictions. The grid-dependence of present model is assessed against some decompression simulation tests.

In Chapter 5, the decompression characteristics of gaseous CO_2 pipeline are examined. Both pure CO_2 and CO_2 with impurities are chose to investigate the decompression behaviours. Simulations are implemented to predict the gaseous CO_2 pipeline decompression behaviour. The experiments commissioned by National Grid are mainly utilized to validate the current model. Additionally, the effects of wall friction and heat transfer are examined. The predictions with different equations of state are compared.

Likewise, the decompression behaviours of dense CO_2 pipeline are investigated in Chapter 6. The initial conditions such as temperature and pressure, impurities and EOS employed in the simulation are evaluated to identify the influences on

decompression wave curve. The experimental data of dense CO_2 shock tube are used to further validate the current model. Additionally, the effects of heat transfer and wall fraction are also examined. Finally, non-equilibrium effect is particularly investigated by comparing the prediction with HEM and HRM.

In Chapter 7, the main findings of the thesis are summarized. Lastly, suggestions for future research are proposed.

Chapter 2 Mathematical Methods: Literature Review and Proposed Improvements

2.1. Introduction

Numerical models of two-phase flows range from the simple HEM to more rigorous two-fluid models. Under the homogeneous equilibrium assumption, the two-phase mixture can be treated as a pseudo-fluid governed by the same conservation equations as a single-phase flow. The HEM has been widely used in the literature [20]–[27] and proven to be accurate enough for long pipeline where there is sufficient time to reach equilibrium conditions between two phases. The more rigorous two-fluid models [28]–[30] take account of heterogeneous and non-equilibrium conditions of two-phase flows by solving two sets of conservation equations for each phase, which can have different velocities, temperatures and pressures, more detailed flow information can be taken into account. However, in spite of its potential superiority to HEM for the problems of short tube decompression, the two-fluid models pose severe closure problems [31]. An averaging technique is required to obtain the averaged conservation equations. Additionally, the exchanges of mass, momentum and energy between each phase appear in the equations with unknowns which need to be modelled by empirical correlations in order to close the system of conservation equations. There are also adjustable coefficients, which need to be tuned against experimental data. This poses practical difficulties for the method to be used in the case of pipeline decompression since there is very little data available and hardly any in the public domain, particular for the decompression of CO_2 pipelines. The few proprietary experimental data sets available from industry hardly contain

sufficient details to facilitate the fine tuning and closure of the two-phase heterogeneous and non-equilibrium approach.

Most previously published work on pipeline decompression [20]–[24] is concerned with the depressurizations of water and hydrocarbons in nuclear and petrochemical industries. In the nuclear industry, the typical pipe length scale is relatively small and the decompression rate is fast. To handle the highly inhomogeneous and non-equilibrium flows resulting from the fast decompression rate, the blowdown models (e.g. RELAP5 [32]) are generally based on two-fluid models, since the HEM will underestimate the critical flow rate [33]. The situation is slightly different for the petrochemical industry. Since the length scale of pipelines is much larger, the non-equilibrium condition is only significant for the locations close to the rupture plane during the very early stage of release and the inhomogeneous conditions are more significant in the very late stage of the decompression process. The benefit of the two-fluid models is generally very limited, especially for decompression studies.

For typical hydrocarbon pipelines, working fluids generally comprise multi-component hydrocarbon mixtures, and for CO_2 pipelines working fluids should comprise CO_2-rich mixtures (CO_2 with limited volume fraction of impurities). To deal with the phase transitions of the mixture equilibrium flash calculations are usually conducted to calculate the mole fractions of the two phases under a thermally equilibrium condition from two independent variables. General CFD codes do not provide functions to handle this kind of phase transition; hence models for pipeline decompression have been developed in the literature. Most models are based on the homogeneous equilibrium and isentropic flow assumptions to predict the slow transient release. However they are not suitable for the prediction of fast moving decompression wave propagation due to the limitation on computational time-step.

The chapter first reviews the studies on two-phase flows, and then provides the description on the popular mathematical models particularly for decompression flows. Next, the chapter introduces the mathematical formulations for non-reactive two-phase compressible flows. The mathematical description is based on the assumption that the fluid is a continuum, so that all the transport equations arising from the fundamental principles of conservation of mass, momentum and energy can be applied. A pipeline decompression model suitable for fast decompression as well as slow blowdown has been developed with homogeneous equilibrium approach. Also, the model is extended with relaxation approach to the non-equilibrium condition between phases. As the important factor of flow behaviours, the thermodynamic relations of two-phase fluid are established firstly. Finally, the boundary conditions, i.e. wall transfer and friction, are specified for pipeline decompression flow.

2.2. Two-phase Flow Models

Two-phase flow is a highly complex phenomenon, and there are a large variety of two-phase flows. Based on the work of Ishii [34], two-phase flows can be classified into three categories: separated flows, mixed flows and dispersed flows. The separated flow occurs when the fluids of two phases move separately, and there exists obvious interfaces between two regimes, for example, film condensation or boiling, jet condenser. The dispersed flow means that one phase fluid disperses into the other one, such as gas bubbles in liquid or liquid droplets in gas. The decompression process of pressurized pipeline is far more complicated two-phase flow because various flow regimes occur at different times. For example, decompression from a dense-phase liquid may evolve from bubbly flow to slug flow and then to droplet flow.

There are a large number of models to simulate two-phase flows. The two-phase flow caused by the pressurized pipeline decompression is a

particular critical two-phase flow. A brief review on various analytical approaches of critical two-phase flow was given by Wallis [33]. With consideration of their complexity and practical applicability, three types of models are usually derived: (1) homogeneous equilibrium model; (2) models incorporating limiting assumptions; and (3) non-equilibrium models.

2.2.1. HEM

HEM is one of the most simplified models to treat two-phase flows. It is a widely used in many simulation codes. HEM was proposed on the basis of assumption that two-phase mixture is treated as a pseudo-fluid, namely, the two phases are in equilibrium everywhere sharing same velocity and temperature and pressure. In other words, the two-phase system is assumed to be in mechanical and thermal equilibrium between phases. It is worthy to note that the chemical equilibrium is not considered in the study because of actual situation in pipeline decompression. Therefore, the system of conversation equations for an equivalent single-phase flow [20] can be employed to describe two-phase flow.

Wallis [33] claimed that HEM shows reasonably good predictions for the critical mass flux in long pipes where there is enough time to achieve the equilibrium condition. However, for shorter pipes where there is insufficient equilibrium time, the model can predict with a large error. Additionally, HEM has been widely used for modelling of pipeline decompression in the literature [21], [29], [35] and it also has been proven to be accurate for long pipeline decompression where there is sufficient time for equilibrium conditions to establish between two phases [29].

2.2.2. Models Based on Limiting Assumptions

HEM is based on the complete assumptions with mechanical and thermal equilibrium. With consideration of the possibility to make alternative limiting assumptions, a set of other models are derived but the details of the non-equilibrium phenomena are not yet taken into account.

Frozen flow model is made with the limiting assumption that there do not exist any interphase transfers between phases so that flow is not allowed any phase change and the quality remains constant. This assumption is nearly satisfied for flow in short pipes or nozzles. While no interphase transfer is the key assumption in this model it may be combined with other assumptions [36] such as those of isentropic expansion and no slip.

Slip flow model is developed with consideration of the relationship between the velocities of each phase. In the slip flow model, the limiting assumption is in the equilibrium between the phases. Two principal slip flow models are those by Fauske [37], [38] and Moody [39].The difference of these two models is how the exit conditions are determined. In the Fauske model, the exit conditions are determined by a momentum balance and the maximum flow rate occurs at a slip ratio $\varepsilon = V_G/V_L = (\rho_L/\rho_G)^{1/2}$, while in the Moody model, the exit conditions are determined by an energy balance and the maximum flow rate occurs at $\varepsilon = V_G/V_L = (\rho_L/\rho_G)^{1/3}$. Therefore, the slip flow models treat the velocity ratio as a variable to be determined to obtain the maximum flow rate, without describing how this condition is actually achieved.

Apart from the frozen flow model and slip flow model, an isentropic stream tube model is described by Wallis and Richter [40], which is based on isentropic expansion of individual stream tubes originating from the

vapour-liquid interface as flashing. In this model, the thermodynamic equilibrium is assumed and the velocity field is continuous.

In brief, there is no any evidence to prove that one of these limiting models is inherently a "better" model than any others. Additionally, the representation of the parameters of the fluid behaviour cannot be actually obtained from any models. Hence, this type of models is unsuitable to study the decompression flow.

2.2.3. Non-equilibrium Models

The third type of models attempts to take into account non-equilibrium effects. These models range all the way from an empirical model to account for non-equilibrium by introducing a simple empirical correction factor or function to complicated two-fluid models by establishing a complete set of equations of conversation of mass, momentum and energy for each phase coupled with treatments for phase change.

Empirical Models

The employment of empirical correction factor or function is a simply way to handle non-equilibrium effects. Henry and Fauske [36] introduced a single coefficient to treat the non-equilibrium vapour generation. The coefficient is correlated as a function of the equilibrium vapour generation. The calculated non-equilibrium vapour rate is then utilized to predict the critical flow with a further simple no-slip assumption. Additionally, Simpson and Silver [41] proposed a model incorporating two empirical coefficients to take into account nucleation. An empirical fitting of data was employed to determine both coefficients and no-slip assumption is used.

Relaxation model was proposed by several authors [42]–[44] with the basic idea that the vapour generation rate is proportional to the departure of the actual condition from unconstrained equilibrium condition. Hence the rate of change of quality is made as the simplest linear approximation which can be regarded as the first term in a Taylor-series expansion [44]. The necessary coefficient may be determined by a function of local conditions. For example, the relaxation time, as an important coefficient to describe the degree of departure from equilibrium condition, is proposed by Bilicki and Kestin [44] to be correlated to the partial derivation of Helmholtz free energy with respect to the equilibrium quality. Afterwards, based on the classical measurements conducted by Réocreux [45], Downar-Zapolski et al. [31] stated that the relaxation time is correlated with void fraction and non-dimensional pressure difference.

Physically Based Models for Thermal Equilibrium

Other non-equilibrium models emphasize the physical descriptions of the process of phase change, such as nucleation and vapour generation.

Nucleation

Bubble nucleation occurs near walls or at the bulk of the liquid or by entrainment from other parts of the system. Nucleation characteristics are a key factor for the behaviours of two-phase flow [46]. There are various assumptions of the source or bubbles, but all of them are empirical. Some are made based on the assumed density of bubble with a certain initial radius, whereas the magnitudes of initial bubble are selected to match the behaviour of two-phase flow rather than to describe the actual characteristics of bubble nucleation. Moreover, Ardron and Ackerman [47] claimed that actual numbers of bubble nuclei may be orders of magnitude lower than that assumed.

Vapour generation

The rate of bubble growth is assumed to be dominated by the thermal conduction between liquid and bubble [48]–[52] once the initial influences of surface tension are overcome. Noted that the interactions of bubbles are ignored and a thermal boundary layer approach is often used to specify the conduction between the phases. Hence the inherent restriction makes the method only be available at very low qualities [33]. Moreover, the boundary thermal conduction theories predicted too low rate of bubble growth because the convective contribution to heat transfer is of the same order of magnitude as conduction but it is not taken into account [50]. Also, the equal phase velocities are assumed in the model.

Wallis [33] summarized that the development of such models does not offer much improvement on the purely empirical models. Moreover, many physical uncertainties are necessarily reconsidered to describe the actual physical phenomena. Improvement to this situation may be achieved with the establishment of the detailed physical characteristics of bubbles and nuclei and the evolvement of model to compatible with this physical evidence. However, this may be impossible in the practical usefulness due to the lack of actual physical characteristics.

Two-fluid (separated flow) Models

Two-fluid or separated flow models [53]–[56] are known as more complicated mathematical methods to represent most of the recognized non-equilibrium phenomena. A system of equations of conservation of mass, momentum, energy for each phase is built and interaction terms are incorporated to represent the interphase heat, mass and momentum transfer. Upstream conditions, which may contain a description of nucleation points, are supplied as one boundary

condition. The solution is implemented numerically in the downstream direction.

The key problem of this approach is in determining what coefficients and functions to incorporate the basic system of equations to represent the interactions between the phases and to close the system. To identify the inter-phase drag and apparent mass, for example, one must know at least the flow pattern and void fraction. We should assume the usefulness of steady-state drag correlation to unsteady flows, and determine the effects of interface size and shape changes on inter-phase forces.

In order to reduce the number of equations of a full two-fluid model, drift-flux models [28], [57], [58] are proposed by characterizing the relative motion of the phases [42]. The model calculates the drift flux from independent correlation rather than through the solution of transport equations. This approach is ill-advised. The relative movement in a rapidly accelerating flow with a changing void fraction is obtained from a different set of terms in the momentum balance terms rather than would be determined under the conditions from which the correlations were derived. Additionally, one should require another equation based on the mechanistic principle to determine the drift flux.

On balance, the stage of development of two-fluid models is not such as to make them more useful than the empirical ones [33], unless there is the adequate basis of detailed experimental data from which the components of the model, such as nucleation characteristics, interphase mass and heat transfer, can be determined independently. But this should necessarily require a set of thorough comprehensive study with the additional instrumentation to measure quantities such as interphase area, temperature and velocities of each phase or other parameters, for example, Réocreux's works [45]. To do this, the collection of the information can only be conducted under very carefully controlled

laboratory conditions. Briefly, the two-fluid models are sophisticated approaches, but the specification of physical phenomena on the nucleation characteristics and upstream flow condition, such as temperatures of each phase, void friction and flow pattern, is quite different even almost impossible in a practical system.

2.3. Mathematical Models for Decompression Flow

The decompression phenomenon caused by the rupture of pressurized pipeline is a subject of particular interest to the chemical, oil/gas and CCS industries. Some popular mathematical models for decompression flow are mentioned in this section. They are classified into two major categories: Finite difference methods (FDM) and method of characteristics (MOC). Most existing numerical models for pipeline decompression are based on the FDM in the Eulerian frame. The MOC is based on characteristics of wave propagation. Here, the group of FDM involves three models: DECAY, OLGA and BLOWDOWN. Furthermore, UCL model and PipeTech as popular MOC models are also reviewed.

2.3.1. DECAY

DECAY [59] is a model developed by British Gas to study the high-pressure gas mixture decompression behaviour following pipeline rupture. The assumptions of isentropic and homogeneous equilibrium flow were made to disregard the effects of heat transfer and friction. Additionally, the model can only deal with the flow inside the horizontal pipelines. In order to consider the fluid properties particularly when decompression path enters into the two-phase region, the Soave-Redlich-Kwong equation of state (SRK EOS) [60] was built into the model to calculate the thermodynamic properties.

A series of shock tube experiments with different fluid compositions were presented to validate the model, involving 9 British Gas shock tube experiments, 5 BMI shock tube tests, one University of Calgary shock tube test, one Shell full-scale test, 2 Foothills full-scale tests and 3 CAGSL full-scale tests. The predicted pressure- and temperature-time traces (British Gas shock tube experiments) and decompression curves (the others) were compared with the experimental data. The researchers stated that there is a good agreement between the predicted results and experimental data. However, the involved cases did not take account of the pipelines conveying liquid or flashing fluids. More importantly, disregarding the effects of friction and heat transfer on decompression behaviour may under-predict the flow parameters following the pipeline rupture.

2.3.2. OLGA

OLGA [30] is a dynamic two-fluid model to simulate the two-phase oil and gas flow in pipelines. The development of OLGA started in 1979. It was initially developed by Institute for Energy Technology. Then Statoil financed its development for the hydrocarbon industry in 1983 to simulate slow transient flow associated with mass transport, rather than fast transients flow. Therefore the model can be stable for long timestep and not restricted by speed of sound to simulate the case with the range from hours to weeks. Its physical model was initially based on small diameter data for low-pressure air/water flow. The early model of OLGA could successfully simulate bubble/slug flow regime, but the stratified/annular flow regime was not described adequately due to neglecting of a droplet field moving approximately at the velocity of gas. Bendiksen et al. [30] addressed this problem and extended the model to deal with hydrocarbon mixtures.

OLGA traditionally treats two-phase flow as separate gas and liquid flow. The mass conservation equations are separately modelled for gas, liquid bulk and liquid droplets, which are coupled interfacial mass transfer. Two momentum equations are applied: a combined equation for the gas and liquid droplets and a separate equation for liquid film. A mixture energy-conservation equation for all phases is used, in consideration of heat transfer from the pipe walls by a user specified heat transfer coefficient. Implicit methods are applied for solving the conservation equations to meet the requirement to simulate the slow and small breaks flow. All fluid properties are calculated and tabulated as pressure and temperature before OLGA is run, and the actual values at a given point during calculation are found by interpolating in these tables.

Several studies validated OLGA under the slow and fast transients flow situations. Shoup et al. [61] implemented the simulations with OLGA and compare with filed data obtained by Deepstar for the blowdown of an onshore pipeline, the precise mixture composition was not given in the prediction and measurement. It was supposed that release happens through a valve installed at the end of the pipeline in order to simulate blowdown of the pipeline. The variations of pressure with time were presented in graphs for comparing with the measured data of field test. There was a reasonable agreement between the predicted pressure-time traces by OLGA and measurements. Recently, Botros et al. [62] conducted 10 decompression tests using a 172m long instrumented shock-tube rig containing inventories ranging from pure nitrogen, conventional gas to typical rich gas mixtures. The decompression of the shock tube was triggered by failure of a rupture disc located at the end of the shock tube. The fast response pressure transducers and temperature probes were mounted along the test section of shock tube to measure pressure and temperature in time, respectively. The results of 4 cases were only shown in Botros et al. (2007) [62] due to the space limitation and more details and results can be found in Botros

et al. (2004) [63]. The pressure- and temperature-time traces were calculated by OLGA, but the perditions were not in good agreement with the measurements. OLGA over-predicted the pressure decline during blowdown, and the predictions of temperature-time traces were lower than the measurement. The predicted speed of frontal wave by OLGA was significantly lower than experimental data. Botros et al. claimed that the use of isothermal correlation in the formulation of the energy equation causes the disagreement. It was suggested that the thermodynamic properties module, such as the speed of sound, should be further investigated, particularly at phase crossing and two phase region.

The further development of OLGA is very limited progress due to dependency on the availability of empirical data such as the phase transition between the different flow regimes, as well as the instability problems of numerical simulation. Moreover, there is little research literature with respect to the correct modelling of highly transient flows and formulation of the choking conditions at rupture plane. Finally, the solution of separate conservation equations for each constituent phase in the two-fluid models is actually extremely time-consuming. The behaviour of phase change is not appropriately incorporated, due to the inherent limitations in the numerical methods and two-fluid model in OLGA [64],

2.3.3. BLOWDOWN

BLOWDOWN [65] was a computer code developed by Imperial College to simulate the expansion process following the blowdown or depressurisation of network of pressure vessels and associated pipes containing hydrocarbons, then extended to simulate the depressurization of pipelines [66], [67]. Mahgerefteh et al. [68] developed a modified version of BLOWDOWN which incorporates the cubic equations of state including SRK EOS [60] and Peng-Robinson

equation of state (PR EOS) [69] for simulating blowdown of vessels containing multi-component hydrocarbon mixtures.

BLOWDOWN included non-equilibrium effects, heat transfer between fluid and vessel wall, inter-phase fluxes due to phase change such as condensation and evaporation. BLOWDOWN can predict the pressure, the temperature of fluid and vessel wall and discharge rate from the vessel through the release orifice, and their variations with time. A series of variable pressure increments were approximately given during the depressurisation process.

The extended version of BLOWDOWN can simulate the depressurisation of pipelines in consideration of the frictional pressure drops along the pipeline. During the calculation process, a pipeline is divided axially into many elements. The sizes of elements are varied dynamically during the calculation assuming that the changes of physical properties along pipeline can be neglected. The flow in pipeline is assumed to be quasi-steady for single or two-phase flow. Homogeneous flow is also given for two-phase flow, namely two phases sharing the same velocity. Heat transfer between fluid and pipeline wall is assumed to be forced convection. Heat transfer between pipeline wall and atmosphere is given as forced or natural convection. The mass, energy and momentum conservation equations are solved at each element in the pipeline with the specific boundary condition of ambient and choking pressure at the plane of exit plane or orifice.

Some experiments were conducted by Haque [70] with three vessels. BLOWDOWN was validated against the experimental measurements. Additionally, Isle of Grain full-scale experiments [71] were conducted jointly by Shell Oil and BP with two 100m long pipelines, nominal inner diameter 154 mm and 52 mm respectively. Eighty four main tests were conducted with LPG (ca. 95 mole % Propane and 5 mole % Butane), which involved the full bore

rupture and orifice discharge. The pressure of experiment ranged from 8bar to 21bar.The pressure, temperature and fluid inventory were measured and recorded in time. The predictions of 8 tests in Isle of Grain full-scale experiments were presented in the literature[66], more details can be found in the literature [67]. There was a reasonable agreement between the predictions and experimental data, but there were relatively large discrepancies in temperature-time traces towards the end of the blowdown. This may be caused by the inadequate treatment of heat transfer between the fluid and pipeline wall. Although BLOWDOWN produced reasonable agreement with experiments, the model did not take account of the expansion wave propagation which has a significant effect on the release process particularly for the blowdown of long pipelines [72].

2.3.4. UCL Model and PipeTech

The research group of Prof. Mahgerefteh in the Department of Chemical Engineering at University College London (UCL) has carried out a series of researches on the problems of the depressurization or blowdown of pipeline since 1997 [14], [26], [27], [35], [68], [73]–[76]. The transient modelling was developed for simulating the blowdown flow following pipeline rupture based on the solution of hyperbolic conservation equations for one-dimensional flow using the rigorous numerical scheme method of characteristics (MOC) [77].

Mahgerefteh et al. [26] firstly developed a transient outflow model to study the flow of pipeline rupture with three conservation equations for one-dimensional flow including the mass, momentum and energy equation based on MOC. The dynamic response of emergency shutdown valves following full bore rupture of pressurized gas pipelines was investigated. The working fluid in pipelines was treated as an ideal gas in order to reduce the requirements of calculation and demonstrate the different dynamic effects in pipelines. Some important

conclusions were drawn to analyse the effect of flow behaviour following full bore rupture of gas pipeline on the dynamic response of emergency shutdown valves. Mahgerefteh et al. [35] introduced the PR EOS [69] to calculate the real fluid behaviour and involved the pertinent hydrodynamic relations which took account of the slip velocity between two phases. The simulations were conducted with HEM [28], [29] in which the two-phase mixture was assumed to be locally at thermal and phase equilibrium. Then, the real fluid model was used to predict the effect of phase transition on the dynamic behaviour of emergency shutdown valves [27]. Vahedi [78] extended the model to investigate the influence of enlargement and inclination of pipeline on the flow behaviour following pipeline rupture. Oke et al. [76] studied the outflow characteristics following the puncture of pipelines. Mahgerefteh et al. [75] accomplished the simulation on the outflow following the rupture of pipeline network. A fast numerical interpolation technique was developed [74] to reduce the computational runtime.

PipeTech [79] was developed with a combination of the previous further developments of Mahgerefteh et al. UCL model. PipeTech was a simulation software for calculating the outflow following the rupture or puncture of long pipelines containing the pressurized fluid such as hydrocarbons. It was developed based on the existing studies on simulation of pressurized pipeline blowdown in UCL. PipeTech was able to calculate the outflow under complex conditions, such as inclined pipelines, puncture orientation, real fluid multi-component mixtures and multiple segment pipelines. It was reported that the validation against the experiment data has been made for hydrocarbon pipelines. Nowadays, PipeTech is widely used by some corporations such as BP, Shell and regulatory body UK Health and Safety Executive.

2.3.5. GASDECOM

GASDECOM [15] is also involved here as a widely used program to calculate the decompression wave speed for mixtures of hydrocarbons [80], [81]. The Benedict-Webb-Rubin- Starling (BWRS) equation of state [82] is implemented into GASDECOM to give accurate estimates of the properties of heavy hydrocarbons and complex hydrocarbon mixtures. GASDECOM is based on the assumptions of isentropic decompression, one-dimensional and homogeneous equilibrium flow. The effects of heat transfer and pipe wall friction are neglected. GASDECOM was also validated against the measurement of decompression curves for natural gas shock tube tests [62]. However, the code uses analytic methods to calculate the decompression wave speed without solving any transport equations. Therefore, it cannot provide any transient information like pressure-time and temperature-time traces.

2.4. Unsteady Navier-Stokes Equations

With consideration of the presence of decompression wave and fluid compressibility, the unsteady NS equations for a transient multi-component compressible decompression three-dimensional flow are first presented. Pipeline decompression can be treat as a typical one-dimensional flow, but the conservation system is written in three-dimensional form because the model may possibly be extended to be capable of predicting other decompression flow such as vessel blowdown. Moreover, although the mass fractions for each species keep constant during decompression process, they are also presented here in order to facilitate the further particular application, such as the decompression from the pipeline of high concentration to other part with low concentration.

For compactness, most of the conservation equations are firstly written in vector notation with bold symbols representing vector and tensor quantities. The unit vectors in the x, y and z directions are denoted by $\mathbf{i}$, $\mathbf{j}$ and $\mathbf{k}$ respectively. The position vector $\mathbf{x}$ is defined by

$$\mathbf{x} = x\mathbf{i} + y\mathbf{j} + z\mathbf{k} \tag{2.1}$$

The vector operator ∇ is given by

$$\nabla = \mathbf{i}\frac{\partial}{\partial x} + \mathbf{j}\frac{\partial}{\partial y} + \mathbf{k}\frac{\partial}{\partial z} \tag{2.2}$$

and the fluid velocity vector $\mathbf{u}$ is given by

$$\mathbf{u} = u(x,y,z,t)\mathbf{i} + v(x,y,z,t)\mathbf{j} + w(x,y,z,t)\mathbf{k} \tag{2.3}$$

where t is time.

In an Eulerian description of a multi-component transient flow for pipeline decompression, the complete transient conservation equations for mass, momentum, and energy are given as below [83]:

- **Mass Conservation Equation**

$$\frac{\partial \rho}{\partial t} + \nabla \cdot (\rho \mathbf{u}) = 0 \tag{2.4}$$

Mass fraction equation for species m:

$$\frac{\partial \rho Y_m}{\partial t} + \nabla \cdot (\rho Y_m \mathbf{u}) = \nabla \cdot [\rho D \nabla Y_m] \tag{2.5}$$

- **Momentum Conservation Equation:**

$$\frac{\partial(\rho \mathbf{u})}{\partial t} + \nabla \cdot (\rho \mathbf{u}\mathbf{u}) = -\nabla P + \nabla \cdot \boldsymbol{\sigma} + \rho \mathbf{g} \tag{2.6}$$

where

$$\boldsymbol{\sigma} = \mu \left[\nabla \mathbf{u} + (\nabla \mathbf{u})^T \right] - \frac{2}{3} \mu (\nabla \cdot \mathbf{u}) \mathbf{I} \tag{2.7}$$

- **Energy Conservation Equation:**

$$\frac{\partial(\rho I)}{\partial t} + \nabla \cdot (\rho \mathbf{u} I) = -P \nabla \cdot \mathbf{u} + \boldsymbol{\sigma} : \nabla \mathbf{u} - \nabla \cdot \mathbf{J} \tag{2.8}$$

$$\mathbf{J} = -K \nabla T - \rho D \sum_m h_m \nabla (\rho_m / \rho) \tag{2.9}$$

2.5. Equation of State

In order to facilitate the description of the following section, equation of state is firstly presented. An equation of state is usually required to close the above conservation equations. The PR EOS [69] and PRSV EOS [84] are employed to obtain the relevant fluid thermodynamic and phase equilibrium data. The PR EOS has become one of the most widely applied equations of state in industries due to its good agreement with experimental data for high-pressure fluid and its advantages in the prediction of liquid phase properties [85]. The PRSV EOS is employed to reproduce more accurately the vapour pressure data for a wide variety of substances due to the introduction of a single pure compound parameter [84]. The PRSV EOS equally well represents the properties of polar and non-polar compounds. In addition, the more accurate Span-Wagner equation of state (SW EOS) [86] is also implemented as a reference EOS for

pure CO_2. Finally, GERG-2004 is also involved to calculate thermodynamic properties of mixture.

2.5.1. PR EOS

The PR EOS is expressed as [69]:

$$P = \frac{RT}{\upsilon - b} - \frac{a(T)}{\upsilon(\upsilon + b) + b(\upsilon - b)} \tag{2.10}$$

where:

$$a = 0.45724 \frac{R^2 T_c^2}{P_c} \left(1 + \kappa \left(1 - \sqrt{\frac{T}{T_c}}\right)\right)^2 \tag{2.11}$$

$$b = 0.07789 \frac{RT_c}{P_c} \tag{2.12}$$

$$\kappa = 0.37464 + 1.54226\omega - 0.26992\omega^2 \tag{2.13}$$

$$\rho = \frac{w}{\upsilon} \tag{2.14}$$

P, T, ρ, υ and w are the absolute pressure, absolute temperature, density, mole volume and molecular weight of the fluid, respectively. It is worth noting that the density and mole volume using in the PR EOS are for the single phase. Characteristic pure-component parameters T_c, P_c are critical temperature and critical pressure of fluid respectively; ω denotes acentric factor, and R is universal gas constant.

For mixtures, the parameters a and b specified in Eqs. (2.11) and (2.12) are redefined below:

$$a = \sum_i \sum_j Z_i Z_j a_{ij} \tag{2.15}$$

$$b = \sum_i Z_i b_i \tag{2.16}$$

$$a_{ij} = \left(1 - \delta_{ij}\right) \sqrt{a_i a_j} \tag{2.17}$$

Where a_i, b_i are the parameters of PR EOS for pure substance i and j, Z_i is the mole fraction of component i. δ_{ij} is an empirically determined binary interaction coefficient characterizing the binary formed by component i and component j; and the recommended values of binary interaction coefficient and acentric factor can be found in [87], which are listed in the Appendix A. Additionally, the critical pressure, temperature and acentric factor for some components are also presented in the Appendix A.

2.5.2. PRSV EOS

Stryjek and Vera [84] modify the attraction term in the PR EOS and significantly improve the accuracy by introducing an adjustable parameter of pure component and by modifying the polynomial fit of the acentric factor. The PRSV EOS [84] reproduces more accurately the vapour pressure data for a wide variety of substances. In comparison with the PR EOS, the characteristic constant κ for each substance is modified based on Eq. (2.13). It is dependent not only on the acentric factor but also on the specific temperature, and is formulated in Eq. (2.18).

$$\kappa = \kappa_0 + \kappa_1 \left(1 + T_R^{0.5}\right)\left(0.7 - T_R\right) \tag{2.18}$$

where κ_0 is defined by Eq. (2.19), κ_1 is an adjustable parameter for each substance determined by experimental data (see Appendix A) and T_R is the reduced temperature which equals to a specified temperature over the critical temperature of the substance.

$$\kappa_0 = 0.378893 + 1.4897153\omega - 0.17131848\omega^2 + 0.0196554\omega^3 \quad (2.19)$$

2.5.3. SW EOS

Span and Wagner [86] present a new EOS for pure CO_2 in the form of a fundamental equation explicit in the Helmholtz free energy. It applies modern strategies for the optimization of the mathematical form of the equation of state and for the simultaneous nonlinear fit to the data of all these properties, within the minimum difference with the experimental data. SW EOS is valid for the entire fluid region covered by reliable date, namely for 216K $\leq$T$\leq$ 1100K and 0MPa $\leq$P $\leq$ 800MPa. On the other hand, independent equations for the vapour pressure and for the pressure on the sublimation curve, and for the saturated liquid and vapour densities are also included.

The most accurate SW EOS is also implemented as a reference EOS for pure CO_2. The fundamental equation is expressed in form of the dimensionless Helmholtz energy ϕ with the two independent dimensionless variables, the reduced density $\delta = \rho/\rho_c$ and the inverse reduced temperature $\tau = T_c/T$. The dimensionless Helmholtz energy is divided into a part dependent on the ideal-gas behaviour ϕ^0 and a part which takes into account the residual fluid behaviour ϕ^r, namely

$$\phi(\delta,\tau) = \phi^0(\delta,\tau) + \phi^r(\delta,\tau) \quad (2.20)$$

All the thermodynamic properties are correlated with the dimensionless Helmholtz energy and its derivatives, for example, pressure are presented in Eq. (2.21).

$$p(\delta,\tau)=\rho RT\left(1+\delta\left.\frac{\partial\phi^r}{\partial\delta}\right|_\tau\right) \tag{2.21}$$

2.5.4. GERG-2004

GERG-2004 equation of state (well-known as GERG-2004) was proposed by Kune et al. [88] with support from " Groupe Européen de Recherches Gazières". The equation is described by dimensionless Helmholtz free energy of mixture models based on multi-fluid approximation. On the basis of the traditional cubic equations, GERG-2004 introduces a large number of regression coefficients obtained from fitting experimental data so that it becomes the most comprehensive method to calculation of natural gas properties. It is applicable to calculate the gas component mixture including CH_4, N_2 and CO_2, totally 18 kinds of natural gas, and covering gas, liquid, vapour-liquid and supercritical states. The basic structure of GERG-2004 for mixture is repeated as below:

$$\alpha(\delta,\tau,x)=\alpha^o(\rho,T,x)+\alpha^r(\delta,\tau,x) \tag{2.22}$$

$$\alpha^o(\rho,T,x)=\sum_{i=1}^{N}x_i\left[\alpha_{oi}^o(\rho,T)+\ln x_i\right] \tag{2.23}$$

$$\alpha^r(\delta,\tau,x)=\sum_{i=1}^{N}x_i\alpha_{oi}^r(\delta,\tau)+\sum_{i=1}^{N-1}\sum_{j=i+1}^{N}x_ix_jF_{ij}\alpha_{ij}^r(\delta,\tau) \tag{2.24}$$

$$\delta=\frac{\rho}{\rho_r(x)} \tag{2.25}$$

$$\tau = \frac{T_r(x)}{T} \tag{2.26}$$

Where i and j denote two species; N is the number of components in the mixture; α^o is the dimensionless form of the Helmholtz free energy for ideal gas mixture; α^r is the residual part of the reduced Helmholtz free energy of the mixture; δ is the reduced density and τ is the inverse reduced temperature; F_{ij} is the binary specific parameter; $\rho_r(x)$ and $T_r(x)$ are density and temperature of the mixture, respectively; x is the mole fraction of the component in the mixture.

It is claimed that GERG-2004 is capable to accurately compute a number of thermodynamic properties of mixtures of natural gas components [89]. However, Li et al. stated that the applications of GERG-2004 are limited [90] due to its complexness.

2.6. Model Assumptions

To solve the problem of two-phase flows, the modelling inevitably involves some assumption. In this study, the main assumptions made in the development of the model for pipeline decompression are stated as below:

- The flow inside the pipeline is predominantly one-dimensional flow, and it means that the rate of change of the flow parameters normal to the streamline direction is negligible relative to those along the axial direction.

- The flow field is homogeneous, namely equal velocities for each phase.

- The cross section area of pipeline is constant.

2.7. HEM

Theoretical models for two-phase flow range from the simple HEM, which is actually a single-phase flow technique [33], to sophisticated two-fluid models that try to represent the non-equilibrium phenomena using assumptions, analyses or empiricism. The HEM has been widely used for many years in the literature [20]–[27] and proven to be accurate for long pipeline where there is sufficient time to establish equilibrium conditions between two phases.

The HEM approach is applicable. According to the studies of Chen et al. [29] and Mahgerefteh et at. [35], HEM model shows good agreement against the experimental data for the decompression of long pipe (>100m) containing flashing liquids and condensable gas mixture. Therefore, the application of HEM can be the best choice to be a basic model to study decompression flow.

2.7.1. Conservation Equations

During the decompression of pipeline containing pressurized gas or liquid fluid, the droplet or vapour will generate as decompression path enters two-phase envelope. According to the HEM, equation of state is only used for the closure of fore-mentioned two-phase conservation equations, and generation rate will be evaluated by energy equilibrium between two phases based on the specified equation of state. The fore-mentioned NS equations for two-phase flow of pipeline decompression can be rewritten as the one-dimensional form:

- **Mass Conservation Equation:**

$$\frac{\partial \rho}{\partial t}+\frac{\partial(\rho u)}{\partial x}=0 \tag{2.27}$$

- **Momentum Conservation Equation:**

$$\frac{\partial(\rho u)}{\partial t}+\frac{\partial(\rho u u)}{\partial x}=-\frac{\partial p}{\partial x}+\tau_w+\rho g\sin\theta \tag{2.28}$$

- **Energy Conservation Equation:**

$$\frac{\partial(\rho I)}{\partial t}+\frac{\partial(\rho u I)}{\partial x}=-p\frac{\partial u}{\partial x}-u\tau_w+Q_w \tag{2.29}$$

where ρ, u, p, and I are the total mass density, velocity, pressure and internal energy per unit mass of the homogeneous fluid as function of time, t, and space, x. Here the properties of fluid are for the working fluid which may be single phase or two-phase mixture if other phase generates. For pipeline decompression flow, the flow is assumed as one-dimensional flow, and the space variable x denotes dimension along the axial direction. g and θ are scalar gravity and angle of inclination of the pipeline to the horizontal, respectively. Q_w is heat transfer per unit volume between pipeline wall and the fluid; τ_w is the frictional force term of pipeline wall. Q_w and τ_w will be defined in following sections.

In the system of conservation equations, the HEM approach is to treat the two-phase fluid as a pseudo-fluid that can be handled as a "single-phase" and described by the conservation equations for single-phase flow. The quality of two-phase fluid can be determined from the equation of state. The velocities and pressures and temperatures for each phase are simply written as below:

$$u=u_l=u_v \tag{2.30}$$

$$P=P_l=P_v \tag{2.31}$$

$$T = T_l = T_v \tag{2.32}$$

HEM requires suitable thermodynamic and transport properties for the two-phase mixtures. The next section will present the procedure of calculation of two-phase properties.

2.7.2. Thermodynamic Relations under HEM

Thermodynamic relations in the HEM are described here. Thermodynamic properties of two-phase mixture are necessarily expatiated to establish the procedure of calculation based on equation of state. Additionally, the speed of sound of two-phase mixture, which is a key factor to determine the rate of pipeline decompression, is also specified.

2.7.2.1. Thermodynamic Properties of Two-phase Mixture

In the HEM approach, the thermodynamic properties of two-phase mixture are determined by

$$\zeta = \frac{\alpha\rho_v\zeta_v + (1-\alpha)\rho_l\zeta_l}{\rho} \tag{2.33}$$

or

$$\zeta = x_{qv}\zeta_v + (1-x_{qv})\zeta_l \tag{2.34}$$

Here, ζ denotes the thermodynamic parameter, such as specific internal energy, specific enthalpy, specific entropy, and specific heat capacity at constant pressure and volume. The term x_{qv} is the quality or dryness fraction of fluid, and the mass fraction of vapour phase per unit mass of bulk fluid; α is the void fraction of vapour/gas phase per unit volume of bulk fluid. The

subscript v and l denote vapour/gas and liquid phase, respectively. The thermodynamic parameters ζ_v and ζ_l can be computed from the specific EOS. More details can be found in Appendix B.

In addition, a density of two-phase mixture ρ is calculated by:

$$\rho = \frac{\rho_l \rho_v}{\rho_v \left(1 - x_{qv}\right) + \rho_l x_{qv}} \tag{2.35}$$

or

$$\rho = \alpha \rho_v + \left(1 - \alpha\right) \rho_l \tag{2.36}$$

The densities of individual phase are calculated according to the following formulas:

$$\rho_v = \frac{P w_v}{Z_v R T} \tag{2.37}$$

$$\rho_l = \frac{P w_l}{Z_l R T} \tag{2.38}$$

where, Z is fluid compressibility, which is obtained under the given pressure and temperature using the specified EOS. The subscript v and l denote vapour/gas and liquid phase respectively.

Additionally, the mole volume of pseudo-fluid is also given by:

$$\upsilon = \frac{w}{\left(1 - \alpha\right) \rho_l + \alpha \rho_v} \tag{2.39}$$

Based on the Eqs. (2.14), (2.35) and (2.39), the correlation between void fraction α and quality x_{qv} is given as:

$$x_{qv} = \frac{w_l(1-\alpha)}{w_l(1-\alpha)+w_v\alpha} \tag{2.40}$$

To determine void fraction α, the iterative should be implemented using the density and thermodynamic parameter of two-phase fluid which are computed from the conservation equations. In the study, the density and internal energy will be used to calculate the void fraction.

2.7.2.2. Speed of Sound for Single Phase and Two-phase Fluid

Speed of sound is one of the most important parameters to determine the behaviour of pipeline decompression. The thermodynamic speed of sound is normally defined by:

$$C_s^2 = \left.\frac{\partial P}{\delta\rho}\right|_s \tag{2.41}$$

where C_s is the speed of sound through the fluid; P and ρ are the absolute pressure and density of bulk fluid, respectively, s is the specific entropy of bulk fluid. For single phase real fluids, the isentropic speed of sound can also be expressed as [91]:

$$C_s^2 = \left.\frac{\partial P}{\partial\rho}\right|_T + \frac{T}{C_v\rho^2}\left(\left.\frac{\partial P}{\partial T}\right|_\rho\right)^2 \tag{2.42}$$

where the term $\left.\frac{\partial P}{\partial\rho}\right|_T$ and $\left.\frac{\partial P}{\partial T}\right|_\rho$ can be derived from cubic Equation of State, e.g. PR EOS; C_v is the specific heat capacity at constant volume.

In the Eq. (2.42), the two terms of partial differentiation can be obtained analytically by differentiating the PR EOS (Eq. (2.10)) to give:

$$\left.\frac{\partial P}{\partial \rho}\right|_T = \left\{\frac{RT}{(\upsilon-b)^2} - \frac{2a(\upsilon+b)}{\left[\upsilon(\upsilon+b)+b(\upsilon-b)\right]^2}\right\}\frac{w}{\rho^2} \tag{2.43}$$

$$\left.\frac{\partial P}{\partial T}\right|_\rho = \frac{R}{\upsilon-b} - \frac{da}{dT}\frac{1}{\upsilon(\upsilon+b)+b(\upsilon-b)} \tag{2.44}$$

where the term, $\frac{da}{dT}$ will be given in the Appendix B.

For two-phase fluid, the analytical form Eq. (2.42) will not be applicable due to the discontinuities of thermodynamic properties. There exist various methods to calculate the speed of sound of two-phase fluid [92]–[95]. With consideration of feasibility of application in the model, the numerical method [94] is used to calculate the speed of sound.

For multi-component fluid mixture, the properties of two-phase fluid can be determined with both temperature and pressure. Therefore, the numerical solution of speed of sound is given as

$$C_s^2 = \left(\frac{\Delta P}{\rho(P,T)-\rho\left(P-\Delta P,T^*\right)}\right)_s \tag{2.45}$$

Here, ΔP is the infinitesimal change in pressure, taken as $0.001P$; the subscript , s denotes a constant entropy process, T^* is evaluated from the isentropic condition

$$s(T,P) = s\left(T^*,P-\Delta P\right) \tag{2.46}$$

To solve T^* with the above Eq. (2.46), a Newton-Raphson method is employed. The entropy for two-phase fluid are calculated by

$$s = x_{qv} s_v + \left(1 - x_{qv}\right) s_l \tag{2.47}$$

The objective function $\xi\left(T^*\right)$ is defined at given temperature T and pressure P as

$$\xi^{(n)}\left(T^*\right) = s\left(T, P\right) - s\left(T^{*(n)}, P - \Delta P\right) \tag{2.48}$$

where superscript (n) indicates the iteration time. The derivative of objective function is calculated by

$$\frac{d\xi}{dT} = \frac{\xi\left(T^* + \Delta T\right) - \xi\left(T^* - \Delta T\right)}{2\Delta T} \tag{2.49}$$

Convergence is determined by the relation

$$\left| \frac{s\left(T, P\right) - s\left(T^{*(n)}, P - \Delta P\right)}{s\left(T, P\right)} \right| \le 10^{-8} \tag{2.50}$$

Note that the thermodynamic properties of the two-phase one-component fluid are only dependent on pressure or temperature and quality of vapour, namely, temperature can be specified under pressure for the two-phase one-component fluid. Therefore, the speed of sound is redefined as

$$C_s^2 = \left(\frac{\Delta P}{\rho\left(P, x_{qv}\right) - \rho\left(P - \Delta P, x_{qv}^*\right)} \right)_s \tag{2.51}$$

where x_{qv}^{*} is found based on the isentropic condition Eqs. (2.52) and (2.47).

$$s\left(P, x_{qv}\right) = s\left(P - \Delta P, x_{qv}^{*}\right) \tag{2.52}$$

Here, based on HEM, the entropy for two-phase mixture is calculated as Eq. (2.47).

2.8. HRM

Three types of models for two-phase flow have been carefully described in the last chapter. The HEM is one of the simplest models to be widely used with complete equilibrium assumptions. The HEM can be applicable to be a basic model to study decompression flow, particular for the long pipeline [29], [35]. Models based on limiting assumptions exhibit little practicability to investigate pipeline decompression due to the inherent disadvantage of description of the high transient decompression flow. Besides, non-equilibrium models attempt to represent the non-equilibrium effects of two-phase flow. The non-equilibrium models are divided into three subgroups: empirical models, physically based models for thermal equilibrium and two-fluid models. Due to the lack of actual physical characteristics, empirical models are more practical than others to be employed to study decompression flow.

The HEM approach implies that the phase change occurs instantaneously and the interphase heat transfer is infinitely fast. However, the rate of heat transfer is finite for the practical condition and the change of phase takes time to occur. Therefore, the HRM [31], [44], one of empirical non-equilibrium models, is proposed to account for the thermodynamic non-equilibrium effect by establishment of mass source term.

The HRM is employed to study the decompression flow because of not only its practicality but also other aspects, such as controllable empirical coefficients. Normally, the change of phase will occur during the procedure of decompression, and the two-phase flow is in the thermodynamic non-equilibrium and mechanical non-equilibrium condition. But the effects caused by the thermodynamic non-equilibrium are larger than the mechanical non-equilibrium at the initial stage of decompression. During the process of pipeline decompression, the pressurized fluid is escaping quickly from pipeline and two-phase flow will occur. The decompression process may be so fast that there is no enough time to reach thermodynamic balance. The effect of mechanical non-equilibrium is relatively minor because the velocity slip is an order of magnitude smaller than the chocked velocity of two-phase flow [96]. Additionally, Jones [97] claimed that the HRM is an appropriate model to describe the effects of thermal non-equilibrium from the phenomenological viewpoint, and the effects of phase change, i.e. vaporization, are assumed to be more important than that caused by the mechanical non-equilibrium.

2.8.1. Governing Equations

Bilicki and Kestin [44] proposed HRM to describe the adiabatic, one-component, one-dimensional, two-phase flows. The HRM takes into account the non-thermal equilibrium conditions which exist between liquid and vapour.

Based on the governing equation of the HEM, the HRM is constructed by adding a rate equation to determine the thermal non-equilibrium effects. One-dimensional flow is assumed to study pipeline decompression. The mass, momentum and energy conservation equations are presented as below, respectively.

- **Mass Conservation Equation:**

$$\frac{\partial \rho}{\partial t}+\frac{\partial(\rho u)}{\partial x}=0 \tag{2.53}$$

- **Momentum Conservation Equation:**

$$\frac{\partial(\rho u)}{\partial t}+\frac{\partial(\rho u u)}{\partial x}=-\frac{\partial p}{\partial x}+\tau_w+\rho g \sin\theta \tag{2.54}$$

- **Energy Conservation Equation:**

$$\frac{\partial(\rho I)}{\partial t}+\frac{\partial(\rho u I)}{\partial x}=-p\frac{\partial u}{\partial x}-u\tau_w+Q_w \tag{2.55}$$

where ρ, u, p, and I denote the total mass density, velocity, pressure, and internal energy of the two-phases mixture.

Besides, the additional rate equation, namely the equation of vapour mass balance, is added into the governing system to evaluate the generation of vapour phase by an approach of relaxation.

- **Rate Equation:**

$$\frac{\partial(\rho x_{qv})}{\partial t}+\frac{\partial(\rho x_{qv} u)}{\partial x}=\Gamma_{GR} \tag{2.56}$$

Here, the mass transfer source term, Γ_{GR} denotes the generation rate of vapour.

It is worth noting that the HRM neglects the velocity slip between the phases since the slip is of secondary important factor to the non-equilibrium effects during pipeline decompression.

2.8.2. Mass Transfer Source Term

The mass transfer source term correlates with the rate of phase change, which can be determined by the empirical or analytical approaches. Normally it depends on the interphase heat transfer, nucleation and non-equilibrium effects. Relaxation is an analytical method which evaluates the difference between the actual conditions and the equilibrium conditions according to empirical correlations. Relaxation represents the transition of the thermodynamic system from non-equilibrium to equilibrium state [98]. The relaxation method for phase changes is widely used not only because of its simplicity, but because of its adequately practical application.

Since the vapour mass generation rate vanishes when the quality reaches its unconstrained equilibrium value, the rate of change of quality can be presented by a simple linear approximation, namely the first term of the evaporation intensity Taylor series expansion. In other words, the rate of change of quality is proportional to the difference between the equilibrium quality and the actual quality [31], [44], [96], [99]. Hereby, the rate of vapour mass generation is given by

$$\Gamma_{GR} = -\left(\frac{x_{qv} - \overline{x_{qv}}}{\Theta} \right) \rho \tag{2.57}$$

where Θ denotes relaxation time, x_{qv} and $\overline{x_{qv}}$ are the actual and equilibrium qualities of vapour phase, respectively. The latter is determined by

$$\overline{x_{qv}} = \frac{I - I_{sl}}{I_{sv} - I_{sl}} \tag{2.58}$$

Here, I represent the internal energy for single phase or two-phase mixture; the subscripts sv and sl denote the properties of saturated vapour and saturated liquid respectively.

Relaxation time is proved to be a monotonically decreasing function of void fraction and non-dimensional pressure difference [31]. For water flashing, according to Moby Dick experiments [46], the relationship for the relaxation time is determined by

$$\Theta = \Theta_0 \alpha^{-0.257} \psi^{-2.24} \tag{2.59}$$

or

$$\Theta = \Theta_0 \alpha^{-0.54} \varphi^{-1.76} \tag{2.60}$$

where $\Theta_0 = 6.51 \times 10^{-4}$ and $\Theta_0 = 3.84 \times 10^{-7}$ are used in Eqs. (2.59) and (2.60) respectively; void fraction, α can be calculated by Eq. (2.61). Non-dimensional parameters of pressure difference ψ and φ are defined by Eqs. (2.62) and (2.63).

$$\alpha = \frac{x_{qv} \upsilon_v}{\upsilon} \tag{2.61}$$

$$\psi = \frac{P_s(T_{in}) - P}{P_s(T_{in})} \tag{2.62}$$

$$\varphi = \frac{P_s(T_{in}) - P}{P_c - P_s(T_{in})} \tag{2.63}$$

In the Eqs. (2.62) and (2.63), the term $P_s(T_{in})$ is the saturation pressure at given initial temperature T_{in}. Noted that the correlation presented in the Eq. (2.62) is comparatively better for small pressure (up to 1MPa) [31]; for high pressures, the correlation shown in Eq. (2.63) is proposed. For our study, the pressure is normally higher than 1MPa during the process of decompression. Therefore, the Eqs. (2.60) and (2.63) are chose to calculate the relaxation time.

Additionally, the correction above is proposed based on the experimental of water flashing. In order to adopt the correction for CO_2, Angielczyk et al [100] make a comparison between calculation and experimental data conducted by Nakagawa [101] with converging–diverging nozzles, and propose that the constant Θ_0 in Eq. (2.60) should be decreased to 2.14×10^{-7}, but the residual coefficient remains unchanged. Since there are no available experimental data for the pipeline decompression of dense phase CO_2 and CO_2 mixture. The current framework allows for tuning of these constants when such data becomes available. In this study, the local relaxation time for the dense CO_2 adopts the revised corrections proposed by Angielczyk et al [100].

$$\Theta = 2.14\times10^{-7}\left(\frac{x_{qv}\upsilon_v}{\upsilon}\right)^{-0.54}\left(\frac{P_s(T_{in})-P}{P_c-P_s(T_{in})}\right)^{-1.76} \tag{2.64}$$

The decompression flow inside the pipeline was initially pure liquid without generation of vapour. Therefore, when there was no vapour, the relaxation timescale of phase change would be unbounded and the vaporization would never begin. In order to avoid numerical overflow and to provide a means of considering the incipiency of vapour generation, a very small lower bound of 10^{-8} was used.

2.8.3. Thermodynamic Relations under HRM

The definitions of thermodynamic properties for two-phase fluid under HRM are described in more detail. It is worth to note that the HRM is originally developed for one-component, such as pure water. This study is to extend the HRM for the simulation of dense CO_2 decompression, taking account of multi-component mixture.

2.8.3.1. Thermodynamic Properties of Two-phase Mixture under HRM

For one-component fluid [31], the total specific volume and specific internal energy of the two-phase mixture can be given by

$$\upsilon = x_{qv}\upsilon_{sv}(P) + (1 - x_{qv})\upsilon_{ML}(P, I_{ML}) \tag{2.65}$$

$$I = x_{qv}I_{sv}(P) + (1 - x_{qv})I_{ML} \tag{2.66}$$

where the symbols without subscript denote the properties for two-phase mixture; x_{qv} is the quality or dryness fraction of vapour under non-equilibrium condition; subscripts *sv* and *ML* denote saturated vapour and metastable liquid, respectively. When the initial phase condition for decompression flow is dense phase or liquid, for the two-phase flow, the vapour is assumed under saturated condition and the liquid is assumed in non-saturated or metastable conditions.

The specific volume of saturated vapour and liquid can be obtained by combining the Eqs. (2.14), (2.37) and (2.38) with specified EOS. The thermodynamic properties of metastable conditions can be calculated by following section.

It is worth to note that the specific volume and internal energy of saturated liquid and vapour in Eqs. (2.65) and (2.66) are only dependant on the pressure or temperature of fluid when the fluid is one-component. In other words, the temperature of phase generated during pipeline decompression equals to the saturated temperature at given pressure. However, the temperature of initial phase of bulk fluid is not equal to the saturation temperature, i.e. $T_{ML} \neq T_s(P)$. Briefly, the non-equilibrium effects for HRM behave with the temperature difference between two phases.

For multi-component fluid, the thermodynamic properties of two-fluid mixture are slightly different from one-component fluid. The total specific volume and specific internal energy of two-phase mixture depend not only on the local pressure but also on the composition of each phase.

$$\upsilon = x_{qv}\upsilon_{sv}(P,Y) + (1-x_{qv})\upsilon_{ML}(P,I_{ML},X) \tag{2.67}$$

$$I = x_{qv}I_{sv}(P,Y) + (1-x_{qv})I_{ML} \tag{2.68}$$

where X and Y denote the compositions of liquid and vapour phase, respectively, and they can be determined by flash calculation under equilibrium condition.

2.8.3.2. Thermodynamic Properties of Metastable Liquid

The qualities with subscript *ML* represent the metastable fractions of two-phase mixture. The thermodynamic properties of metastable fluid should be determined based on the specified EOS. The density of metastable liquid can be obtained by an extrapolation of the isochors of the liquid region into a two-phase region [100]. Based on Eq. (2.65), the density of metastable liquid for one-component fluid can be obtained for given pressure P and internal energy of metastable liquid I_{ML}. The pressure P can be calculated by

solving the conservation equation, and the internal energy I for two-phase mixture can also be solved, then internal energy of metastable liquid I_{ML} can be found by Eq. (2.66). Fifth order spline functions are adopted to extrapolate the metastable liquid density.

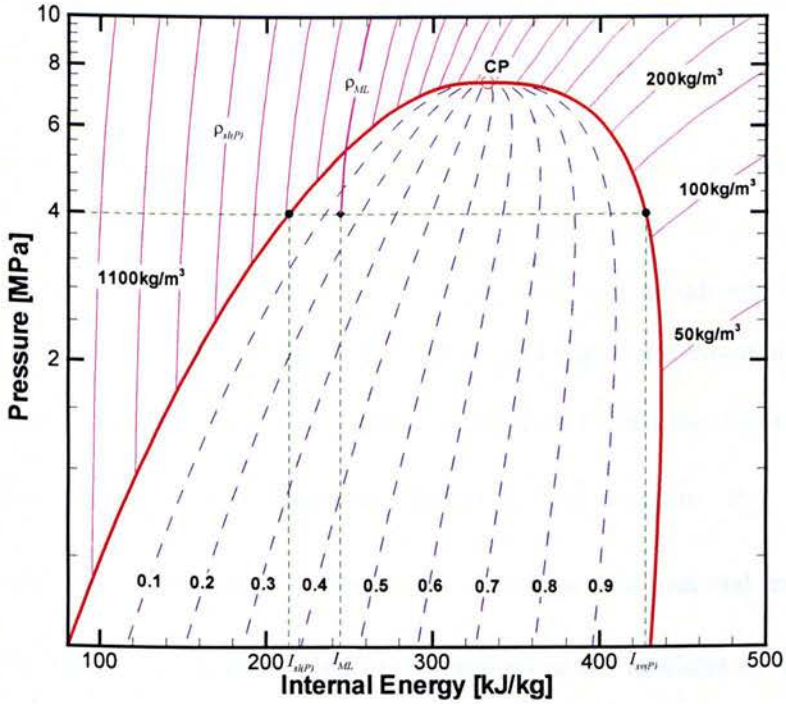

Figure 2.1 Illustration of metastable fluid density for one-component fluid [100].

The quality under unconstrained equilibrium condition $\overline{x_{qv}}$ can be calculated by Eq. (2.58) based on the fluid pressure and internal energy for single component two-phase mixture given in Eqs. (2.65) and (2.66).

2.8.3.3. Solution Procedure of Thermodynamic Properties Based on HRM

The thermodynamic relationships are used to close governing system. The solution of thermodynamic properties is a complicated procedure which inevitably involves the iterative calculation of thermodynamic properties.

Additionally, the presence of metastable liquid makes the solution procedures more complicated. The solution procedure of multi-component fluid is quite different from the one-component fluid because the non-constant compositions of two phases are required to be determined. The Newton-Raphson method is employed to implement the solution. The solution procedures for one-component fluid and multi-component fluid under non-equilibrium condition are shown in Figure 2.2 and Figure 2.3, respectively.

For one-component fluid, the solution is carried out by estimating local pressure. Firstly, the total specific volume and specific internal energy of the two-phase mixture are calculated by solving governing equations. Then the thermodynamic properties of saturated vapour and liquid are calculated under the estimated local pressure. The specific volume of metastable liquid v_{ML} is solved from the Eq. (2.65). With the estimated local pressure P_{guess} and the specific volume of metastable liquid v_{ML}, the specific internal energy of metastable liquid I_{ML} is calculated by extrapolating the isochors of the liquid into a two-phase region. Then the total internal energy of two-phase mixture I_{cal} is obtained from Eq. (2.66), and compared with I. The convergence criterion is given in Eq. (2.69), and the residual is set equal to 1.0×10^{-5}. The new local pressure is estimated and the progress above is repeated and until the convergence criterion is met. The Newton-Raphson method is employed to update the estimated local pressure. The range of pressure is limited in order to keep the stability of iteration.

$$\frac{(I-I_{cal})}{I}<\varepsilon \tag{2.69}$$

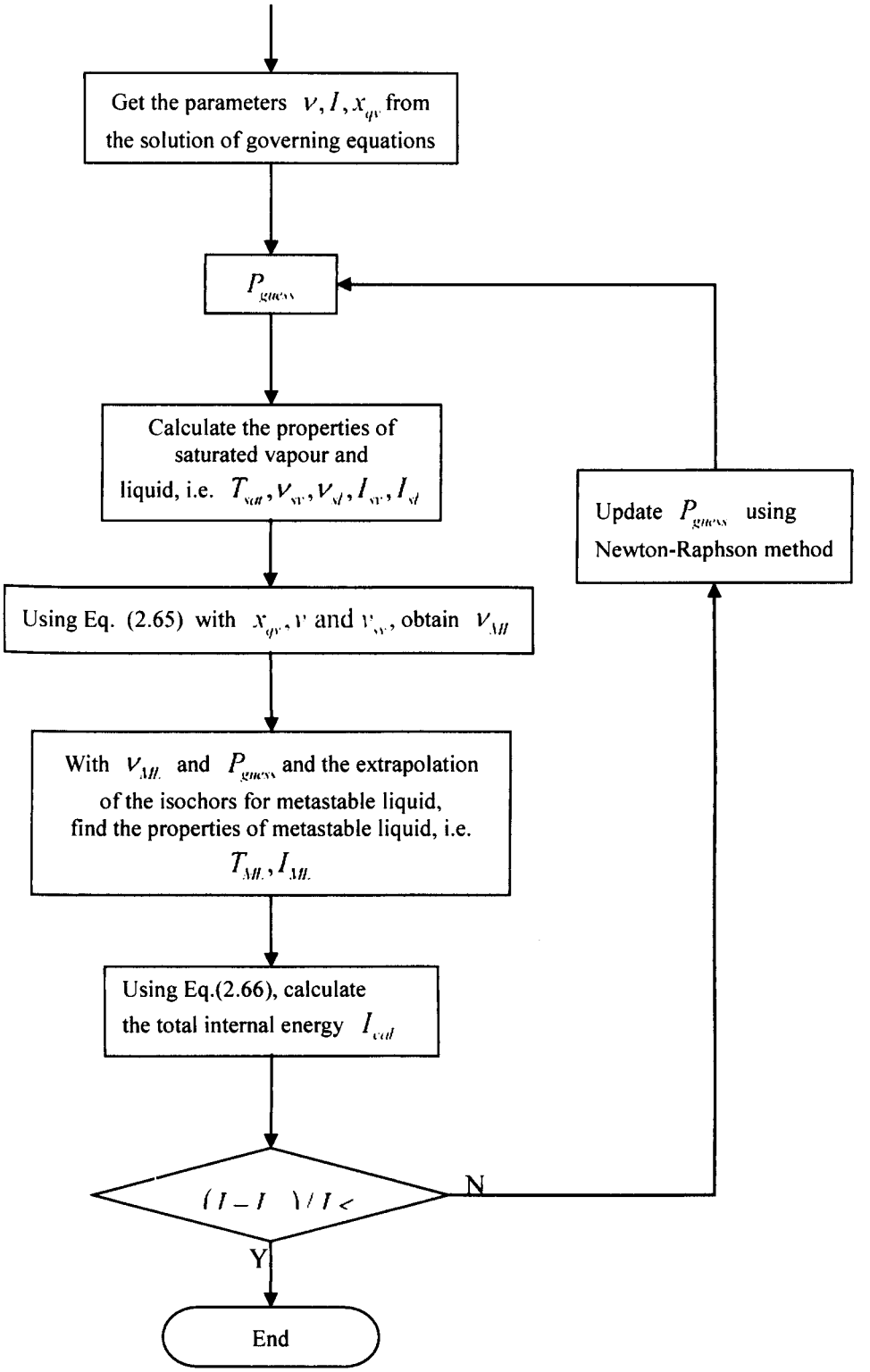

Figure 2.1 The solution procedure for one-component fluid under HRM

For multi-component fluid, the calculation of compositions of liquid and vapour totally changes the solution procedure of thermodynamic properties. Under equilibrium condition, the quality $\overline{x}_{qv}$ is given as below:

$$\overline{x_{qv}} = \overline{x_{qv}(P,I)} = \overline{x_{qv}(v,I)} \tag{2.70}$$

It indicates that the given pressure and internal energy can determine one quality. Therefore, when the actual quality x_{qv} equals to $\overline{x_{qv}(P,I)}$, the specific set of variables $\langle x_{qv}, P, I \rangle$ or $\langle x_{qv}, v, I \rangle$ will define that the system is in the equilibrium state.

If the actual quality x_{qv} is less than $\overline{x_{qv}(P,I)}$, the system is in the non-equilibrium state and the liquid phase is in the metastable condition. For the specific set of variables $\langle x_{qv}, v, I \rangle$, the properties of metastable liquid are calculated by extrapolating their values from the closest liquid-phase regions. Lee et al [102] propose that the enthalpy of the two-phase fluid should be conserved during the extrapolation. In current study, the internal energy of the two-phase fluid is chosen to investigate the non-equilibrium effect. Likewise, the internal energy of two-phase fluid remains conservative during the extrapolation.

Under non-equilibrium condition, the thermodynamic properties are evaluated with the specific set of variables $\langle x_{qv}, v, I \rangle$. Firstly, the reference pressure P_{equ} is calculated with the assumption as following

$$x_{qv} = \overline{x_{qv}(P_{equ}, I)} \tag{2.71}$$

Based on Eq. (2.71), the pressure-quality flash calculation is carried out with the estimated reference pressure P_{equ}. The compositions of liquid and vapour, X, Y are determined, and the internal energy I_{sv}, I_{sl} are also calculated. Then the total internal energy of two-phase fluid I_{cal} is obtained from Eq. (2.68). The new reference pressure is updated and the above calculations are repeated until the convergence criterion in Eq. (2.72) is met.

$$\frac{I - I_{cal}}{I} < \varepsilon_1 \tag{2.72}$$

The compositions of liquid and vapour, X, Y and the internal energy, I_{sv}, I_{sl} are acquired under the equilibrium state at the reference pressure P_{equ} and the total internal energy I. The calculated compositions of liquid and vapour is assumed to be fixed [102] when extrapolating the properties of metastable liquid.

Afterwards, the actual pressure P_{act} is evaluated by the extrapolation of the properties of metastable liquid. Firstly, the actual pressure P_{act} is estimated, and then the specific volumes of vapour and metastable liquid are calculated using the compositions and internal energy under the reference pressure. Finally, the total specific volume is calculated using Eq. (2.67), and the actual pressure is updated with Newton-Raphson method and the calculation is repeated until the convergence criterion below is satisfied.

$$\frac{\left(v - v_{cal}\right)}{v} < \varepsilon_2 \tag{2.73}$$

The residuals ε_1 and ε_2 are 5.0×10^{-6} and 5.0×10^{-4}.

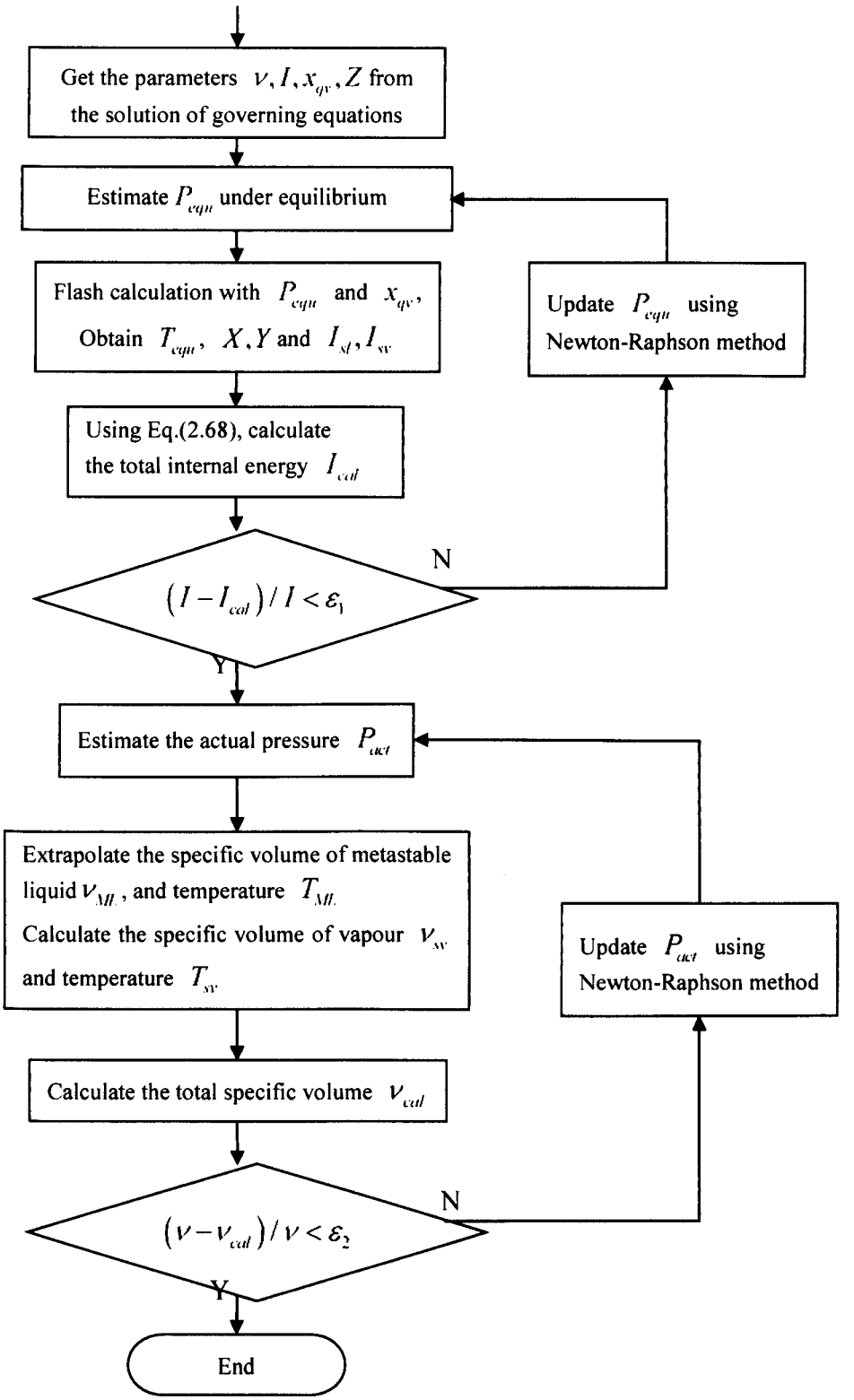

Figure 2.2 The solution procedure for multi-component fluid under HRM

2.8.3.4. Speed of Sound for Two-phase Flow under HRM

Based on HRM, the speed of sound can also be obtained with the numerical method

$$C_{s,HRM}^2 = \left(\frac{\Delta P}{\rho\left(P, x_{qv}\right) - \rho\left(P - \Delta P, x_{qv}\right)} \right)_s \tag{2.74}$$

where the symbol x_{qv} is the quality obtained from the governing equations; $\rho\left(P, x_{qv}\right)$ and $\rho\left(P - \Delta P, x_{qv}\right)$ can be calculated by combining Eq. (2.14) and (2.65). $\rho\left(P - \Delta P, x_{qv}\right)$ denotes the density at given infinitesimal change of pressure with the assumption that the actual quality remains unchanged during infinitesimal isentropic process. This assumption is consistent with the definition of the frozen velocity proposed by Bilicki and Kestin [44]. Additionally, the entropy is calculated with HRM by

$$s = x_{qv} s_{sv}\left(P\right) + \left(1 - x_{qv}\right) s_{ML} \tag{2.75}$$

The entropy of metastable liquid is calculated by extrapolating the entropy of liquid into the two-phase region.

2.9. Boundary Conditions

Previous studies [29], [35], [103] on pipeline decompression have revealed that the effects of wall friction and heat transfer are important for accurate predictions. Two types of wall boundary conditions are implemented in the current study. For multi-dimensional simulations, a wall function [104] (not used in the pipeline decompression study) is used to compute wall heat transfer and friction. For the one-dimensional pipeline decompression model, empirical correlations are employed to compute wall friction and heat transfer.

2.9.1. Friction

Influences of friction on pipe flow are quite significant, particularly for relative long time release. For one-dimensional simulation, friction is treated as one of source terms. The treatment of wall friction of two-phase mixture for one-dimensional simulations is similar to that of single phase flow calculations.

The source term of wall friction for single phase appearing in Eq. (2.28) and (2.29) is defined as

$$\tau_w = -2\frac{C_f \rho u|u|}{D} \tag{2.76}$$

where C_f is fanning friction factor and D is pipeline inner diameter. The friction factor for single phase [105], [106] is given by

$$C_f = \begin{cases} \dfrac{16}{\mathrm{Re}} & \text{for } \mathrm{Re} < 2000 \\ 0.001375\left[1+\left(20000\dfrac{\varepsilon}{D}+\dfrac{10^6}{\mathrm{Re}}\right)^{1/3}\right] & \text{for } \mathrm{Re} \geq 2000 \end{cases} \tag{2.77}$$

$$\mathrm{Re} = \frac{\rho u D}{\mu} \tag{2.78}$$

where ε is the Nikuradse sand-grain roughness for the internal surface, Re is the Reynolds number and μ is the viscosity of working fluid. For two-phase flow, ρ is taken as density of two-phase mixture with Eq. (2.35) and viscosity of two-phase viscosity is calculated according to [107] by

$$\mu = (1-\alpha)(1+2.5\alpha)\mu_l + \alpha\mu_v \tag{2.79}$$

where the subscripts l and v refer to the saturated liquid and vapour respectively.

Regarding to pure CO_2, the viscosity is calculated with the representation proposed by Fenghour et al [108], [109]. Usually, the viscosity is expressed in the customary way as a function of density and temperature, and is decomposed into three separate contributions:

$$\eta(\rho,T)=\eta_0(T)+\Delta\eta(\rho,T)+\Delta\eta_c(\rho,T) \tag{2.80}$$

or

$$\eta(\rho,T)=\bar{\eta}(\rho,T)+\Delta\eta_c(\rho,T) \tag{2.81}$$

where $\eta_0(T)$ is the part of viscosity in the zero-density limit, $\Delta\eta(\rho,T)$ is the part of an excess viscosity which represents the increase of viscosity at increased density over the dilute gas value at the same temperature, and $\Delta\eta_c(\rho,T)$ denotes the critical enhancement incorporating the increase in viscosity in the immediate vicinity of the critical point. The first two terms on the right hand side of Eq. (2.80) are sometimes merged into one term named the background contribution $\bar{\eta}(\rho,T)$. For a lot of fluids, it has been found that the ratio of the critical enhancement viscosity to the total viscosity is greater than 0.01 only within 5 Kelvin area around the critical temperature. Accounting for the practical range of high pressure CO_2 pipeline, the critical enhancement viscosity is neglected in current study. Therefore, the viscosity of pure CO2 is calculated by

$$\eta(\rho,T)\approx\eta_0(T)+\Delta\eta(\rho,T) \tag{2.82}$$

The viscosity in the zero-density limit is expressed [109]

$$\eta_0(T) = \frac{1.00697T^{1/2}}{\exp\left(\sum_{i=0}^{4} a_i \left(\ln T^*\right)^i\right)} \tag{2.83}$$

where the zero-density viscosity $\eta_0(T)$ and the temperature T are in units of μPa?s and Kelvin respectively, and the coefficients a_i can be found in the literature [109], and the reduced temperature T^* is defined as

$$T^* = \frac{T}{\varepsilon/k} \tag{2.84}$$

and ε/k is the energy scaling parameter with a value of 251.196K.

The excess viscosity is described as a form of power series expansion

$$\Delta\eta(\rho,T) = \sum_{i=1}^{n}\left(\sum_{j=1}^{m} d_{ij}/T^{*(j-1)}\right)\rho^i \tag{2.85}$$

where the reduced temperature, T^*, is defined by Eq. (2.84) and the coefficients d_{ij} is given in the literature [109].

For multi-component mixture, the viscosity is determined by the approach proposed by Pedersen et al. [110], which is the most common method in the petroleum industry for calculating the viscosity of fluids. The viscosity of a fluid mixture is expressed by

$$\left[\left(\eta-\eta^0\right)\xi+10^{-4}\right]^{-0.25} = \sum_{j=0}^{4} a_j\left(\frac{\rho}{\rho_c}\right)^j \tag{2.86}$$

$$\xi = \left[\sum x_i T_{ci}\right]^{1/6} \left[\sum x_i M_i\right]^{-1/2} \left[\sum x_i P_{ci}\right]^{-1/3} \tag{2.87}$$

where x_i is the mole fraction of each pure species i, and P_{ci}, T_{ci} and M_i are the critical pressure, critical temperature and molecular weight, respectively. The coefficients a_j are already suggested by Jossi et al. [111]. The zero-density mixture viscosity η^0 is determined by

$$\eta^0 = \frac{\sum_{i=1}^{N} x_i \eta_i^0 M_i^{1/2}}{\sum_{i=1}^{N} x_i M_i^{1/2}} \tag{2.88}$$

where the zero-density mixture viscosity of species i, η_i^0, is calculated by

$$\eta_i^0 \xi_i^0 = \begin{cases} 34.0\times10^{-5} T_R^{0.94} & \text{for } T_R \le 1.50 \\ 17.78\times10^{-5}\left[4.58T_R - 1.67\right]^{5/8} & \text{for } T_R > 1.50 \end{cases} \tag{2.89}$$

where $\xi_i^0 = T_{ci}^{1/6} / \left(M_i^{1/2} P_{ci}^{1/3}\right)$, T_R the reduced temperature.

The critical density in Eq. (2.86), ρ_c, is calculated by an average mixing rule in the literature [110].

2.9.2. Heat Transfer

During the process of pipeline decompression, the temperature of the fluid decreases resulting in the transfer of energy stored in the pipeline wall to the fluid, namely forced convective heat transfer between the pipeline wall and flowing fluid. Meanwhile, the natural or forced convective heat transfer also occurs between the pipeline wall and the outside ambient.

Applying the Newton's cooling law, the source term for pipe wall heat transfer in Eq. (2.29) can be defined as:

$$Q_w = \frac{4h\left(T_w - T_f\right)}{D} \tag{2.90}$$

where T_f is the fluid temperature solved by the flow solver and T_w is the temperature of the inner wall surface. h is the heat transfer coefficient of fluid in the pipeline, which should be calculated with different flow and phase condition. There is a small difference of temperature between the fluid and pipeline wall at the stage of initial decompression. The heat transfer can be ignorable due to the small temperature difference. As the decompression continues, the temperature difference will increase, and the flow will be fully developed and turbulent. Therefore, it is assumed that the heat transfer will be considered after the decompression flow following the pipeline rupture is fully developed and turbulent.

For single phase fully developed flow, the heat transfer coefficient is determined according the correlation proposed by Gnielinski [112]. This correlation was verified with the wide range of applicability and accuracy [113]. Therefore the heat transfer coefficient for single phase is given as

$$h = \frac{\left(\mathrm{Re}-1000\right)\mathrm{Pr}\left(C_f/2\right)}{1+12.7\left(C_f/2\right)^{0.5}\left[\mathrm{Pr}^{2/3}-1\right]}\frac{k}{D} \tag{2.91}$$

where Pr and Re are the Prandtl and Reynolds numbers, respectively. k is the thermal conductivity of fluid. The fanning friction factor, C_f can be obtained from Eq. (2.77).

During the process of pipeline decompression, the decompression path will enter two-phase envelope and the fluid will be two-phase mixture. In the case of two-phase flow, the heat transfer coefficient is re-evaluated with the consideration of the initial phase condition. If the initial phase of fluid is gas phase, the condensation of bulk fluid will occur when the pressure decrease under the saturation pressure. If the initial phase of fluid is dense/liquid phase, the boiling of bulk fluid will happen during the decompression flow. For the two-phase with gas condensation, the heat transfer coefficient during gas condensation is estimated by the correlation proposed by Shah [114], which is given by

$$h = h_{f0}\left[\left(1-x_{qv}\right)^{0.8} + \frac{3.8x_{qv}^{0.76}\left(1-x_{qv}\right)^{0.04}}{\left(P/P_c\right)^{0.38}}\right] \tag{2.92}$$

where h_{f0} is the heat transfer coefficient assuming all the mass flowing as liquid, and is obtained from the Dittus-Boelter equation by

$$h_{f0} = 0.023\,\mathrm{Re}_{f0}^{0.8}\,\mathrm{Pr}_l^{0.4}\,k_l / D \tag{2.93}$$

where

$$\mathrm{Re}_{f0} = \rho u\left(1-x_{qv}\right)D/\mu_l \tag{2.94}$$

$$\mathrm{Pr}_l = \mu_l C_{pl} / k_l \tag{2.95}$$

The subscript *l* denotes the corresponding properties of liquid phase, and the subscript *f0* identifies the parameters on the assumption that all the mass flowing is liquid phase. The liquid thermal conductivity, k_l, can be are determined by Dymond and Assael schemes [115], [116]. The specific heat

capacity under constant pressure of liquid/dense phase, C_{pl}, can be calculated from the specified EOS. Noted that, the term ρu in Eq. (2.94) is the mass flux of pseudo-fluid, which is specified by the homogeneous mixture for two-phase flow.

For the two-phase with liquid boiling, the correlation of Liu and Winterton [117], which is the improvement of the earlier correlation proposed by Gungor and Winterton [118], is used to determine the two-phase boiling heat transfer coefficient. The new form of the correction is given by

$$h=\left[\left(E_1E_2h_{f0}\right)^2+\left(S_1S_2h_{NB}\right)^2\right]^{1/2} \tag{2.96}$$

$$E_1=\left[1+x_{qv}\,\mathrm{Pr}_l\left(\frac{\rho_l}{\rho_v}\right)\right]^{0.35} \tag{2.97}$$

$$S_1=\frac{1}{1+0.055E_1^{0.1}\,\mathrm{Re}_{f0}^{0.16}} \tag{2.98}$$

Here, Re_{f0} and Pr_l are also defined by Eqs. (2.94) and (2.95), respectively. One part of heat transfer coefficient h_{f0} in Eq. (2.96) is obtained from the Dittus-Boelter equation by Eq. (2.93). The another heat transfer coefficient for nucleate boiling in Eq. (2.96), h_{NB} is calculated by

$$h_{NB}=55\left(\frac{P}{P_c}\right)^{0.12}\left(-\log_{10}\frac{P}{P_c}\right)^{-0.55}w^{-0.5}q_w^{2/3} \tag{2.99}$$

When the pipeline is horizontal and dimensionless Froude number, $\mathrm{Fr}_{f0} = \dfrac{(\rho u)^2}{\rho_l g D}$, is not more than 0.05,

$$E_2 = \mathrm{Fr}_{f0}^{(0.1-2\mathrm{Fr}_{f0})} \tag{2.100}$$

$$S_2 = \sqrt{\mathrm{Fr}_{f0}} \tag{2.101}$$

For vertical pipelines, and for horizontal pipelines which $\mathrm{Fr}_{f0} > 0.5$,

$$E_2 = S_2 = 1 \tag{2.102}$$

The heat flux q_w in Eq. (2.99) is determined by

$$q_w = h\Delta T_f = h\left(T_w - T_f\right) \tag{2.103}$$

Combining the Eqs. (2.96), (2.99) and (2.103), the new correlation of q_w are given as

$$q_w^2 = \left[E_1 E_2 h_{f0} \Delta T_f\right]^2 + \left[A_p S_1 S_2 \Delta T_f\right]^2 q_w^{4/3} \tag{2.104}$$

where

$$A_p = 55\left(\frac{P}{P_c}\right)^{0.12}\left(-\log_{10}\frac{P}{P_c}\right)^{-0.55} w^{-0.5} \tag{2.105}$$

Define the new intermediate parameter q_{w*} and q_L as

$$q_L = E_1 E_2 h_{f0} \Delta T_f \tag{2.106}$$

$$q_{w*}^3 = \left[\frac{q_w}{E_1 E_2 h_{f0} \Delta T_f}\right]^2 = \left[\frac{q_w}{q_L}\right]^2 \tag{2.107}$$

and

$$C = \left[\frac{A_p S_1 S_2}{E_1 E_2 h_{f0}}\right]^2 q_L^{4/3} \tag{2.108}$$

Rewrite the Eq. (2.104) as

$$q_{w*}^3 - C q_{w*}^2 - 1 = 0 \tag{2.109}$$

Therefore the q_{w*} can be directly solved one single real root from Eq. (2.109). Then the heat transfer coefficient can be obtained from

$$h = E_1 E_2 h_{f0} q_{w*}^{3/2} \tag{2.110}$$

In Eq. (2.90), T_w is solved by a conjugate wall heat transfer model similar to Fairuzov's approach [103] in which a separate heat transfer problem is simultaneously solved with the flow solver. It is assumed that the heat transfer occurs predominantly in the radial and axial direction of the pipeline, and the heat flow along the tangential conduction inside the pipeline wall is neglected. Hence the heat transfer equation in the two-dimensional format is written as:

$$\rho_w c_w \frac{\partial T}{\partial t} = k_w \left[\frac{1}{r}\frac{\partial}{\partial r}\left(r\frac{\partial T}{\partial r}\right) + \frac{\partial^2 T}{\partial x^2}\right] \tag{2.111}$$

where ρ_w, c_w and k_w are the density, specific heat and heat conductivity of the pipeline wall, respectively, which are assumed to be constant. r is the

coordinate along the radial direction. The coupling hydrodynamic model with heat transfer model is achieved at the inner wall boundary by satisfying:

$$k_w \left.\frac{\partial T}{\partial r}\right|_{r=\frac{D}{2}} = h\left(T_w - T_f\right) \tag{2.112}$$

Additionally, the heat transfer between the ambient and pipeline wall can also defined based on the Newton's cooling law as

$$q_{amb} = h_{amb}\left(T_{amb} - T_w\right) \tag{2.113}$$

where, q_{amb}, h_{amb} and T_{amb} are the heat flux and heat transfer coefficient between the surrounding ambient and the pipeline wall and ambient temperature, respectively. The heat transfer between the ambient and pipeline wall are calculated based on the approach of Mahgerefteh and Atti [119]. Firstly, the heat transfer coefficient h_{amb} is given by [120]

$$h_{amb} = \left(h_{nat}^3 + h_{for}^3\right)^{1/3} \tag{2.114}$$

where h_{nat} and h_{for} are the natural and forced heat transfer coefficients, respectively, which are determined by the Eq. (2.115) and (2.120).

$$h_{nat} = \left\{0.60 + \frac{0.387\mathrm{Ra}_D^{1/6}}{\left[1+\left(0.559/\mathrm{Pr}_{film}\right)^{9/16}\right]^{8/27}}\right\}^2 \tag{2.115}$$

The dimensionless Rayleigh number Ra_D is

$$\mathrm{Ra}_D = \mathrm{Gr}_{film}\,\mathrm{Pr}_{film} \tag{2.116}$$

Here, Gr_{film} and Pr_{film} are Grashof and Prandtl number, respectively. They are defined as

$$\mathrm{Gr}_{film} = \frac{\rho_{film}^2 g \beta_{film} \left(T_w - T_{amb}\right) D_{out}^3}{\mu_{film}^2} \tag{2.117}$$

$$\mathrm{Pr}_{film} = \frac{C_{pfilm} \mu_{film}}{k_{film}} \tag{2.118}$$

where D_{out} is the outer diameter of pipeline; the subscript *film* denotes the ambient properties calculated at the film temperature $T_{film} = \left(T_w + T_{amb}\right)/2$; β_{film} is the isobaric volumetric expansion coefficient, which can be obtained analytically from the EOS. For simplicity, the ambient is assumed as the prefect gas, so β_{film} is calculated by

$$\beta_{film} = \frac{1}{T_{film}} \tag{2.119}$$

The force convection heat transfer coefficient is calculated based on the Churchill and Bernstein correlation [121] as

$$h_{for} = 0.30 + \frac{0.62\,\mathrm{Re}_{film}^{1/2}\,\mathrm{Pr}_{film}^{1/3}}{\left[1+\left(0.4/\mathrm{Pr}_{film}\right)^{2/3}\right]^{1/4}} \left[1+\left(\frac{\mathrm{Re}_{film}}{28200}\right)^{5/8}\right]^{4/5} \tag{2.120}$$

Therefore, at the outer wall of pipeline, the external heat transfer between the pipeline and ambient is calculated by Eq. (2.113). In other words, the heat transfer model, Eq. (2.111), is achieved at the outer wall boundary by satisfying

$$k_w \left.\frac{\partial T}{\partial r}\right|_{r=\frac{D_{out}}{2}} = -h_{amb}\left(T_{amb} - T_w\right) \tag{2.121}$$

2.9.3. Choked Outflow

An outflow boundary is required at the open plane for solving problems of pipeline decompression/blowdown. Two distinct types of flow are used to conduct the outlet boundary at the release plane during pipeline failure: non-choked flow and choked/critical flow. The non-choked flow will occur at the initial pipeline decompression. At this stage, fluid inside the pipeline start to be released from still, then the decompression flow is quickly accelerated in a short time due to the large difference of pressure between pipeline and atmosphere. The speed of fluid is quick increased up to the local speed of sound, and then the chocked/critical flow is established at the open plane. Subsequently, the pipeline pressure will decrease and the fluid velocity at outlet plane will decrease below the local speed of sound. The non-choked flow is then re-established at the late stage of decompression flow.

When the high pressure pipeline abruptly ruptures, the flow at the open end will quickly choke due to the large ratio of pipeline pressure to atmospheric pressure. Therefore, an outflow boundary condition is applied at the open end according to the choked condition. Prior to the establishment of the sound speed at the outflow boundary, the pressure at the outflow plane is interpolated from a combination of the inner cell pressure next to the outflow plane and ambient pressure. As the choked flow develops, downstream disturbance cannot propagate upstream to influence the upstream pipe flow. Therefore, the pressure at the outflow boundary is only interpolated from the inner cell pressures if the outflow velocity is greater than or equal to its local speed of sound. With this technique, a choked condition can be ensured at the exit during the decompression process.

2.10. Concluding Remarks

This chapter first reviewed the studies on two-phase flows and described the models particularly for pipeline decompression flows. Most of models are based on the homogeneous equilibrium and isentropic flow assumptions to predict the slow transient release. However they are not suitable for the prediction of fast moving decompression wave propagation due to the limitation on computational time-step. Additionally, to handle the phase transition of mixture, mole fractions of two phases are calculated under a thermally equilibrium condition from two independent variables by flash calculation. General CFD codes do not provide functions to handle this kind of phase transition. Therefore, the model was developed for pipeline decompression based on the HEM and HRM to treat two-phase flow. For simplicity, the model assumptions for pipeline decompression flow were made: one-dimensional flow and homogeneous two-phase flow.

The HEM was given to treat two-phase fluid as a pseudo-fluid. Namely, the two-phase flow is described by the conservation equations of single-phase flow. In the HEM approach, the two-phase mixture was assumed to be locally in equilibrium with thermodynamic and kinetic, i.e. two phases sharing the same velocity, temperature and pressure. The HEM has been widely used for many years in the literature [20]–[27] and proven to be accurate for long pipeline where there is sufficient time to establish equilibrium conditions between two phases.

In consideration of the fact that the interphase heat transfer is finite for the practical condition and the change of phase takes time to occur, the HRM was proposed to account for the thermodynamic non-equilibrium effect. An analytical relaxation method was incorporated to represent the non-equilibrium mass transfer source by a simple linear approximation of the rate of quality

change. Relaxation time is one of key parameter to determine the non-equilibrium degree of departure in the actual conditions from the equilibrium conditions. Relaxation time correlated with void fraction and non-dimensional pressure difference.

The thermodynamic relationships of two-phase fluid under the HEM and HRM were described. The calculation of mole fractions of two phases were presented by employing flash calculation under a thermally equilibrium condition. Particularly, the thermodynamic modules were incorporated into the current model. Additionally, the HRM initially developed for one-component fluid was extended to be capable to deal with the non-equilibrium effects of multi-component two-phase flow. Whatever models are employed, the speed of sound of two-phase fluid is a key factor to determine the rate of pipeline decompression. The numerical method was employed to calculate the speed of sound for two-phase fluid. More attentions should be paid to calculate the thermodynamic properties under the HRM, particularly for metastable liquid.

Finally, the relevant boundary conditions were specified for pipeline decompression flow. The effects of friction and heat transfer were carefully taken into account. Noted that the heat transfer between fluid and pipeline wall were evaluated by a conjugate wall heat transfer model in which a separate heat transfer problem was simultaneously solved with the flow solver. The chocked outflow boundary condition was applied at the open end by establishment of the sound speed at the outflow plane.

Chapter 3 Numerical Methods

3.1. Introduction

Chapter 2 described Homogeneous Equilibrium Model and Homogeneous Relaxation Model for the transient two-phase flow during pipeline decompression. All the conservation equations and EOS, together with the initial boundary conditions, specified a closed system of mutually coupled non-linear equations. As it is impossible to solve it by analytical methods, a numerical procedure must be used to solve the aforementioned equations. Most models are not suitable for the prediction of fast moving decompression wave propagation due to the limitation on computational time-step.

This chapter presents the relevant numerical methods to solve the HEM and HRM. ALE method is employed to discretize the governing equations by dividing the time solution into Lagrangian phase and Eulerian phase. The convection terms are solved separately from the other terms in the conservation equations to simplify the solution procedure of the difference equations. In this manner, the computational efficiency is increased by using a sub-timestep that is only a fraction of the main computational timestep.

In this chapter, discretization of temporal and spatial terms is first presented. Secondly, the difference equations of the HEM are described in more detail. Finally, the additional difference equations for the HRM are stated, and the solution procedure of the HRM is presented here. Additionally, the numerical errors is carefully evaluated.

3.2. Arbitrary Lagrangian-Eulerian Method

The numerical solution techniques of fluid dynamic problems often need to deal with large distortion of the continuum. An important criterion is the suitability of the kinematical description of the continuum [122]. Therefore, the correlation between the deforming continuum and the finite difference mesh for simulating region is determined for the purpose of capability to deal with large distortions and give an accurate resolution of fluid zone. There exist many numerical techniques to solve fluid dynamic problems. Nearly all of these numerical solution techniques can be divided into two categories, depending on the vertices of mesh with Lagrangian or Eulerian kinematical descriptions [123]. In a Lagrangian framework, the vertices of mesh are moved with the fluid. In an Eulerian framework, the vertices of mesh are held fixed. ALE method [124]–[127] was developed to attempt to combine the advantages of both above kinematical descriptions, while minimizing their respective shortcomings. Additionally, ALE method was validated by implementing serious of consideration to such issues as computational stability, accuracy, boundary condition and so on [127].

ALE method adopts a finite difference mesh with vertices that move arbitrarily or are held fixed. In the ALE approach, the convective terms are solved separately from the other terms, for instance pressure gradient in the momentum equation. Each computational time step is divided into two phases: a Lagrangian phase and an Eulerian phase. In the Lagrangian phase, computational meshes move with fluid velocity, so the convection terms are not solved. In the rezone phase, the vertices of computational meshes are moved back to their original locations and the convective fluxes are computed.

3.3. Temporal Discretization

The transient effect should be taken into account in the highly transient flow. The aforementioned conservation equations must be discretized at time dimension. Since the conservation equations describe a marching or propagation problem, the solution at time t depends upon its history rather than on its future. The time steeping procedure is used to take account of the transient effects with a specified initial condition. The time dimension is discretized by a set of sequenced time, t^n $(n = 0,1,2,...)$. The solution procedure is marched forward in time, with solving the conservation equations at each time step $\Delta t^n = t^{n+1} - t^n$. The integer n is the cycle number.

As aforementioned, a solution cycle is performed in two phases: Lagrangian phase and Eulerian phase. The temporal discretization in both phases has changed considerably. In the calculation of Lagrangian phase, the conservative equations are integrated over control volumes. Because the computational control volumes move with the fluid in the Lagrangian phase, no convective fluxes are solved and the non-linear convective terms are dropped out in the Lagrangian phase. Therefore the solution procedure in the Lagrangian phase is greatly simplified. The resulting difference equations are only weakly coupled and can be solved individually rather than simultaneously. In the Eulerian phase the solutions to the Lagrangian phase are frozen and the convective fluxes are explicitly calculated by moving the computational grids back to their original Eulerian locations. To ensure the solution stability, it is necessary to limit the numerical time step. The Courant–Friedrichs–Lewy (CFL) condition [128] should be satisfied to keep the balance between the temporal discretization and the convection terms.

$$C_{CFL} = \frac{|\mathbf{u}|\Delta t}{|\Delta \mathbf{x}|} \tag{3.1}$$

The exact limitation of C_{CFL} depends on the numerical methods used in the solution of governing equations. For most explicit schemes it should be less than unity. The limitation can be avoided when an implicit method is used. Normally, the NS equations are solved with a derived Poisson equation for the pressure. The Poisson Equation for the pressure is used to compute the pressure correction variable at new iteration step. Semi implicit method for pressure linked equation (SIMPLE) [129] type numerical method is designed to solve the system of NS equations with the pressure iteration and pressure correction method using the Poisson Equation for the pressure. For the elliptic pressure equation, a disturbance signal at some point can travel in all directions trough the interior solution. Thus, an implicit method has to be used to compute the pressure field.

For the temporal discretization, it should also be required that the truncation error in the temporal term should be of the same magnitudes as the truncation error in the spatial terms. In this study, all time derivatives are approximated with the first-order difference as

$$\frac{\partial Q}{\partial t} \approx \frac{Q^{n+1} - Q^n}{\Delta t^n} \tag{3.2}$$

where $Q(t)$ denotes the variable evolving in the calculation, $Q^n = Q(t^n)$. In the current decompression models for a compressible two-phase flow, each time step is performed in two phases: Lagrangian phase and Eulerian phase.

3.3.1. Lagrangian Phase - Fluid Diffusion

In this Lagrangian phase, fluid diffusion is mainly calculated using a semi-implicit Theta-method [130], where Θ is used to represent the implicitness parameter. For example, a theta-method with $\Theta = 0.5$ is the familiar Crank-Nicolson method, and $\Theta = 1$ will produce the backward Eulerian method. In this study, an implicit time-stepping scheme, a theta-method for time discretization, is employed to allow the parameter Θ to vary with time. The varied implicit parameter can be calculated with the methods in the literature [104].

In the Lagrangian phase, the control volume synchronously move with the flow unit in the same velocity $\mathbf{u}$, therefore there is no convection across the control volume boundaries and only the fluid diffusion will be calculated. Moreover, the fluid advection terms will be considered in Eulerian phase. The fluid diffusion terms and effects in Lagrangian phase include implicit momentum and heat diffusions, mass diffusion, mesh and calculations of pressure, densities and energy.

3.3.2. Eulerian Phase - Fluid Advection and Mesh Rezoning

The effects of fluid advection are taken into account in Eulerian phase, in which the mesh is rezoned and the convective transport associating with moving the mesh relative to the fluid is calculated. The subcycled, explicit calculation is performed with a time step Δt_c that meets the requirement as

$$\Delta t_c = \frac{\Delta t}{n_c} \tag{3.3}$$

where Δt is the main computational time step; n_c is the undefined integer which can be specified by the Courant condition

$$\frac{u_r \Delta t_c}{\Delta x} < 1 \tag{3.4}$$

Here, u_r is the fluid velocity relative to the grid velocity. Noted that the code can run with $\frac{u_r \Delta t}{\Delta x} > 1$, because there is no exact upper bound for n_c. Therefore, the convective calculation saves computational time due to the time for Eulerian phase spending only about a tenth of the calculation time for Lagrangian phase.

In the Eulerian phase, the calculations mainly include grid velocities and rezoning the grid, explicit advection of mass, energy and momentum equations, and equations of state.

3.4. Spatial Discretization

The spatial discretization employed in current models is based on the ALE method [127], which is a Finite Volume (FV) method for a mesh made up of arbitrary hexahedrons. ALE method exhibits clear physical meanings, diffusion and convection characteristics of fluid flow. ALE method also ensures the local and global conservation of fluid properties. Additionally, the calculation with complex geometries can be done with easy implementation of boundary conditions. ALE method presents an efficient solution for the resulting simultaneous algebraic equations.

The spatial region of research is divided into a number of small cells, which connect each other and compose the object region. The corners of cell are the

vertices. All the cells constitute the computational region in which spatial discretization is built. For the mesh with ALE method, a typical cell is shown in Figure 3.1. Each cell is composed of eight vertices numbered as shown. The cell is indexed by integers (i, j, k), which is regarded as the coordinates in logical space. The vertex 4 for the cell can also be labeled by indices (i, j, k). Thus, in the Cartesian, the coordinate of vertex is $\left(x_{ijk}, y_{ijk}, z_{ijk}\right)$, which generally depends on the time t. The position vector to vertex (i, j, k) is given by

$$\mathbf{x}_{ijk} = x_{ijk}\mathbf{i} + y_{ijk}\mathbf{j} + z_{ijk}\mathbf{k} \tag{3.5}$$

The centre of cell is also one of most important parameters to determine the cell position. The centre is calculated as

$$x_{ijk}^{c} = \frac{1}{8}\sum_{\alpha=1}^{8} x_{\alpha} \tag{3.6}$$

$$y_{ijk}^{c} = \frac{1}{8}\sum_{\alpha=1}^{8} y_{\alpha} \tag{3.7}$$

$$z_{ijk}^{c} = \frac{1}{8}\sum_{\alpha=1}^{8} z_{\alpha} \tag{3.8}$$

where α is the index of vertex for cell (i, j, k).

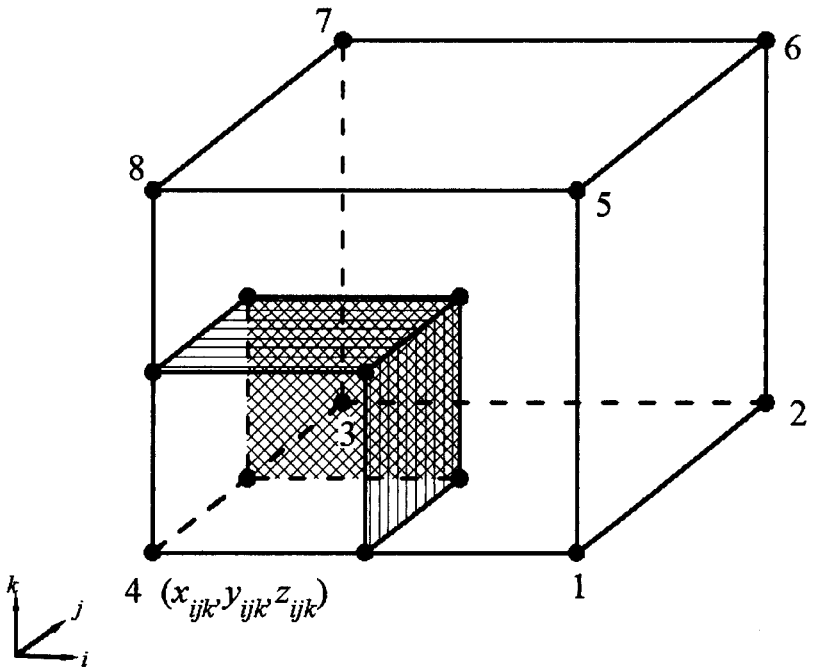

Figure 3.1 Typical cell associated with a portion of momentum cell

Momentum cell with center on the vertices of regular cell is also defined to facilitate the solution of momentum conservation equation. Momentum cell has twenty-four faces, and each of them is comparable in size to one-fourth of a regular cell face. Three faces with hatching, shown in Figure 3.1, lie within each of the eight regular cells. The vertexes of momentum cell are defined as the midpoint of the surrounding regular cell edges. With the definition of momentum cells, interpolation is not required to determine vertex motion during the Lagrangian phase calculation. But the introduction of momentum cells also incurs a major drawback that ALE method solutions are severely susceptible to parasitic models in the velocity field [131]. In order to improve the ALE method, the velocities centered on the cell faces are introduced to alleviate the drawback. So the normal velocity components on the cell faces are used to calculate the change of cell volume in Lagrangian phase and the fluxing volumes in Eulerian phase. The resulting scheme extremely reduces the requirement of node coupling [127].

Normally, quantities of velocities and coordinates are located at the mesh points or vertices as Eq. (3.9). Thermodynamic quantities are assigned to the cell centers by Eq.(3.10), such as cell volume, pressure, internal energy, mass density, etc.

$$\mathbf{u}_{ijk} = \mathbf{u}\left(x_{ijk}, y_{ijk}, z_{ijk}\right) \tag{3.9}$$

$$Q_{ijk} = Q\left(x^c_{ijk}, y^c_{ijk}, z^c_{ijk}\right) \tag{3.10}$$

where $Q = P, T, \rho, I,$ or ρ_m, as well as turbulent kinetic energy k and turbulent dissipation ε. In current study, the quantity Q with subscript "*ijk*" denotes value of the quantity at a cell point (i, j, k); otherwise, the quantity Q with a subscript single character, such as "α" or "*r*", "*l*" and so on, describes value at the centre of a face rather than a normal mesh point.

In terms of the governing equations, the differential terms in conservation equations can be integrated over the volume of a typical cell or momentum cell, in order that spatial differences can be performed. Applying the divergence theorem, the volume integrals of gradient terms are generally converted into surface area integrals, namely as

$$\int_V \nabla \cdot \mathbf{F} dV = \oint_S \mathbf{n} \cdot \mathbf{F} dS \tag{3.11}$$

where $\mathbf{F}(\mathbf{x})$ represents any sufficiently smooth function; V is a close volume, and S is the surface of this volume.

With the assumption that the integrands in the volume and surface area integrals are uniform within the cells or on cell surface, surface area integrals become sums over cell faces:

$$\oint_S \mathbf{n}\cdot\mathbf{F}dS \to \sum_{\alpha}\mathbf{F}_{\alpha}\cdot\mathbf{A}_{\alpha} \tag{3.12}$$

where α denotes the index of six faces of cell; $\mathbf{F}_{\alpha}$ is the gradient of function $\mathbf{F}$; $\mathbf{A}_{\alpha}$ is the area vector of face α for the cell, which can be described as

$$\mathbf{A}_{\alpha} = \alpha_{lr}\left(\mathbf{x}_l - \mathbf{x}_r\right) + \alpha_{tb}\left(\mathbf{x}_t - \mathbf{x}_b\right) + \alpha_{fd}\left(\mathbf{x}_f - \mathbf{x}_d\right) \tag{3.13}$$

In Eq. (3.13), the subscript l,r,t,b,f and d denotes indicates *right*, *left*, *top*, *bottom*, *front* and *back* respectively, and α_{lr},α_{tb} and α_{fd} are the geometric coefficients for face α. As shown in Figure 3.2, the points $\mathbf{x}_l$ and $\mathbf{x}_r$ are the centers of the cells on either side of face α, and $\mathbf{x}_t,\mathbf{x}_b,\mathbf{x}_f$, and $\mathbf{x}_d$ are the centers of the four edges bounding face α.

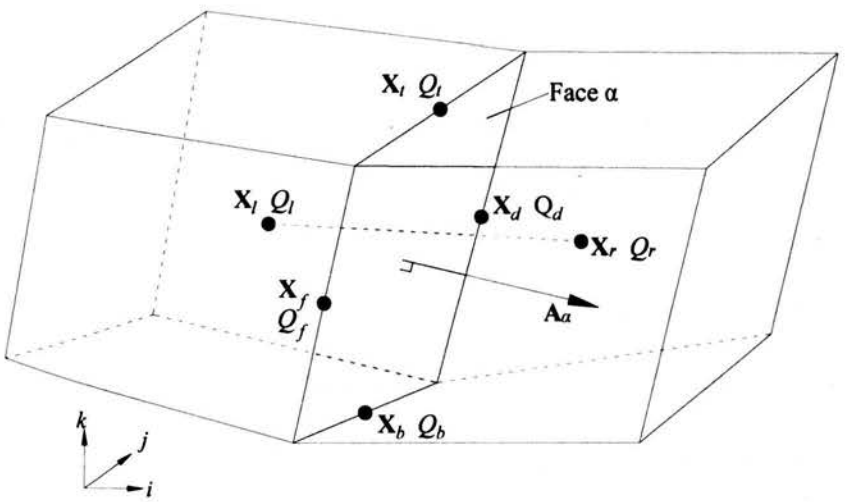

Figure 3.2 The definition of the gradient of cell-centered quantity Q on cell face α

When the object function $\mathbf{F}$ is the diffusion terms for cell-centered quantities Q, Eq. (3.12) will transform as

$$\oint_S \nabla Q \cdot d\mathbf{A} \rightarrow \sum_{\alpha} (\nabla Q)_{\alpha} \cdot \mathbf{A}_{\alpha} \tag{3.14}$$

The gradient of quantity Q on the cell face α can be determined as follows

$$(\nabla Q)_{\alpha} \cdot \mathbf{A}_{\alpha} = \alpha_{lr}(Q_l - Q_r) + \alpha_{tb}(Q_t - Q_b) + \alpha_{fd}(Q_f - Q_d) \tag{3.15}$$

where the terms Q in the right hand side of Eq. (3.15) are the averaged quantities at identified points as shown in Figure 3.2. Note that Q_l and Q_r are the quantities Q on the regular cells on either side of face α; Q_t, Q_b, Q_f and Q_d are the calculated value by averaging the quantities Q in the four cells surrounding the cell edge "*t*", "*b*", "*f*" and "*d*", respectively.

Also, volume integrals over momentum cells are converted to area integrals over the faces of momentum cells using the divergence theorem. Momentum cells are built around vertices and involve 8 regular cells which surround one vertex and share it, and a portion of momentum is shown in Figure 3.1. As the procedure of area integrals over regular cell, the area vectors of momentum cell are specified firstly. The momentum cell faces, hatched in Figure 3.1, are used to evaluate the area integrals over faces of momentum cells. The area vectors $\mathbf{A}'$ for the three momentum cell faces are usually substituted by the area vectors $\mathbf{A}$ of the regular cell. Therefore, the area integral of quantities Q over the three momentum cell faces is given below:

$$\int Q d\mathbf{A} = Q_{ijk}\left(\mathbf{A}'_a + \mathbf{A}'_b + \mathbf{A}'_c\right) = -\frac{1}{4} Q_{ijk}\left(\mathbf{A}_d + \mathbf{A}_e + \mathbf{A}_f\right) \tag{3.16}$$

where the subscript *a*, *b* and *c* denote there momentum cell faces; subscript *d*, *e* and *f* denote there cell faces of regular cell.

During the procedure of finite volume discretization, several quantities related to the mesh must be calculated. These quantities must be updated every time after the mesh moves in the Lagrangian phases. The quantities involved in the calculation are:

V_{ijk} = volume of regular cell (i,j,k), calculated based on vertex positions;

$V_{ijk}^{'}$ = volume of momentum cell (i,j,k);

M_{ijk} = mass of regular cell (i,j,k), $M_{ijk} = \rho_{ijk} V_{ijk}$;

$M_{ijk}^{'}$ = mass of momentum cell (i,j,k), $M_{ijk}^{'} = \rho_{ijk} V_{ijk}^{'}$;

$\mathbf{A}_{\alpha}$ = outward area vector of faces α for a regular cell (i,j,k);

$\mathbf{A}_{\alpha}^{'}$ = outward area vector of faces α for a momentum cell (i,j,k);

$(uA)_{\alpha}$ = $\mathbf{u}_{\alpha} \cdot \mathbf{A}_{\alpha}$, regular cell face normal velocities;

$(uA^{'})_{\alpha}$ = $\mathbf{u}_{\alpha} \cdot \mathbf{A}_{\alpha}^{'}$, momentum cell face normal velocities.

3.5. Difference Equations for HEM

The difference equations for HEM are firstly described. A finite volume approach based on the ALE [127] method is employed to solve the conservative equations, namely Eqs. (2.4), (2.6) and (2.8). With the assumptions, the pipeline decompression flow is treated as a one-dimensional two-phase flow, and one-dimensional domain is constructed to discretize the simplified conservative equations based on HEM, which are discretized on staggered grids as shown in Figure 3.3. The values of fluid velocity and grid locations are stored at the centres labelled by the crosses and thermodynamic variables such as density, internal energy and pressure at the centres labelled by the solid points. Two kinds of integral cells are used to difference the conservative

equations: scalar cell (or regular cell) and momentum cell. The scalar cells are used to integrate the scalar equations while the momentum cells are used to integrate the momentum equations.

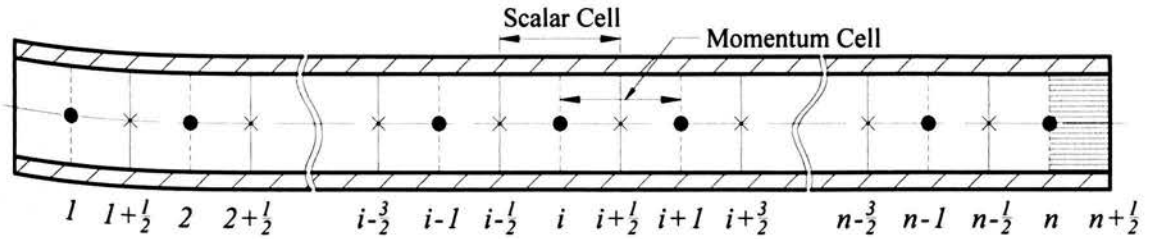

Figure 3.3 Definitions of the staggered grids for one-dimensional pipeline

The solution procedure is divided into two phases: Lagrangian phase and Eulerian phase. In the Lagrangian phase, the conservative equations are integrated over control volumes moving with fluid velocity hence no convective fluxes are involved. Since the non-linear convective terms are removed, the solution procedure in the Lagrangian phase is extremely simplified. The resulting difference equations are only weakly coupled and can be solved individually rather than simultaneously. In the Eulerian phase the solutions to the Lagrangian phase are frozen and the convective fluxes are explicitly calculated by moving the computational grids back to their original Eulerian locations. To ensure the solution stability, the convective fluxes can be calculated in a number of sub-cycles.

3.5.1. Lagrangian Phase

With the above descriptions, the Lagrangian phase difference approximation to the conservation equations, Eqs. (2.27), (2.28) and(2.29), can be given in terms of the one-dimensional pipeline grids in Figure 3.3.

3.5.1.1. Difference Equations in Lagrangian Phase

- **Total Mass Density Equations**

$$\rho_i^L V_i^L = \rho_i^n V_i^n = M_i^L = M_i^n \tag{3.17}$$

where the superscripts n and L denote old time level and new time level at the Lagrangian phase respectively; subscript i represents the scalar cell or regular cell i; M is the mass of fluid in current cell.

Equation (3.17) implies that the mass of scalar cells is conserved during the Lagrangian phase. The volume of scalar cell at the old time level is computed as follows:

$$V_i^n = A\Delta x_i^n \tag{3.18}$$

where A is the cross-sectional area of pipeline, $\Delta x_i^n = x_{i+1/2}^n - x_{i-1/2}^n$, x denotes the locations of cells or vertices. The subscripts $i-1/2$ and $i+1/2$ are the indices of two faces at each sides of scalar cell i, shown in Figure 3.3.

- **Momentum Equation**

$$\frac{M_{i+1/2}^n \left(u_{i+1/2}^L - u_{i+1/2}^n\right)}{\Delta t} = \left(P_i^L - P_{i+1}^L\right) A + \left(\tau_w + \rho g cos\theta\right)_{i+1/2}^n V_{i+1/2}^n \tag{3.19}$$

Here, the pressure gradient term is treated implicitly in order to eliminate the acoustic CFL stability condition. According to Eq.(3.17), the mass of scalar cell is conserved during the Lagrangian phase. Hence, the mass of momentum cells is also conserved as

$$\rho_{i+1/2}^L V_{i+1/2}^L = \rho_{i+1/2}^n V_{i+1/2}^n = M_{i+1/2}^L = M_{i+1/2}^n \tag{3.20}$$

The mass and volume of momentum cells at old time level can be described in terms of that of the scalar cells respectively as below:

$$M_{i+1/2}^{n} = \left(M_{i}^{n} + M_{i+1}^{n}\right)/2 \tag{3.21}$$

$$V_{i+1/2}^{n} = \left(V_{i}^{n} + V_{i+1}^{n}\right)/2 \tag{3.22}$$

The mass and volume of momentum cells at new time level at the Lagrangian phase are calculated analogously.

- **Energy Equation**

$$\frac{M_{i}^{n}\left(I_{i}^{L} - I_{i}^{n}\right)}{\Delta t} = -\frac{P_{i}^{n} + P_{i}^{L}}{2}\left(V_{i}^{L} - V_{i}^{n}\right) + \left(-u\tau_{w} + Q_{w}\right)_{i}^{n} V_{i}^{n} \tag{3.23}$$

In the Eq. (3.19) and (3.23), the source terms, friction and heat transfer terms, are treated explicitly, because the characteristic time scales of the source terms are usually much slower than those of the convection and sonic propagation for the problem of pipeline depressurization. The solution procedure in the Lagrangian phase is greatly simplified by the explicit treatment.

3.5.1.2. Iterative Solution Procedure

If the pressure P^{L} is known, Eqs.(3.17), (3.19) and (3.23) would be fully explicit. In order to solve the pressure P^{L}, the three difference equations will be solved individually with an iterative approach. Prior to the iterative solution the velocity and internal energy are first explicitly updated by the contribution of the source terms as follows:

$$\frac{M_{i+1/2}^{n}\left(u_{i+1/2}^{E} - u_{i+1/2}^{n}\right)}{\Delta t} = \left(\tau_{w} + \rho g cos\theta\right)_{i+1/2}^{n} V_{i+1/2}^{n} \tag{3.24}$$

$$\frac{M_{i}^{n}\left(I_{i}^{E} - I_{i}^{n}\right)}{\Delta t} = \left(-u\tau_{w} + Q_{w}\right)_{i}^{n} V_{i}^{n} \tag{3.25}$$

where the superscript E denotes the intermediate quantity.

During the implicit calculation of pressure P^L in the Lagrangian phase, the implicit solution procedure is depicted in Figure 3.4. Firstly, the initial predicted pressure is given by Eq. (3.26) or Eq. (3.27)

$$P_i^p = \left(P_i^L\right)^{n-1} + \frac{\Delta t^n}{\Delta t^{n-1}}\left[\left(P_i^L\right)^{n-1} - \left(P_i^L\right)^{n-2}\right] \tag{3.26}$$

$$P_i^p = \left(P_i\right)^{n-1} \tag{3.27}$$

where $\left(P_i^L\right)^{n-1}$ denotes the Lagrangian phase pressure from the previous time step $n-1$; $\left(P_i\right)^{n-1}$ is the final pressure from the previous time step $n-1$.

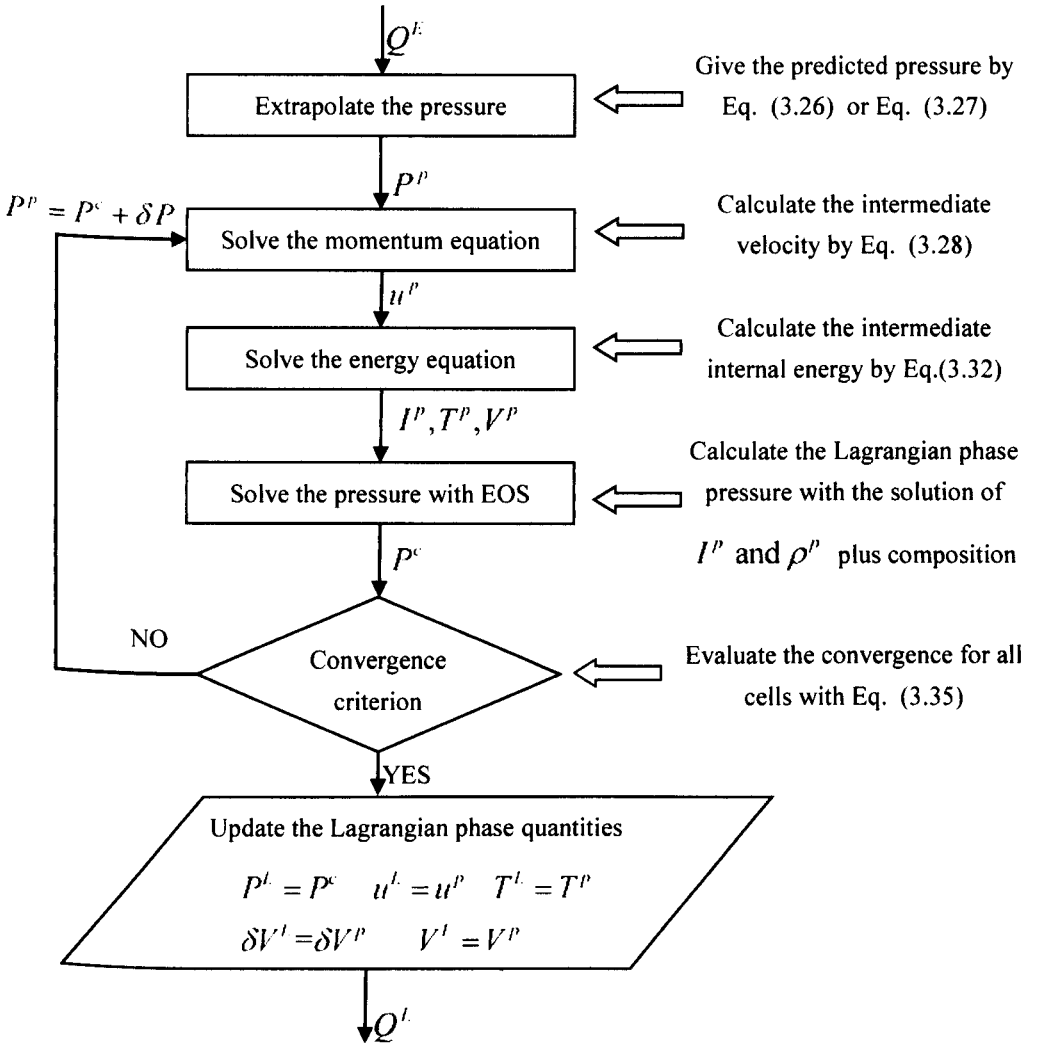

Figure 3.1 The procedure of implicit solution in the Lagrangian phase

Secondly, the predicted velocities are calculated by Eq. (3.28) associating with the initial predicted pressure and the intermediate velocities. The predicted volume in the Lagrangian phase is computed by Eq. (3.29).

$$\frac{M^n_{i+1/2}\left(u^p_{i+1/2} - u^E_{i+1/2}\right)}{\Delta t} = \left(P^p_i - P^p_{i+1}\right) A \tag{3.28}$$

$$V^p_i = V^n_i + \left(\delta V^p_{i+1/2} + \delta V^p_{i-1/2}\right) \tag{3.29}$$

where $\delta V^p_{i+1/2}$ and $\delta V^p_{i-1/2}$ are the volumes swept by the scalar cell face $i+1/2$ and face $i-1/2$ in the Lagrangian phase, respectively, and they can be simply obtained by

$$\delta V^p_{i+1/2} = \Delta t \cdot u^p_{i+1/2} \cdot A \tag{3.30}$$

$$\delta V^p_{i-1/2} = -\Delta t \cdot u^p_{i-1/2} \cdot A \tag{3.31}$$

Then the predicted internal energy is solved from Eq. (3.32) using the predicted volume of scalar cell and predicted pressure and intermediate internal energy. Accordingly, the predicted total density is updated by Eq. (3.33).

$$M^n_i \left(I^p_i - I^E_i\right) = -\frac{P^n_i + P^p_i}{2}\left(V^p_i - V^n_i\right) \tag{3.32}$$

$$\rho^p_i = \rho^n_i V^n_i / V^p_i \tag{3.33}$$

With the solutions of I^p and ρ^p plus bulk composition $Z = \left(Z_1, Z_2, \ldots, Z_N\right)$ which is assumed to be constant in the pipeline decompression study, the thermodynamic state at the end of the Lagrangian phase is determined by flash calculation as following:

$$\left(P^c, T^c, X, Y, x_{qv}\right) = f\left(I^p, \rho^p, Z\right) \tag{3.34}$$

Here the left hand side of Eq. (3.34) is the output of the flash calculation, and the right hand side is the input parameter for the flash operation. Among the output T^c is the temperature in the Lagrangian phase, $X = \left(X_1, X_2, \ldots, X_N\right)$ is the composition of liquid phase, $Y = \left(Y_1, Y_2, \ldots, Y_N\right)$ is the composition of

vapor phase and x_{qv} is the vapor quality under homogeneous equilibrium condition. It is worth noting that the approach to solve the equation of state in the HRM model should be different with that in the HEM model, and the solution for HRM will be particularly described in the following section. The flash calculation is applied to both the single and two-phases. In the case of single phase, P and T are computed directly from an EOS. Here the aforementioned real gas EOSs are applicable to calculate the properties of real fluid with consideration of the deviation from the prefect gas behaviour.

Finally, the pressure of the Lagrangian P^c is calculated from the flash calculation $f(I_i^p, \rho_i^p, Z)$. Then the convergence condition is evaluated for all the cells by

$$\left| \frac{P_i^c - P_i^p}{P_{max}} \right| < \varepsilon = 5 \times 10^{-4} \tag{3.35}$$

In Eq. (3.35), the term $P_{\max}$ is the maximum pressure on the calculation region at current time step. If the convergence condition is met for all cells, the iterative solution terminated. Otherwise, the new predicted pressure is given as

$$P^p = P^c + \frac{P^c - P^p}{S} \tag{3.36}$$

where S is a relaxation factor, which is set to be 1.25 to keep the pressure change in bound and progressing in the right direction for the pipeline decompression study. A smaller S will increase iterative loops while a larger S tends to incur iterative oscillations. The relaxation factor is verified to stabilize the iterative solution in the Lagrangian phase.

The iterative solution is repeated by solving Eq. (3.28) and (3.32) using the new predicted pressure by Eq. (3.36). In order to reach the criterion of convergence, the number of iterations [127] can be estimated by $\left(\frac{u\ \delta t}{\delta x}\right)\frac{1}{\varepsilon^{1/2}}$. Therefore, the implicit scheme converges in a finite number of iterations once the tolerance of pressure has been specified.

3.5.2. Eulerian Phase

In the Eulerian phase, the convective fluxes are explicitly calculated by moving the computational grid from their Lagrangian locations back to the original Eulerian locations, i.e. $x_{i+1/2}^{n+1} = x_{i+1/2}^{n}$. The Lagrangian locations are obtained by

$$x_{i+1/2}^{L} = x_{i+1/2}^{n} + u_{i+1/2}^{L}\Delta t \tag{3.37}$$

As the grid points are moved back to the original location after the Eulerian phase, for the sake of simplicity, the superscript for the grid locations are omitted thereafter. In the proposed method the computational timestep is not restricted by the convective CFL condition and the calculation of convective fluxes are computed in a sub-cycle explicit manner with the sub-timestep satisfying the Eq. (3.38) for each cell.

$$\Delta t_c \le min\left|\frac{\Delta x_i}{u_i}\right| \tag{3.38}$$

The number of sub-cycle can be determined by

$$NS = \Delta t/\Delta t_c \tag{3.39}$$

Therefore the volume fluxes across the cell faces of scalar cell i during each sub-cycle are computed by

$$\delta V^{C}_{i+1/2} = -\delta V^{L}_{i+1/2} / NS \tag{3.40}$$

and

$$\delta V^{C}_{i-1/2} = -\delta V^{L}_{i-1/2} / NS \tag{3.41}$$

where the superscript C denotes the quantities in the Eulerian phase.

In the Eulerian phase, the sub-timestep totally satisfies the Courant condition to ensure the stability of the solution of Eulerian phase. Additionally, the computational time is saved for the sub-cycle of convective term because the calculation in Eulerian phase takes only about one tenth of the time of the Lagrangian phase calculation [104].

3.5.2.1. Difference Equations in Eulerian Phase

The calculations of convection flux are divided into several sub-cycles. The quantities in Eulerian phase are updated after every single cycle, then the next cycle is successively performed until the all the sub-cycles are finished.

- **Mass Convection**

The density after ν sub-cycles is updated by

$$\rho_i^{\nu} V_i^{\nu} = \rho_i^{\nu-1} V_i^{\nu-1} + \left[\rho_{i-1/2}^{\nu-1} \delta V^{C}_{i-1/2} + \rho_{i+1/2}^{\nu-1} \delta V^{C}_{i+1/2} \right] \tag{3.42}$$

where the density of the last iteration $\rho_i^{\nu-1}$ is initialized at the first sub-cycle using the Lagrangian value $\rho_i^0 = \rho_i^L$, the cell volume at the current iteration is

given by $V_i^{\nu} = \left[\nu V_i^n + (NS-\nu)V_i^L\right]/NS$. $\rho_{i-1/2}^{\nu-1}$ and $\rho_{i+1/2}^{\nu-1}$ are face densities evaluated using a quasi-second-order upwind scheme (QSOU) [104] as:

$$\rho_{i+1/2}^{\nu-1} = \begin{cases} \rho_i^{\nu-1} + \left.\dfrac{\partial \rho}{\partial x}\right|_i^{\nu-1} (x_{i+1/2} - x_i)\left(1 - \dfrac{\delta V_{i+1/2}^C}{V_i^{\nu-1}}\right) & \text{if } \delta V_{i+1/2}^C \geq 0 \\ \rho_{i+1}^{\nu-1} + \left.\dfrac{\partial \rho}{\partial x}\right|_{i+1}^{\nu-1} (x_{i+1} - x_{i+1/2})\left(1 + \dfrac{\delta V_{i+1/2}^C}{V_{i+1}^{\nu-1}}\right) & \text{if } \delta V_{i+1/2}^C < 0 \end{cases} \tag{3.43}$$

where the scalar cell centre is computed as $x_i = (x_{i-1/2} + x_{i+1/2})/2$ and the gradient of density in the scalar cell is given by:

$$\left.\frac{\partial \rho}{\partial x}\right|_i^{\nu-1} = \begin{cases} sign(\Delta\rho_i^{\nu-1})\, min\left(\dfrac{|\Delta\rho_i^{\nu-1}|}{\Delta x_i}, \dfrac{|\Delta\rho_{i-1}^{\nu-1}|}{\Delta x_{i-1}}\right) & \text{if } \rho_i^{\nu-1} \cdot \rho_{i-1}^{\nu-1} \geq 0 \\ 0 & \text{if } \rho_i^{\nu-1} \cdot \rho_{i-1}^{\nu-1} < 0 \end{cases} \tag{3.44}$$

where $\Delta x_i = x_{i+1} - x_i$ and $\Delta\rho_i^{\nu-1} = \rho_{i+1}^{\nu-1} - \rho_i^{\nu-1}$.

- **Energy Convection**

The internal energy after ν sub-cycles is updated by

$$\rho_i^{\nu} V_i^{\nu} I_i^{\nu} = \rho_i^{\nu-1} V_i^{\nu-1} I_i^{\nu-1} + \left[(\rho I)_{i-1/2}^{\nu-1} \delta V_{i-1/2}^C + (\rho I)_{i+1/2}^{\nu-1} \delta V_{i+1/2}^C\right] \tag{3.45}$$

To conserve the total energy, the internal energy is initialized by $I_i^0 = I_i^L + \frac{1}{4}\left[\left(u_{i-1/2}^L\right)^2 + \left(u_{i+1/2}^L\right)^2\right]$. Similar to the face densities, the face energy densities $(\rho I)_{i-1/2}^{\nu-1}$ and $(\rho I)_{i+1/2}^{\nu-1}$ are also evaluated using the QSOU scheme.

- **Momentum Convection**

The velocity after ν sub-cycles is updated by

$$M_{i+1/2}^{\nu} u_{i+1/2}^{\nu} = M_{i+1/2}^{\nu-1} u_{i+1/2}^{\nu-1} + \left[\delta M_i^{\nu-1} u_i^{\nu-1} + \delta M_{i+1}^{\nu-1} u_{i+1}^{\nu-1} \right] \tag{3.46}$$

where the mass of momentum cell is initialized by $M_{i+1/2}^{0} = M_{i+1/2}^{L}$ and the mass at sub-cycle ν is computed as $M_{i+1/2}^{\nu} = M_{i+1/2}^{\nu-1} + \left(\delta M_i^{\nu-1} + \delta M_{i+1}^{\nu-1} \right)$. The mass fluxes across the faces of the momentum cell $\delta M_i^{\nu-1}$ and $\delta M_{i+1}^{\nu-1}$ are computed in terms of those of the scalar cells as:

$$\delta M_i^{\nu-1} = \rho_{i-1/2}^{\nu-1} \delta V_{i-1/2}^{C} - \rho_{i+1/2}^{\nu-1} \delta V_{i+1/2}^{C} \tag{3.47}$$

$$\delta M_{i+1}^{\nu-1} = \rho_{i+3/2}^{\nu-1} \delta V_{i+3/2}^{C} - \rho_{i+1/2}^{\nu-1} \delta V_{i+1/2}^{C} \tag{3.48}$$

In Eq. (3.46), the terms $u_i^{\nu-1}$ and $u_{i+1}^{\nu-1}$ are at the momentum cell faces and evaluated by the QSOU scheme as follows:

$$u_i^{\nu-1} = \begin{cases} u_{i-1/2}^{\nu-1} + \left. \dfrac{\partial u}{\partial x} \right|_{i-1/2}^{\nu-1} \dfrac{\left(x_{i+1/2} - x_{i-1/2} \right)}{2} \left(1 - \dfrac{\delta M_i^{\nu-1}}{M_{i+1/2}^{\nu-1}} \right) & \text{if } \delta M_i^{\nu-1} \geq 0 \\ u_{i+1/2}^{\nu-1} + \left. \dfrac{\partial u}{\partial x} \right|_{i+1/2}^{\nu-1} \dfrac{\left(x_{i-1/2} - x_{i+1/2} \right)}{2} \left(1 + \dfrac{\delta M_i^{\nu-1}}{M_{i+1/2}^{\nu-1}} \right) & \text{if } \delta M_i^{\nu-1} < 0 \end{cases} \tag{3.49}$$

where the gradient of velocity in the momentum cell is given by

$$\left. \frac{\partial u}{\partial x} \right|_{i-1/2}^{\nu-1} = \begin{cases} sign\left(\Delta u_{i-1/2}^{\nu-1} \right) min\left(\dfrac{\left| \Delta u_{i-1/2}^{\nu-1} \right|}{\Delta x_{i-1/2}}, \dfrac{\left| \Delta u_{i-3/2}^{\nu-1} \right|}{\Delta x_{i-3/2}} \right) & \text{if } \Delta u_{i-1/2}^{\nu-1} \Delta u_{i-3/2}^{\nu-1} \geq 0 \\ 0 & \text{if } \Delta u_{i-1/2}^{\nu-1} \Delta u_{i-3/2}^{\nu-1} < 0 \end{cases} \tag{3.50}$$

where $\Delta x_{i-1/2} = x_{i+1/2} - x_{i-1/2}$ and $\Delta u_{i-1/2}^{\nu-1} = \Delta u_{i+1/2}^{\nu-1} - \Delta u_{i-1/2}^{\nu-1}$.

After the completion of *NS* convective sub-cycles, the solution variables at the new time level $n+1$ are updated by:

$$\begin{cases} \rho_i^{n+1} = \rho_i^{NS} \\ u_{i+1/2}^{n+1} = u_{i+1/2}^{NS} \\ I_i^{n+1} = I_i^{NS} - \dfrac{1}{4}\left[\left(u_{i-1/2}^{NS}\right)^2 + \left(u_{i+1/2}^{NS}\right)^2\right] \end{cases} \tag{3.51}$$

Finally, flash calculation $\left(P^{n+1}, T^{n+1}, X^{n+1}, Y^{n+1}, x_{qv}^{n+1}\right) = f\left(I^{n+1}, \rho^{n+1}, Z\right)$ is conducted for each scalar cell to update the solutions at the new time level $n+1$.

3.6. Numerical Method for HRM

3.6.1. Lagrangian Phase

Under the HRM, the Lagrangian phase difference approximation to the conservation equations can be given based on the spatial discretization along the one-dimensional pipeline shown in Figure 3.3. The difference equations for HRM in the Lagrangian phase are same as HEM, namely total mass equations Eq. (3.17), momentum equations Eq. (3.19) and energy equations Eq. (3.23). The supplemental difference equation for rate equation will be presented below.

3.6.1.1. Difference Equation for Rate Equation

The source term of mass generation Γ_{GR}, are calculated implicitly using Eq. (2.57) with the quantities at the Lagrangian phase. Therefore the difference equation of rate equation can be given as follow

$$\frac{x_{qv,i}^{L}-x_{qv,i}^{n}}{\Delta t}=-\frac{x_{qv,i}^{L}-\left(\overline{x_{qv}}\right)_{i}^{L}}{\Theta_{i}^{L}} \tag{3.52}$$

Then the actual quality of two-phase fluid in the Lagrangian phase can be derived from (3.52) as following:

$$x_{qv,i}^{L}=\left(x_{qv,i}^{n}+\frac{\Delta t}{\Theta_{i}^{L}}\left(\overline{x_{qv}}\right)_{i}^{L}\right)\Big/\left(1+\frac{\Delta t}{\Theta_{i}^{L}}\right) \tag{3.53}$$

3.6.1.2. Iterative solution procedure for HRM

Unlike the iterative solution procedure for HEM, the actual quality of two-phase fluid under HRM can be directly solved from difference equation, not from the thermodynamic equation of state. But the unconstrained equilibrium quality $\overline{x_{qv}}$ is still calculated by the specified EOS.

In the Lagrangian phase, the solution procedure of pressure P^{L} for HRM is similar to HEM. Briefly, the three normal difference equations plus one rate equation will be solved individually using an iterative approach. Firstly, the actual quality, velocity and internal energy are first explicitly updated by the contribution of the source terms prior to the iterative solution. Then, the quantities in the Lagrangian phase, density ρ^{L}, pressure P^{L}, velocity u^{L}, internal energy I^{L} as well as actual quality x_{qv}^{L} are calculated and updated with the iterative solution method until the convergence criterion is satisfied.

Noted that the Lagrangian phase pressure is solved by means of the EOS and predicted parameters such as density, internal energy and actual quality. Of importance that the actual quality is applicable to solve the pressure in the Lagrangian phase.

3.6.2. Eulerian Phase for Rate Equation

The actual quality after ν sub-cycles is updated by

$$\rho_i^{\nu} x_{qv,i}^{\nu} V_i^{\nu} = \rho_i^{\nu-1} x_{qv,i}^{\nu-1} V_i^{\nu-1} + \left[\left(\rho x_{qv} \right)_{i-1/2}^{\nu-1} \delta V_{i-1/2}^{C} + \left(\rho x_{qv} \right)_{i+1/2}^{\nu-1} \delta V_{i+1/2}^{C} \right] \quad (3.54)$$

where the density and actual quality of the last iteration $\rho_i^{\nu-1}$, $x_{qv,i}^{\nu-1}$ are initialized at the first sub-cycle using the Lagrangian value $\rho_i^0 = \rho_i^L$, $x_{qv,i}^0 = x_{qv,i}^L$. Similar to the face densities, $\left(\rho x_{qv} \right)_{i-1/2}^{\nu-1}$ and $\left(\rho x_{qv} \right)_{i+1/2}^{\nu-1}$ are face densities evaluated using the QSOU scheme.

3.7. Numerical Errors

Numerical errors should be inevitably introduced during the solution of non-linear equation system using CFD technique. The numerical errors are mainly produced by three recognised sources [159]: roundoff error, iterative convergence error and discretization error. Roundoff errors are caused by the fact that the real numbers are computationally represented by a finite number of significant digits which related with the finite machine precision. A plan of floating-point arithmetic operations is generally required to control this kind of numerical error, for example, keeping away from subtraction of almost equalized large numbers or addition of numbers with quite large different magnitude. In this section, the iterative convergence error and discretization error will be mainly discussed.

Iterative convergence errors

Figure 3.4 shows that the procedure of a numerical solution requires an iterative process. In the Lagrangian phase, the final results should satisfy the discretised equations for the calculated domain, i.e. Eqs. (3.17), (3.19) and

(3.23), and the given boundary conditions. As the number of iterations increases, if the difference between the final calculation and the current calculation after n iterations decreases, the iterative solution is convergent. The implementation of the iterative process will be terminated until the convergence criterion is met. This termination will generate a contribution to the numerical error as an iterative convergence error. Commonly, the residual is used to evaluate the iterative convergence error. In the current study, the iterative solution of pressure-velocity coupling in the Lagrangian phase is implemented with the specified convergence criterion. For the pressure P_i at the cell i, the iterative convergence error is

$$\left(R_i^P\right)^{(k)} = \left(P_i^L\right)^{(k)} - \left(P_i^L\right)^{(k-1)} < \varepsilon P_{\max} \tag{3.55}$$

where $\left(R_i^P\right)^{(k)}$ is the residual of the local pressure at current iteration number k in the Lagrangian phase.

The iterative convergence error of quantity Q is generally evaluated as follows:

$$\left(R_i^Q\right)^{(k)} = \left(Q_i^L\right)^{(k)} - \left(Q_i^L\right)^{(k-1)} < \varepsilon_Q Q \tag{3.56}$$

where the convergence criterion ε_Q for quantity Q is implicitly correlated with the criterion ε for pressure. Conclusively, these iterative convergence errors can be totally controlled by the specific convergence criterion of the implicit solution in the Lagrangian phase.

Discretisation Errors

The conservative equations are discretized on the chosen grids for the calculated domain. The temporal and spatial derivatives are approximated on the specified time-step and space grid. The temporal and spatial discretization employed in the current study has been shown in the previous sections. The temporal derivatives are approximated with the first-order difference. The convective terms related to the spatial derivatives are approximated with the evaluation of variables at the cell faces using the QSOU scheme.

These approximations correspond to the truncation of a Taylor series. For a function $f(x)$ the Taylor series expansion of $f(x+\Delta x)$ around the point n at x is

$$f(x+\Delta x)=f(x)+\left(\frac{\partial f}{\partial x}\right)_x \Delta x+\left(\frac{\partial^2 f}{\partial x^2}\right)_x \frac{\Delta x^2}{2}+\ldots \tag{3.57}$$

In the current notation the discrete value Q_i and Q_{i+1} at two discretized points i and $i+1$ respectively, therefore the Eq. (3.57) can be written as

$$Q_{i+1}=Q_i+\left(\frac{\partial Q}{\partial x}\right)_i \Delta x+\left(\frac{\partial^2 Q}{\partial x^2}\right)_i \frac{\Delta x^2}{2}+\ldots \tag{3.58}$$

The derivate of variable Q with respect to space x is given as

$$\left(\frac{\partial Q}{\partial x}\right)_i=\frac{Q_{i+1}-Q_i}{\Delta x}+O(\Delta x) \tag{3.59}$$

where $O(\Delta x)=-\left(\frac{\partial^2 Q}{\partial x^2}\right)_i \frac{\Delta x}{2}-\ldots$, the truncated terms. Generally, the $O(\Delta x)$ is the high-order terms, which can be neglected as the grid is refined. So, the Eq. (3.59) can be rearranged as

$$\left(\frac{\partial Q}{\partial x}\right)_i \approx \frac{Q_{i+1}-Q_i}{\Delta x} \tag{3.60}$$

The derivate with respect to time t can be given analogous to the way of space.

$$\left(\frac{\partial Q}{\partial t}\right)_n \approx \frac{Q_{n+1}-Q_n}{\Delta t} \tag{3.61}$$

Where Δt is the time-step, n is the nth time scale.

Eqs. (3.60) and (3.61) are both first-order accurate. Here the derivate with respect to time t is widely employed in the current study to calculate the temporal terms. Particularly, the QSOU differencing scheme is used in the Eulerian phase due to strong-monotonicity [104] and nearly (or fully when the variation of density along x is constant) second-order space accuracy. Finally, the residual of variable Q with respect to space x is determined during the solution procedure of Eulerian phase as follows:

$$\left(R_i^Q\right)^n = \begin{cases} O\left(\Delta x^2\right), \text{ for all } j, \left(\rho_{j+1}-\rho_j\right)/\Delta x_j = const \\ O\left(\Delta x^k\right), \ 1 < k < 2, \end{cases} \tag{3.62}$$

In summary, the numerical errors related to the discretisation errors can be greatly controlled by the time-step Δt and the grid size Δx. The current study strictly verified the time-step and the grid size to minimize the discretisation errors.

3.8. Concluding Remarks

In this chapter, the relevant numerical methods were presented. The conservation equations for HEM and HRM were discretized using the ALE method. In this manner, only the sub-timestep needs to satisfy the convective

CFL condition while the main convective CFL can be greater than one, resulting in increased computational efficiency on the premise of ensuring computational stability.

The difference equations for both models were described in details. Meanwhile, the solutions of these difference equations were performed in the Lagrangian and Eulerian phase respectively based on the theory of ALE. In the Lagrangian phase, the source terms and diffusion terms of conservation equations were solved, and the iterative solution procedure was executed to solve the Lagrangian phase pressure. With the predicted results from the Lagrangian phase, the convective terms were calculated in the Eulerian phase. Additionally, a quasi-second-order upwind scheme calculating the quantities on the cell face was applied here.

Chapter 4 Validation of the Two-phase Model

4.1. Introduction

Chapter 2 presented HEM and HRM models for two-phase flow to predict the decompression behaviours of high pressure pipelines. Both models were developed for pipeline decompression. The relevant boundary conditions such as friction and heat transfer and chocked outflow were stated. Chapter 3 introduced the numerical methods to expatiate on the discretization and difference schemes for both approaches.

In order to establish the credibility of the models as a tool for CO_2 decompression studies, the models must be validated against experimental data. In this chapter, decompression curve as one of the key factors for pipeline control is compared with experiments with conventional fluid, rich gas and LPG. Besides, validation on decompression curve is also made for CO_2 with the available experimental data. Additionally, comparison is also made between the predicted pressure-time and temperature–time traces at different locations and the measurements.

Many researchers investigated the characteristics of pipeline decompression [21], [22], [59], [62], [66], [67], [94], [132]–[139]. There exist various experiments of pipeline decompression for conventional fluid. Groves et al. [22] studied the decompression wave speed for natural gas pipelines. Jones and Gough [59] reviewed various experimental and theoretical studies on the behaviours of two-phase decompression following rich gas pipelines rupture. Botros et al. carried out a series of experiments to study the behaviour of rich gas pipeline decompression [62], [133]–[140]. Richardson and Saville [66], [67] carried out LPG pipeline depressurisation tests, known as Isle of Grain

full-scale experiments, and developed computer code BLOWDOWN to predict the decompression flow of LPG pipeline. In addition, Maxey [141] examined the decompression behaviour of dense phase CO_2. Hence, these experiments are selected to validate current models in this section.

4.2. Decompression Wave Curve

As a pipeline ruptures, a leading decompression wave propagates away from the rupture plane into the undisturbed compressed fluid at the local speed of sound. Behind the leading decompression wave, the decompression wave speed is equal to the local speed of sound minus the local escaping velocity as the decompression wave travels in the opposite direction of the escaping flow until it reaches the closed end of the pipe and is reflected back. On arrival of the deflected wave from the closed end, the decompression process will be accelerated. The time for the reflected wave to reach the open end is very short for most shock tube tests, therefore the decompression process is normally assumed to be isentropic prior to the arrival of the deflected wave.

The decompression curve, or more precisely the decompression wave speed versus pressure, is an important factor concerning fracture control of pipelines [139]. BTCM is often used to determine the toughness required to arrest a running ductile fracture in a pipeline [142]. The key input to BTCM is the decompression curve, a relationship between the pressure and velocity of the pressure wave, which is highly dependent on the thermodynamic properties of the fluid, its initial pressure and temperature. The theoretical definition of decompression wave speed is:

$$W = C - |u| \tag{4.1}$$

where W is the decompression wave speed; C and u are the local speed of sound and fluid velocity, respectively.

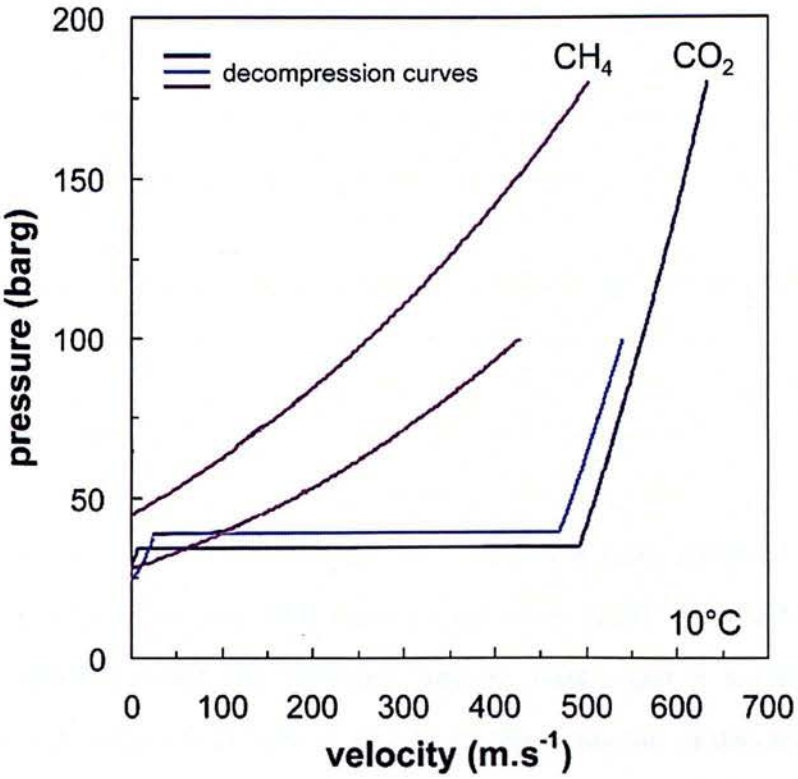

Figure 4.1 The typical decompression wave curves [142]

The typical decompression curves [142] are shown in Figure 4.1. For methane, the decompression curve is essentially a smooth curve regardless of the initial conditions. However, for rich gas and CO_2, this often contains a plateau due to the discontinuity in the speed of sound caused by phase transition [138], [142]. The existence of the plateau in the decompression curve will result in a higher toughness requirement for the pipeline according to the BTCM based design calculations. Therefore, it is significant to predict the accurate decompression wave curve for fracture control of high pressure pipelines.

The models are validated against measured decompression curves for a series of rich gas and CO_2 shock tube tests [22], [62], [139], [141], [143]. Eight cases

of rich gas, two cases of dense phase CO_2 and two cases of supercritical CO_2 have been considered. All the measurements were taken at locations close to the open end of shock tubes. Apart from the assumptions made in the Chapter 2, the following assumptions are added in this section:

- The rupture rate is infinitely fast;
- The flow is isentropic by neglecting heat transfer and wall friction;
- The pre-rupture flow velocity is negligible.

It is noted that the assumption of isentropic flow resulting from neglecting heat transfer and wall friction will be removed in the following sections.

4.2.1. Rich Gas Cases

The gas compositions and initial conditions of rich gas cases are listed in Table 4.1. The first two cases are BMI experimental cases [139]. Battelle Memorial Institute (BMI) studied the full-scale fracture tests using a 6.096m long, 10.16cm in diameter shock tube to investigate the behaviour of decompression wave. Calgary case was implemented with a 30.48m long 6.03cm internal diameter shock tube [22]. Shell case is the full scale fracture test [143] carried out by British gas for Shell. The last four cases are conducted by Botros et al. [62] with a total length of 172m, internal diameter of 49.325mm and wall thickness of 5.5mm decompression tube test rig to examine the decompression behaviour in conventional gas mixtures and rich gas mixtures. Finally, the comparisons between the measured and predicted decompression curves are presented in Figure 4.2, Figure 4.4 to Figure 4.10.

Table 4.1 Compositions and initial conditions for validation cases of rich gas

Name		BMI PB	BMI PM	Calgary	Shell	Case 1	Case 2	Case 3	Case 4
Pressure [MPa]		11.514	11.583	8.687	14.311	10.58	20.545	14.21	9.949
Temperature [°C]		-22.78	-23.33	0.0	10.0	-25.59	-24.8	4.61	-4.99
Composition [mol%]	CH_4	86.33	90.18	9.608	9.12	95.474	95.127	76.493	68.509
	C_2H_6	7.86	5.91	3.597	4.91	2.936	3.288	16.627	21.406
	C_3H_8	3.45	2.26	0.3414	0.73	0.19	0.204	5.745	9.08
	iC_4	0.24	0.21	0.4581	1.03	0.016	0.017	0.012	0.026
	nC_4	0.27	0.23	0.0403	0.19	0.025	0.027	0.017	0.014
	iC_5	0.03	0.05	0.0342	0.269	0.004	0.004	0.003	0.002
	nC_5	0.03	0.04	0.0046	0.185	0.003	0.003	0.002	0.002
	nC_6	0.01	0.02	0.0013	0.401	0.002	0.002	0.002	0.001
	N_2	0.76	0.44	1.498	0.76	0.569	0.566	0.457	0.408
	CO_2	1.02	0.66	0.53	0.781	0.781	0.764	0.642	0.553
	Other	-	-	0.0013	0.401	-	-	-	-
Literature		[139]	[139]	[22]	[143]	[62]	[62]	[62]	[62]

All the decompression curves start from the leading decompression wave ahead of which is the undisturbed compressed fluid under its initial states. The highest points in the decompression curves correspond to the pressure and speed of sound under the initial states. A smooth section of each decompression curve, corresponding to the decompression of a single phase fluid, is observed immediately after its initial decompression point. The decrease in the decompression velocity is mainly due to an increase in the escaping velocity. Depending on the initial states, the decompression path may enter a two-phase region. The speed of sound is discontinuous across the phase boundary and drops sharply as a two-phase mixture emerges. The discontinuity in the speed of sound across the phase boundary and the continuity in the escaping velocity result in a discontinuity in the decompression wave speed exhibiting as a "plateau" on the decompression curve. Following phase transition, the pressure of the two-phase mixture continues to drop while the escaping velocity keeps on increasing. As the speed of sound for a two-phase mixture varies slowly with the pressure, the

decompression velocity is found to decrease with pressure and drops to zero at the choked rupture plane, i.e. the open end of the shock tube.

In the cases of shock tube experiment BMI PB, the decompression path is clearly shown in Figure 4.3. Compared with the decompression wave curve in Figure 4.2, the pressure at the plateau is clearly consistent with the pressure at the intersection between the decompression path and the phase envelope. It is proved that the plateau occur at the moment of phase transition. Namely, the plateau of the decompression wave curve indicates that the decompression path is crossing the phase envelope into the two-phase region.

Comparisons are also made between the predictions of the current model with that of the DECAY model [59], Exxon model [59] and GASDECOM model [15]. Overall, the predictions of the current model are slightly different from the predictions by the other models mainly in the features of plateau of decompression wave curve. The features of plateau involve the width and position of the plateau. The width is determined by the difference of speeds of sound between single and two-phase fluid, and the position is decided by the pressure when the phase transition happens. Both are greatly correlated with the thermodynamic properties which are calculated by the specified EOS. It is believed that the difference is partly owing to the EOS. In the case of BMI PB, Figure 4.2 shows the decompression wave curve for BMI PB. DECAY and Exxon models present the same pressure plateaus. It is because that the same EOS, SRK EOS, is employed for both models. But the current model employs PR EOS which should predict more accurate saturated properties for natural gas. It is seen that the pressure of the plateau is higher than the prediction of DECAY and Exxon model. However the discrepancy of the pressure of the plateau between experiment and prediction is larger. It is not evident to explain that the DECAY or Exxon model predict more accurate. Because the phase transition actually occurs below the saturation pressure due to the

non-equilibrium effect. But all models mentioned here are based on the assumption of homogeneous equilibrium, which is another significant factor to impact the prediction of decompression wave curve.

On the whole, the predictions are in reasonably good agreement with the experimental data, but there still exist some discrepancies. The maximum differences of pressure plateaus are 15%. Two major assumptions are thought to be the most likely cause of the discrepancies, i.e. the HEM assumption and the infinite fast rupture rate.

In the shock tube tests, the measurements were taken near the rupture plane where inhomogeneous and non-equilibrium conditions prevail and the validity of the HEM assumption is challenged. In non-equilibrium conditions, phase transition would take place at a pressure lower than the thermodynamic equilibrium pressure. This may account for the over-predictions of the plateau pressure for BMI PB, BMI PM, Calgary and Shell cases. The plateau is under-predicted in Case1 and Case2, which can be attributed to the following reasons. The actual rupture process has a finite rupture rate, i.e. full-bore rupture is achieved only after a period of time during which the release flow at the rupture plane has a three-dimensional nature. This implies that the actual outflow rate would be smaller than the infinitely fast rupture rate assumed during the very early stage of the release. Hence the infinitely fast rupture rate may also account for some of the discrepancies. However, it is likely that the finite rate rupture process only affects the very early stage of the release. Finally, the discrepancies among the plateau pressures might also be attributed to the choice of EOSs which would predict slightly different dew/bubble points.

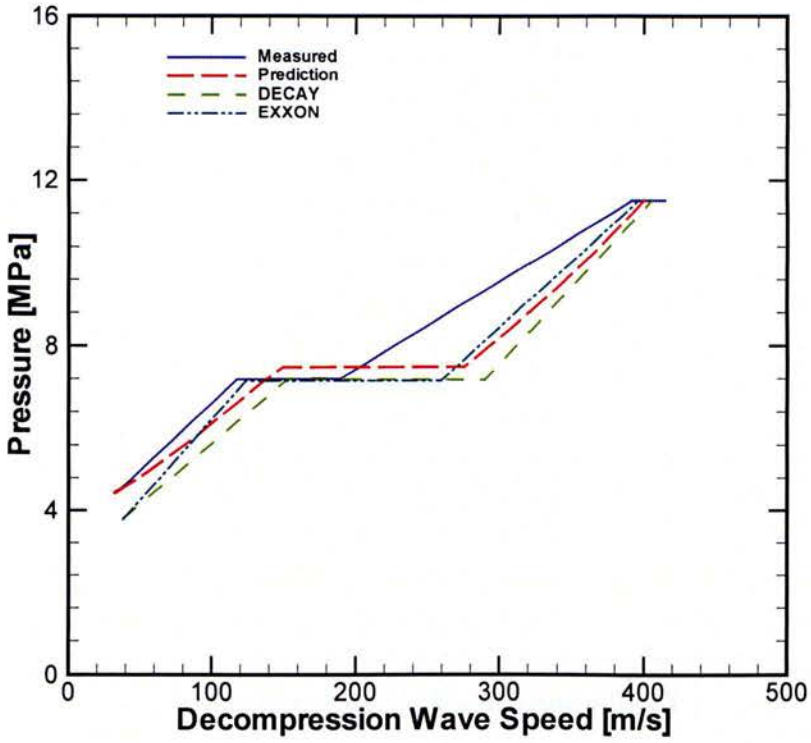

Figure 4.2 Decompression curve of BMI PB

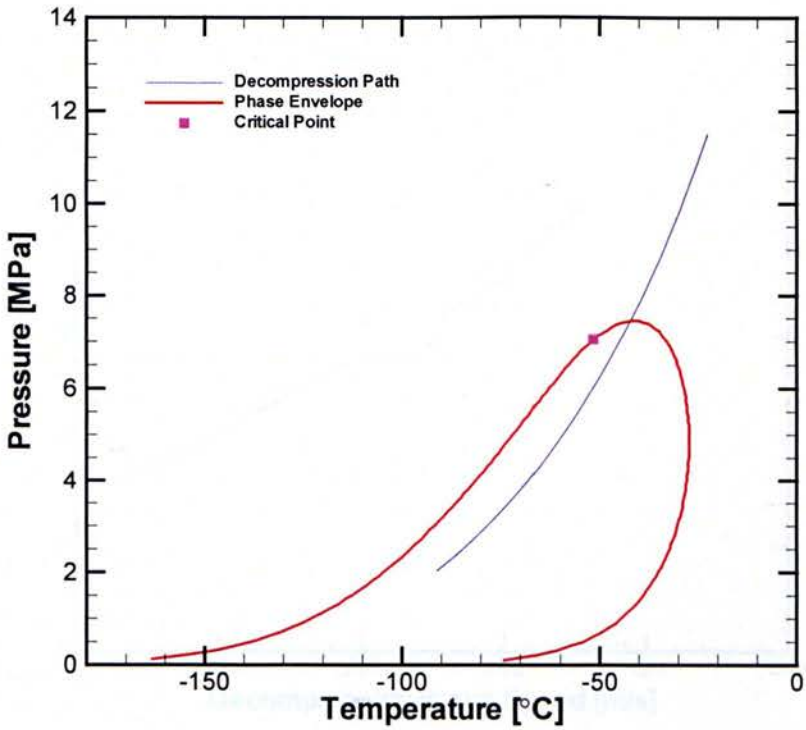

Figure 4.3 Decompression path for BMI PB

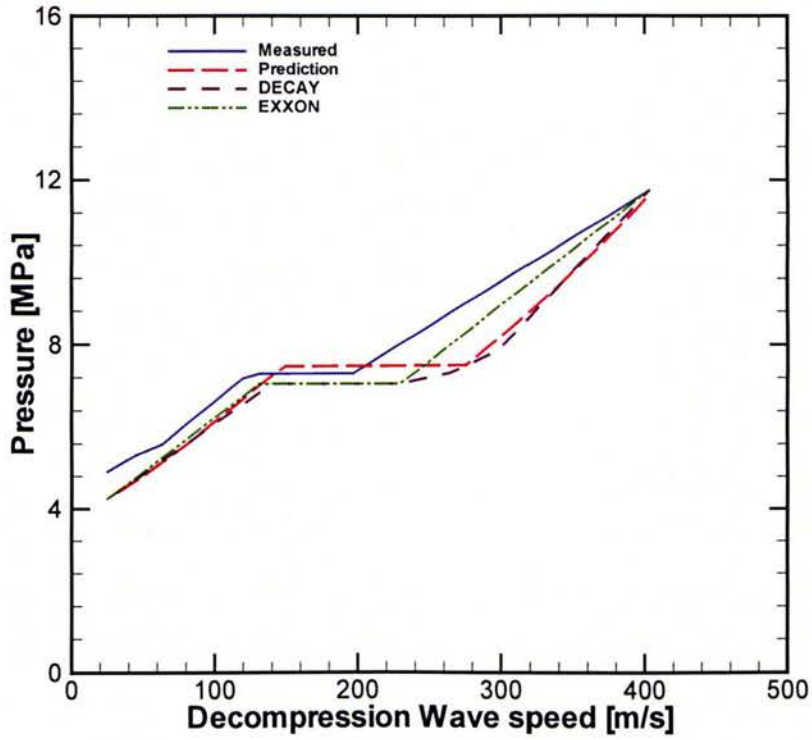

Figure 4.4 Decompression curve of BMI PM

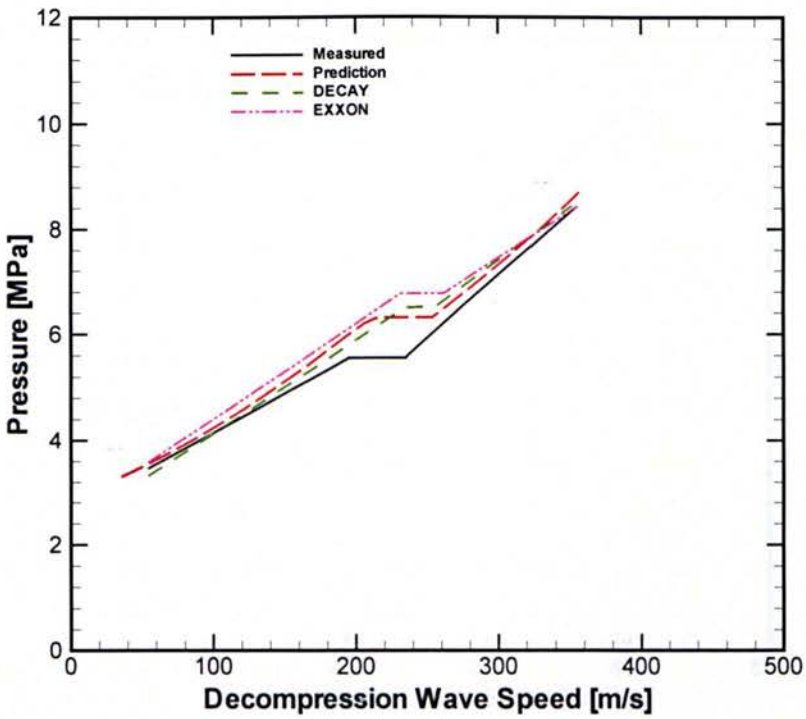

Figure 4.5 Decompression curve of Calgary

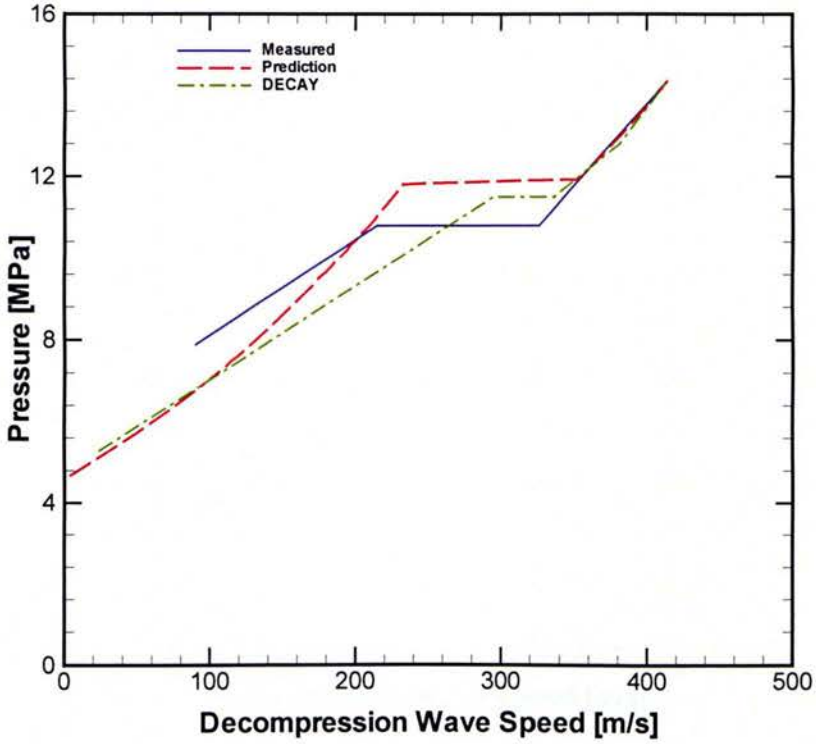

Figure 4.6 Decompression curve of Shell

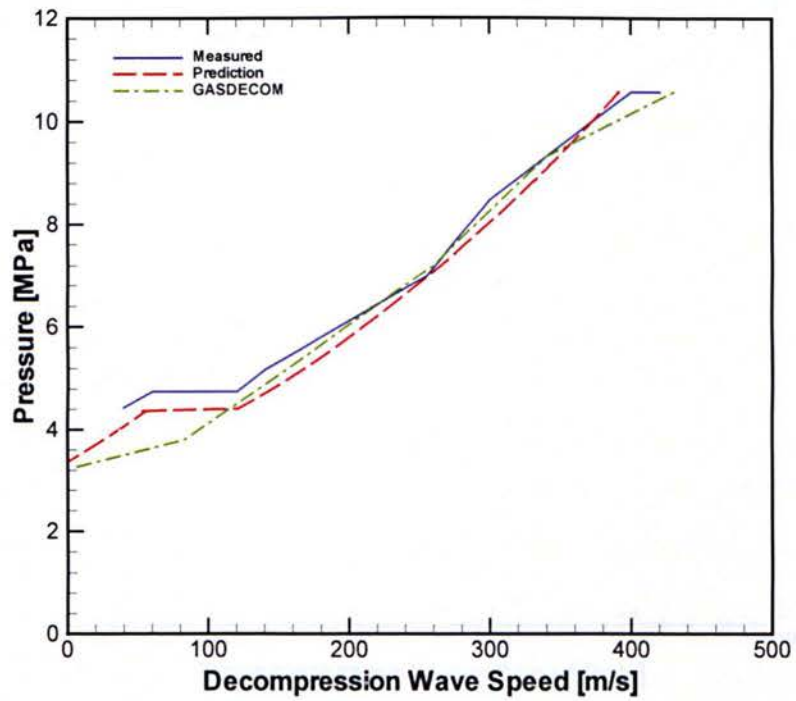

Figure 4.7 Decompression curve of Case1

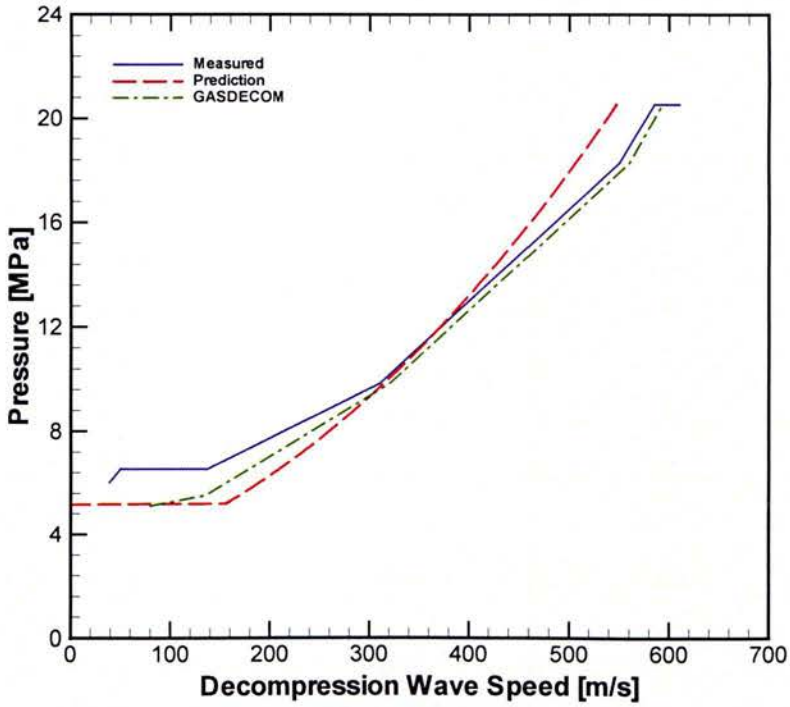

Figure 4.8 Decompression curve of Case2

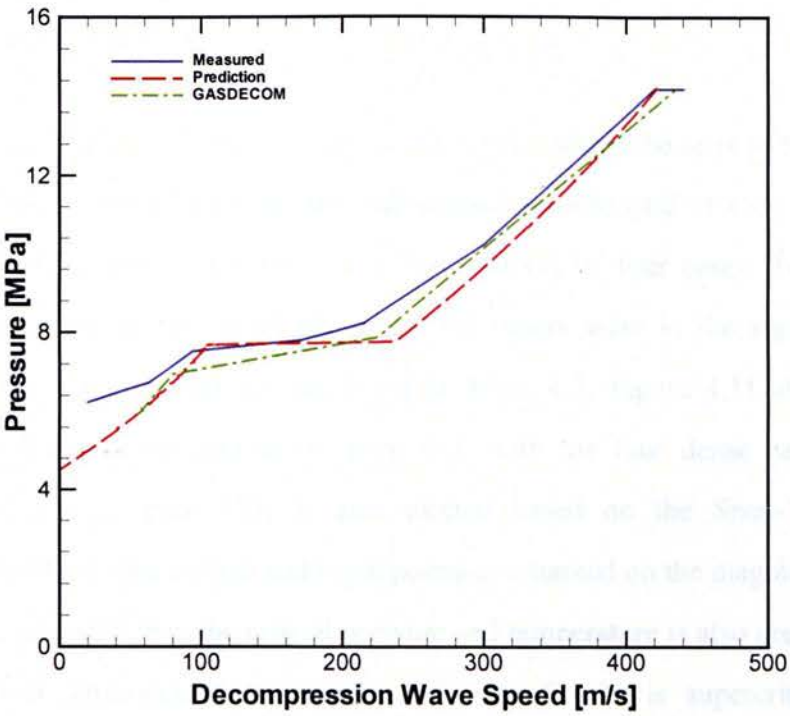

Figure 4.9 Decompression curve of Case3

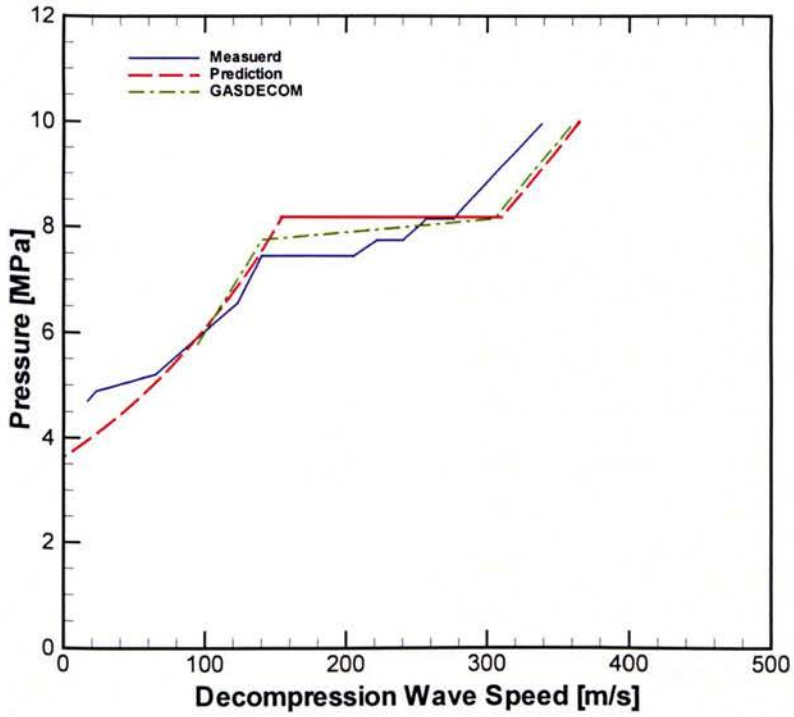

Figure 4.10 Decompression curve of Case4

4.2.1. CO_2 Cases

The Battelle Memorial Institute carries out seven shock tube tests in the 1980s [141], [144] to investigate the decompression characteristic of CO_2 pipeline. Maxey [141] reported decompression wave curves of four cases. Two cases were performed in the liquid phase and the others were in the supercritical phase. The initial conditions are listed in Table 4.2. Figure 4.11 shows the Pressure-Temperature diagram of pure CO_2 with the four dense cases. The saturated line of pure CO_2 is also plotted based on the Span-Wagner's correlation [86]. The critical and triple points are marked on the diagram. When pressure is greater than the critical pressure and temperature is also greater than the critical temperature, the phase condition of CO_2 is supercritical, for example Case 3 and Case 4.

Table 4.2 Initial Conditions of BMI CO_2 shock tube tests

Case No.	Initial Pressure [MPa]	Initial Temperature [°C]	Phase Condition
1	12.0622	26.67	Liquid
2	6.3773	23.11	Liquid
3	9.3291	34.44	Supercritical
4	14.5402	42.22	Supercritical

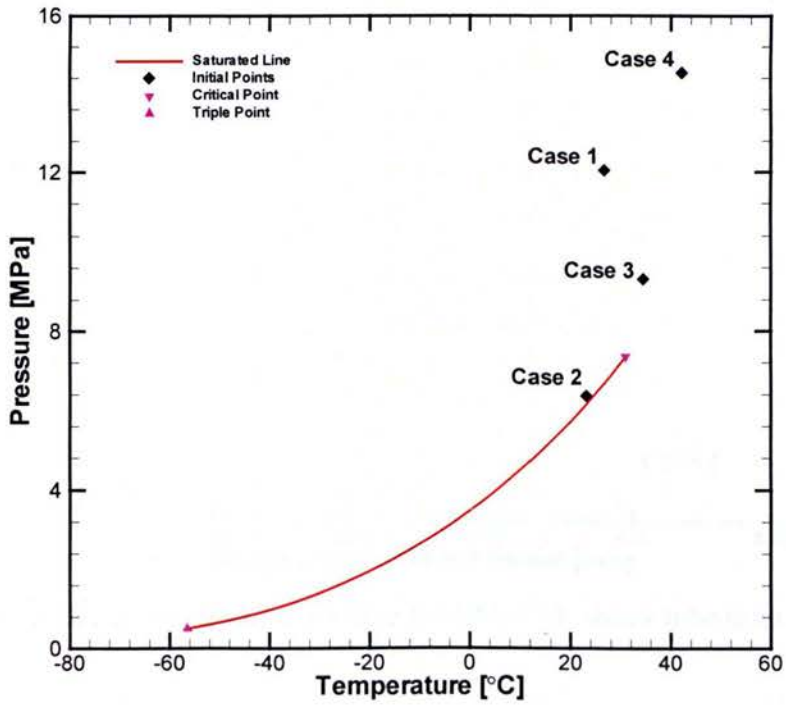

Figure 4.11 Diagram of Pressure-Temperature for CO_2

Comparison for the BMI shock tube tests is presented in Figure 4.12 to Figure 4.15. All the four cases involve dense phase (liquid or supercritical) CO_2 decompression. The predictions by Cosham and Eiber [142] using GASDECOM are also included for comparison. Good agreement is achieved for the predictions of the plateau pressure and the maximum difference is approximately 6%, while apparent discrepancies in the speed of sound under the initial states are observed. Three equations of state, i.e. Peng-Robinson Equation of State [69] and Span-Wagner Equation of State [86] which were implemented in current model, and the Benedict-Webb-Rubin-Starling (BWRS)

Equation of State [82] employed by Cosham and Eiber [142] are found to result in slightly different predictions for the local speed of sound. The discrepancies are thought to be mainly due to the small compressibility of CO_2 in the dense phase.

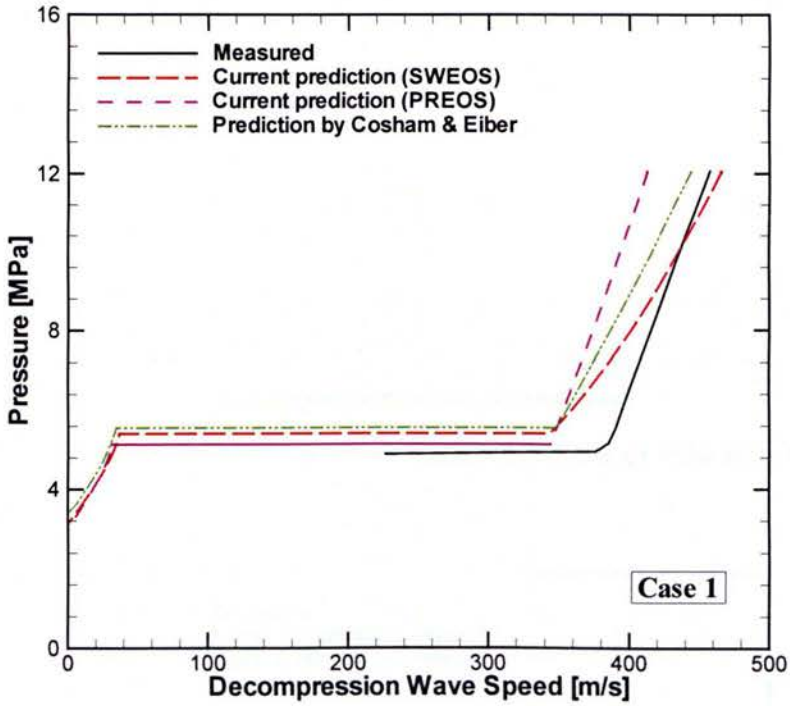

Figure 4.12 Decompression wave curve for BMI CO_2 shock tube tests (Case 1).

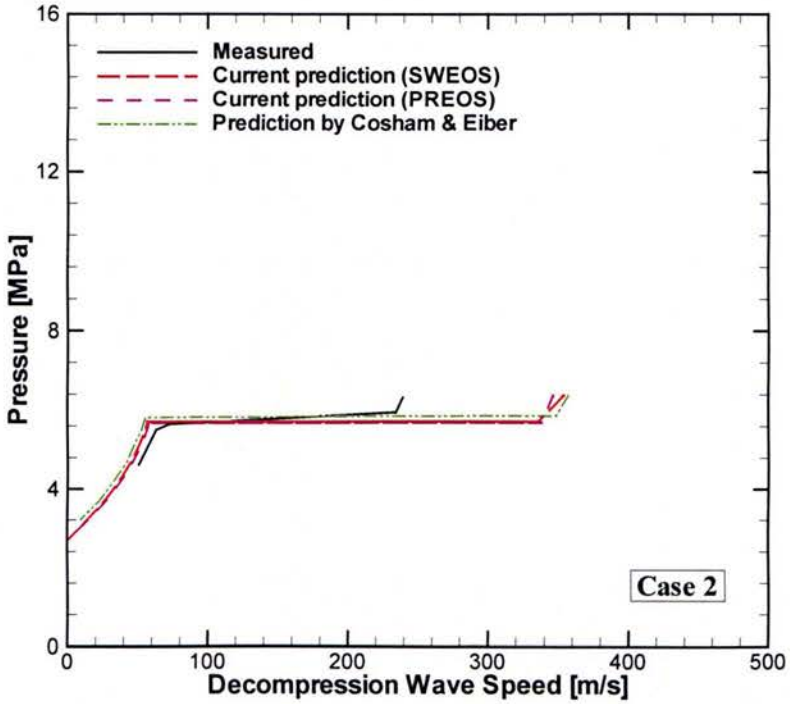

Figure 4.13 Decompression wave curve for BMI CO_2 shock tube tests (Case 2).

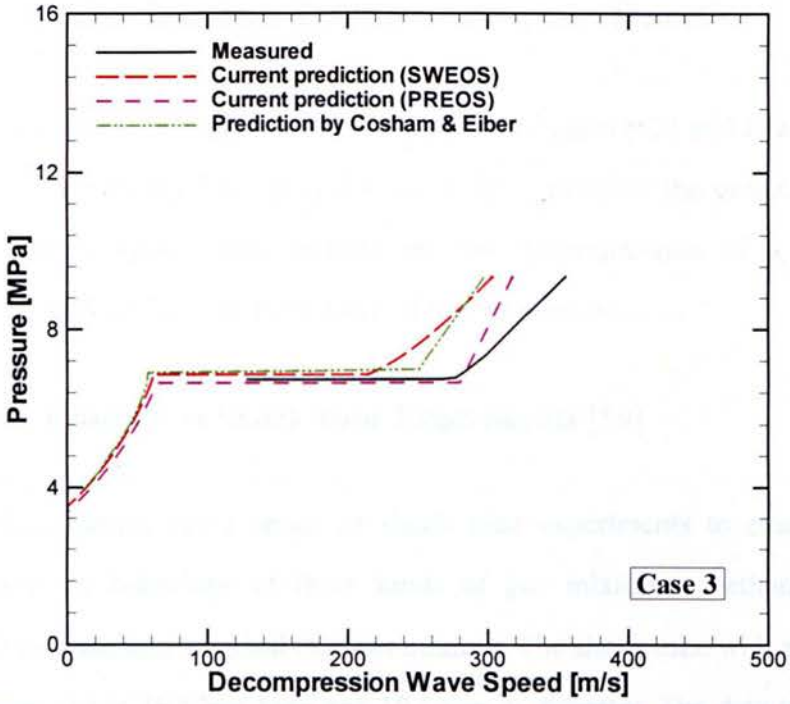

Figure 4.14 Decompression wave curve for BMI CO_2 shock tube tests (Case 3).

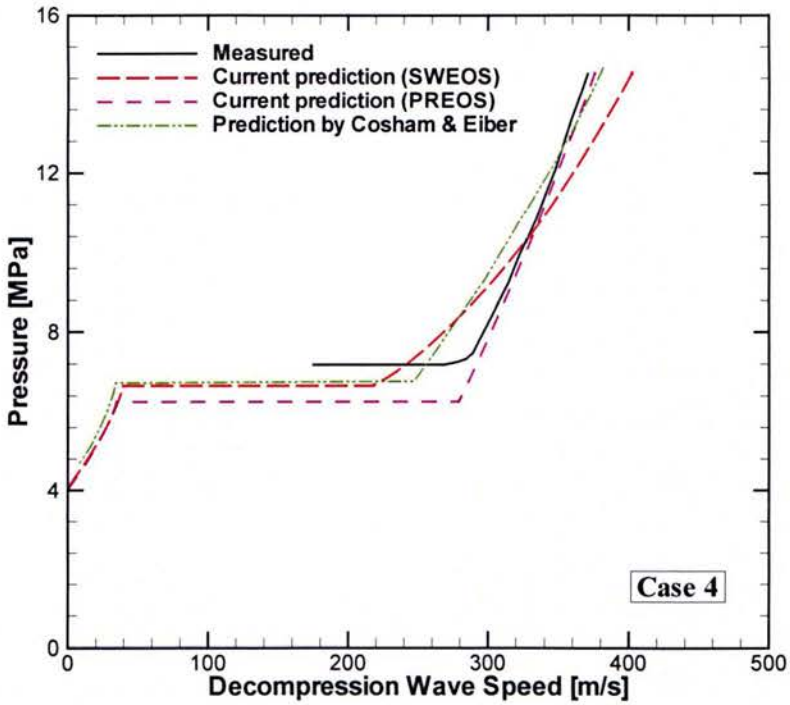

Figure 4.15 Decompression wave curve for BMI CO_2 shock tube tests (Case 4).

4.3. Pressure-time and Temperature-time Traces

British Gas shock tube experiments [59], Botros's cases [62] and Isle of Grain full-scale experiments [66], [67] are involved to evaluate the creditability of current model. These cases include the fast decompression of a rich gas pipeline as well as the slow blowdown of a LPG pipeline.

4.3.1. British Gas Shock Tube Experiments [59]

British Gas carries out a series of shock tube experiments to examine the decompression behaviour of three kinds of gas mixtures: methane/ethane, methane/propane and a typical rich gas mixture. The shock tube with a bursting disk at one end is 36.576m long and 10.16cm in diameter. The data of friction and wall thickness are not available, thus the friction and wall heat transfer are neglected here. The initial conditions and the gas compositions of shock tube experiments are listed in Table 4.3. The corresponding phase envelopes and

initial conditions are plotted in Figure 4.17. The monitoring points are tabulated in Table 4.4. Nine cases are calculated and only the results of pressure-time traces are compared with the experimental data. For the sake of brevity, the predictions of three typical cases are reported here.

Table 4.3 Initial conditions and compositions of British Gas shock tube experiments

Name		BGC 1	BGC 2	BGC 3	BGC 4	BGC 5	BGC 6	BGC 7	BGC 8	BGC 9
Pressure [MPa]		10.0	11.3	12.5	7.5	10.0	12.8	7.0	10.0	12.5
Temperature [°C]		13	13	15	21	28	30	29	25	25
Composition [mol%]	CH_4	85	85	85	90	90	90	82.4	82.3	82.8
	C_2H_6	15	15	15				7.89	7.85	7.83
	C_3H_8				10	10	10	5.2	5.3	5.1
	iC_4							0.45	0.47	0.43
	nC_4							1.21	1.28	1.15
	iC_5							0.25	0.27	0.24
	nC_5							0.35	0.37	0.33
	nC_6							0.64	0.63	0.56
	nC_7							0.003	0.003	0.002
	O_2							0.022	0.017	0.018
	N_2							0.91	087	0.89
	CO_2							0.62	0.62	0.61

Table 4.4 Location of monitoring points for British Gas shock tube experiments

Point No.	PT1	PT2	PT3	PT4	PT5	PT6	PT7
Distance from the rupture plane [cm]	30.48	60.96	121.92	243.84	396.24	609.6	914.4
Point No.	PT8	PT9	PT10	PT11	PT12	PT13	
Distance from the rupture plane [cm]	1371.6	1828.8	2286.0	2743.2	3200.4	3627.12	

Mesh sensitivity is first investigated for tests and the results are shown in Figure 4.18. The pressure-time traces at two points are presented here. The results of mesh sensitivity study show that the predictions with five different meshes produce similar results. Therefore the predictions are not sensitive to

the grid resolution. Here, a structured mesh with 200 non-uniform cells in the axial direction and one cell in the radical direction is used to calculate all the British shock tube tests. The grid size gradually increases in the axial direction away from the rupture plane at a ratio of 5 between the maximum grid size and the minimum grid size at the rupture plane, and then the grid keeps uniform for the rest of pipe length. It is found that when the length of pipe zone with uniform mesh is two third of the length of whole pipe, it is more suitable to balance the computational efficiency and capability to predict the fast decompression behaviours. For a cylindrical pipe, a sector of a full circle is taken as the computational region to discretize and create the mesh. The use of sector region is more efficient than modelling a full 360 degree cylinder by taking advantage of the surface symmetry, and half degree sector is applied in the study. The computational mesh is illustrated in Figure 4.16. The boundary is demonstrated in the figure, and the finer grids are employed close to the open end of pipe in order to capture the rapid decompression behaviours. Generally, the approach of discretizing the computational domain is similar. Therefore, the details of discretization are not re-stated in the following section in order to avoid repeating.

The minimum size of cell is 0.03m in the axial direction. For the fast decompression process a small timestep is needed to resolve the fast decompression rate. Here, the computational timestep is varied during the simulation by ensuring that the maximum CFL number is less than 0.2, and the maximum of the computational timestep is approximately $1.5*10^{-5}$.

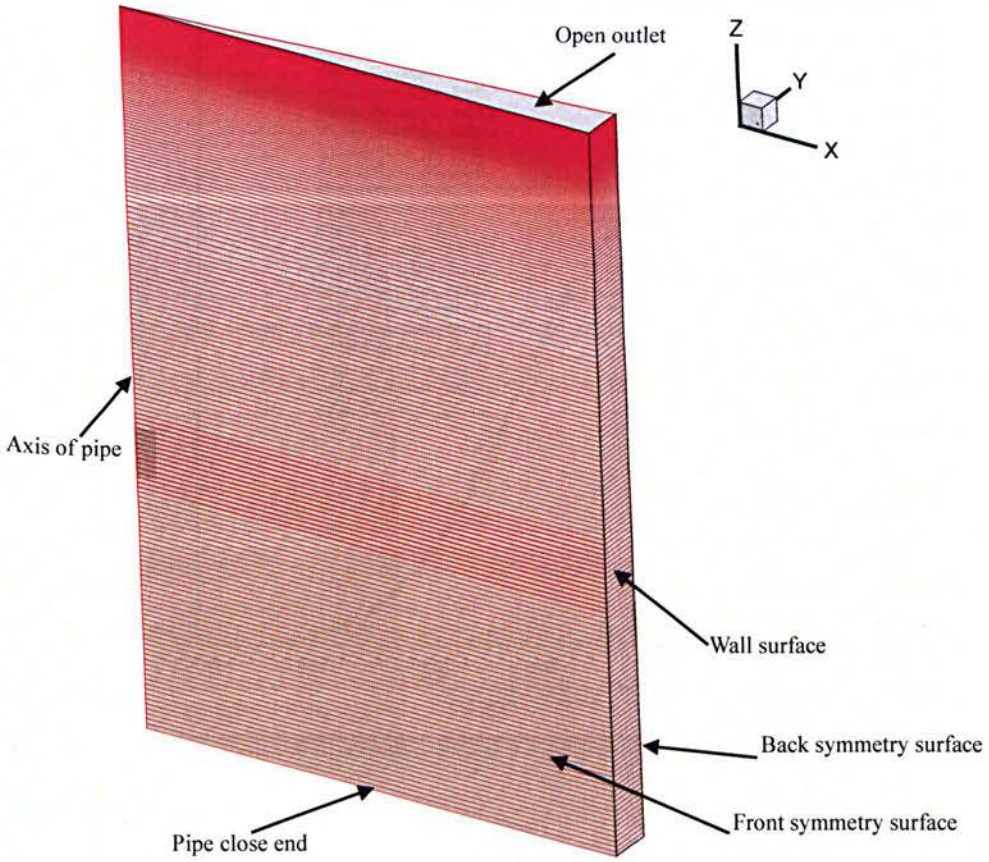

Figure 4.16 The demonstration of computational mesh.

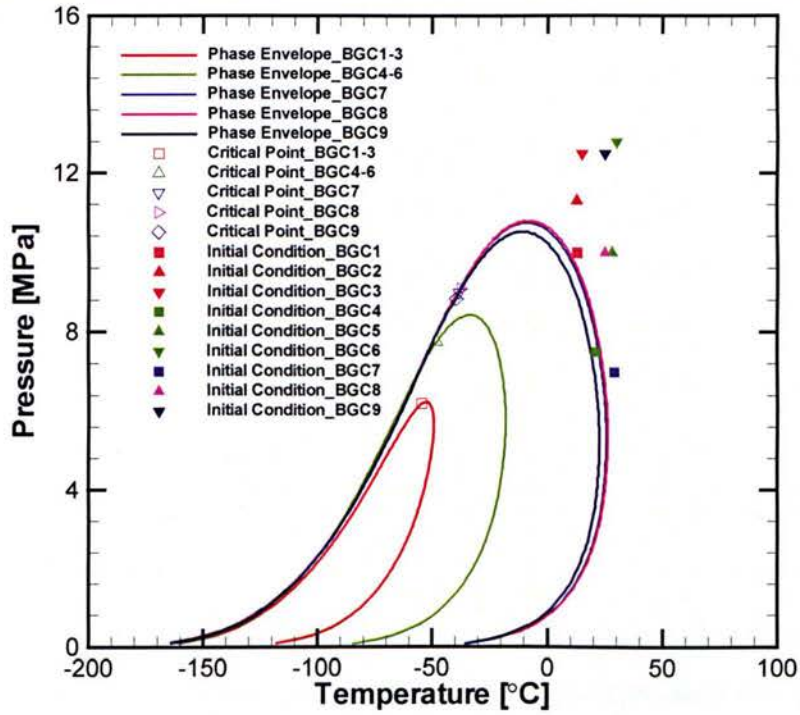

Figure 4.17 Diagram of phase envelopes and initial conditions for British Gas shock tube tests

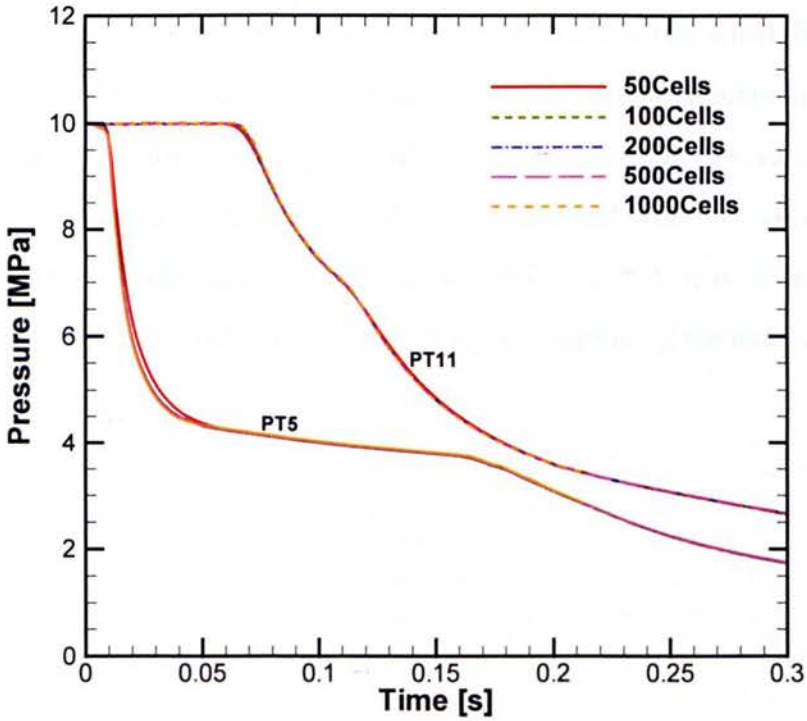

Figure 4.18 Mesh sensitivity study for BGC1 test

When the shock tube ruptures, a decompression wave is triggered and propagates away from the rupture plane into the undisturbed compressed fluid at the local speed of sound. As the decompression wave reaches the closed end, it is reflected back propagating towards the rupture plane. Figure 4.19 shows a comparison of pressure-time traces between predictions of current model and DECAY and the experimental data at five monitoring points. The calculated value of speed of sound for BGC1 using the PR EOS is 388.5m/s, which is close to the measured value of 389.9m/s. The pressure-time trace shows that the pressure varies with time. At the beginning of decompression, the decompression rate is extremely fast in the location close to the rupture plane, and the pressure drops sharply at PT2, PT4 and PT5. The fast decompression is well captured by the numerical simulation. The decompression rate becomes milder at the location from PT8 to PT11. Figure 4.20 shows the decompression path of BGC1. As the pressure drops to the value around the saturation pressure, the decompression rate decreases. For the location of PT11, an apparent increase is observed in the decompression rate around t=0.11s, which is caused by the reflected wave. This is well predicted by the present simulation. As the release goes on, the pressure is slightly under-predicted. Overall, BGC1 prediction of current model has shown better agreement with the experimental data than DECAY (the maximum difference: 5% vs. 20%). It is believed that the improvements are owing to the current model employing the more accurate equation of state.

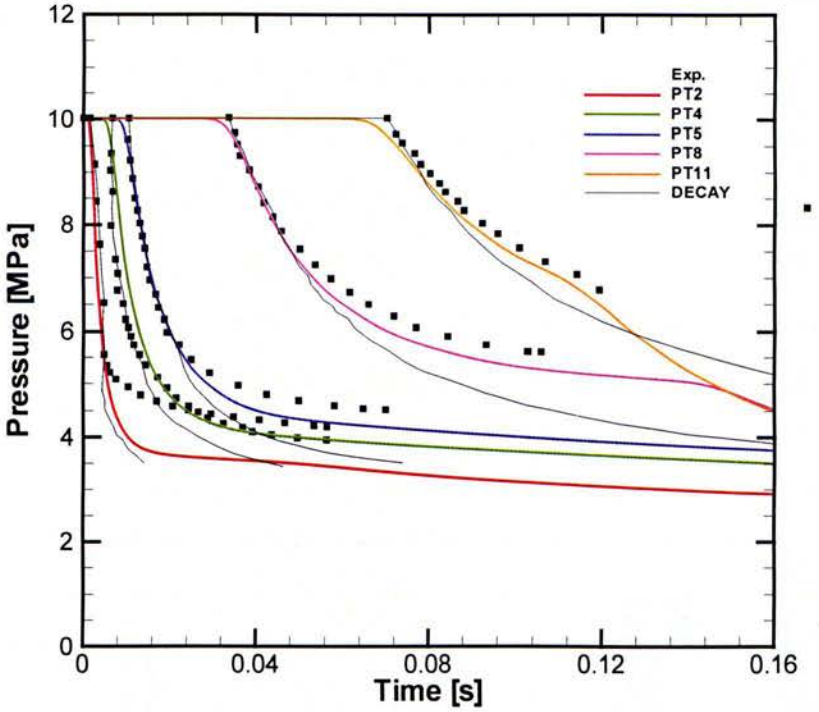

Figure 4.19 Pressure-time traces of BGC1

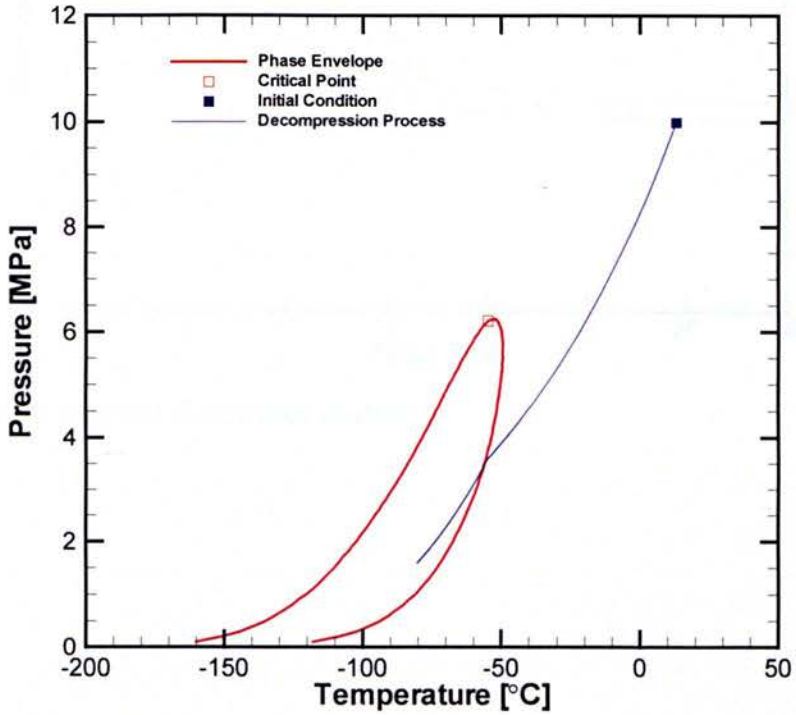

Figure 4.20 Decompression process for BGC1

The comparison of pressure-time traces and decompression path for BGC5 are shown in Figure 4.21 and Figure 4.22, respectively. The results of BGC5 are totally similar to BGC1. The predicted pressure-time traces at PT2 and PT3 have a reasonably good agreement with experimental data. It is unexpected that there is comparatively large difference (about 15%) at PT5 between the predictions by current model and DECAY. It is believed that the large difference is partly owed to the uncertainty of the experiment. The prediction with current model shows better agreement than DECAY.

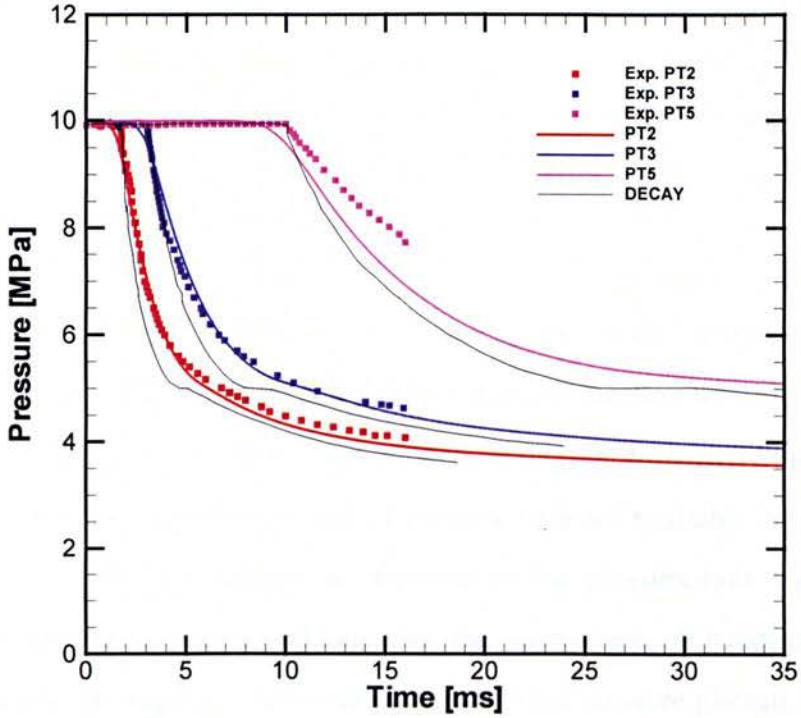

Figure 4.21 Pressure-time traces of BGC5

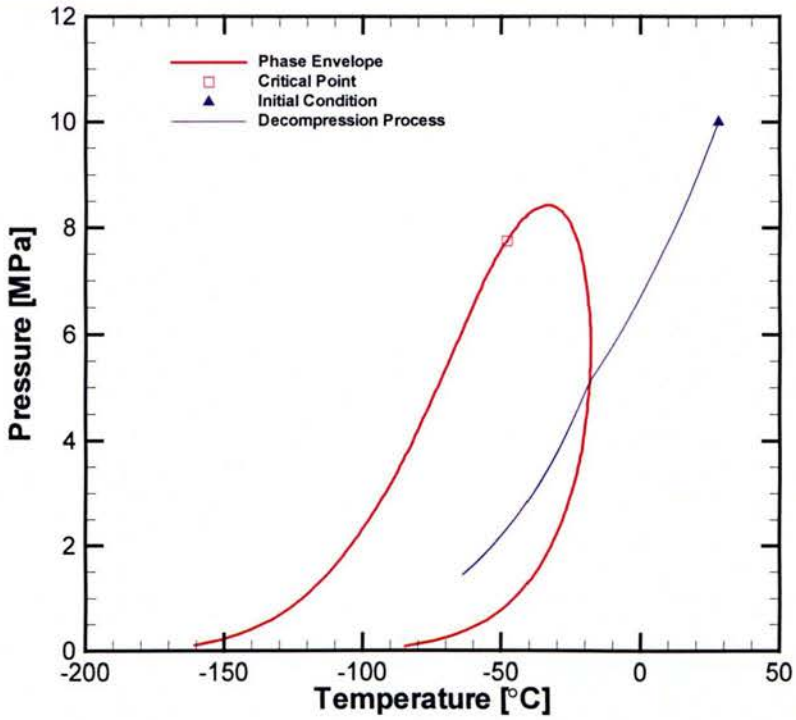

Figure 4.22 Decompression path for BGC5

The decompression behaviour of shock tube with multi-component hydrocarbons is studied in BGC7-9. The curves of pressure vs. time and the decompression path for BGC7 are plotted in Figure 4.23 and Figure 4.24 respectively. The experimental data of pressure-time are available only at PT3 and PT5. An obvious plateau is observed in the pressure-time trace. The pressure plateau is maintained due that the latent heat of condensation is released into the vapour. Additionally, the predicted pressure plateau is higher than the measurement. The discrepancy is most likely explained by the delayed nucleation. The decompression process is quite rapid. The pressure may fall below the saturation pressure without triggering a phase change. Therefore, the gas fluid may temporarily become supersaturated. Then the phase change will occur at a lower pressure than the predicted pressure with HEM assumption.

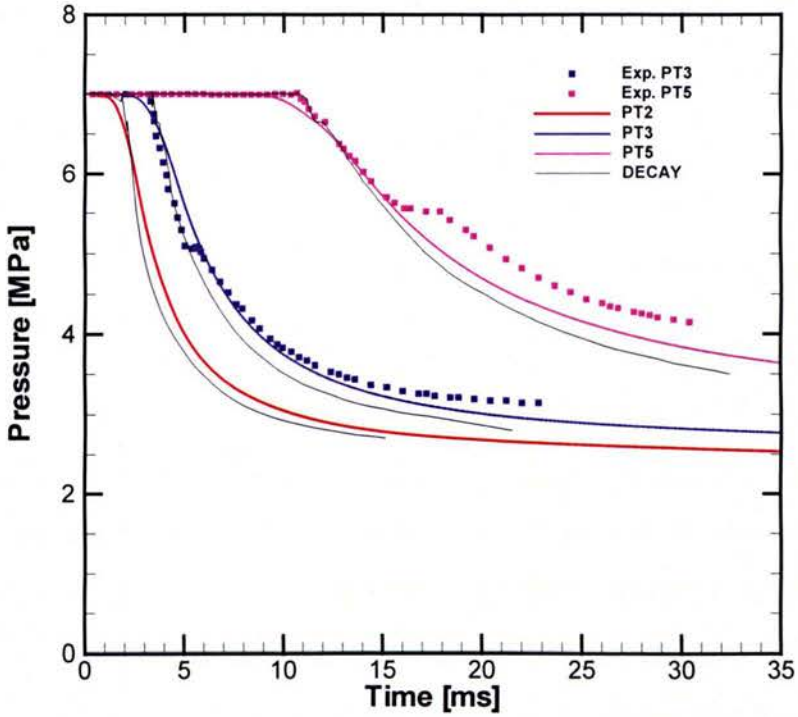

Figure 4.23 Pressure-time traces of BGC7

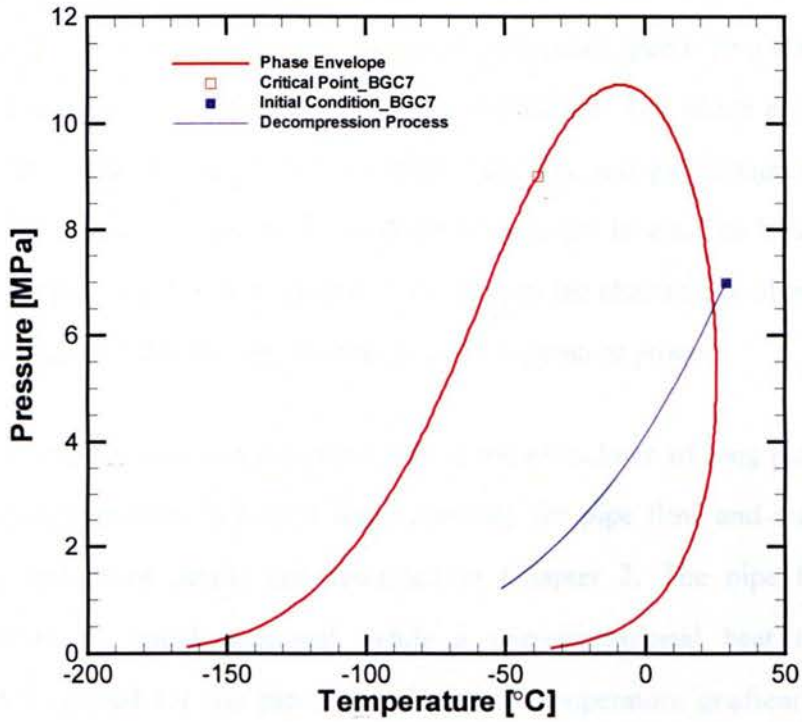

Figure 4.24 Decompression path for BGC7

In conclusion, the predicted pressure-time traces for British Gas shock tube tests are in reasonably good agreement with the experiment data, and show better agreement than the predictions of DECAY.

4.3.2. Botros's Cases [62]

Comparison is made between the predictions of pressure-time and temperature–time traces and the experimental data obtained from the literature [62]. A NPS 2 stainless steel decompression tube test rig is used to measure the flow parameters following pipeline rupture. The test tube has a total length of 172m, internal diameter of 49.325mm and wall thickness of 5.5mm. The wall roughness of test tube is 0.05mm and the insulated material fitted on the outside of the test tube is 25mm thickness. A rupture disc is installed at one end of the test tube and it will initiate the rupture. Several fast response pressure transducers and temperature probes are mounted along the test tube to record the flow parameters and decompression wave speed. Two test cases (Case1 and Case4 in Table 4.1) have been considered. The phase envelopes and initial conditions are plotted in Figure 4.25. The test gas mixtures cover conventional gas to rich gas with two different pressure levels. The location of monitoring points is listed in Table 4.5. P# denotes the channel no. of pressure transducer and T# denotes the channel no. of temperature probe.

Wall heat transfer plays an important role in the blowdown of long pipelines. A conjugated problem is solved simultaneously for pipe flow and wall heat transfer, and more details are described in Chapter 2. The pipe flow is assumed to be one-dimensional, while a two-dimensional heat transfer problem is solved for the pipe wall. The wall temperature gradient in the radial direction is much larger and needs to be resolved.

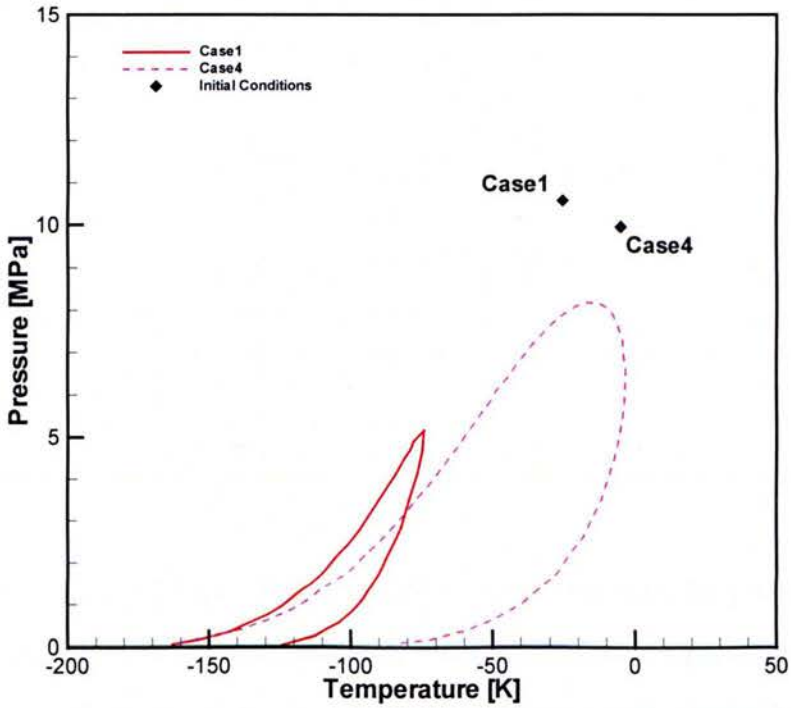

Figure 4.25 Phase envelopes and initial conditions for Case1 and Case4

The test tube is discretized by a non-uniform mesh in the axial direction with the grid size gradually increasing away from the rupture plane at a ratio of 5 between the maximum grid size at the closed end and the minimum grid size at the rupture plane. An initial grid sensitivity study demonstrated that 500 non-uniform cells in the axial direction and 10 uniform cells in the radial direction for the pipe wall are sufficient to obtain grid-independent results and to resolve the measurement points. The test tube is assumed to be well insulated, so an adiabatic condition is applied at the outer pipe wall for the wall heat transfer. The initial temperature of the pipe wall is assumed to be the same as that of the fluid. At the beginning of the simulation the pipe is assumed to be abruptly ruptured and an ambient pressure of 0.1MPa is directly applied to the rupture plane to artificially initiate the decompression process.

The minimum size of cell is 0.05m in the axial direction. A small timestep is needed for the fast decompression process likewise the British Gas Shock Tube cases. Here, the computational timestep is also varied during the simulation by

ensuring that the maximum CFL number is less than 0.2, and the maximum of the computational timestep is approximately $2.5*10^{-5}$.

Table 4.5 Location of monitoring points of test cases by Botros [62]

Point No.	P6	P7	P8, T8	P10	P11	P14,T14	P19,T19	P24,T24
Location [cm]	84	124	164	404	804	2305.6	4707.2	7108.8
Point No.	P31,T31	P36,T36	P41,T41					
Location [cm]	10315.7	12717.3	15118.9					

The comparisons of pressure-time traces for Case1 between the prediction and measurement are shown in Figure 4.26. The predictions of pressure-time and temperature-time traces by OLGA 2000 software [145] obtained from the literature [62] are also presented. It can be clearly found that the decompression rate is fast close to the rupture plane (P6 and P7) and the pressure drops abruptly before stabilizing at a relatively low value. The initial fast drop of pressure is captured quite well. The propagation speed of decompression wave is very accurately predicted by current model, while it is severely under-predicted by OLGA. For location away from the rupture plane, the decompression rate tends to be slower. For the location near the close end, i.e. P31, P36 and P41, the decompression rates are seen to be suddenly accelerated at 610ms, 550ms and 490ms, respectively. This is thought to be caused by the reflected leading decompression curve. The sudden acceleration of decompression rates are well predicted by current model, but OLGA failed to reproduce this phenomenon. For all the locations, the predictions of current model are in reasonably good agreement with the measurements although the discrepancies are relatively larger for the location closer to the rupture plane due to the HEM assumption. The maximum difference is less than 10%. The predictions of pressure-time traces show much better agreement than OLGA predictions.

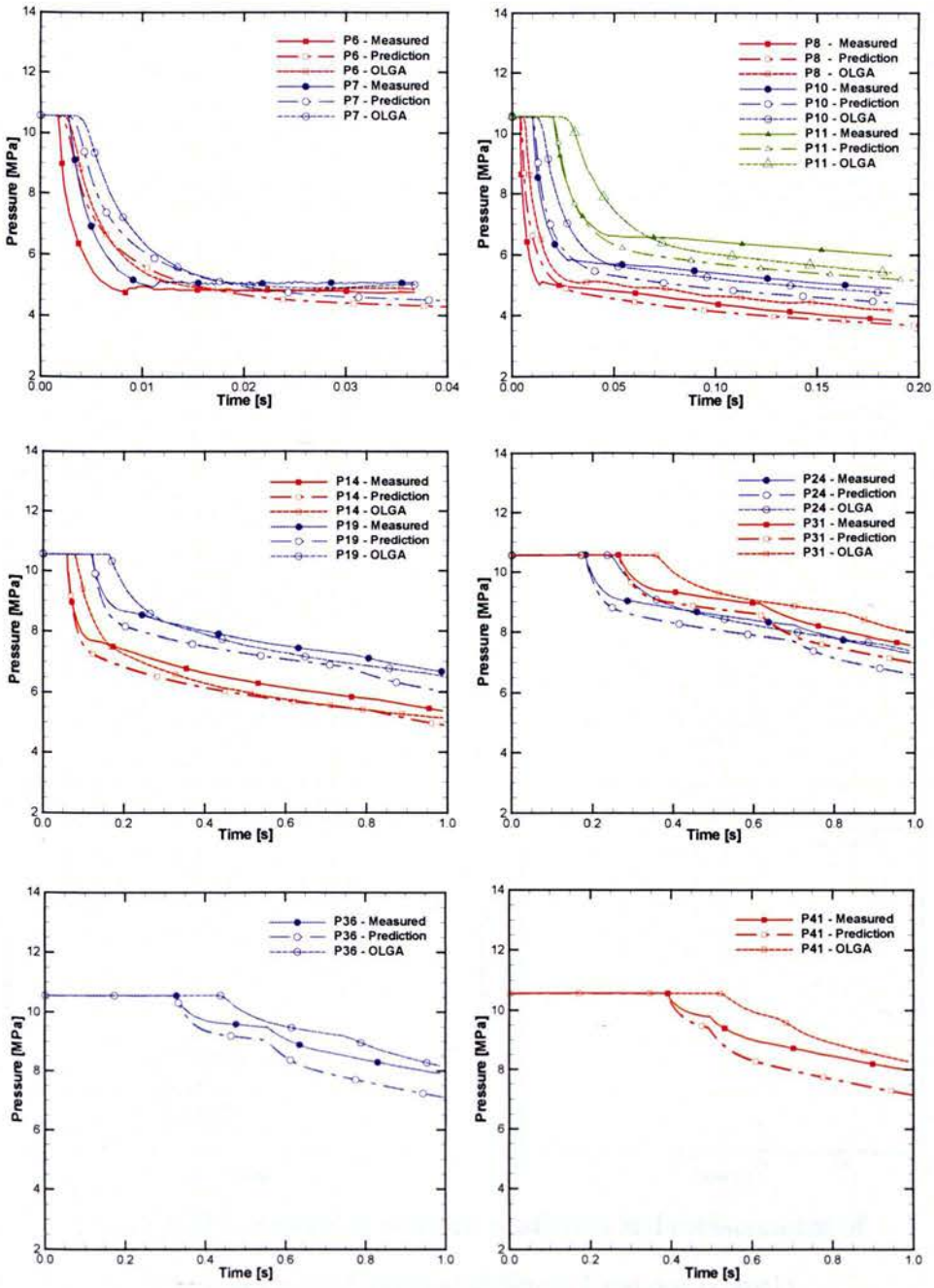

Figure 4.26 Comparison between prediction and measurement of pressure-time traces at different locations (Case1)

Figure 4.27 displays the plots of temperature-time traces at different locations for Case1. The changing trend of temperature is quite similar to that of pressure. It drops quickly to a very low value at locations close to the rupture plane due to the fast decompression rate. For all the locations, the predicted

temperature agrees well with the experiment data. The maximum difference of temperature is about 6°C. The results show that current model is able to predict well on the trend of temperature, while OLGA significantly over-predicts the temperature and exhibits a larger discrepancy with measurements than current model.

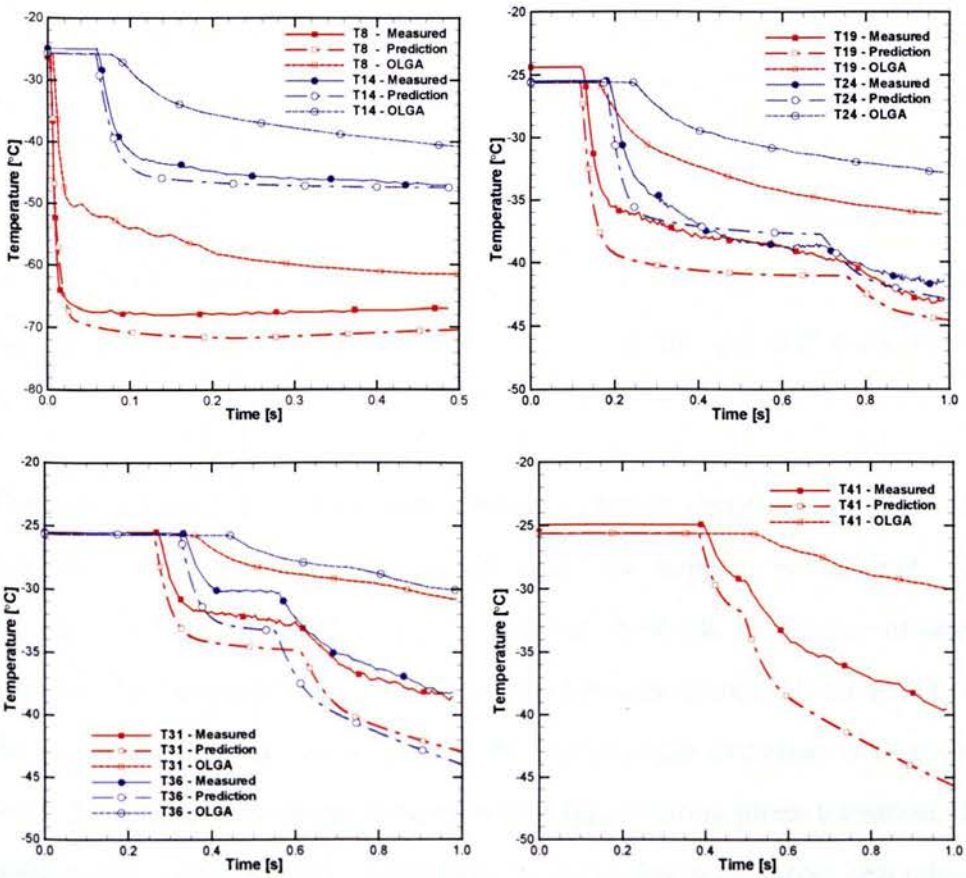

Figure 4.27 Comparison between prediction and measurement of temperature-time traces at different locations (Case1)

Figure 4.28 shows a comparison of pressure-time traces at different locations for Case4. In the absence of OLGA predictions for comparison, the predictions are only compared with the experimental data. As the initial decompression rate is extremely fast near the rupture plane, the pressure drops sharply at P8 and P10. The fast decompression is well captured by the numerical simulation. Away from the rupture plane, the decompression rate becomes milder at the

location from P11 to P36. Additionally, for the location of P31 and P36, an apparent increase in the decompression rate is also predicted at about 600ms due to the arrival of the reflected wave. Generally, it is seen that agreement is similar to Case1. However, there exists an apparent change of the slope in the pressure-time traces, which is almost like a plateau (roughly at P=8MPa) for each of the three monitoring locations close to the rupture plane (P8, P10 and P11). These sudden slope changes are believed to be caused by heating from the released latent heat during gas condensation. They represent sharp recovery in pressure and are well captured by current model. For a fixed location, phase transition, i.e. the plateau on the decompression curve, corresponds to one point on the pressure-time trace. However, condensation may continue after the phase transition, which releases latent heat to warm up the gas and increases its pressure.

The occurrence of the sudden slope changes is highly dependent on the initial conditions and gas compositions. It will not happen in all rich gas decompression processes. To trigger condensation shock, the release of latent heat must be sufficient to produce significant pressure changes. If the quality of the two-phase mixture resulting from the initial phase transition is relatively small, for example, more gas condenses into liquid during phase transition, the condensation shock would be more likely to occur due to the larger heat release. Comparing Case4 (Figure 4.28) with Case1 (Figure 4.26), it can be seen that the pressure plateau in the decompression curve of Case4 is much wider than that in Case1 due to the smaller speed of sound of the two-phase mixture resulting from the smaller quality.

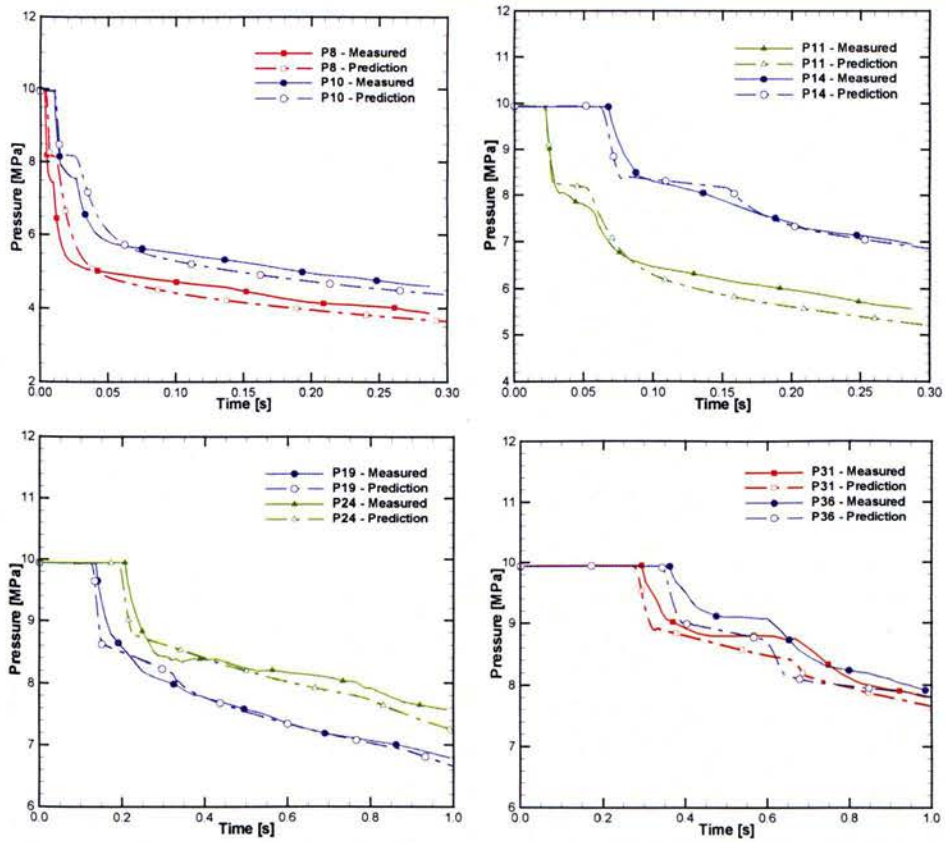

Figure 4.28 Comparison between prediction and measurement of pressure-time traces at different locations (Case4)

Comparison of the T-t traces at different locations for Case4 is shown in Figure 4.29. Similar to Case1, the predictions are also in reasonably good agreement with the experimental data. Abnormal increases in temperature, which are not explained in the experiment, are observed for the locations at T24, T31 and T36 during the decompression process. The highly non-homogenous and non-equilibrium local flow conditions are most likely responsible for these abnormal increases which are not captured by the model.

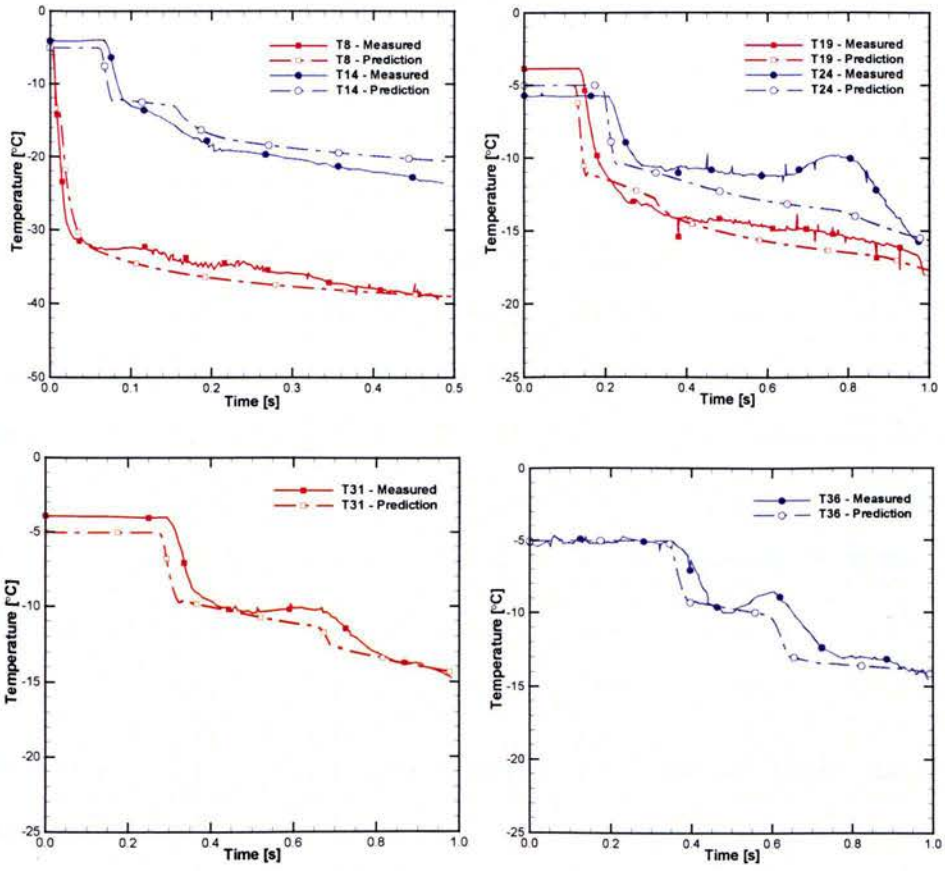

Figure 4.29 Comparison between prediction and measurement of temperature-time traces at different locations (Case4)

On the whole, the predictions of pressure-time and temperature-time traces, agree reasonably well with the measurements. Moreover, the predictions make better agreement than predictions of commercial software OLGA 2000. The acceleration of the decompression rate resulting from the reflected wave is accurately captured. The sudden slope changes at the pressure-time trace can be clearly predicted with current model, which would be more likely to occur due to the larger heat release during phase transition.

4.3.3. Isle of Grain Full-scale experiments [66], [67]

Isle of Grain full-scale experiments [66], [67] were reported to investigate the blowdown behaviour of LPG pipeline following full-bore rupture. The

experimental data were presented in the literature [67], [71]. The experiments have been widely used as benchmark data for the purpose of validation [25], [29], [35]. The experiments involved two carbon steel pipelines with different diameter. The large pipeline with an internal diameter of 15.4cm was used in Test P40 and P42. The small pipeline with an internal diameter of 5.2cm was used in Test P65. The wall thickness of the large and small pipelines is 0.73cm and 0.445cm, respectively. Both of them are 100m long and horizontal pipelines. Three tests are selected to validate the proposal model and the test conditions are listed in Table 4.6. The working fluid is LPG, which is made up of 95% propane and 5% butane in molar unit. The locations of monitoring points are given in Table 4.7.

Table 4.6 Initial conditions and composition of Isle of Grain full-scale experiments

Test Name		P40	P42	P65
Initial Pressure [MPa]		2.16	1.13	1.16
Initial Temperature [°C]		17.8	20	13.8
Composition [mol%]	C_3H_8		0.95	
	iC_4		0.05	

Table 4.7 Location of monitoring points of Isle of Grain full-scale experiments

Test Name	P40, P42		P65	
Distance from the rupture plane [cm]	Open End	Closed End	Open End	Closed End
	10	9850	30	9500

The predictions of current model are compared with the measurements. An initial grid sensitivity study demonstrated that 200 non-uniform cells in the axial direction and 10 uniform cells in the radial direction for the pipe wall are sufficient to obtain grid-independent results and to resolve the measurement points. The minimum size of cell is 0.07m in the axial direction. The

computational timestep is varied. CFL=2 is used to speed up the calculation. It is worth noting that simulations of CFL=0.5, the less CFL number were also tested, showing no obvious effects of the CFL number on the predictions. The maximum of the computational timestep is approximately $2.0*10^{-4}$. The boundary conditions of computations were set up in a similar way to the Botros's case.

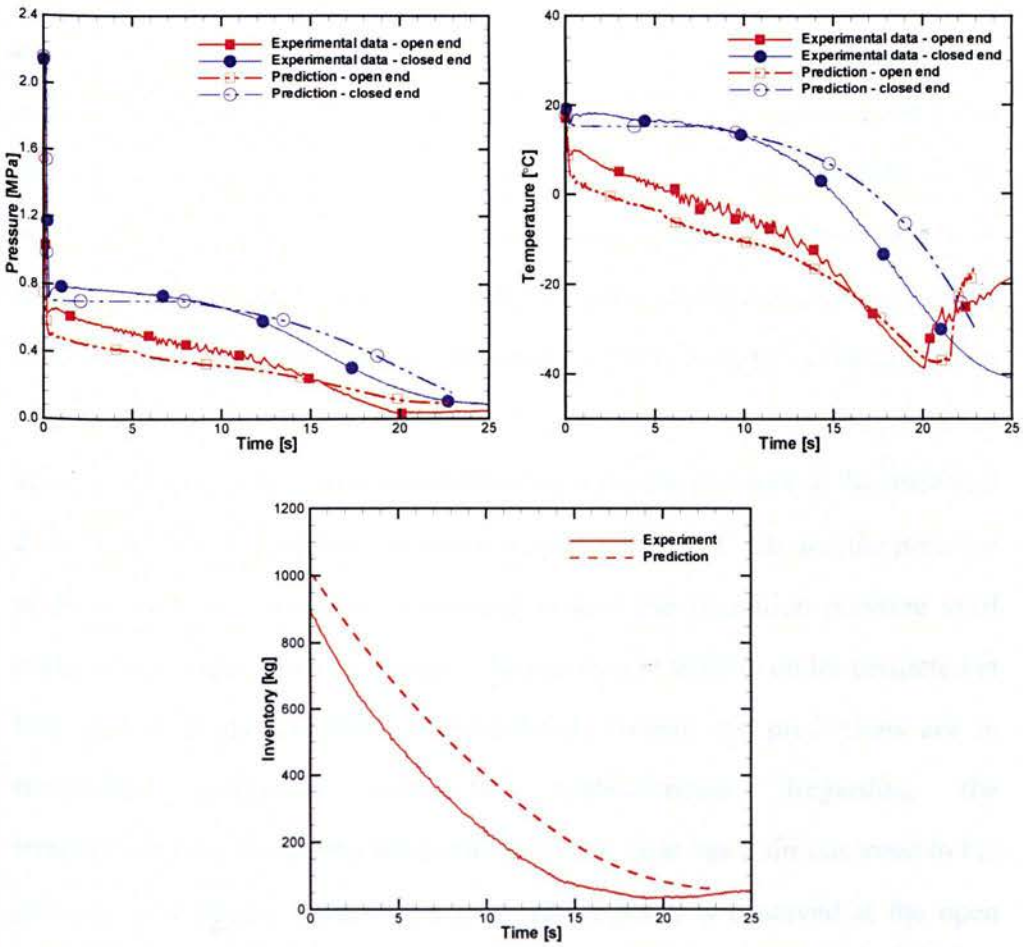

Figure 4.30 Comparison of the predicted and measured pressure (upper left), temperature (upper right)-time traces at the closed and open ends as well as the remaining inventory (lower) for Test P40.

Figure 4.30 displays the predictions and measurements of pressure, temperature at the open and closed ends for Test P40, as well as the total inventory remaining in the pipeline. The pressure-time traces clearly

demonstrate the decompression behaviour of Test P40. As the initial decompression wave travels at the local speed of sound through the dense LPG within the pipeline, the pressure of compressed dense LPG drop abruptly to the saturation pressure due to the small compressibility of LPG. Then the pressure tends to stay nearly constant until phase transition takes place. The prediction of pressure-time traces agrees reasonably well with the measurement. The maximum difference of pressure is roughly 0.26MPa. The extremely fast initial decompression process is nicely captured by current model. At the saturation pressure around 0.7MPa, the depressurized LPG starts to flash into a two-phase mixture. At the same time, the fluid in the pipeline is accelerated rapidly toward the rupture plane until the release flow is choked at the rupture plane. A slight pressure undershoot observed in the measured pressure-time traces at the open end is caused by non-equilibrium effects, which is not reproduced in current simulation due to the HEM assumption. After the initial decompression wave the pressure at the open end drops steadily to the ambient pressure at approximately t=20s and the pressure at the closed end stays almost constant around the saturation pressure until t=10s when phase transition occurs. The pressure is slightly under-predicted at both ends initially and then over-predicted. Overall the predictions are in reasonable agreement with the measurements. Regarding the temperature-time traces, the temperature at both ends has a similar trend to the pressure-time traces. Evidently, a temperature jump is observed at the open end when the pressure drops to atmospheric pressure. Current model can predict the temperature increase at 20s, which is caused by the wall heat transfer. Most previous studies [25], [29], [35], [67] failed to produce the temperature increase. Overall the predicted temperature shows a good agreement with the measurement. The maximum difference of temperature is about 2°C. Additionally, the remaining inventory via release time is plotted. The experimental data of the remaining inventory are obtained from the sum

of twenty values measured by load-cells .The location of load-cells on the pipeline can be available in the literature [67]. The prediction of the remaining inventory is obtained by subtracting the outflow mass at the rupture plane from the initial total fluid mass in the pipeline. The remaining inventory is over-estimated by 40%. The released efflux rate is correspondingly lower than the measurement. One of reasons is thought to be the employment of homogeneous equilibrium assumption. Nevertheless, the predicted trend of the remaining inventory is in good agreement with the experiment.

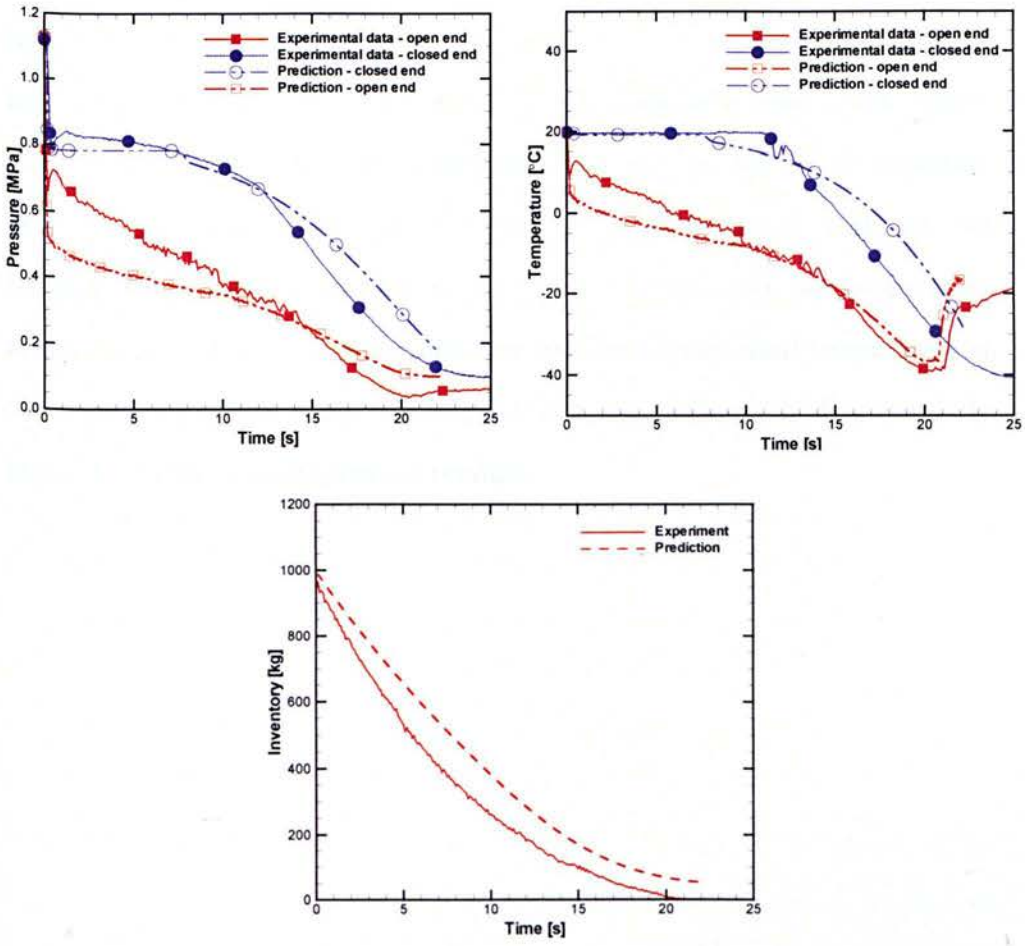

Figure 4.31 Comparison of the predicted and measured pressure- (upper left), temperature- (upper right) time traces at closed and open ends and remaining inventory (lower) for Test P42.

The variations of pressure, temperature and total fluid inventory with time for Test P42 are shown in Figure 4.31. The initial pressure of Test P42 is about half of the one in Test P40 and the initial temperature is closed to that of Test P40. Similar trends of pressure, temperature and remaining inventory are observed in Test P42. The predictions of pressure and temperature are slightly under-estimated by the maximums of 0.12MPa and 8°C, respectively. It is also owing to the HEM assumption.

The predicted pressure, temperature and remaining inventory for Test 65 are compared with the measurements in Figure 4.32. It is found that the measured temperature at closed end at the beginning of the release is nearly 10°C higher than the specified initial fluid temperature. This may be one of the important factors which lead to the big discrepancies of temperature at closed end between the predictions and the measurements. Additionally, the temperature at open end is about 7°C lower than the specified initial fluid temperature at the beginning of the release. It implies that the working fluid is not fully mixed to achieve a homogeneous mixture.

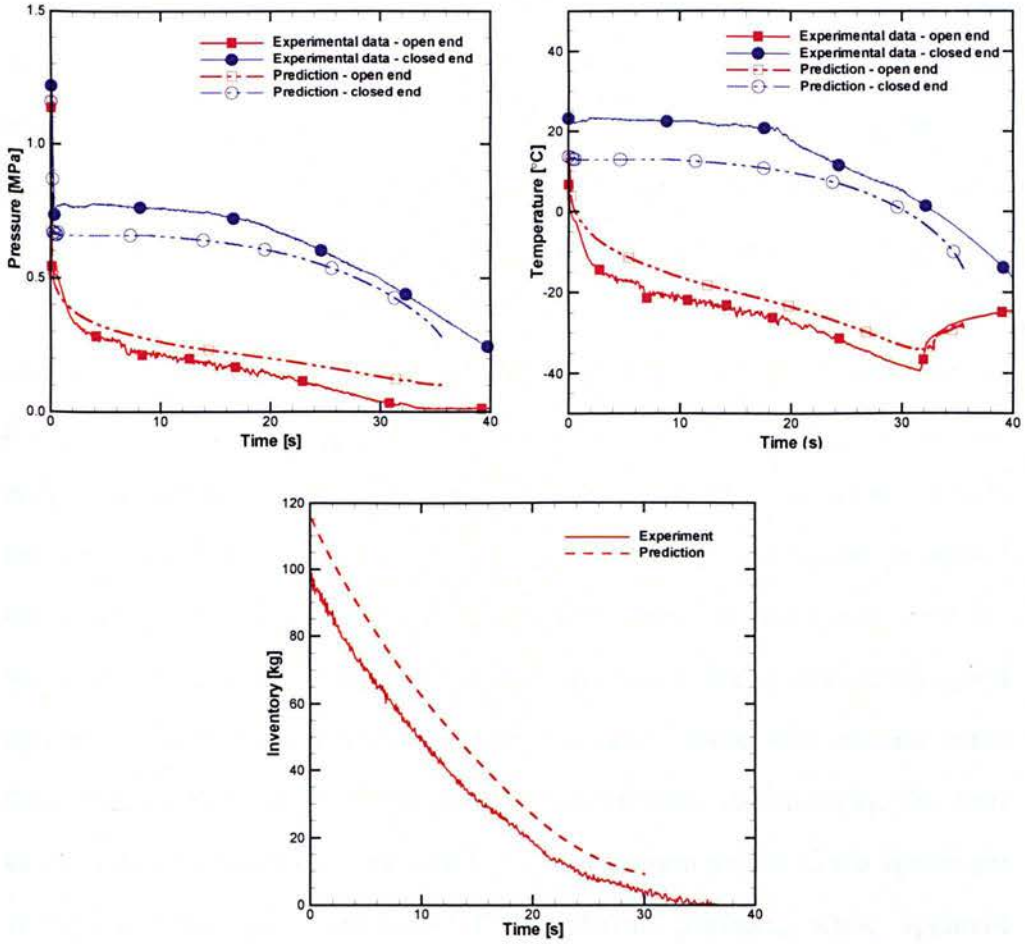

Figure 4.32 Comparison of the predicted and measured pressure- (upper left), temperature- (upper right) time traces at closed and open ends and remaining inventory (lower) for Test P65.

4.4. Concluding Remarks

Current model with HEM assumption was extensively validated against experimental data. The experiments cover a wide range which is from the conventional gas, rich gas to LPG, as well as dense phase CO_2. The validation cases involve fast decompression as well as slow blowdown. The predictions of decompression wave curve and pressure-time and temperature-time traces were compared with the measurements.

Regarding the decompression wave curve, it is one of the key factors to determine the toughness required to arrest a running ductile fracture in a pipeline, particularly for rich gas and CO_2 due to the existence of the plateau. The predictions were compared with the experimental data. Also, comparisons were made between the predictions of the current model with that of other models, such as DECAY, Exxon and GASDECOM. Overall, the predictions of the current model are similar to other models. The similarity of the predictions is partly due to the fact that the homogeneous equilibrium assumption was adopted in all the models. It is thought that the homogeneous equilibrium assumption and the employment of EOS are two significant factors to impact the accuracy of model for predicting the decompression wave curve. On the whole the predictions of decompression wave curve are in reasonably good agreement with the experimental data. However, there still existed some discrepancies between predictions and measurement. Additionally, the four cases of dense phase CO_2 were used to validate current model. Good agreement is achieved for the predictions of the plateau pressure, while apparent discrepancies in the speed of sound under the initial states are observed due to the small compressibility of CO_2 in the dense phase. Different equations of state, i.e. PR, SW and BWRS EOSs are found to result in slightly different predictions for the local speed of sound.

Comparison was also made between the predicted pressure-time and temperature–time traces at different locations and the measurements. British Gas shock tube experiments [59], Botros's cases [62] and Isle of Grain full-scale experiments [66], [67] were predicted to evaluate the credibility of current model. With respect to British Gas shock tube tests, the prediction of pressure-time traces are in reasonably good agreement with the experiment data, and show better agreement than DECAY. For Botros's cases, the predictions of current model are in reasonably good agreement with the measurements

although the discrepancies are relatively larger for the location closer to the rupture plane due to the HEM assumption. The predictions of pressure-time traces show much better agreement than OLGA predictions. The propagations of both the decompression wave and the reflected wave are accurately captured. Furthermore, Isle of Grain full-scale experiments, which are widely used as benchmark data for the purpose of validation, was carefully calculated to validate the current model. There is good agreement between the prediction and measurement of the pressure-time and temperature-time traces. Besides, the predicted trend of the remaining inventory is in good agreement with the experiment.

In summary, the results show that there is in reasonably good agreement between the predictions and experimental data. The model is successfully validated against the experiments covering the fast decompression and slow blowdown.

Chapter 5 Gaseous CO_2 Shock Tube Decompression

5.1. Introduction

Pipeline is considered as the most economical and feasible way [146] to long-distance transport the large quantities of CO_2 captured with CCS technology. CO_2 may be compressed and transported via pipeline under high pressure in gaseous state when the demand is low, or when re-using the existing natural gas pipelines [147]. The decompression behaviour of CO_2 pipeline is great significant to evaluate the feasibility of re-using the existing natural gas pipelines.

Shock tube tests are usually carried out to investigate the decompression behaviours. However, the CO_2 shock tube tests are rarely available in the literature. Battelle Memorial Institute carries out several shock tube test with CO_2 [143], [144]. The decompression wave curve has been validated against the experimental data of CO_2 shock tube test in Chapter 4. Cosham et al. [147], reported some experimental data of gaseous phase CO_2 shock tube tests. The shock tube tests were conducted to address and investigate the key issues related to the design, construction and operation of pipeline [149].

This chapter will carry out the prediction of gaseous phase CO_2 shock tube test using the proposed model with homogeneous equilibrium assumption. Comparison is made between prediction and measurement. The decompression flow of gaseous phase CO_2 shock tube test is analysed in more detail, and the effects of wall friction and heat transfer on decompression behaviours are fully evaluated, and the effects of different EOSs and impurities on the decompression behaviour are also examined.

5.2. CO_2 Shock Tube Tests

An industrial research project [149], [150] was conducted to address and investigate the key issues related to the design, construction and operation of pipelines to transport high pressure CO_2. A programme of shock tube tests is used to investigate the decompression behaviour of dense phase CO_2 and CO_2 with impurities. The CO_2 with impurities is also referred as CO_2-rich mixture. The programme involves CO_2 in the gaseous and dense phase. The gaseous phase shock tube tests were reported in the literatures [147], [151], and Cosham et al. [148] also published part of experimental data of dense phase shock tube tests.

The shock tube test rig consists of a 144m long, 146.36mm nominal internal diameter and 10.97mm wall thickness pipe and a smaller diameter circulating loop attached to either end of the pipe, see Figure 5.1. The average internal surface roughness of the pipe (Ra) is 0.005mm. A rupture disc is installed at the end of the pipe. The rupture disc will be explosively cut to initiate the shock tube test. It is worth noting that the method of initiating a test is different from the other test rigs (i.e. Jones & Gough [59] and Botros et al.[62], [133], [138]), and the latter uses a bursting disc. Furthermore, the test rig is insulated with a 25mm thick layer of closed-cell rubber foam insulation. The fast-response pressure and temperature transducers are mounted at different locations along the pipe section to measure the flow parameters and the decompression wave propagation following the tube rupture. The spacing between the transducers increases with the increasing distance between the transducer and the open end of the shock tube. The detailed locations of the transducers are tabulated in Table 5.1.

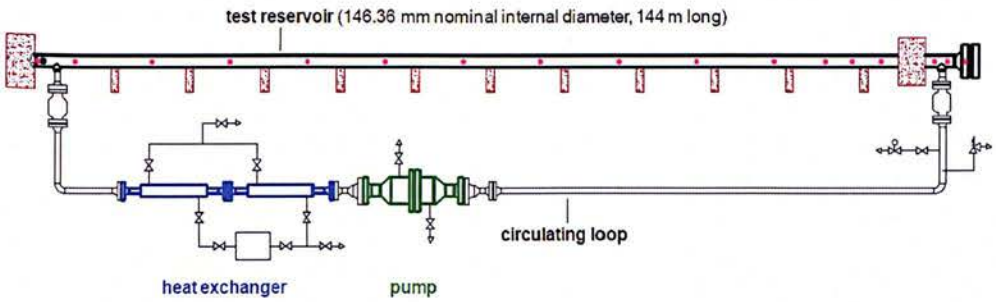

Figure 5.1 CO_2 shock tube test rig [148]

Table 5.1 Locations of the pressure and temperature transducers for CO_2 shock tube tests [148]

pressure transducers	temperature transducers	distance from open end, [m]	pressure transducers	temperature transducers	distance from open end, [m]
P01, P02		0.0864	P23	T04	18.04
P03, P04	T01	0.34	P24		22.54
P05, P06		0.54	P25	T05	30.04
P07, P08		0.74	P26	T06	42.04
P09, P10		0.94	P27	T07	54.04
P11, P12		1.24	P28	T08	66.04
P13, P14	T02	1.84	P29	T09	77.94
P15, P16		2.44	P30	T10	89.94
P17, P18		3.64	P31	T11	101.94
P19		4.84	P32	T12	113.94
P20	T03	6.04	P33	T13, FT07	125.94
P21		9.04	P34	T14, FT01	137.94
P22		13.54	P35		143.775

Notes:

1. 'P' indicates a fast-response pressure transducer.
2. 'T' indicates a temperature transducer installed on the external surface of the shock tube. These transducers measure the temperature of pipe wall.
3. 'FT' indicates a temperature transducer installed on a probe in the centre of the shock tube. These transducers measure the fluid temperature.

The shock tube tests involve 14 cases with pure CO_2 and CO_2 mixtures in the gaseous phase and 14 cases with pure CO_2 and CO_2 mixtures in the dense phase. The initial state and compositions of all the cases are listed in Table 5.2. The initial pressure is within the range between 3.8MPa and 15MPa, and pressure is measured by the static pressure transducer. The initial temperature is in the

range between 0°C and 35°C, and the initial temperature is obtained by averaging the wall temperature measured by all of the external thermocouples. Some impurities such as H_2, N_2, SO_2, O_2 and CH_4 are involved to assess the effects on the decompression behaviour.

Table 5.2 Initial condition and compositions of CO_2 shock tube tests [148]

Test No.	composition, mol.%						Pressure [MPa]	Temperature [°C]	Phase
	CO_2	H_2	N_2	SO_2	O_2	CH_4			
02	100						3.90	4.9	
03	100						3.91	5.1	
04	100						3.90	20.2	
05	96.99	3.01					3.90	5.1	
06	95.97		4.03				3.89	5.3	
07	99.14			0.86			3.90	9.9	
08	95.70	3.30		1.00			3.90	10.0	Gaseous
09	94.81		4.15	1.04			3.90	10.0	
10	88.89		7.92	1.07	1.11	1.01	3.90	5.1	
11	89.23	3.24	3.84	1.24	1.32	1.13	3.90	5.0	
12	100						3.68	16.3	
13	100						3.68	10.9	
14	100						3.68	10.9	
16	100						3.88	5.0	
18	100						15.39	14.0	
19	100						15.34	5.0	
20	100						3.89	0.1	
21	100						4.63	5.0	
22	100						10.15	20.0	
23	100						15.04	35.6	
24	100						6.14	20.0	Liquid/
25	100						10.19	20.0	Dense
26	95.96		4.04				14.14	19.7	
27	97.38	2.62					14.20	19.9	
28	91.71	4.00	4.29				14.16	19.8	
29	96.19	0.90	1.03		0.97	0.91	14.12	20.0	
30	93.03	0.95	2.02		1.87	2.13	14.12	19.9	
31	91.03	1.15	4.00		1.87	1.95	15.05	10.0	

Notes:

A bursting disc is used in Tests 12, 13, 15 and18, and a rupture disc is used in the other tests.

Predictions are carried out for the decompression flow of gaseous and dense phase CO_2 via the shock tube. The predictions of flow parameters and decompression curve are compared with the experimental data.

In order to facilitate to describe, the results of gaseous and dense CO_2 shock tube tests are separately presented in this chapter and next chapter, respectively.

5.2.1. Introduction of Gaseous CO_2 Shock Tube Tests

The gaseous CO_2 is transported in relatively low capacity due to large volume. This leads to low efficiency transportation. However, the gaseous CO_2 shock tube tests were investigated because it is practical way to transport in gaseous CO_2 when the demand is low, or when re-using the existing natural gas pipelines [147]. All the gaseous tests were carried out at the same level of pressure of 3.9MPa, and within the temperature range between 5°C and 20°C, as shown in Table 5.2.

Tests 02-04, 12-14 and 16 were for pure CO_2. Tests 02, 03 and 16 were carried out under almost the same initial conditions. The initial temperature of Test 04 was higher than that of Test 03 and 04. Tests 13 and 14 were conducted under the same initial conditions using the bursting disc and rupture disc respectively. Tests 12 and 13 were carried out at the same pressure but at the different temperatures of 16.3°C and 10.9°C, respectively.

Tests 05-11 were for CO_2-rich mixture. Tests 05 and 06 were conducted nearly under the same initial conditions with binary mixtures. Test 07 was also binary mixtures at the 3.9MPa and 9.9°C. Tests 08 and 09 were ternary mixtures at the same initial conditions. Tests 10 and 11 were higher order mixtures.

Cosham et al. [147] presented some experimental data for gaseous CO_2 shock tube tests, such as decompression wave curves and pressure-time traces. It is

noted that the detailed pressure-time traces are available only for Test 03. Prediction of Test 03 is compared with the experimental data. Additionally, the other gaseous tests are also predicted and discussed.

The numerical setup is similar to that described in Section 4.3.2. The shock tube is discretized by a non-uniform mesh in the axial direction. The size of mesh gradually increases with increasing distance from the open end of the shock tube. The ratio of size is 5 between the largest mesh and smallest mesh. The pipe wall is divided into a uniform mesh in the radial direction. Grid sensitivity is performed using different numbers of meshes, and 1000 cells in the axial direction for the pipe and 10 uniform cells in the radial direction for the pipe wall are selected for all the simulations of CO_2 shock tube tests. The minimum size of cell is 0.035m in the axial direction. The computational timestep is varied and the maximum of the computational timestep is approximately $1.1*10^{-4}$. The maximum CFL number 2 is specified to speed up the simulation.

The heat transfer coefficient of internal pipe wall is calculated using Shah's correlation [114]. The initial wall temperature is set equal to the fluid temperature. The ambient pressure of 0.1MPa is applied to the rupture plane to initiate the decompression process.

5.2.2. Results of Gaseous CO_2 Shock Tube Test

5.2.2.1. Test 03 (Pure Gaseous CO_2 Shock Tube Test)

The distributions of pressure, temperature, void fraction, escaping velocity and speed of sound along the shock tube at different release moments are shown in Figure 5.2. The leading decompression wave reaches the closed end at approximately t=0.66s. Behind the decompression wave, pressure and temperature fall significantly accompanied by fast flow acceleration. The

initial decompression also causes a phase transition from gas to liquid droplets. At the inception location of phase change, the speed of sound is discontinuous. As the difference in the speed of sound between gaseous phase and two-phase mixture is relatively small, the propagation speed of the inception of phase transition is close to the leading decompression speed. Therefore a large pressure gradient forms almost along the whole section of the shock tube at t=0.66s. As the decompression wave is reflected and propagates towards the open end, the pressure gradient quickly decreases. Large pressure gradient is observed due to flow acceleration only close to the open end after the reflected wave moves out of the shock tube. From then on, the pressure continues to fall gradually across the whole length of the tube. Due to the large difference in temperature between the tube wall and the escaping gas close to the open end, the effect of wall heat transfer is pronounced. After t=1.24s, void fraction is found to increase gradually and a second phase transition from liquid droplets back to gaseous phase is observed close to the open end after roughly t=3.62 s.

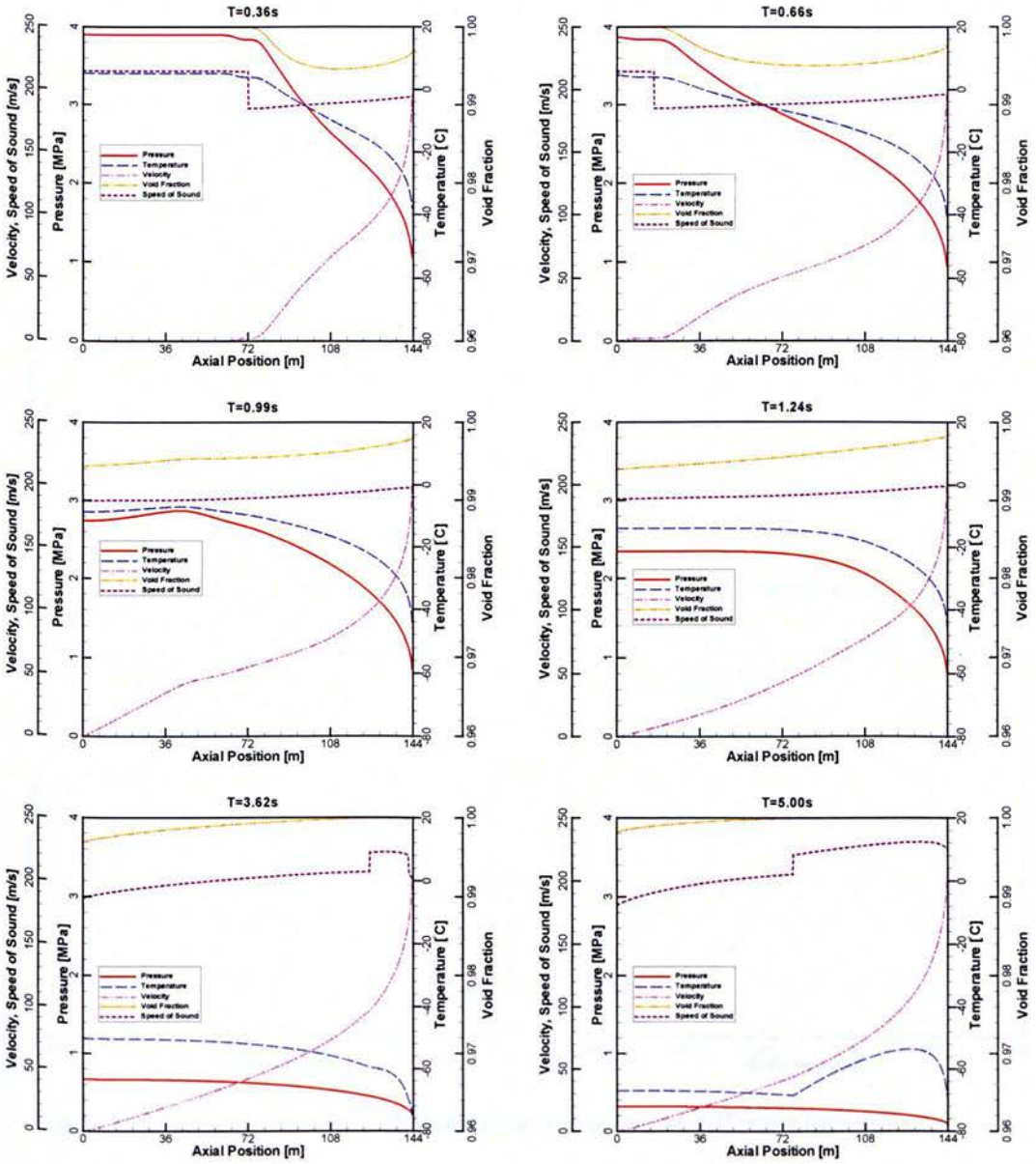

Figure 5.2 Distributions of pressure, temperature, void fraction, escaping velocity and speed of sound along the shock tube at different release moments for Test 03.

Figure 5.3 shows the decompression path and phase envelope at the different monitoring locations for Test 03. It can be seen that the initial gaseous phase CO_2 is close to the right-hand side of the dome-shaped phase boundary. Enthalpy decreases initially due to the fast flow acceleration. At the later stage of the decompression process, it starts to increase due to heating from the wall.

Accordingly, the predicted decompression paths move towards the right-hand side of the dew line due to a second phase transition.

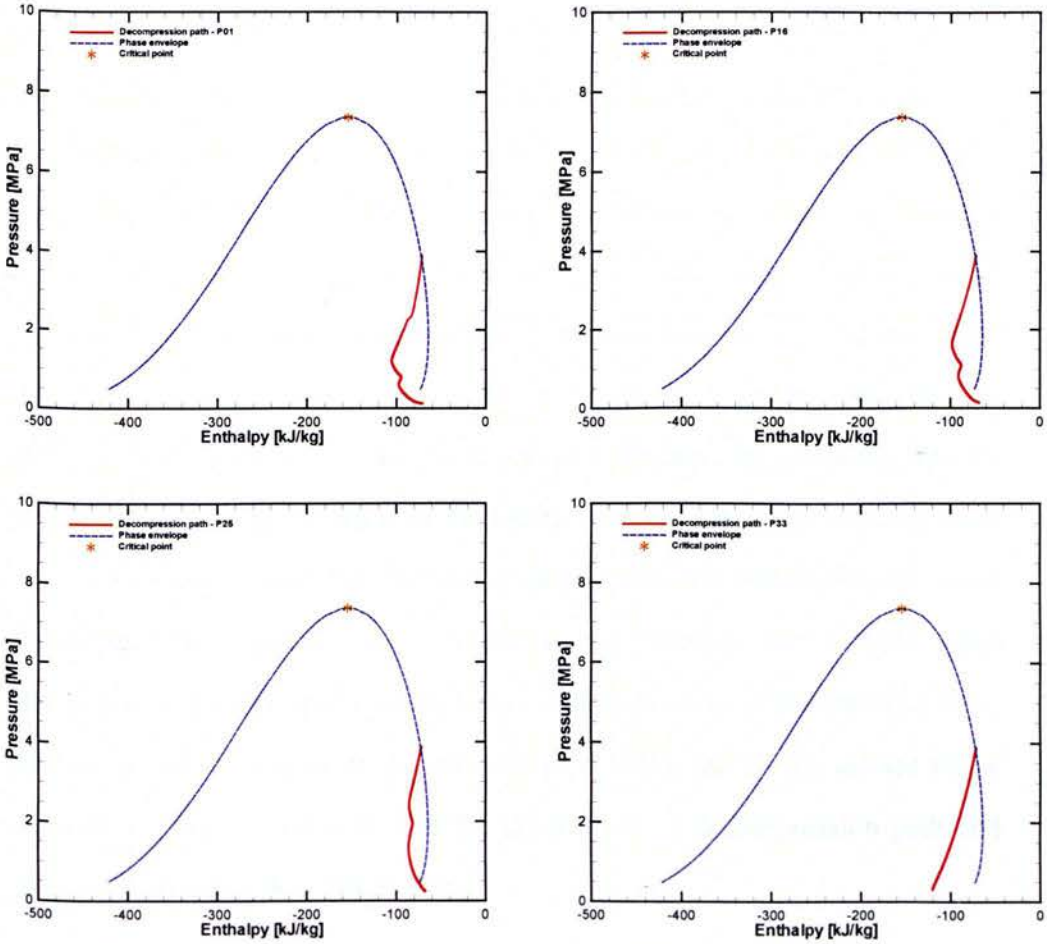

Figure 5.3 Decompression path and phase envelope at different locations for Test 03

Figure 5.4 presents the decompression wave curves individually calculated for different monitoring locations for Test 03. The decompression wave speed is theoretically calculated by Eq. (4.1), namely it is calculated as the predicted speed of sound minus the escaping velocity. The discontinuity in the speed of sound across the phase boundary and the continuity in the escaping velocity result in a discontinuity in the decompression wave speed exhibiting as a "plateau" on the decompression curve. The width of the pressure mainly depends on the difference in speed of sound between the initial single phase

and two-phase mixture after phase transition. The results exhibit the same plateaus of the decompression wave curves at the different monitoring locations. Decompression wave speed gradually decreases as pressure decreases. The turn points (marked in Figure 5.4) are found at the decompression wave curves. The decompression curves are suddenly changed at the turn points. The reason for this is the arrival of wave reflected by the close end. Totally, the predicted decompression wave curves at different monitoring points are almost similar when the pressure is above the turn point. However, there are large differences when the pressure is below the turn point. The large differences are caused by the different escaping velocities at different locations under certain local pressure. Because the escaping velocity at the same pressure decrease as the location moves far away from the open end. For example, with the decreasing of pressure, the decompression wave curve at P16 abruptly turns around at the pressure of 1.7MPa, then decompression curve speed nearly keep constant because of the chocked flow, finally suddenly increase at the pressure of 0.4MPa due to the second phase transition. This is consistent with the description of decompression path and the distributions of flow parameters.

The decompression wave curve above turn point is generally required by the design of pipeline. Therefore, for the shock tube test, the more monitoring points are particularly established near the open end.

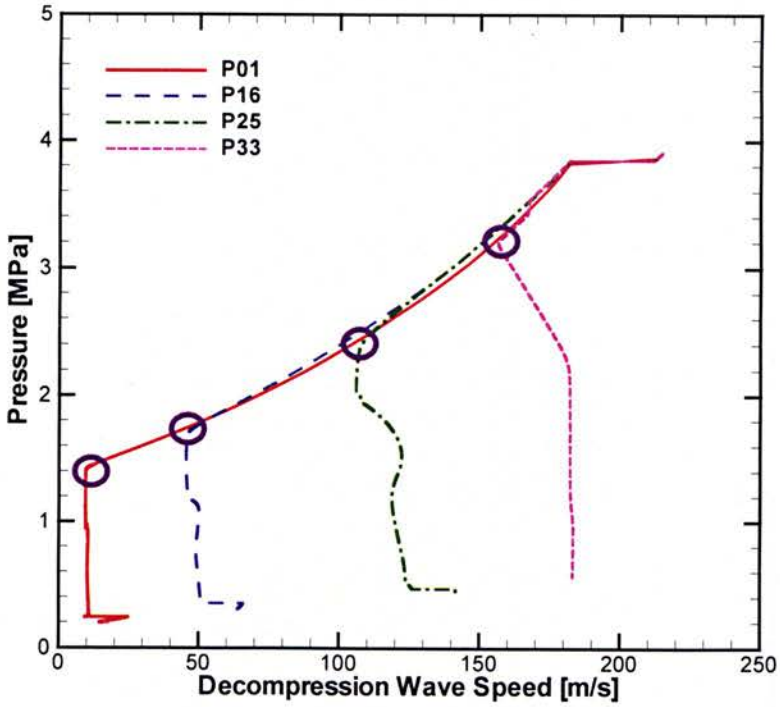

Figure 5.4 Decompression wave curves at four different locations for Test 03.

A comparison between predictions and measurement of decompression wave curve is presented for Test 03 in Figure 5.5. The predictions of decompression wave curve are calculated at the location close to the open end. Three different EOSs such as PR, PRSV and SW EOSs are employed and the SW EOS is used as the reference equation. The predictions of decompression wave curve with these three EOSs are similar. The predicted pressure plateau using PRSV EOS is slightly close to SW EOS, because the saturation pressure using the PRSV EOS is more accurate than PR EOS. The speed of sound corresponding to the initial state is about 217.4m/s. The predicted plateaus occur at roughly 3.83MPa, while it is 0.68MPa higher than the measured value of 3.05MPa. It is caused by the non-equilibrium phenomena which cannot be captured by the HEM assumption. When the decompression path enters the phase envelop, the decompression process is affected by non-equilibrium effects such as super-saturation or delayed nucleation similar to the decompression of rich gas cases. The pressure rapidly drops below the saturation pressure without phase

change. At this time, the gas phase may temporarily become supersaturated. Then the phase change will happen at a lower pressure rather than at the saturation pressure.

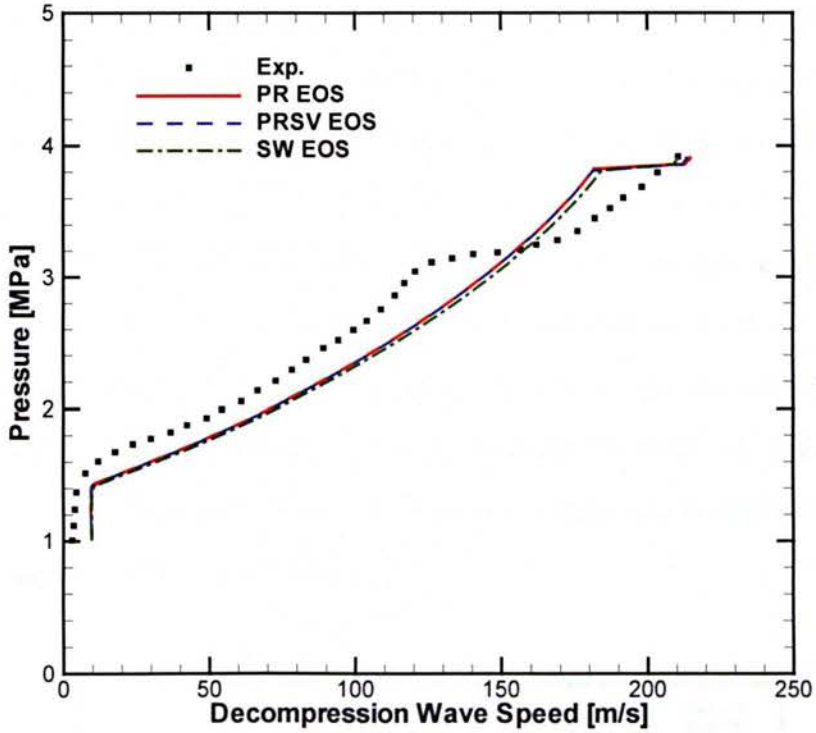

Figure 5.5 Comparison of the predicted and measured decompression wave curves for Test 03.

Figure 5.6 shows a comparison of the predicted pressure-time traces of first 1000ms at different monitoring points with the measurements. Only the results calculated with the PR EOS are presented. When the test initiates at time=0ms, the decompression wave rapidly spreads at a local speed of sound from the open end to the close end of the shock tube. After the decompression wave passes through the local point, the pressure sharply decreases and the pressure gradient drive CO_2 to accelerate and escape from the shock tube. Then the decompression rate decreases gradually. The predicted pressure-time trace at P19 close to the open end is in good agreement with the experimental data. For the monitoring locations further away from the open end, the discrepancy

increases gradually. The predicted and measured pressure starts to decrease at the same moment of decompression, and the predicted pressure first decreases to a value and then remains constant for a while and continues to decrease to the ambient pressure. The observed plateaus are apparently lower than the predicted plateaus. These discrepancies are caused by the non-equilibrium effect during the fast decompression process. When the decompression path intersects the phase envelope, i.e. decompression process shown in Figure 5.3, liquid-drop should occur in principle. However, there is no enough time to generate the liquid phase at the phase boundary, and the pressure continues to drop and the gas becomes superheated. Then the liquid phase occurs at a lower pressure rather than the saturation pressure predicted under the homogeneous equilibrium condition. Additionally, the transient increase of pressure is observed due to the explosive charge when the rupture disc is explosively cut. This is neglected in the simulation run.

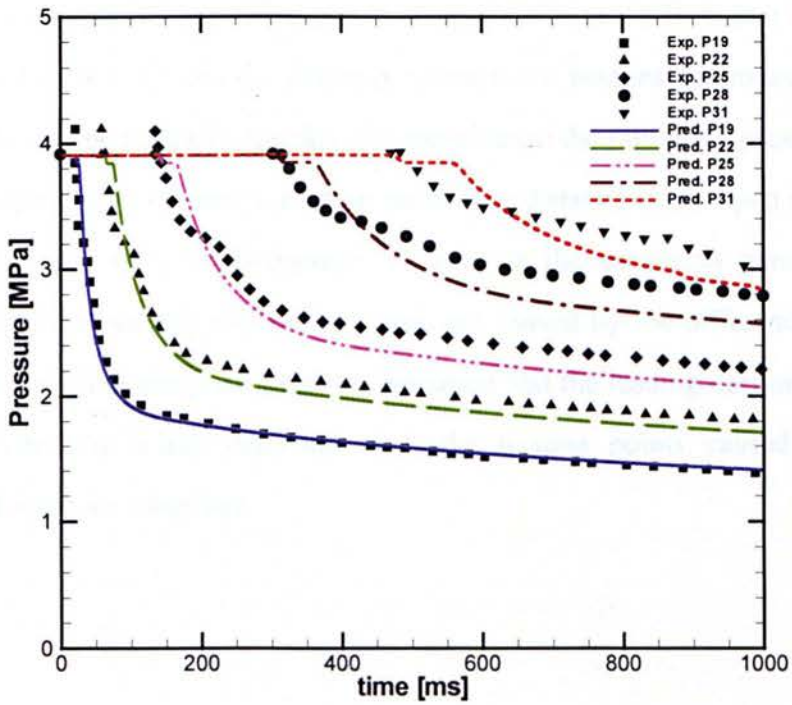

Figure 5.6 Comparison of the predicted and measured pressure-time traces at selected monitoring points for Test 03.

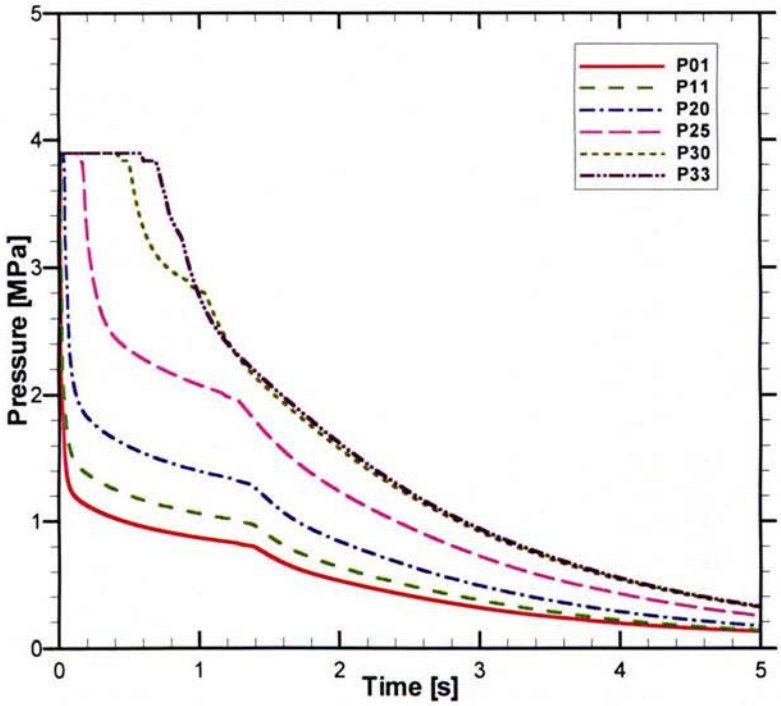

Figure 5.7 Pressure-time traces for the first 5s at the selected monitoring points for Test 03.

Figure 5.7 displays the predicted pressure-time traces for the first 5s at different locations for Test 03. As the decompression wave reaches the measurement points, the compressed CO_2 quickly depressurizes to the saturation pressure and its decompression rate decreases with increasing distance to the open end. For points P30 and P33, small pressure plateaus at the saturation pressure are observed. As previously mentioned, these are caused by the difference in the travel speed of the inception of phase transition and the leading decompression speed. After the initial decompression, the turning points caused by the reflected wave are observed.

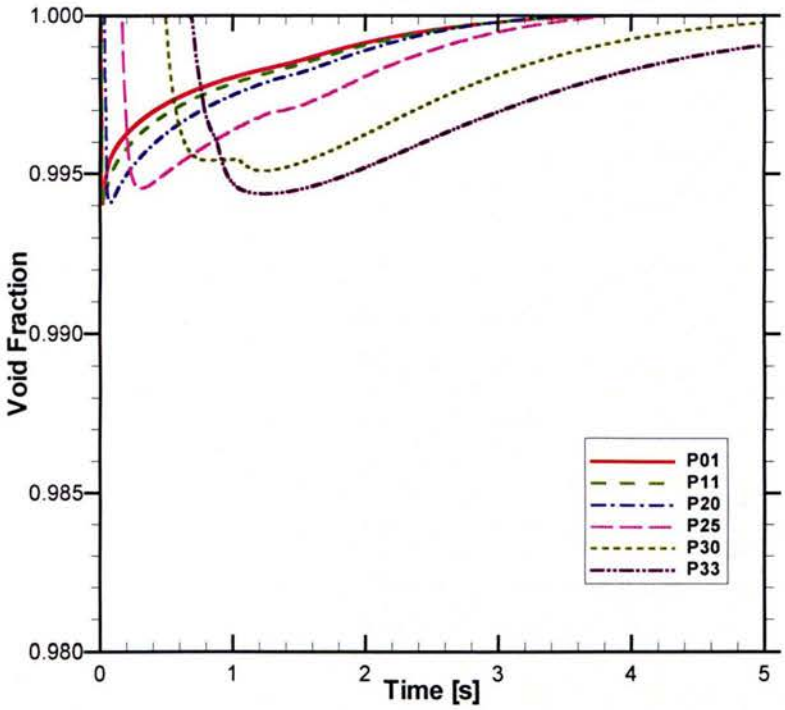

Figure 5.8 Void Fraction-time traces for the first 5s at the selected monitoring points for Test 03.

The predicted void fraction-time traces at different locations are shown in Figure 5.8. It was found that the volume fraction of liquid droplet increase when the decompression wave reaches the monitoring location. Before the location of P20, the volume fraction of liquid droplet abruptly increases, and then suddenly turns around due to the heating of fluid from pipeline wall at the close end. Beyond the P20, the volume fraction of liquid droplet abruptly increases and then mildly increases.

The predicted temperature-time traces at different locations are shown in Figure 5.9. The changing trend closely follows that of pressure. Around t=4s, the increases in the temperature are observed for the locations prior to T06 due to wall heat transfer. However, the measured temperature-time traces are not available for comparison.

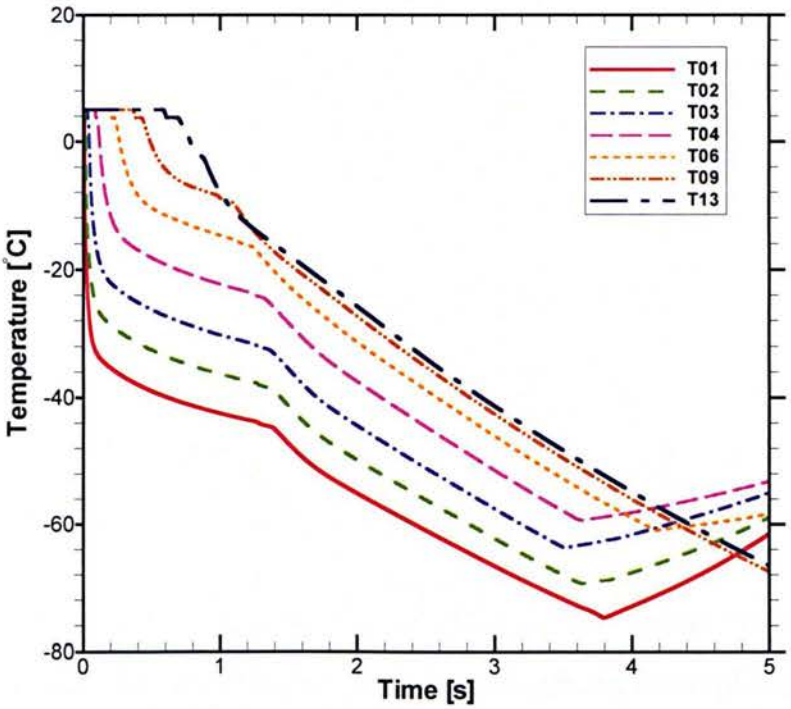

Figure 5.9 Temperature-time traces at different locations for Test 03.

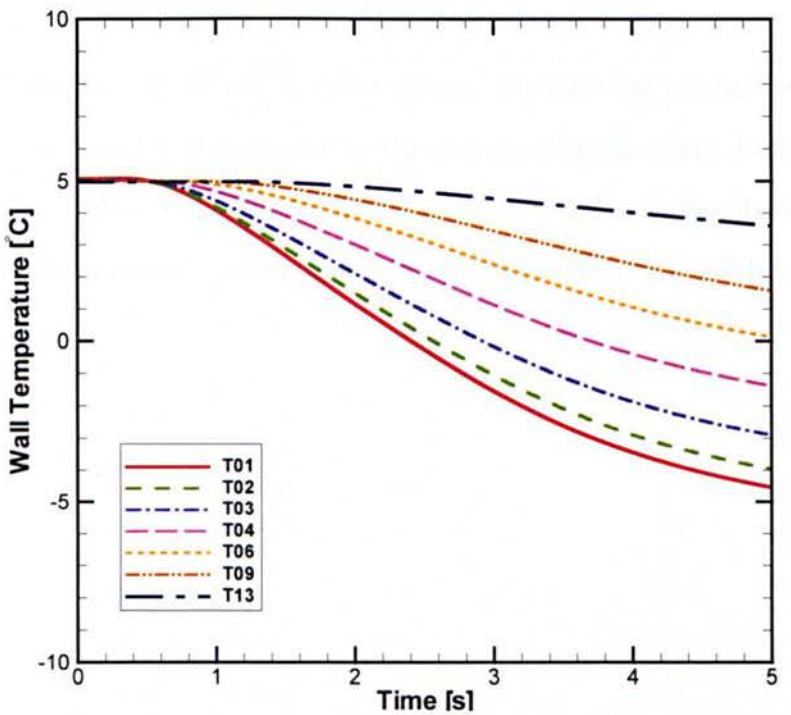

Figure 5.10 Outer wall temperature-time traces at different locations for Test 03

The predicted outer wall temperature-time traces at different locations are shown in Figure 5.10. It can be seen that the outer wall temperature significantly lags behind the fluid temperature and drops quickly close to the rupture plane.

5.2.2.2. Other Pure Gaseous CO_2 Shock Tube Tests

The other pure gaseous CO_2 shock tube tests, Test 04, Tests 12-14 and Test 16, are predicted. The predictions are compared with the available measurements. The prediction of Test 03 is involved as a reference case.

Figure 5.11 shows a comparison of decompression wave curves between Tests 03 and 04. The latter initial temperature is higher. The predicted plateau of Test 04 is lower than that of Test 03, and this is consistent with the measurements, because the decompression path of Test 04 intersects the phase envelope at lower pressure, see Figure 5.12. The measured plateau is lower than the predicted plateau. There exists a discrepancy between the prediction and the measured for Test 04. It is caused by the non-equilibrium effect. However, the discrepancy for Test 04 is smaller than Test 03. It is believed that the closer the initial condition is to the phase envelope, the larger the non-equilibrium effect is.

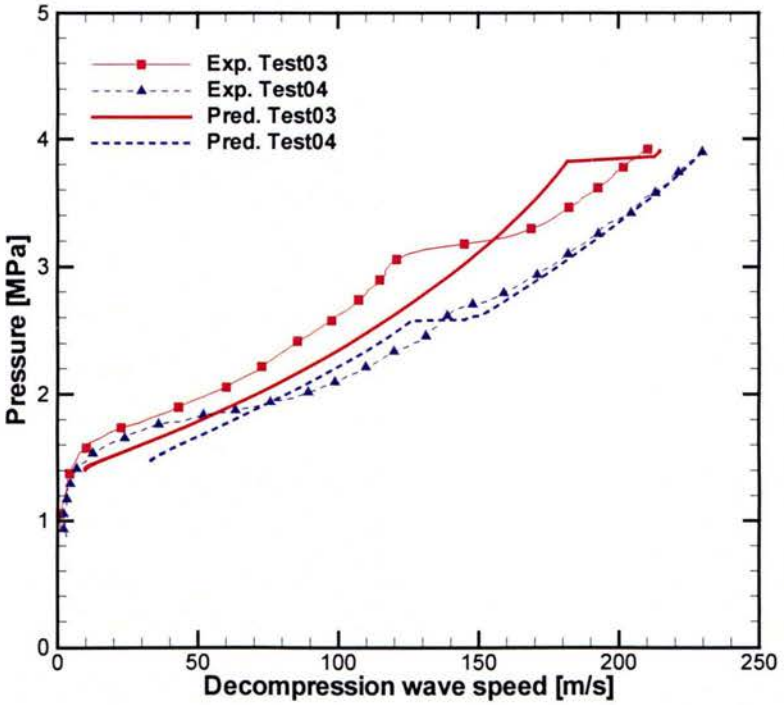

Figure 5.11 The predicted and measured decompression wave curves of Tests 03 and 04

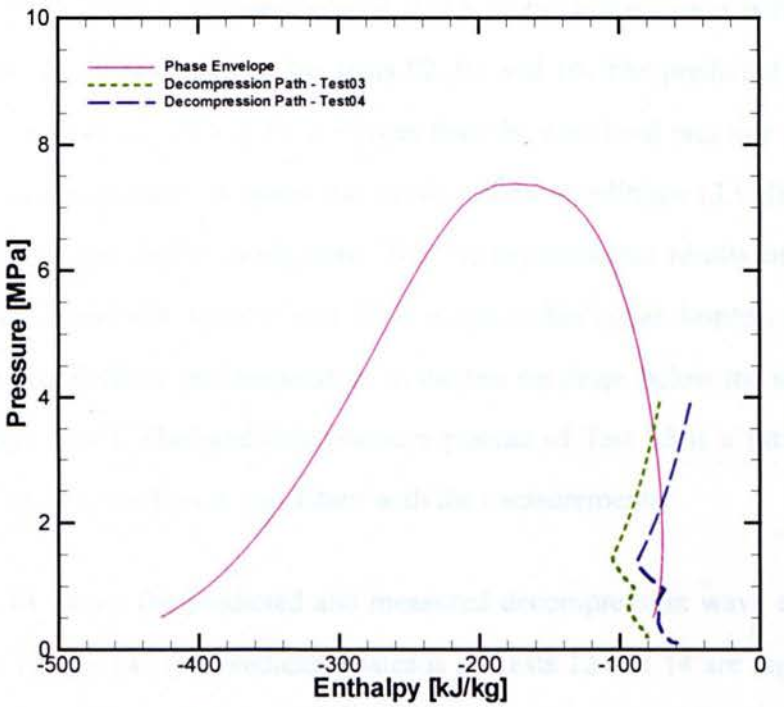

Figure 5.12 Decompression path of Tests 03 and 04

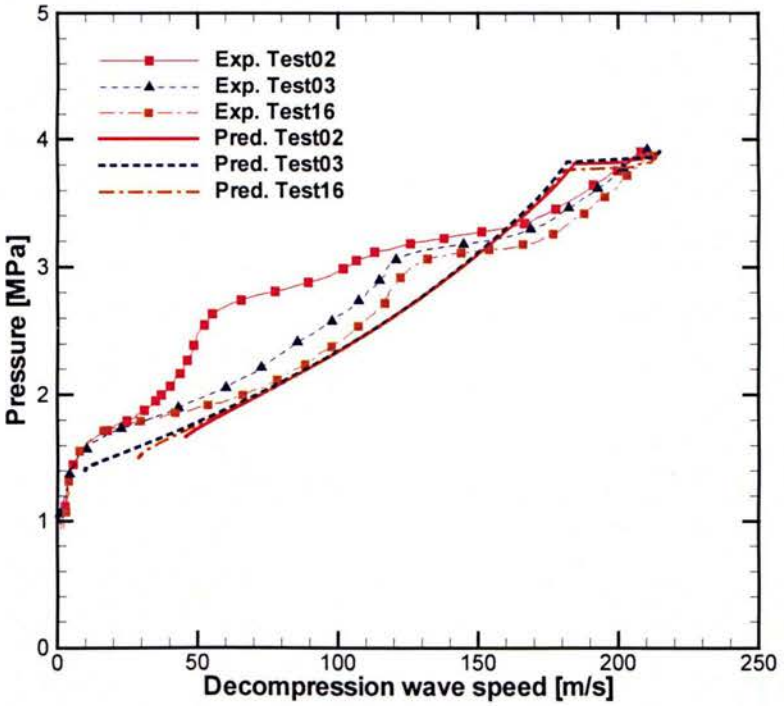

Figure 5.13 The predicted and measured decompression wave curves of Tests 02, 03 and 16

Figure 5.13 displays a comparison of decompression wave curves between the predictions and measurements for Tests 02, 03 and 16. The predicted pressure plateaus for Tests 02, 03 and 16 are lower than the measured pressure plateaus. Three tests are carried out under the similar initial conditions (3.9MPa, 5°C), which lead to the similar predictions. But the experimental results of Test 02 are not consistent with Tests 03 and 16. It is stated that liquid droplets appeared before testing because the temperature in the test rig drops below the saturation temperature [147]. The predicted pressure plateau of Test 03 is a little higher than that of Test 16. This is consistent with the measurements.

Figure 5.14 shows the predicted and measured decompression wave curves of Tests 03, 12 and 14. The predicted plateaus of Tests 12 and 14 are higher than the measured plateaus. The predicted and measured plateaus of Tests 12 and 14 are lower than these of Test 03. This indicates that decreasing the initial pressure at a fixed initial temperature will decrease the pressure of plateau at

the decompression wave curve. Additionally, the fact that the plateau of Test 12 is lower than that of Test 14 (similar to Tests 03 and 04) further confirms that increasing the initial temperature at a fixed initial pressure will decrease the pressure of plateau at the decompression wave curve.

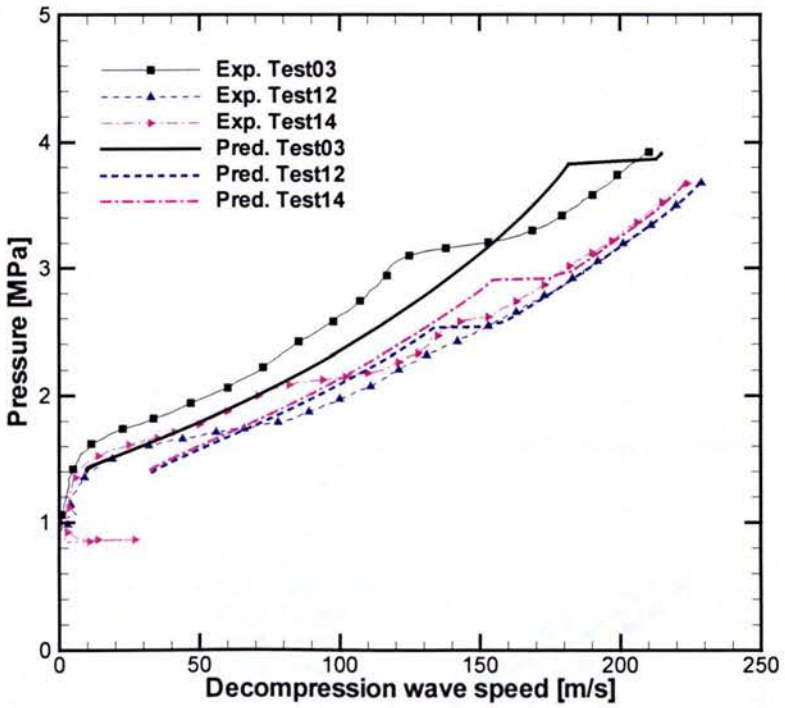

Figure 5.14 The predicted and measured decompression wave curves of Tests 03, 12, and 14.

5.2.2.3. Gaseous CO_2-rich Mixture Shock Tube Tests

Impurities are inevitably introduced during the CCS process. Here tests with CO_2-rich mixture (CO_2 with impurities) will be predicted to determine the effects of impurities on the decompression behaviour. The typical impurities are hydrogen (H_2), nitrogen (N_2), sulphur dioxide (SO_2), methane (CH_4) and oxygen (O_2), etc. In order to obtain more accurate saturation pressure, PRSV EOS is employed to simulate the gaseous CO_2-mixture tests. The flash calculation is used to determine the phase and compositions of each phase.

Tests 05-07 are binary mixtures, CO_2/H_2, CO_2/N_2, and CO_2/SO_2, respectively. The predictions of decompression wave curve for Tests 05-07 are shown in Figure 5.15. The prediction of Test 03 is also plotted as reference to facilitate comparison of decompression wave curve between pure CO_2 and CO_2-rich mixture. The plateau pressures of three tests are under-estimated. The discrepancies are caused by the assumption of homogenous equilibrium. The predictions of Tests 05-07 are lower than Test 03. The predicted pressures of plateaus for Tests 05-07 are 5.3%, 6.3% and 3.4% lower than that of Test 03, respectively. The observed pressure plateaus of Tests 05-07 also are lower than Test 03. The pressure plateaus of gaseous phase CO_2 with impurities such as H_2, N_2 and SO_2 are lower than that of pure gaseous CO_2.

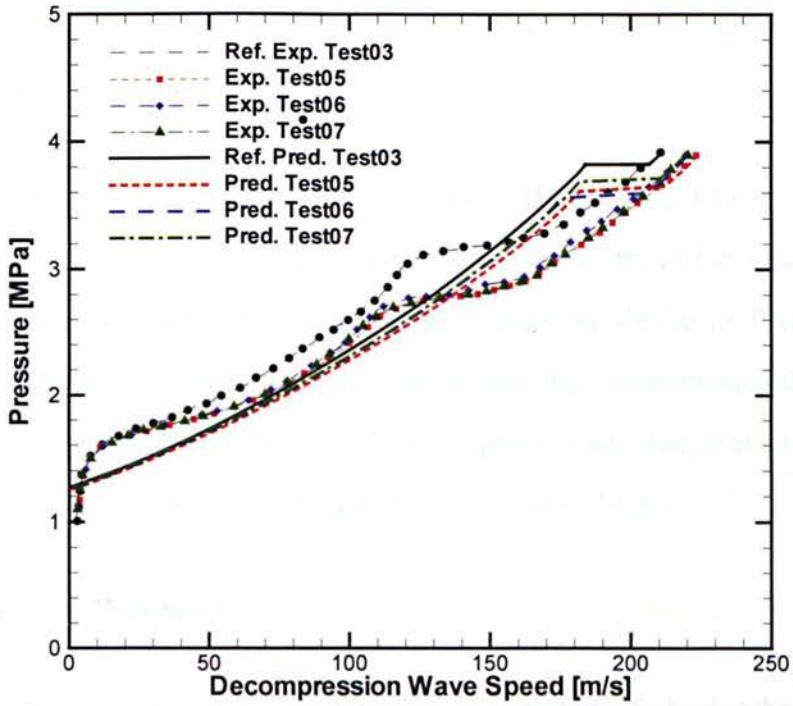

Figure 5.15 The predicted and measured decompression wave curves for Tests 03, 05, 06 and 07.

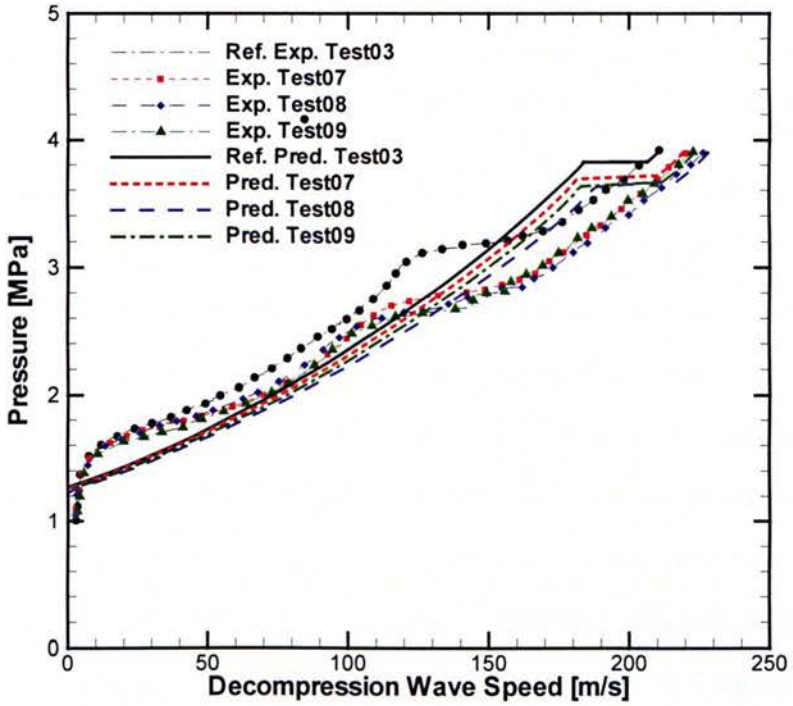

Figure 5.16 The predicted and measured decompression wave curves for Tests 03, 07, 08 and 09.

Tests 08 and 09 are ternary mixtures, CO_2 plus H_2 and SO_2, CO_2 plus N_2 and SO_2, respectively. The predicted decompression wave curves for Tests 08 and 09 are shown in Figure 5.16. The predicted results are similar to Test 07. The pressures of plateaus are over-predicted against the experimental data. The predicted plateaus of Tests 08 and 09 are slightly lower than that of Test 07. This is consistent with the experimental data of Tests 07-09.

5.2.2.4. Summary

Predictions were compared with the experimental data of shock tube tests for gaseous CO_2 and CO_2-rich mixture. Firstly, Test 03 was carefully discussed and analysed to evaluate the decompression behaviours. The pressure-time traces of Test 03 were compared to further evaluate the applicability of current model with HEM for CO_2. There was in reasonably good agreement with the experimental data. The predicted plateaus are consistently higher than the

measured plateaus. The main reason is the non-equilibrium phenomena which are caused by super-saturation. However, the current model with HEM cannot take account of the non-equilibrium effects. Secondly, more pure gaseous tests were predicted to evaluate the effects of initial condition on the decompression wave curve. It was found that increasing initial pressure will increase the pressure of plateau at the decompression wave curve, and increasing initial temperature will decrease the pressure of plateau at the decompression wave curve. Lastly, the tests with CO_2-rich mixture were also predicted to assess the effects of impurities on the decompression wave curve. It was observed that the existence of impurities results in a decrease in the pressure plateau. Additionally, the decompression behaviour of pure CO_2 and CO_2-rich mixture in the gaseous phase was similar to that of rich gas shown in Chapter 4, while the wide of plateau is small in the decompression curve for the gaseous CO_2.

Overall, the predicted decompression curves for the gaseous tests with pure CO_2 and CO_2-rich mixture were in reasonably good agreement with the experimental data.

5.3. Effects of Friction and Heat Transfer

Friction and heat transfer are two important factors to be taken into account in nonisentropic flows. Next, the exploratory numerical studies are carried out to further investigate the effects of pipe wall friction and heat transfer on the decompression behaviour. The investigation is carried out with the typical shock tube test, Tests 03 with the gaseous CO_2. Four cases are simulated as following:

- For **Case 1**, the decompression flow is assumed to be adiabatic and isentropic, and both heat transfer and wall friction are ignored.
- For **Case 2**, friction is taken into account while heat transfer is ignored.
- For **Case 3**, heat transfer is taken into account while friction is ignored.

- For **Case 4**, both heat transfer and friction are considered.

Comparison between four cases is carried out to evaluate the effects of wall friction and heat transfer on the decompression behaviour.

Figure 5.17 shows the comparison between four cases to evaluate the effects of wall friction and heat transfer on the decompression wave curves at P01 for Test 03 with gaseous phase CO_2. The monitoring point is quite close to the open end of the shock tube with the distance of 0.0864m. The same result is observed between four cases at the high pressure above 1.5MPa, while the slightly different results are shown at the "tail" region. For Case 1, as the pressure decreases, the decompression wave speed decreases to the minimum (close to zero) and then increases slightly due to decreasing of flow velocity and remains nearly constant with the decrease in pressure. For Case 2, the decompression wave speed is slightly higher than the predictions in Case 1 at the "tail" region. For Case 3, the difference between Case 3 and Case 1 is that the sudden change of decompression wave speed occurs due to the phase change caused by heat transfer. For Case 4, the decompression wave curve is similar to the prediction in Case 2, and the decompression wave speed slightly increase with consideration of the effect of heat transfer. Totally, it is found that the predictions of decompression wave curve are nearly same except at the late stage of decompression namely the "tail" region. In the "tail" region, the heat transfer and wall friction have a significant effect on the decompression wave curve. However, the decompression wave curve in the "tail" region is affected by the deflected wave and the decompression wave curve under the high pressure, particularly the pressure plateau, might be the key for the safety design of pipeline. The effect of wall friction is consistent with the study of Mahgerefteh et al [155]. However, Mahgerefteh et al reported the opposite effect of heat transfer on the decompression wave speed when pressure drops below a certain value. Additionally, it is worth noting that the opposite effect of

wall friction was claimed by Botros et al [135]. This is due to the difference definitions of decompression wave speed. It was defined by the following [135]:

$$W = \frac{dx}{dt} = -\left(\frac{\partial P}{\partial t}\right)_x \Big/ \left(\frac{\partial P}{\partial x}\right)_t \tag{5.1}$$

However, the theoretical definition [156] is $W = C - |u|$, which is always using in the current study. The former is calculated by the analytical investigation of pressure perturbation, and the latter is calculated by the local sound of speed minus the local flow speed. The local flow speed should be calculated with the consideration of the nonisentropic effects, such as friction and heat transfer. Therefore, the theoretical definition is employed to investigate the effects of friction and heat transfer.

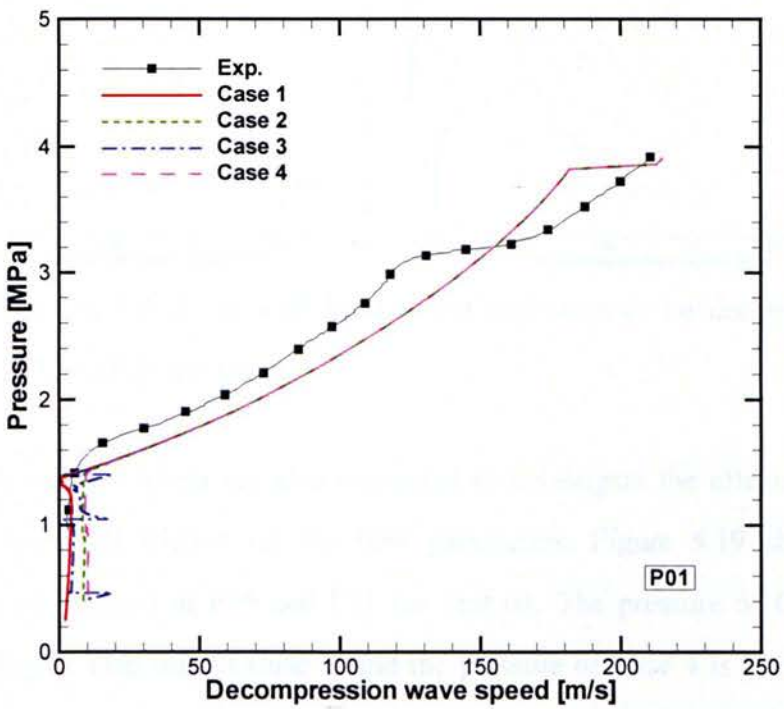

Figure 5.17 The effects of wall friction and heat transfer on decompression curve at P01 for Test 03.

The effects of heat transfer and wall friction are dependent on the location where the flow parameters are obtained to calculate the decompression wave speed. Figure 5.18 show decompression wave curve at two monitoring points P19 and P27. The former is close to the open end of the shock tube with the distance of 4.84m and the latter is 54.04m away from the open end. It is noteworthy that the location of the monitoring point has a significant effect on the decompression wave curve and the "tail" of decompression wave curves is quite different. The closer to the open end the monitoring point is, the smaller the decompression wave speed is at the region of "tail". The reason is that the flow will be chocked and the decompression wave speed will be zero at the open end of the shock tube.

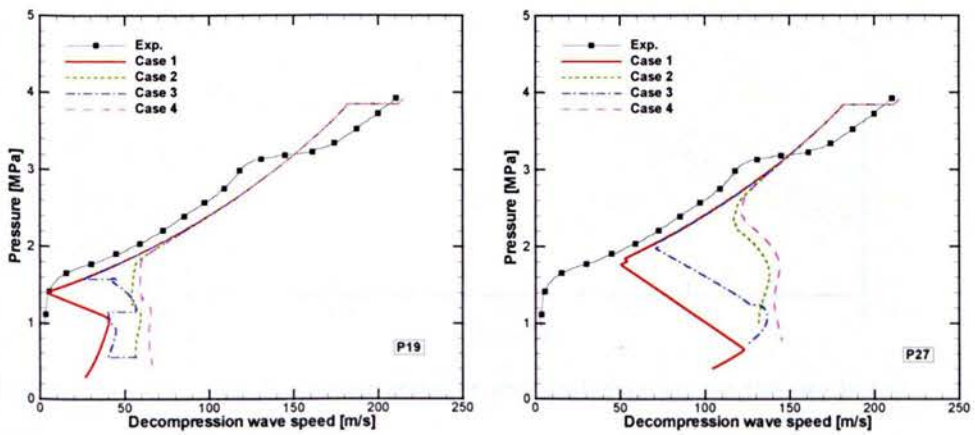

Figure 5.18 The effects of wall friction and heat transfer on decompression curve at P03 and P27 for Test 03.

The pressure-time traces are also compared to investigate the effects of heat transfer and wall friction on the flow parameters. Figure 5.19 shows the variation of pressure at P19 and P31 for Test 03. The pressure of Case 3 is slightly higher than that of Case 1, and the pressure of Case 4 is also slightly higher than that of Case 2. Therefore, heat transfer produces a slight increase in pressure and the decompression rate slightly decreased, and the effect of heat transfer increases as the monitoring point approaches to the open end. This is

caused by the large temperature difference between the wall and the inside flow. Additionally, wall friction produces a decrease in decompression rate, and the effect of wall friction increases as the distance of monitoring point from the open end increases due to the accumulation of friction effect along the length of the shock tube.

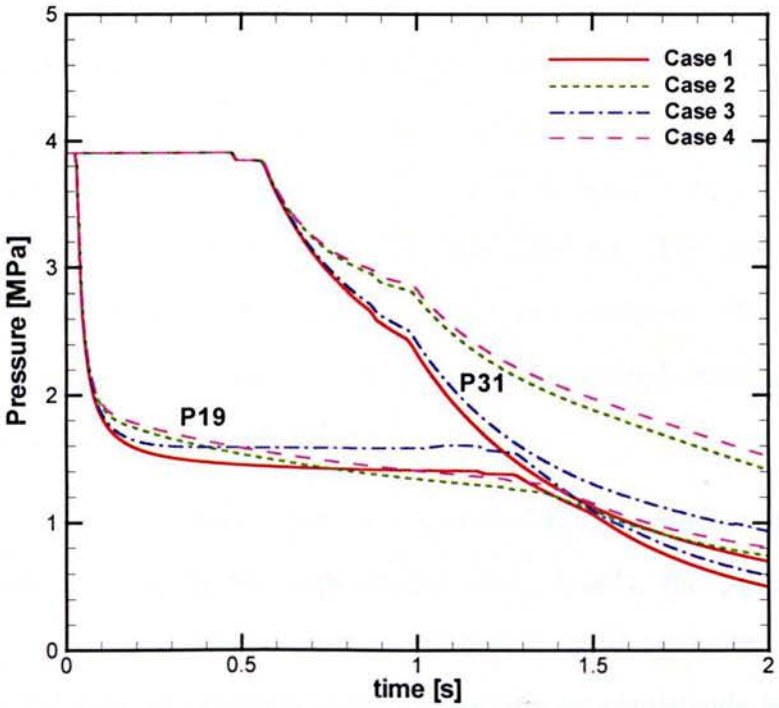

Figure 5.19 The effects of heat transfer and wall friction on the predicted pressure-time traces for Test 03.

In summary, heat transfer and wall friction have a limited effect on the decompression curve and they play an important role in the release flow at the late stage. Heat transfer and wall friction do not have a significant influence on the pressure plateau of the decompression wave curve. However, there is a significant effect at the "tail" region of decompression wave curve, and heat transfer and wall friction produce the increase of decompression wave speed at the "tail" region. The results show that the closer the monitoring point is to the close end, the larger the effects of heat transfer and wall fraction on decompression wave curve are. Additionally, heat transfer and wall friction also

have an important influence on pressure-time trace. Heat transfer produces a slight increase in pressure, and wall friction produces a comparative decrease in the rate of decrease of pressure. For gaseous phase CO_2, wall friction produces a larger effect only at the location close to the close end of the shock tube.

5.4. Concluding Remarks

Several CO_2 shock tube tests with gaseous phase pure CO_2 and CO_2-rich mixture were calculated using current model with HEM assumption. Predictions of pressure-time traces and decompression wave curves were compared with the currently available experimental data. The decompression behaviours of gaseous CO_2 were discussed and analysed. The effect of impurities on the decompression behaviours was examined. Additionally, the effects of friction and heat transfer were assessed.

Fourteen gaseous CO_2 tests were investigated using current model with HEM assumption to compare the experimental data. Totally, the predictions of decompression wave curves were in reasonably good agreement with the experimental data. The predicted pressure plateaus are consistently higher than the measurements. The prediction of pressure-time traces agrees well with the experimental data. More detailed findings from the gaseous phase CO_2 shock tube decompression can be summarized as below:

- The speed of sound is discontinuous across the phase boundary and drops sharply as the two-phase mixture emerges. The discontinuity in the speed of sound across the phase boundary and the continuity in the escaping velocity result in a discontinuity in the decompression wave speed exhibiting as a "plateau" on the decompression curve.
- The width of the pressure plateau on decompression curve mainly depends on the difference in speed of sound between initial single phase

and two-phase mixture after phase transition. For gaseous phase CO_2 decompression, the width of the plateau is relatively small due to the small difference in speed of sound of gas and two-phase CO_2 mixture. As the predictions for gaseous and two-phase CO_2 speed of sound by PR, PRSV and SW EOSs are in good agreement, the predicted decompression curves using the three EOSs are very close.

- For gaseous phase CO_2 decompression, enthalpy is found to decrease initially. During the later stage of the decompression, an increase in enthalpy is observed and a second phase transition from liquid droplets back to gaseous phase is observed close to the open end.

- For gaseous phase CO_2 decompression, the increasing initial pressure will increase the pressure of plateau at the decompression wave curve, and increasing initial temperature will decrease the pressure of plateau at the decompression wave curve.

- The existence of impurities results in the decrease of the pressure plateau for gaseous CO_2. The decompression behaviour of gaseous CO_2 is similar to that of rich gas, while the plateau is shorter in the decompression curve for the gaseous CO_2.

- Phase transition is firstly observed close to the open end due to fast decompression rate at the very early stage of the release and the inception location of phase transition shifts towards the closed end during the decompression process. As the decompression wave reaches the closed end and is reflected back towards the open end, further decompression behind the reflected wave causes the occurrence of phase transition at the close end.

- After the initial decompression caused by the decompression wave, the compressed CO_2 quickly depressurizes to the saturation pressure.

- The outer wall temperature significantly lags behind the fluid temperature.

Additionally, the effects of friction and heat transfer were investigated for gaseous shock tube tests. Heat transfer and wall friction do not have a significant influence on the pressure plateau of the decompression wave curve. However, there is a significant effect at the "tail" region of decompression wave curve, and heat transfer and wall friction produce the increase of decompression wave speed at the "tail" region. The effect of wall friction is consistent with the study of Mahgerefteh et al [155]. However, Mahgerefteh et al reported the opposite effect of heat transfer on the decompression wave speed when pressure drops below a certain value. It was also found that wall heat transfer plays important role only during the later stage of the decompression. The effects of wall heat transfer are pronounced for gaseous CO_2 decompression due to the higher escaping velocity and the lower density. Temperature increases are observed for locations close to the open end.

Chapter 6 Dense CO_2 Shock Tube Decompression

6.1. Introduction

For the pipeline transportation involved in CCS technology, CO_2 is generally compressed and transported under high pressure in liquid or dense states. It is significant to examine the decompression behaviour of dense CO_2 pipeline for the study of pipeline fracture control.

In Chapter 5, the gaseous CO_2 shock tube decompression was investigated, and effects of friction and heat transfer on the decompression behaviours of gaseous CO_2 shock tube were also examined. As mentioned before, Cosham et al [147], [148] presented some experimental data of gaseous and dense CO_2 shock tube tests.

Hereby, this chapter will further study the decompression of dense CO_2 shock tube. The decompression of dense phase CO_2 shock tube will be predicted using the proposed model with homogeneous equilibrium assumption. Then, the predictions will be compared with measurement. Meanwhile, the decompression flow of dense phase CO_2 shock tube test will be analysed in more detail. Also, the effects of friction and heat transfer on the decompression behaviours of dense CO_2 shock tube will be carefully investigated, and the effects of EOSs and impurities on the decompression behaviour are also examined. Additionally, the non-equilibrium effect is examined by employing HRM to evaluate the decompression flow of dense phase CO_2 shock tube test. The predictions from current model with HRM are compared with the predictions based on the assumption of homogeneous equilibrium.

6.2. Dense CO_2 Shock Tube Test

Chapter 5 described the CO_2 shock tube tests, which were reported in the literatures [147], [151]. The description of the test instrument can be found in Chapter 5. The detailed locations of the pressure and temperature transducers were tabulated in Table 5.1. The initial state and compositions of dense CO_2 shock tube tests were listed in Table 5.2.

6.2.1. Introduction of Dense CO_2 Shock Tube Test

A typical pipeline is designed for CCS to transport CO_2 in the dense phase in order to obtain large transportation capacities. The pressure of dense CO_2 is usually above the critical pressure [152], [153] with the consideration of the region of ambient temperature. 14 shock tube tests were conducted with dense CO_2 and CO_2-rich mixtures, listed in Table 5.2.

Tests 18-25 are pure CO_2. Tests 18, 19 and 23 are carried out at the same pressure level (15MPa), but at different temperatures, 14°C, 5°C and 35.6°C respectively. Tests 22, 24 and 25 are conducted at the same temperature (20°C), but at different pressures of 10.15MPa, 6.14MPa and 10.19MPa, respectively. Tests 20 and 21 are carried out under the initial conditions which are close to the phase boundary of pure CO_2.

Tests 26-31 are CO_2-rich mixture. Tests 26 and 27 are binary mixtures at the same pressure and temperature levels, namely 14MPa and 20°C. Test 28 is ternary mixtures. Tests 29 -30 are conducted with higher order mixtures at the same pressure and temperature as Tests 26 and 27. Test 31 is another higher order mixture at the initial condition (15.05MPa, 10°C).

Some experimental data of dense CO_2 shock tube tests were presented in the work of Cosham et al [148]. The decompression wave curves were presented

for 14 tests, and the pressure-time traces were available only for Tests 19 and 31. These experimental data were used to compare the predictions.

The same mesh used in the section 5.2.1 is adopted to implement the simulation. The computational timestep is varied and the maximum of the computational timestep is approximately $8.8*10^{-5}$. The maximum CFL number 2 is employed to accelerate the simulation. The boundary conditions are same as the gaseous tests. Test 19 (pure dense CO2 shock tube test) is first discussed and analysed, and the prediction of pressure-time trace is compared with the experimental data. Additionally, the decompression wave curves for all dense phase CO_2 tests are presented and compared with measurement.

6.2.2. Results of Dense CO_2 Shock Tube Test

6.2.2.1. Test 19 (Pure Dense CO_2 Shock Tube Test)

The distributions of pressure, temperature, void fraction, escaping velocity and speed of sound along the shock tube at different release moments are shown in Figure 6.1. Test 19 differs from gaseous Test 03 mainly in that the initial pressure is much higher. Therefore, during the initial decompression, a substantial higher escaping velocity is generated behind the leading decompression wave. To overcome the wall friction, an appreciable pressure gradient is sustained, which causes the pressure behind the decompression wave to drop to a value slightly above the saturation pressure after the initial decompression. As the leading decompression wave reaches the closed end at approximately t=0.24s, it is reflected from the closed end and travels back towards the open end. The reflected wave is much stronger than that of the gaseous Test 03. Due to the flow acceleration behind the decompression wave, both the temperature and speed of sound drop accordingly. As the decompression wave is reflected, the pressure at the closed end quickly drops

to the saturation pressure and phase transition starts to occur. At t=0.40s, a very low speed of sound is observed close to the closed end indicating the occurrence of phase transition. At t=0.40s, a lower pressure is observed at the closed end. This is thought to be caused by the escaping flow initiating another decompression wave propagating towards the open end. As the reflected wave moves towards the open end, void fraction increases significantly starting from the closed end, causing a positive gradient of pressure at the closed end. As the reflected wave propagates towards the open end, the pressure behind it drops to approximately the saturation pressure and phase transition occurs as indicated by the very low value of speed of sound. After the reflected wave moves out of the shock tube, a two-phase flow develops along the whole tube judging by relatively low speed of sound at t=0.60s. After t=0.60s, both pressure and temperature continue to drop along the whole length of the test tube while void fraction keeps growing.

Figure 6.2 shows the decompression paths and phase envelopes at different locations. It can be seen that the initial state of CO_2 is in the dense/liquid phase while its initial pressure is well above the critical point. Differing from Test 03, the decompression processes slightly deviate from an isenthalpic process because of stronger flow acceleration resulting from the higher initial pressure which causes enthalpy to decrease slightly before the decompression path moves into the two-phase region. At the end of the decompression paths, apparent increases in enthalpy are observed due to wall heat transfer resulting from the increasing temperature difference between wall and escaping fluid.

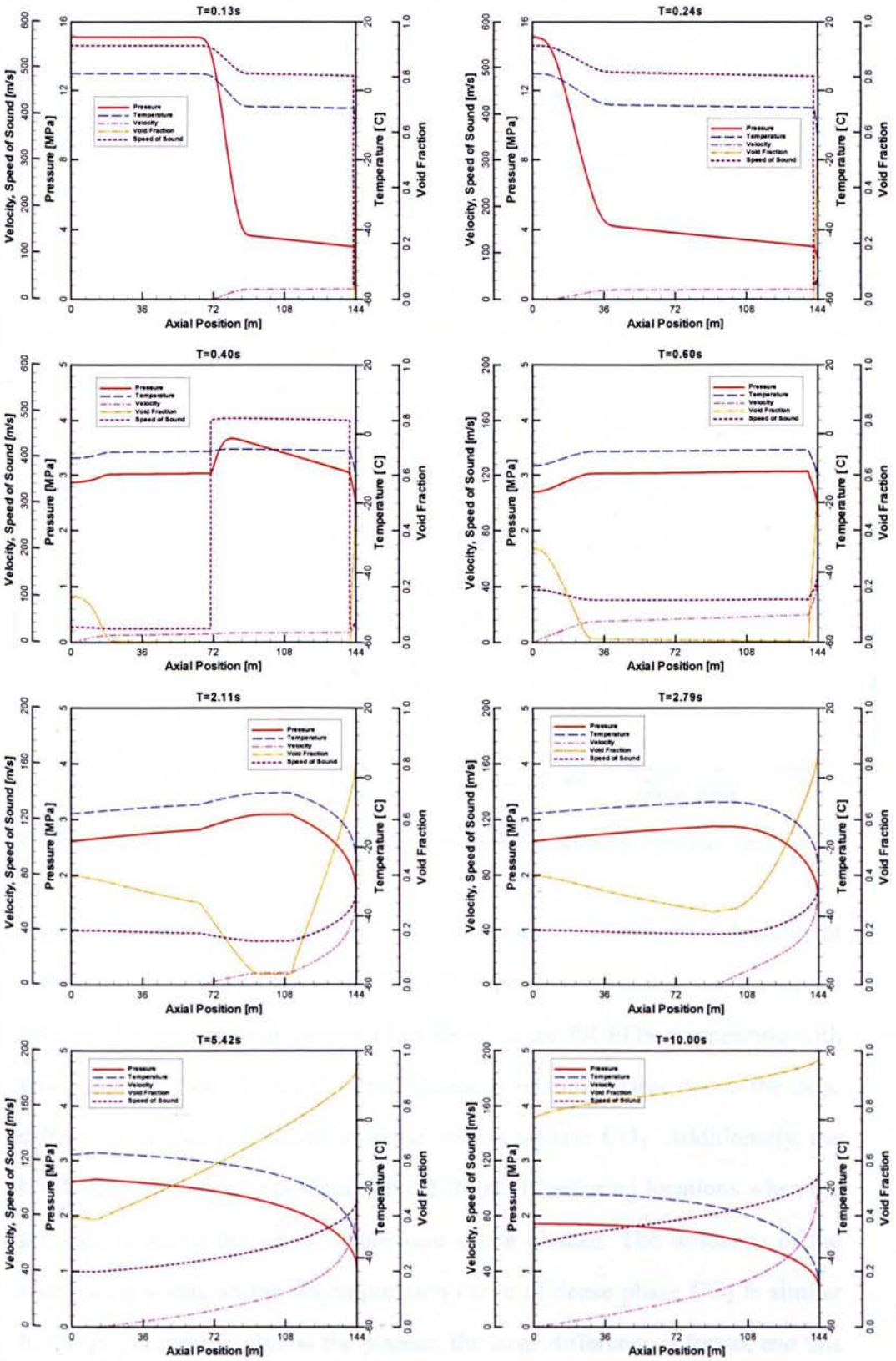

Figure 6.1 Distributions of pressure, temperature, void fraction, escaping velocity and speed of sound along the test tube at different release moments for Test 19.

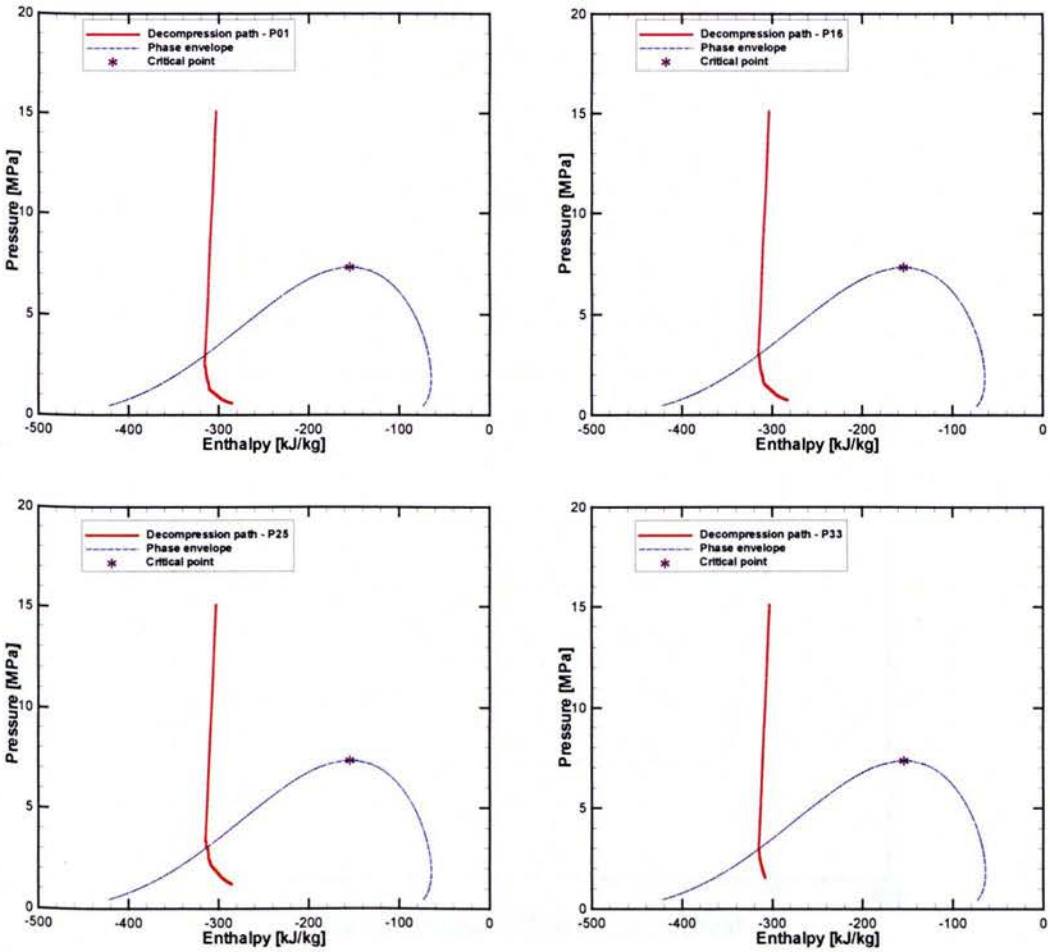

Figure 6.2 Decompression path and phase envelope at different locations for Test 19.

Figure 6.3 presents the decompression wave curves individually calculated at different monitoring locations for Test 19. The decompression wave speed is obtained from prediction by current model with the PR EOS. Comparing with gaseous phase CO_2, the width of the plateau is relatively large due to the large difference in speed of sound of dense and two-phase CO_2. Additionally, the results exhibit the same profiles at the different monitoring locations when the pressure is above the value of pressure at the plateau. The influence of the monitoring points on the decompression curve of dense phase CO_2 is similar to the gaseous phase. Below the plateau, the large difference is found, and this may be caused by the different escaping velocities at different locations. For example, for the location P16, with the decreasing of pressure, the

decompression wave speed abruptly decreases to a small value at the pressure of 3.0MPa, then decompression curve speed slightly increase due to the chocked flow.

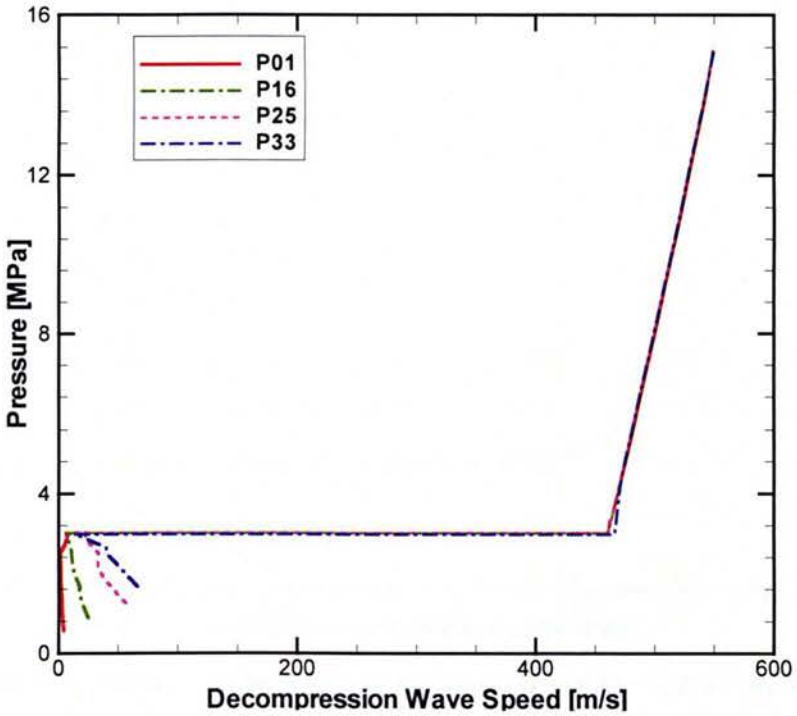

Figure 6.3 Decompression wave curves at four different locations for Test 19.

Predictions of decompression wave curve are also shown in Figure 6.4. Three predictions with different equation of states, PR, PRSV and SW EOSs are involved here. Comparison is carried out with the experimental data. The result exhibits that the predicted pressures of plateau are in reasonably good agreement with the measured pressure of plateau. The predicted plateau pressure with SW, PRSV and PR EOSs are 3.29MPa, 3.16MPa and 3.11MPa, respectively. The predicted pressure of plateau with PRSV EOS is slightly higher than PR EOS. The decompression wave curve predicted with the SW EOS exhibits a higher decompression wave speed before the pressure of dense phase CO_2 drops to the plateau pressure. It is observed that there is in better agreement between the prediction with SW EOS and the measurement.

Particularly at the high decompression wave speed, the prediction with SW EOS shows a quite good agreement with the experimental data.

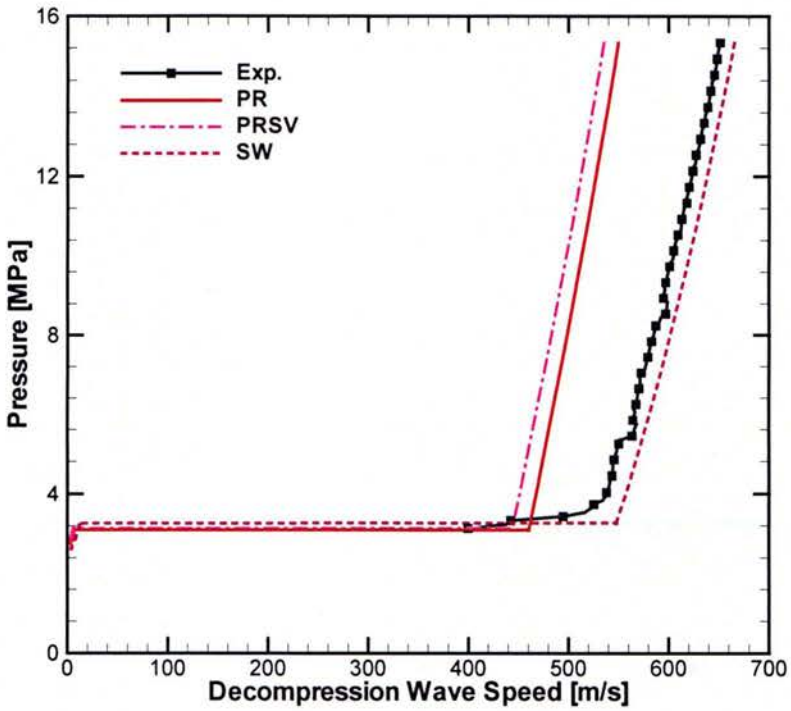

Figure 6.4 Comparison of decompression wave curves for Test 19 predicted with different equations of state.

Prediction of pressure-time trace for the first 50ms is compared with the experimental data obtained from Cosham et al [148]. The results are shown in Figure 6.5. Based on the discussion on the prediction with different EOSs, the prediction with SW EOS are presented in this section. It is observed that there is a reasonable agreement between prediction and measurement. At the beginning of decompression, the decompression rate is fast and then the pressure drops abruptly to a certain value. The initial pressure drop is captured well. There are small discrepancies between the predictions and the measurements, while the discrepancy increases with increasing distance from the open end. After the initial stage of the fast drop of pressure, the pressure is over-predicted owing to HEM assumption. Additionally, two sudden increases in pressure occur during the stage of pressure drop. These are caused by the

explosive cutting of the rupture disc which is neglected by the current model with HEM.

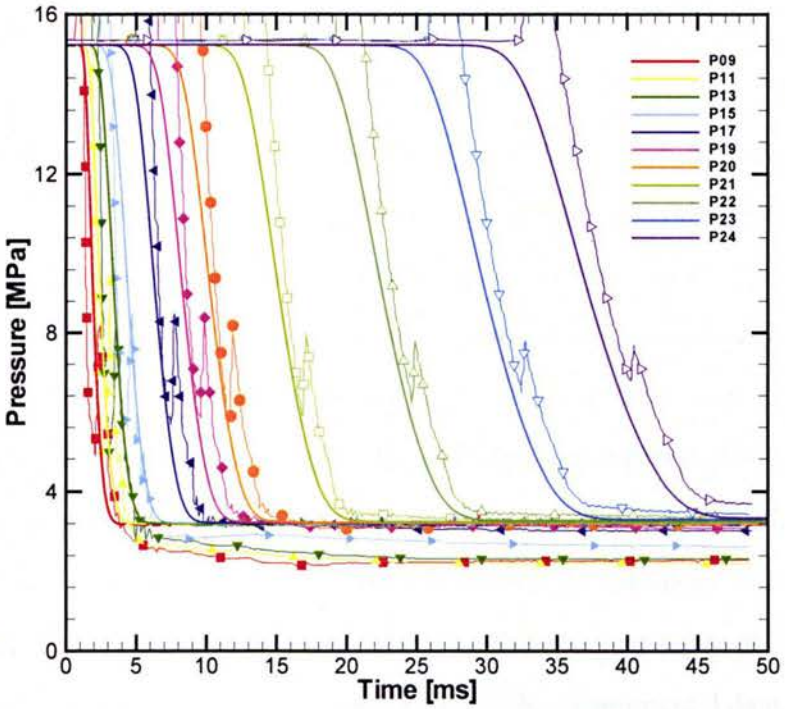

Figure 6.5 Comparison of pressure-time traces for the first 50ms between prediction and measurement (line with symbol) of Test 19.

Comparisons of pressure-time traces for the first second are also shown in Figure 6.6, Figure 6.7 and Figure 6.8. The experiment data of pressure-time traces for the first 1s were obtained from Dr. Cosham, who is a technical coordinator to take charge of the experiment. For the first 1s release time, the reflected decompression wave has already reached back to the open end and rendered the pressure transanders to be unsuitable to derive the decompression wave curve. The predicted pressure-time traces show good agreement with the measurements. At the beginning of the decompresson, the pressure drops sharply at all the monitering points, and then remains constant for a while and then slowly decreases. Totally, the predicted pressure-time traces show a good agreemnt with the measurements. Emphatically, there are large discrepancies of pressure at P10 and P13 (0.94m and 1.84m from the open end, respectivity)

before 0.2s. This is caused by the non-equilibrium effects which dominate near the open end. The measured pressures at P10 and P13 first decrease to a value and then increase slightly. The increase in pressure is a temporal recovery from the phase transition. The predicted pressures are slightly higher than the meaured ones at P10 and P13 after 0.2s. Additionally, the pressure-time traces at P25, P28 and P31 clearly show the second pressure drop at approximately 0.40s, 0.35s and 0.28s, respectively. This is due to the arrival of the reflected wave from the closed end. For the monitoring points far from the open end, i.e. P31, the pressure drops sharply to an intermediate value, which is a little higher than the saturation pressure, and slowly decreases for a while, and then quickly drops to the saturation pressure when the reflected decompression wave arrives. The decompression processes at P28 and P31 are predicted well, and the intermediate pressure is slightly under-predicted. In addition, the observed pressures at P25, P28 and P31 overshoot at the moment when the reflected decompression wave arrives. It is unexpected in the experimental data.

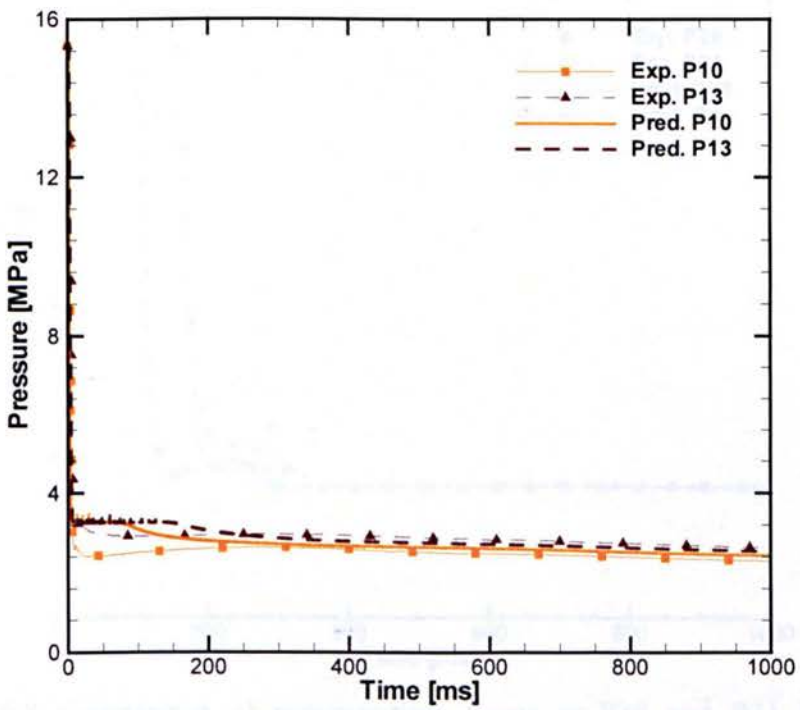

Figure 6.6 Comparison of pressure-time traces at P10 and P13 between prediction and measurement for Test 19.

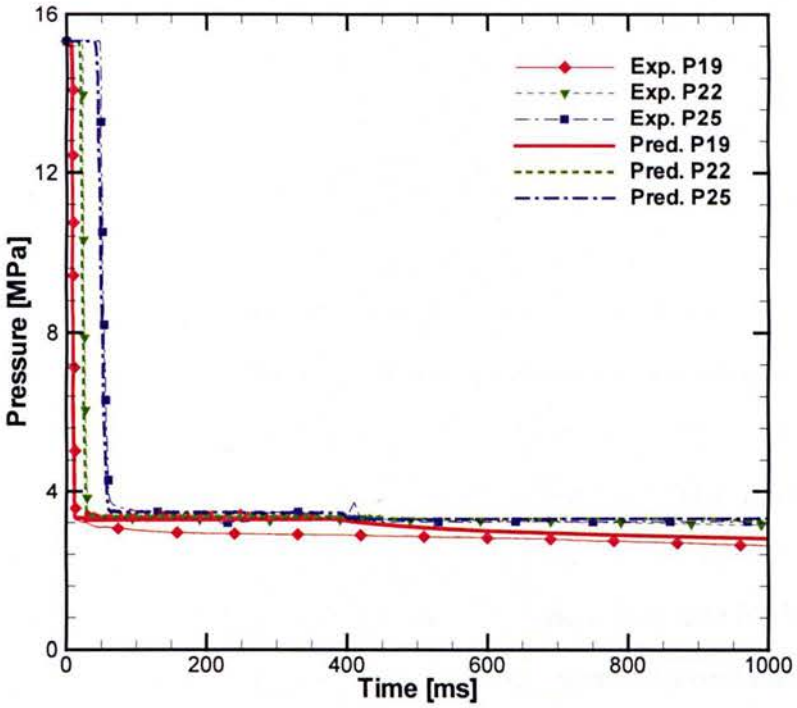

Figure 6.7 Comparison of pressure-time traces at P19, P22 and P25 between prediction and measurement for Test 19.

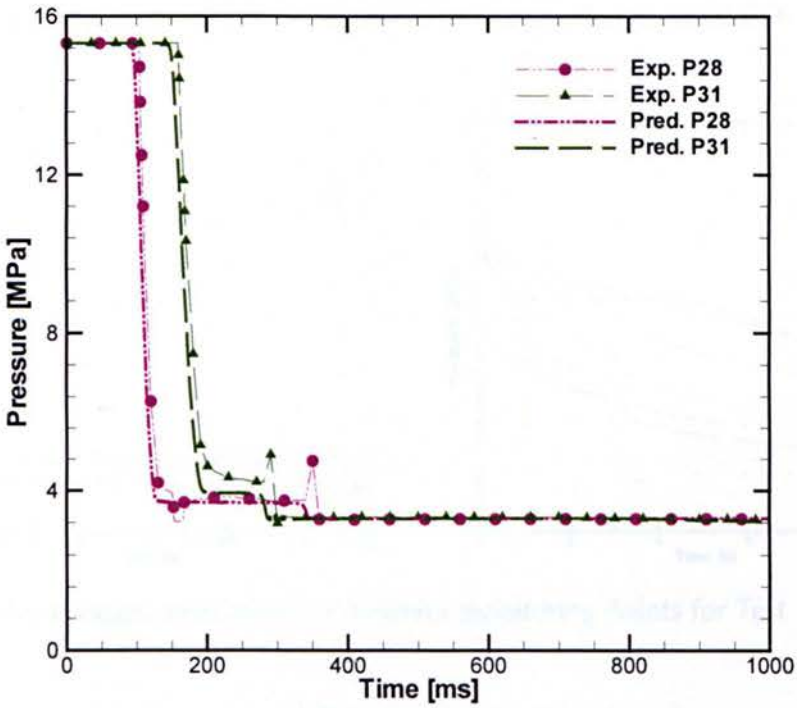

Figure 6.8 Comparison of pressure-time traces at P28 and P31 between prediction and measurement for Test 19.

The predictions of pressure-time trace for the first 10s are shown in Figure 6.9. As the leading decompression wave travelling at the local speed of sound reaches the measurement points, the compressed CO_2 quickly depressurizes to the saturation pressure. After the initial decompression, the pressure stays nearly constant until phase transition takes place. In comparison to the gaseous Test 03, the width of the pressure plateaus is much wider due to the relatively larger differences in the travel speed of the inception of phase transition and the leading decompression speed. For the monitoring points beyond P26, there appear to be second pressure plateaus slightly lower than the first plateaus at the saturation pressure. These second plateaus are caused by the reflected decompression waves from the closed end. Since the initial state is close to the phase boundary, the reflected wave is rather weak. Nevertheless, phase transition starts to take place because the second pressure plateaus are lower than its local saturation pressure. It is worth mentioning that during the computed time the lowest pressure occurring at the rupture plane remains above the triple point. Hence the predictions suggest that no solid CO_2 forms.

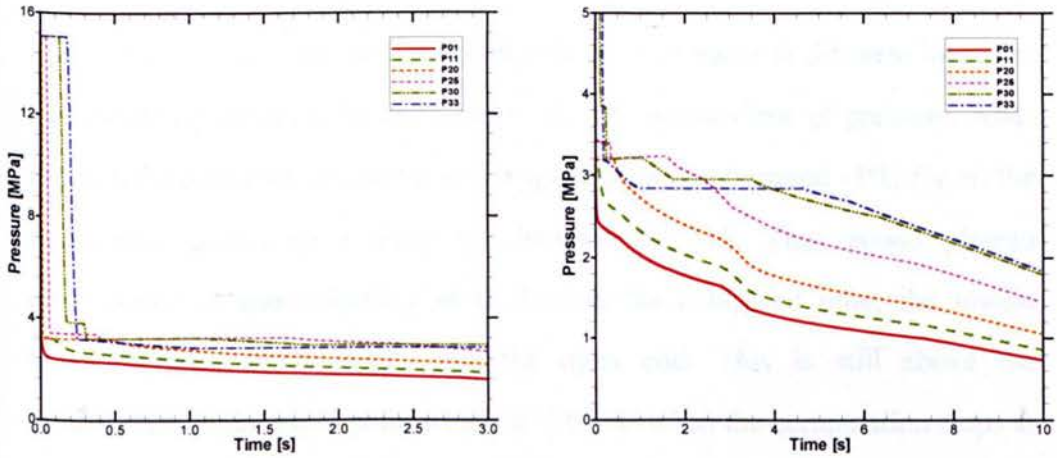

Figure 6.9 Pressure-time traces at different monitoring points for Test 19.

Figure 6.10 displays the predicted void fraction-time traces at different locations for Test 19. At the locations before P20, the void fraction rapidly increases when the decompression wave reach the monitoring points, and then

mildly increases. At the location close to the closed end such as P30 and P33, the void fraction increases and then keeps constant for a while, and continues to increase. The constant void fraction is caused by the chocked flow.

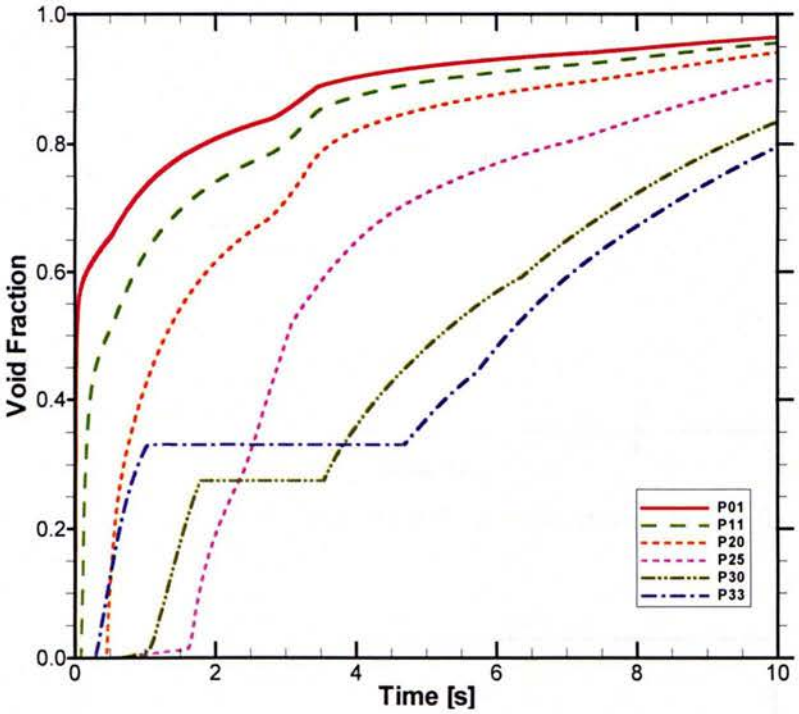

Figure 6.10 Void Fraction-time traces at different monitoring points for Test 19.

Figure 6.11 displays the predicted temperature-time traces at different locations. The changing trend of the temperature closely follows that of pressure. After the initial decompression, temperature quickly drops to around -3°C for all the monitoring points apart from the location at T13. The second plateau corresponds to approximately -8°C. During the computed time, the lowest temperature is about -47°C near the open end. This is still above the temperature of the triple point which is -56.5°C when the computation stops at 10s. However, if the computation was to continue, both temperature and pressure will continue to decrease resulting in solid formation. But because the pressure is below 0.52MPa, the solid will sublimate directly to the vapour state.

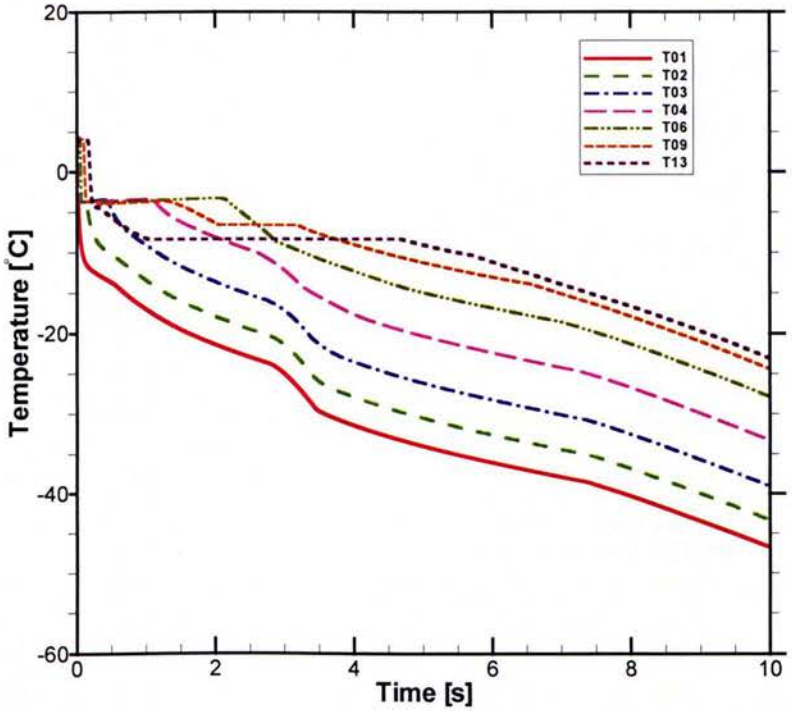

Figure 6.11 Temperature-time traces at different monitoring points for Test 19.

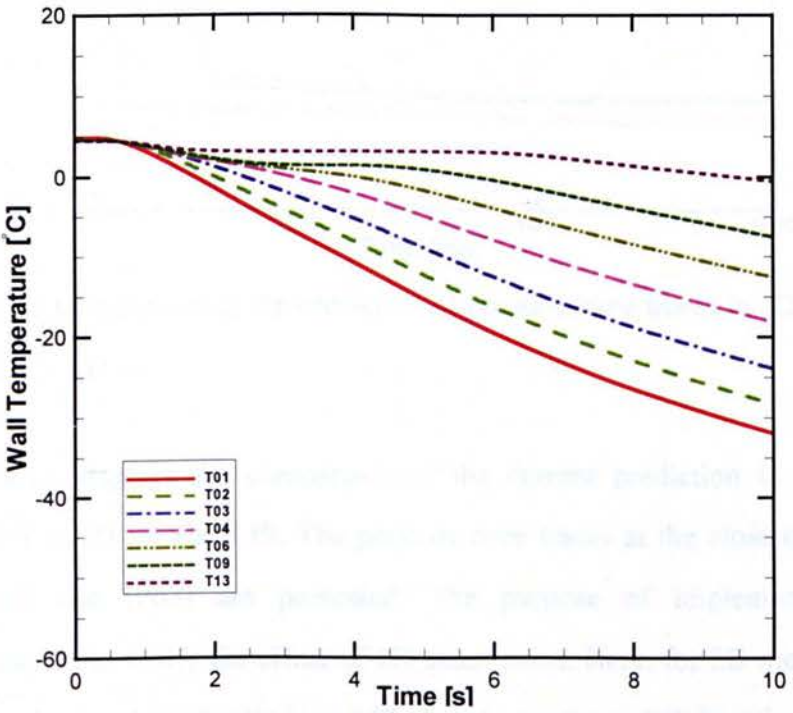

Figure 6.12 Outer wall Temperature-time traces at different monitoring points for Test 19.

Figure 6.12 shows the out wall temperature-time traces at different location for Test 19. Owing to the stronger flow acceleration, the outer wall temperature drops more quickly compared to the gaseous Test 03. For the locations beyond T02, the decreasing rate becomes slower and the temperature stays constant for a period of time due to the small escaping velocity. The wall temperature starts to drop again when the escaping flow is accelerated.

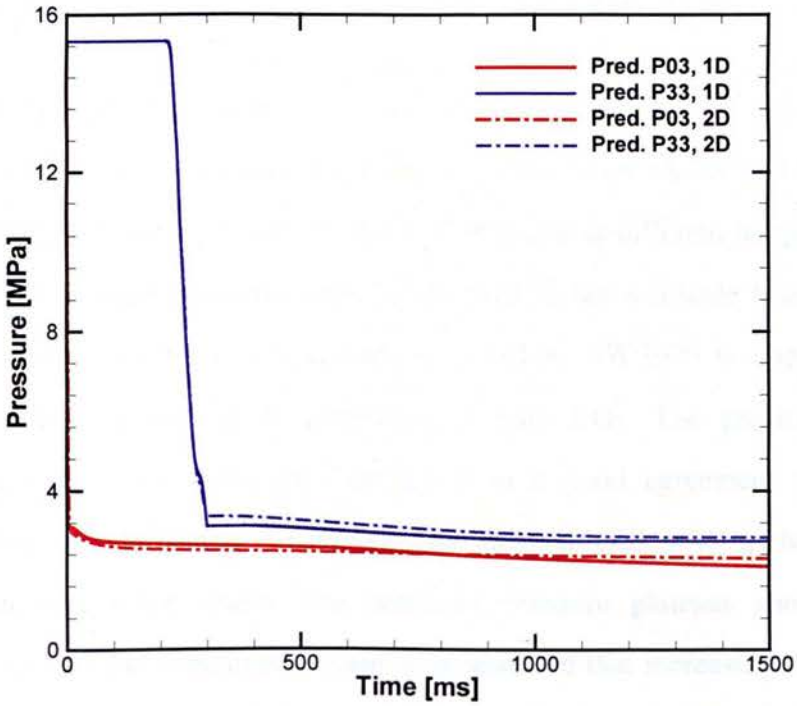

Figure 6.13 Comparison of the prediction of pressure-time traces in 1D with the prediction in 2D.

Figure 6.13 displays the comparison of the current prediction in 1D with prediction in 2D for Case 19. The pressure-time traces at the close end (P33) and open end (P03) are presented. The purpose of implementing the comparison is to verify the effect of 1D assumption. Here, for 2D mesh inside the pipe, the number of cells is specified as 15 on the radial direction and the non-uniform cells are employed. The mesh on the radial direction is refined close to the pipe wall. Explanatorily, the predicted flow parameters in 2D shown here are the surface averaged values on the crossing section at the

measured points. It is clearly seen that the predictions in 1D match better with the predictions in 2D. The slight difference results from the average approach on the section. Generally, the 2D mesh should obtain more flow information. However, the current study mainly focuses on flow along the pipe length. In conclusion, the 1D assumption is well reasonable for predicting the decompression flow inside the pipeline.

6.2.2.1. Other Pure Dense/Liquid CO_2 Shock Tube Tests

Figure 6.14 displays decompression wave curves of Tests 18, 19 and 23. Test 03 and Test 19 are plotted as the reference cases. Tests 18, 19 and 23 were conducted at the same pressure of about 15MPa and at different temperatures. The measured decompression curve of Test 18 is not available because the partial break of the bursting disc leads to its failure. SW EOS is employed to calculate the thermodynamic properties of pure CO_2. The predictions of decompression wave curve for Test 23 is in a good agreement with the measurements. The initial decompressions are predicted well at the higher decompression wave speed. The predicted pressure plateaus show good agreement with the experimental data. It is observed that increasing the initial temperature will increase the pressure of plateau at the decompression wave curve. The trend is obviously reversed compared to the gaseous CO_2. It can be explained from the decompression path on the pressure-temperature diagram, as illustrated in Figure 6.15. When the initial condition is above the saturation line, namely at the dense/liquid phase, the higher initial temperature is, the higher pressure is at the intersection between the decompression path and the saturation line. Therefore, the plateau pressure at which the pressurized CO_2 starts to enter the two-phase region is higher when increasing the initial temperature. Moreover, there are obvious differences between the decompression wave curves of the gaseous and dense/liquid CO_2. For example, the decompression wave curve of Test 03 has a long "tail" below the plateau

with a wide range of decompression wave speed, but the decompression wave curve of Test 23 does not. This needs to pay particular attention to the design and construct of the pipeline transporting dense phase CO_2. Additionally, the pressure plateaus of the dense/liquid CO_2 are clearly visible, and these are much wider than these of the gaseous CO_2 owing to the large difference of speed of sound between the dense-phase and two-phase CO_2.

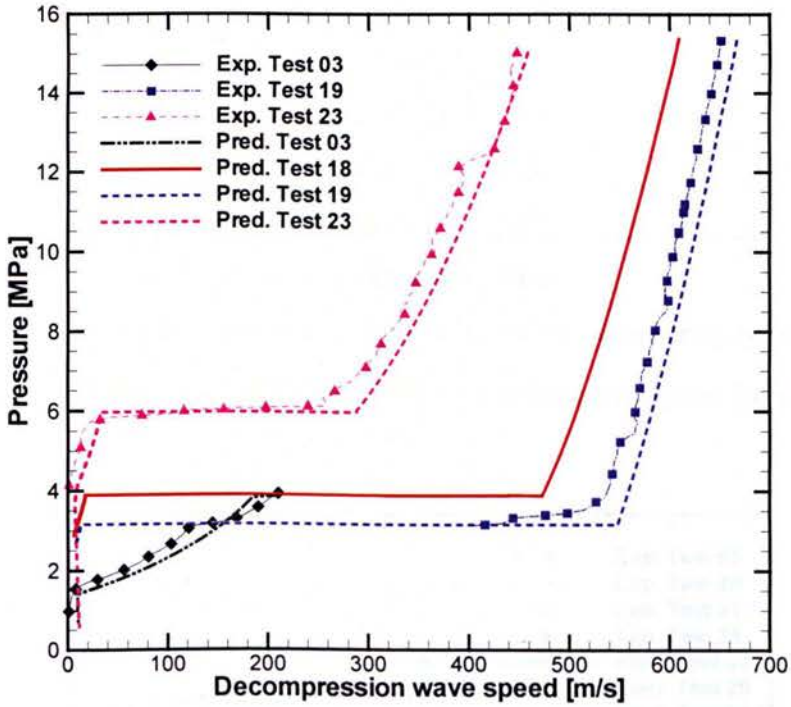

Figure 6.14 The predicted and measured decompression wave curves of Tests 18, 19 and 23.

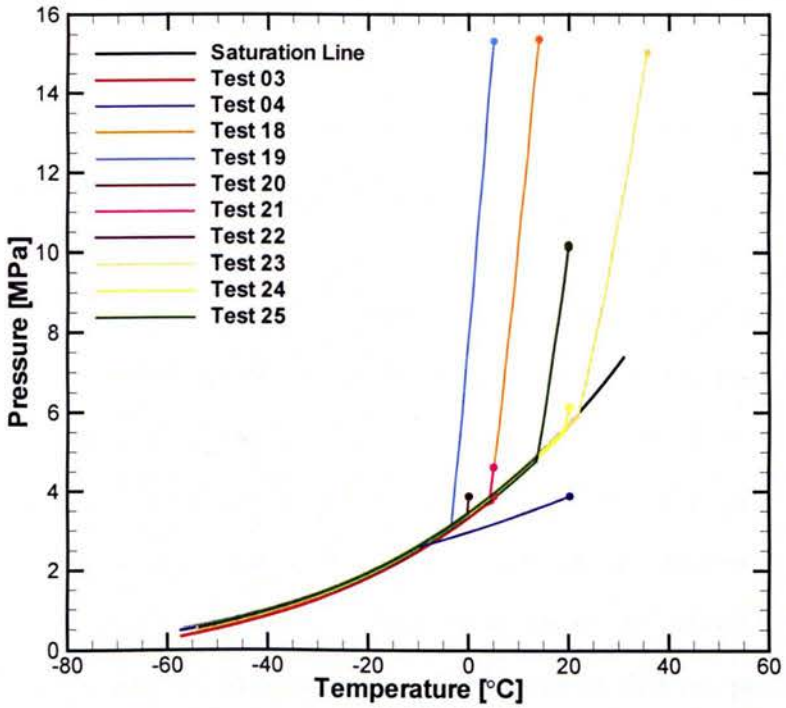

Figure 6.15 The predicted decompression paths at the monitoring point P01 for Tests 03 and 04 (gaseous) and Tests 18-25 (dense/liquid), all pure CO_2.

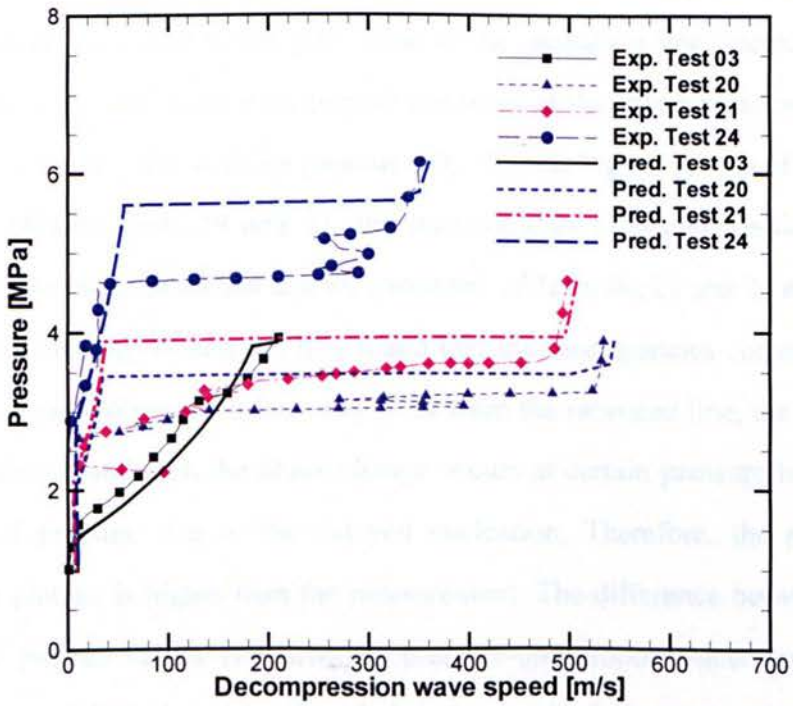

Figure 6.16 The predicted and measured decompression wave curves of Tests 03, 20, 21 and 24.

Comparison of decompression wave curves between predictions and measurements for Tests 20, 21 and 24 is shown in Figure 6.16. Test 03 is plotted as a reference to compare the decompression behaviours of gaseous and dense/liquid CO_2. The initial conditions for the tests are clearly illustrated in Figure 6.15. It is seen that the locations of initial conditions of Tests 20, 21 and 24 on the pressure-temperature diagram are close to the saturation line. The predicted pressure plateau of Test 24 is the highest among the predictions. In terms of the initial condition close to the saturation line, the higher the initial pressures are, the higher the pressure plateaus are. This is consistent with the measurements. The predicted plateaus are higher than the measured plateaus. This is caused by non-equilibrium effect which cannot be reproduced by the proposal model with HEM assumption. HEM assumes that the phase change should happen under the saturation pressure, while the local pressure fall below the saturation pressure without triggering a phase change. In other words, the delayed nucleation occurs due to the rapid decompression.

Furthermore, regarding to the tests close to the saturation line, increasing the initial pressure will increase the plateau pressures of the decompression curves. The trend is consistent with the gaseous CO_2. Comparing the results of Tests 20, 21 and 24 with Tests 19 and 23, the discrepancies of decompression wave curves between the predicted and the measured of Tests 20, 21 and 24 are larger than these of Tests 19 and 23. It is found that the discrepancies correlate with the initial state. When the initial state is far from the saturated line, the pressure sharply drops, and then the phase change occurs at certain pressure below the saturation pressure due to the delayed nucleation. Therefore, the predicted pressure plateau is higher than the measurement. The difference between both pressure plateau values is known as pressure-undershoot, which cannot be captured by HEM. It is also found that the level of pressure-undershoot is closely related to the initial condition, namely, the farther the initial condition is from the saturated line, the smaller the pressure-undershoot is. This is explained

that at the high decompression rates, the non-equilibrium effect is weakened [154]. In conclusion, the location of initial condition is close to the saturated line enhances the effect of non-equilibrium.

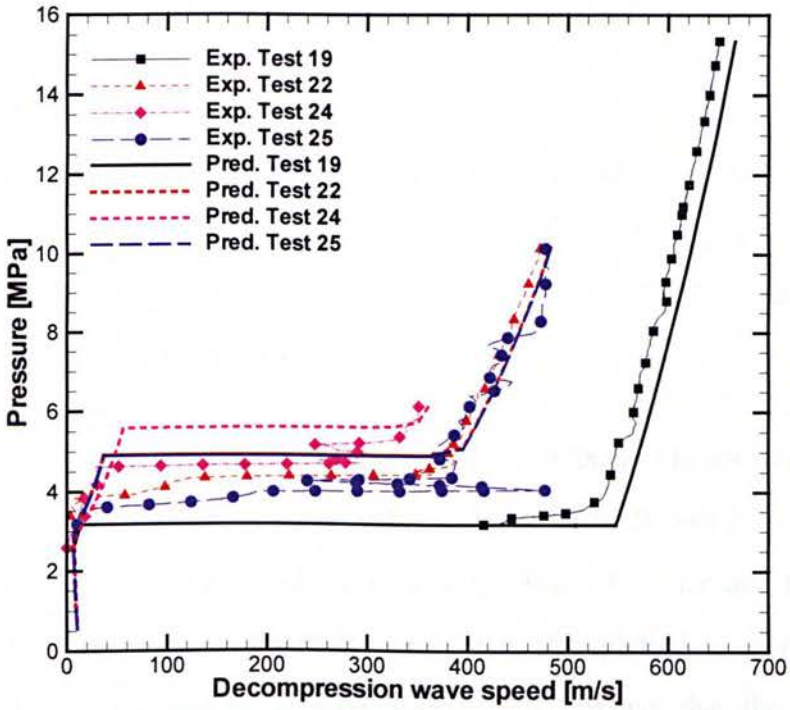

Figure 6.17 The predicted and measured decompression wave curves of Tests 19, 22, 24 and 25.

Figure 6.17 shows the decompression wave curves of Tests 19, 22, 24 and 25. Tests 22, 24 and 25 are conducted at the same temperature (20°C). The initial conditions of Tests 22 and 25 are nearly the same. Therefore, the results of Tests 22 and 25 are similar. The predicted decompression wave curves almost overlap. The experimental decompression wave curves for Tests 22 and 25 exhibit reasonable agreement. Compared with the observed decompression wave curves, the decompression behaviours are accurately calculated before the pressure drops below the saturation pressure. The predicted pressure plateaus of Tests 22, 24 and 25 are higher than the measured pressure plateaus. The discrepancy of decompression wave curve between the prediction and measurement becomes worse as the initial condition of dense phase CO_2

approaches the saturation line, as illustrated in Figure 5.30. This also demonstrates that the effects of non-equilibrium are enhanced when the initial condition is close to the two-phase boundary.

6.2.2.2. Dense CO_2-rich Mixture Shock Tube Tests

The simulations with dense/liquid CO_2-rich mixture are also implemented to investigate the effects of impurities on the decompression behaviour of dense-phase CO_2. Both PRSV EOS and GERG-2004 are employed to calculate the thermodynamic properties. It is noted that GERG-2004 is particularly introduced for dense phase mixture.

The decompression wave curves of Tests 26, 27 and 28 are illustrated in Figure 6.18. Three tests are conducted at 14MPa, 20°C. Tests 26 and 27 are binary mixtures, CO_2/N_2, and CO_2/H_2, respectively. Test 28 is ternary mixtures, $CO_2/H_2/N_2$. The predicted result for Test 19 is also plotted to facilitate the comparison of decompression wave curve. It is obvious that the pressure plateaus of Tests 26-28 are much higher than that of Test 19. The reason is that the bubble point pressures of CO_2 mixtures are higher than the saturation pressure of pure CO_2. For the results predicted with PRSV EOS, the predicted plateaus of Tests 27-28 are over-estimated and the predicted plateau of Test 26 is under-estimated. While, for the results predicted with GERG-2004, the predicted plateaus of Tests 26-27 are over-estimated and the predicted plateau of Test 28 is slightly under-estimated. The discrepancies are due to the inaccurate calculations of the saturation pressure for CO_2 mixture using equation of state. Totally, the plateaus predicted with GERG-2004 show better agreement with the measurements. Additionally, at the beginning of the decompression, the predictions of Tests 26-27 with GERG-2004 are in better agreement with the measurements, while the prediction of Test 28 with PRSV EOS agrees better with the measurement. Hence, it is not definite that the

GERG-2004 presents better prediction than PRSV EOS. It is believed that GERG-2004 is not particularly developed for the mixture with high concentration CO_2. In summary, EOS has a significantly impact on the decompression wave curve for CO_2-rich mixture.

PRSV EOS improves the accuracy of PR EOS and reproduces more accurately the vapour pressure data for a wide variety of substances. GERG-2004 is developed by introducing a large number of regression coefficients obtained from fitting experimental data so that it becomes the most comprehensive method to calculation of natural gas properties. These EOSs are generally validated for hydrocarbon-rich mixtures such as natural gas. However, these EOSs are rarely validated for the dense CO_2-rich mixtures. Therefore, their applicability is be further verified when employing them directly for CO_2-rich mixtures. The more feasibility may be to adopt a new approach to build the correction between the thermodynamic properties, such as coefficients.

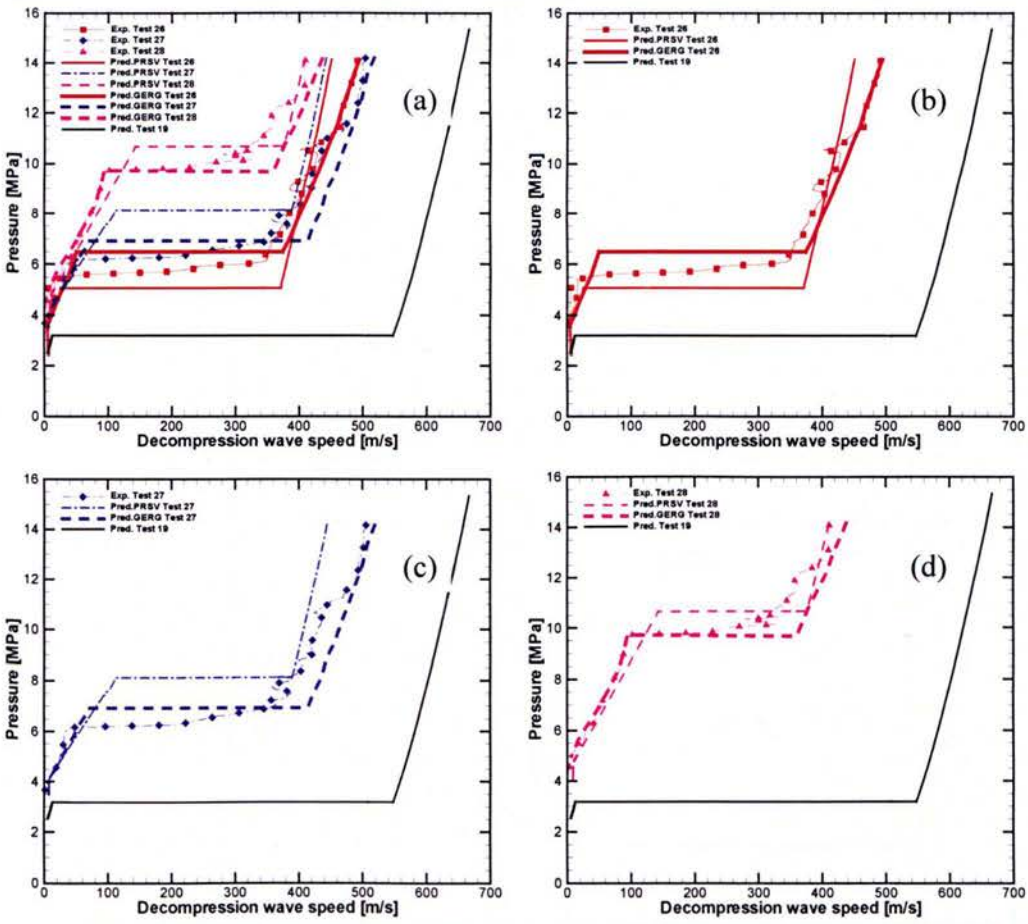

Figure 6.18 The predicted and measured decompression wave curves of Tests 19, 26, 27 and 28.

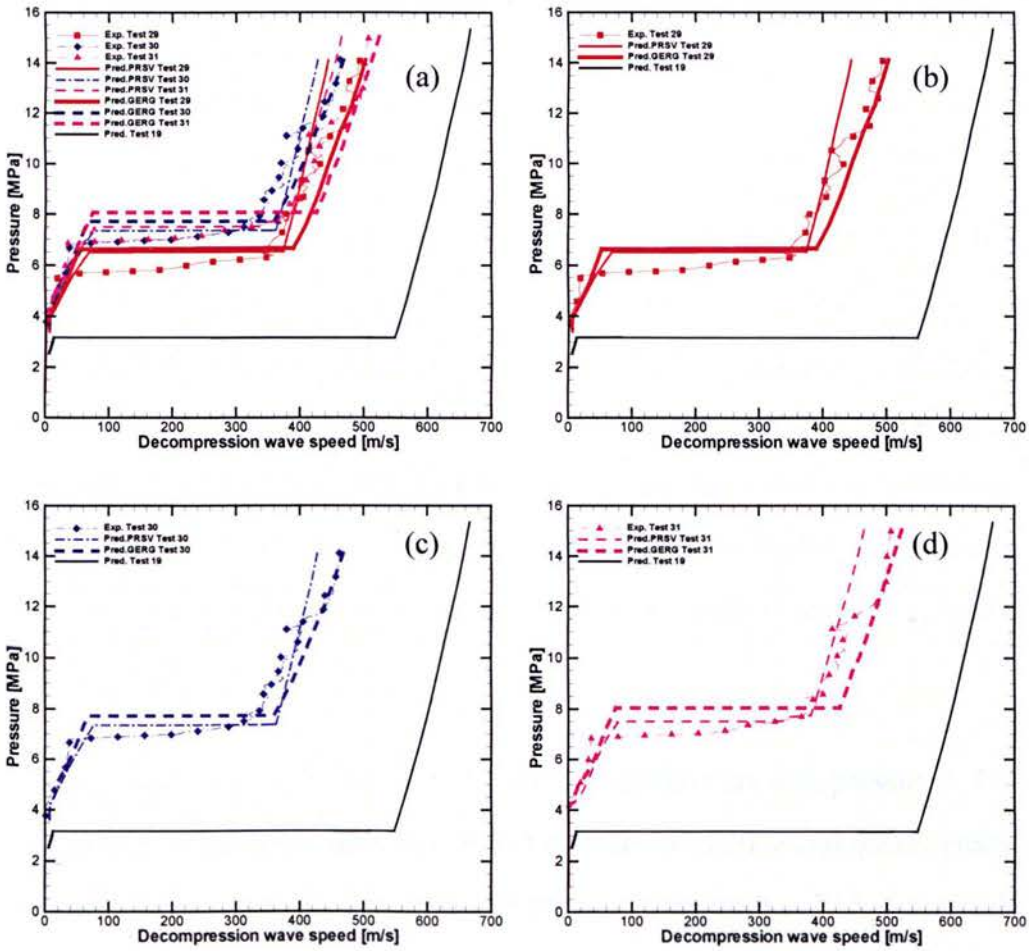

Figure 6.19 The predicted and measured decompression wave curves of Tests 19, 29, 30 and 31.

The comparison of decompression wave curves for Tests 29-31 between the predictions and the measurements is shown in Figure 6.19. The predicted pressure plateaus are slightly higher than the measured pressure plateaus. The pressure plateaus predicted with PRSV EOS agree reasonably better with the measurements than these predicted with GERG-2004, although the predictions with GERG-2004 agree better at the initial stage of decompression. Regardless of GERG-2004 or PRSV EOS, the predicted pressures of plateau are slightly higher than the measurements. Additionally, the decompression wave curve of Test 30 exhibits the similar pressure plateau with Test 31. The pressure plateaus of Tests 29 and 31 are much higher than that of Test 19. However, the pressure

plateaus of Tests 29 and 31 are lower than Test 28. The reason is that the "non-condensable" components (H_2 and N_2) extremely increase the bubble pressure.

Conclusively, the decompression wave speeds of Tests 26-31 are lower than that of Test 19. Furthermore, the plateaus of decompression wave curves for Tests 26-31 are narrower than that of Test 19. Whatever the equation of state is employed, the pressure plateaus of dense CO_2 mixture is obvious higher than that of pure dense CO_2. This fact is a significant feature of decompression behaviours for dense CO_2 mixture. It is proved that the higher toughness of pipelines transporting dense-phase CO_2 mixture is required in order to arrest the running crack.

The pressure-time traces for Test 31 with CO_2 mixture are also presented. The comparison of pressure-time trace at P15 between prediction and measurement is shown in Figure 6.20. The measured pressure-time trace at P15 is available only for the first 1s. The result shows a good agreement with the experimental data. On the whole, the predicted pressure is slightly higher than the measured pressure. The predicted pressure plateau is higher and its duration is shorter than the measured pressure plateau. One of the main reasons is that the non-equilibrium effect cannot be captured by the proposal model with HEM assumption, and another reason is the inaccuracy of equation of state used in the current model. The plateau of pressure-time trace of Test 31 is higher than that of Test 19. This is consistent with the result of decompress wave curves. After the pressure plateau terminates, the pressure continues to decrease at the rapid decompression rate. At this moment, the decompression rate for Test 31 is obviously higher than Test 19. The reason is that the phase envelope of CO_2 mixture at pressure-temperature diagram covers a wide region but not a single line such as the saturation line of pure CO_2.

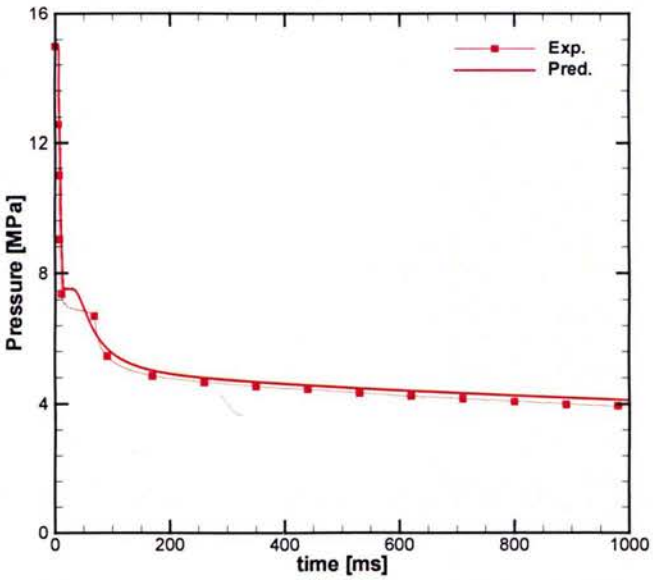

Figure 6.20 Comparison of pressure-time traces at P15 between prediction and measurement for Test 31.

Next, the pressure-time traces for the first 50ms are displayed in Figure 6.21. The initial decompression wave speed is over-predicted and the predicted decompression rate is slightly lower than the measured. Overall, the pressure is over-estimated due to the inaccuracy of the equation of state. Furthermore, the non-equilibrium effect deteriorates to same extent the accuracy of pressure.

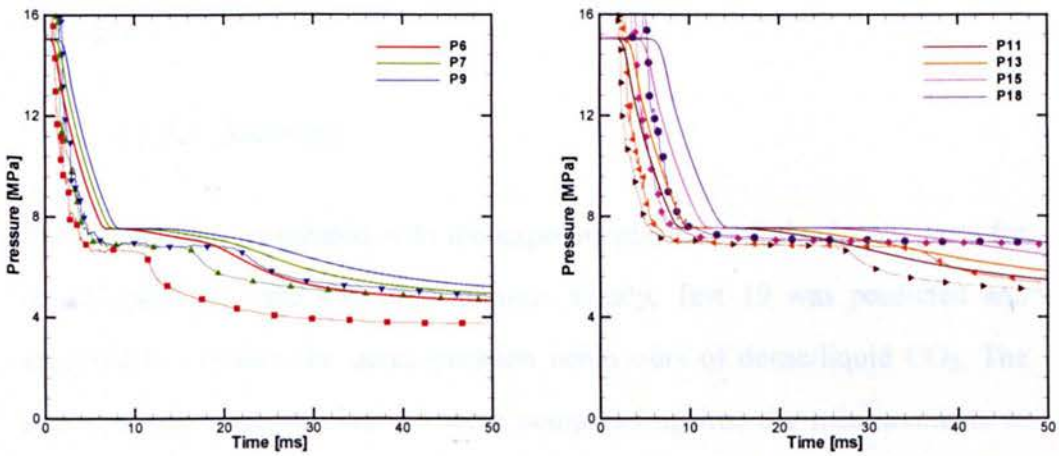

Figure 6.21 The pressure-time traces for the first 50ms between prediction and measurement for Test 31.

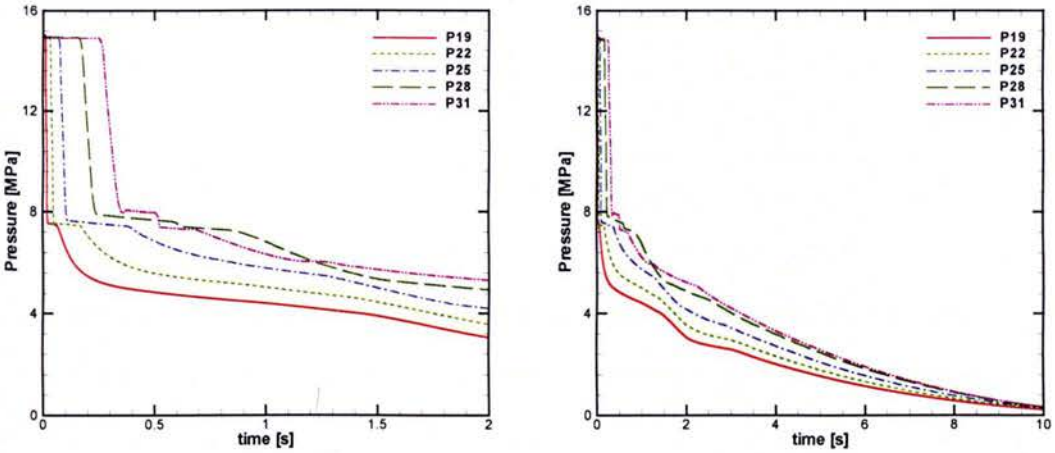

Figure 6.22 The predicted pressure-time traces at P19, 21, 25, 28 and 31 for Test 31.

Apart from the limited experimental data, Figure 6.22 shows the predicted pressure-time traces of Test 31 at other monitoring points. For monitoring points P19, P22 and P25 close to the open end, the pressure drops sharply and then remains constant for a while and then decreases slowly to the bubble pressure and enters the two-phase envelope. For P28 and P31, the decompression behaviours are almost similar, while another sudden drop of pressure occurs at 0.58s and 0.49s respectively due to the arrival of the reflected wave, then the pressure remains nearly constant until phase transition takes place.

6.2.2.3. Summary

Predictions were compared with the experimental data of shock tube tests for dense/liquid CO_2 and CO_2-rich mixture. Firstly, Test 19 was predicted and analysed to evaluate the decompression behaviours of dense/liquid CO_2. The pressure-time traces of Test 19 were compared against the measurements to further validate the current model with HEM for dense phase CO_2. The agreement of the result is reasonably good. The predicted plateaus are consistently higher than the measured ones. The main reason is the

non-equilibrium phenomena. Secondly, more pure dense/liquid tests were predicted to evaluate the effects of initial condition on the decompression wave curve of the dense CO_2. It was found that increasing initial pressure will decrease the pressure of plateau at the decompression wave curve, and increasing initial temperature will increase the pressure of plateau at the decompression wave curve. Lastly, the tests with dense/liquid CO_2-rich mixture were also predicted to assess the effects of impurities on the decompression wave curve of dense CO_2. The decompression wave curves predicted with GERG-2004 did not always show better agreement than these predicted with PRSV EOS. It was also observed that the existence of impurities results in the obvious increase of the pressure plateau.

Overall, the predicted decompression curves for the tests with pure dense CO_2 and CO_2-rich mixture were in reasonably good agreement with the experimental data.

6.3. Effects of Friction and Heat Transfer

Friction and heat transfer are two important factors to be taken into account in nonisentropic flows, specifically when the initial state of fluid are dense phase for decompression flow. Likewise the Chapter 5, the exploratory numerical studies are also employed to further investigate the effects of pipe wall friction and heat transfer on the decompression behaviour of dense CO_2 shock tube. The investigation is carried out with the typical shock tube test, Tests 19 with the dense CO_2. Four cases are also involved and the configurations are same with the Chapter 5. In order to facilitate to describe, the exploratory cases is repeated as following:

- For **Case 1**, the decompression flow is assumed to be adiabatic and isentropic, and both heat transfer and wall friction are ignored.
- For **Case 2**, friction is taken into account while heat transfer is ignored.

- For **Case 3**, heat transfer is taken into account while friction is ignored.
- For **Case 4**, both heat transfer and friction are considered.

The comparative study with four cases is implemented to evaluate the effects of wall friction and heat transfer on the decompression behaviour of dense CO_2 shock tube.

Figure 6.23 show the comparison between four cases to assess the effects of wall friction and heat transfer on the decompression wave curve for dense phase Test 19. The decompression wave speeds at P01 are nearly zero after the pressure decrease below the pressure of plateau due to the choke of decompression flow at the open end. It is observed that the predictions of four cases are almost same, and the effects of wall friction and heat transfer are considerably smaller than that of Test 03. The decompression wave curves at two different points, P19 and P27, are also shown in Figure 6.24. The decompression wave speeds at P19 are nearly zero after the pressure decrease below the pressure of plateau due to the choke of decompression flow at the open end. While the decompression wave speeds at P27 increase slightly as the pressure decrease below the pressure of plateau. Conclusively, wall friction and heat transfer produce slight effects on the decompression behaviour of the dense phase pure CO_2.

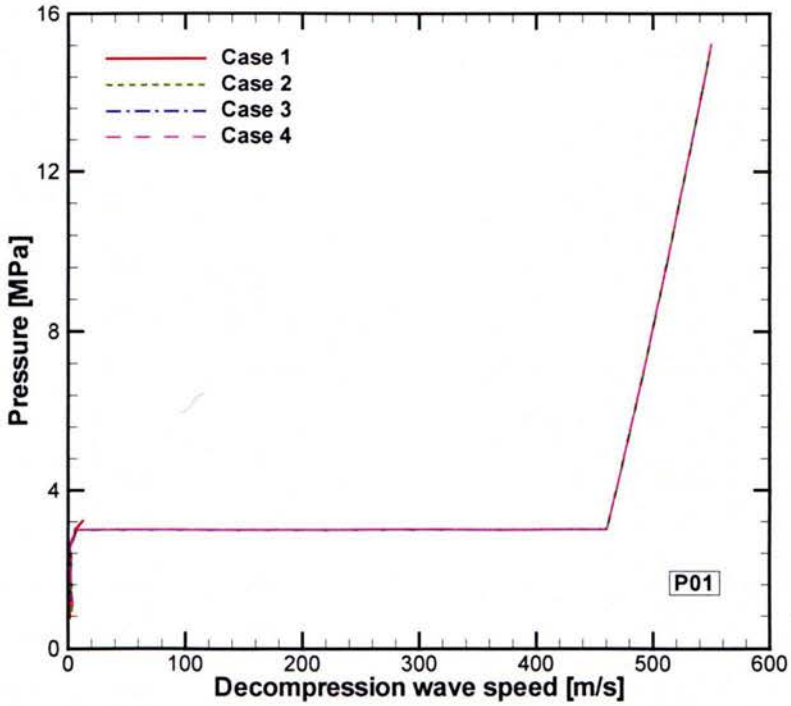

Figure 6.23 The effects of wall friction and heat transfer on the predicted decompression wave curves at P01 for Test 19.

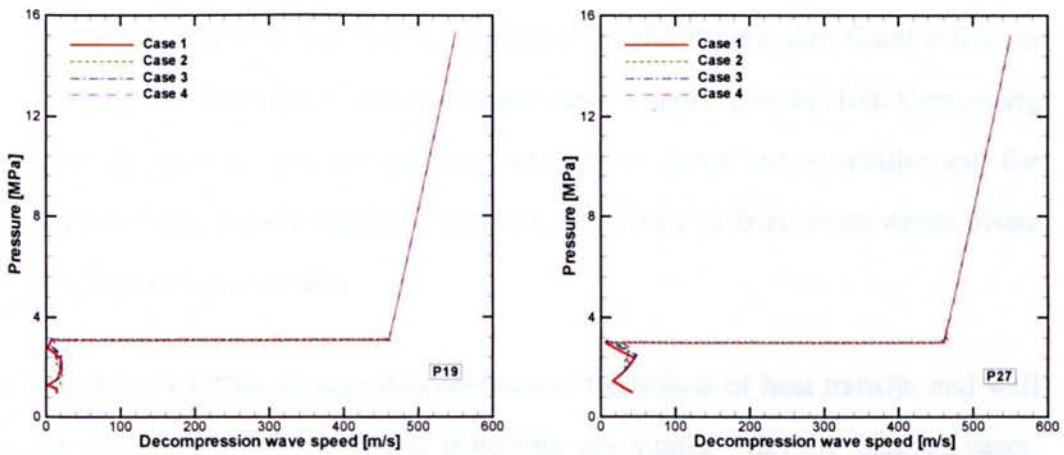

Figure 6.24 The effects of wall friction and heat transfer on decompression wave curve at P19 and P27 for Test 19.

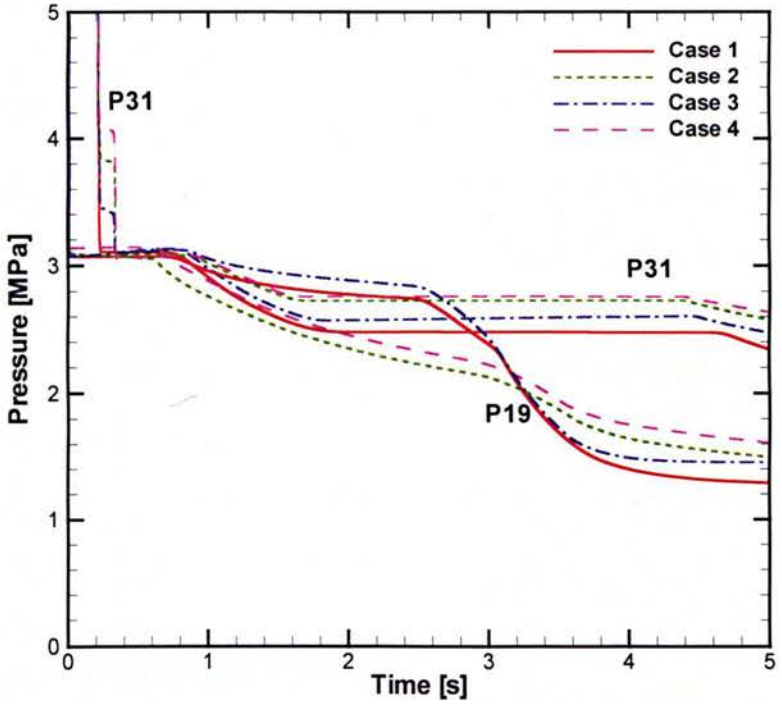

Figure 6.25 The effects of heat transfer and wall friction on the predicted pressure-time traces for Test 19.

The pressure-time traces for dense Test 19 are shown in Figure 6.25. The results indicate that wall friction and heat transfer have a significant effect on the pressure-time traces. The effects are same with the gaseous test. Comparing with the gaseous test, the escaping velocity of dense test is smaller and the friction force is also smaller. Therefore, the effect of friction on dense phase decompression is smaller.

For dense CO_2 shock tube decompression, the effects of heat transfer and wall fraction on the decompression behaviour are similar with the gaseous cases. Also, the heat transfer and wall friction have a limited effect on the decompression curve, but they play an important role in the release flow at the late stage. The pressure plateau of the decompression wave curve is not influenced, and a limited effect on the "tail" region of decompression wave curve, namely, heat transfer and wall friction produce the increase of decompression wave speed at the "tail" region. It is found that the effect is

smaller than the gaseous case. Additionally, heat transfer and wall friction also have an important influence on pressure-time trace. The results show that heat transfer and wall friction have similar influence on the variation of pressure comparing with the gaseous case. A slight increase in pressure is produced by heat transfer between fluid and pipe wall and a comparative decrease in the rate of decrease of pressure is produced by wall friction. Compared with the gaseous CO_2 decompression, the larger effect of wall fraction is also observed at the location close to the open end. Totally, the effect of friction on dense phase decompression is smaller than the gaseous case due that the escaping velocity and the friction force are small.

6.4. Non-equilibrium Effect

Based on the aforementioned discussion, the HEM assumption is one of the key factors to cause the discrepancy between the predictions and the measurements. Two dense phase tests, Test 19 and Test 31, are calculated using the current model with the approach of HRM to assess the non-equilibrium effect. Validations are also carried out to evaluate the current model with HRM. Here the PR EOS is employed to calculate the thermodynamic properties. Predictions with HEM and HRM are compared with the available experimental data. The effect of non-equilibrium is evaluated by the comparisons between the predictions with HEM and HRM.

6.4.1. Pure Dense CO_2

The comparison of pressure-time traces for first 1000ms between the predictions using current model with HEM and HRM at different monitoring locations is shown in Figure 6.26 and Figure 6.27, respectively. The rapid decompression predicted by HRM is completely consistent with HEM due to the single phase. It is found that the changing trend of the pressure predicted

with HRM is similar to that with HEM. For the location P10 close to the open end, a slightly lower plateau is found in the pressure predicted by HRM before 200ms and the pressure of plateau slowly decreases as the decompression continues. A better agreement is reached for the prediction of pressure using HRM at P10 after 400ms. For the locations P13, P19, P22, P25 on the middle part of the shock tube, the pressure-time traces predicted by both approaches show nearly the same results. For the locations P28 and P31 close to the closed end, the agreement of predictions using HRM is worse than that using HEM against the experimental data.

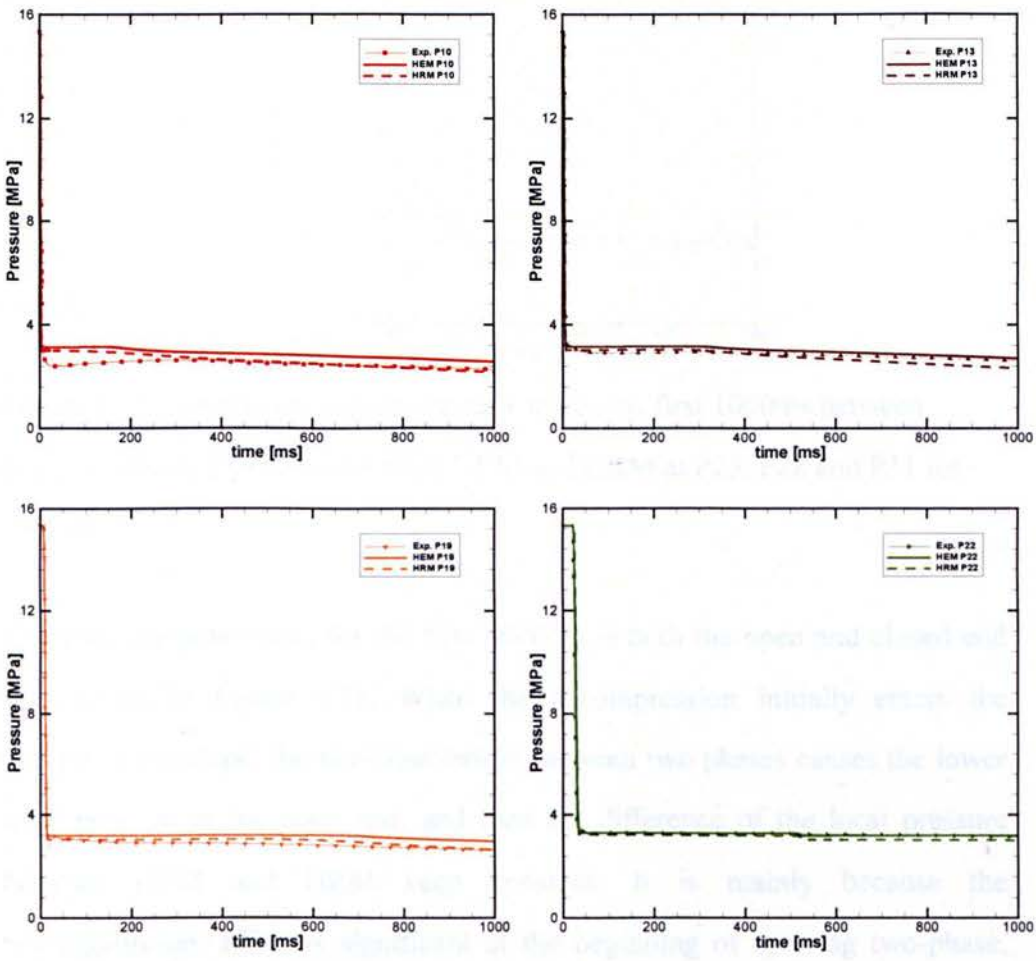

Figure 6.26 Comparison of pressure-time traces for first 1000ms between measurement and predictions using HEM and HRM at P10, P13, P19 and P22 for Test 19.

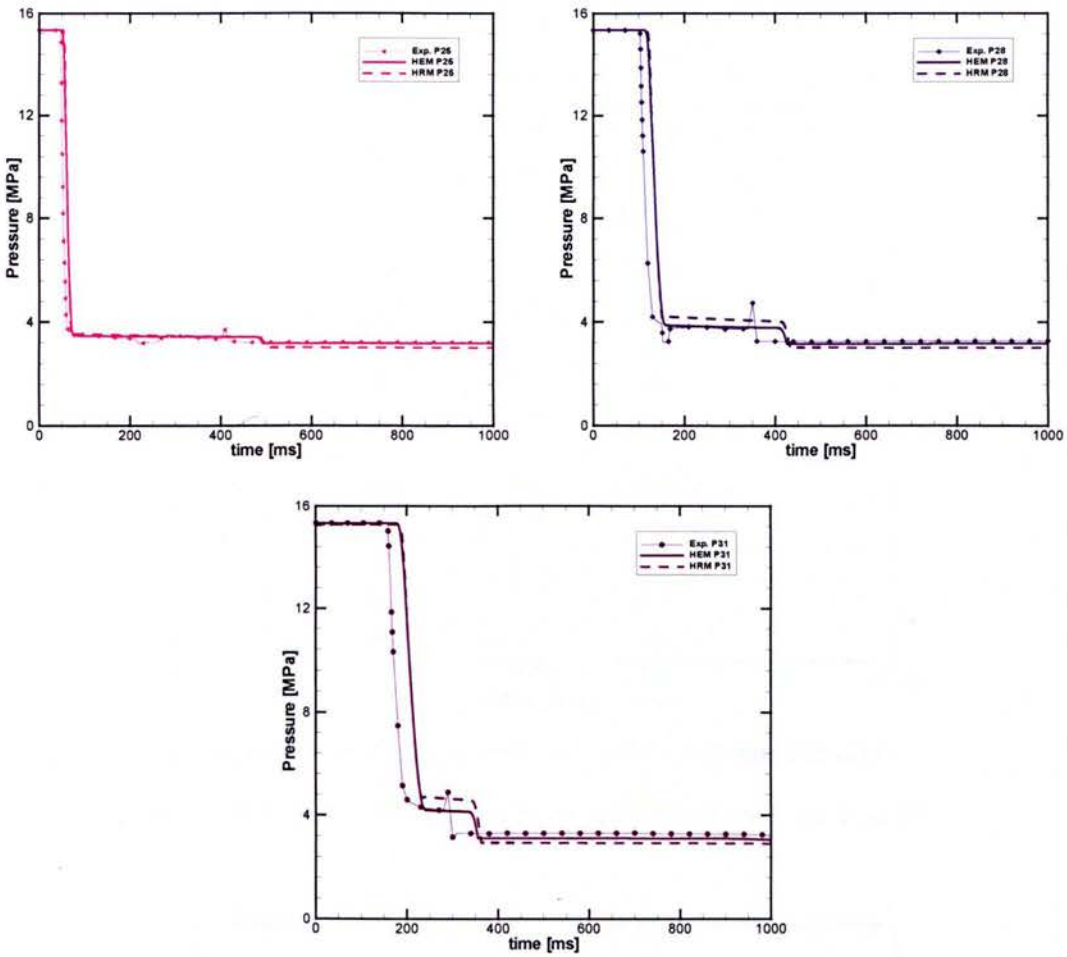

Figure 6.27 Comparison of pressure-time traces for first 1000ms between measurement and predictions using HEM and HRM at P25, P28 and P31 for Test 19.

The pressure-time traces for the first 3000ms at both the open and closed end are present in Figure 6.28. When the decompression initially enters the two-phase envelope, the non-equilibrium between two phases causes the lower local pressure at the open end, and then the difference of the local pressure between HEM and HRM keep constant. It is mainly because the non-equilibrium effect is significant at the beginning of entering two-phase. However, at the closed end, the non-equilibrium effect is not obvious except the moment when the decompression enters the two-phase envelope.

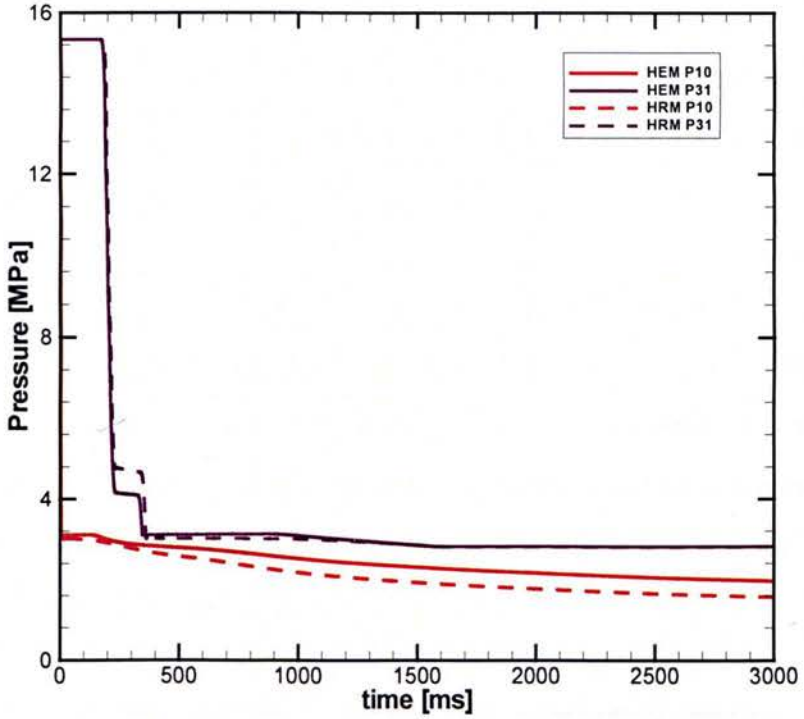

Figure 6.28 Comparison of pressure-time at the first 3000ms between predictions with HEM and HRM at the open and closed ends for Test 19.

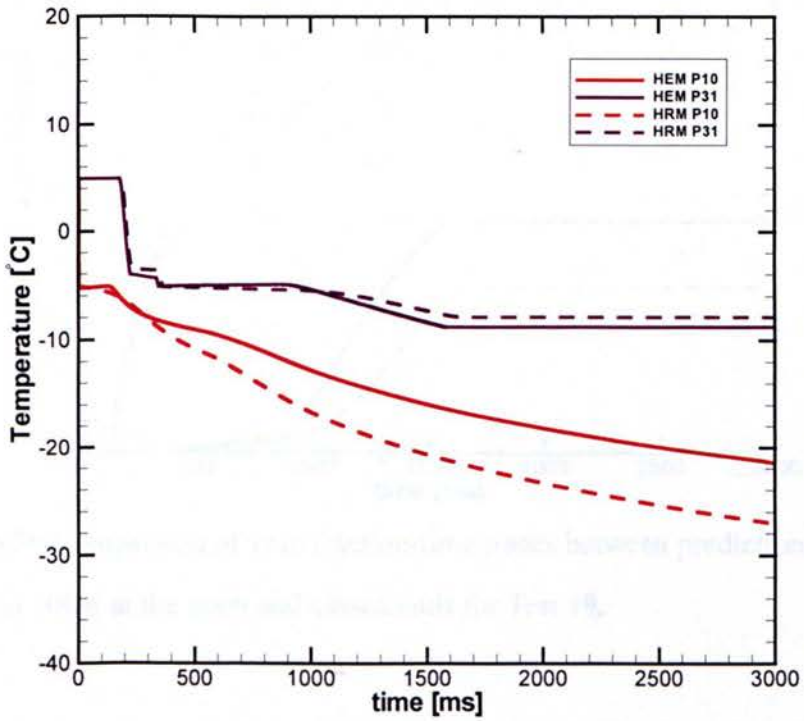

Figure 6.29 Comparison of temperature-time traces between predictions with HEM and HRM at the open and closed ends for Test 19.

Figure 6.29 shows a comparison of temperature-time traces between the predictions using HEM and HRM. The effect of non-equilibrium on the local temperature is similar to the pressure. Non-equilibrium effect is significant particularly at the open end.

Additionally, the void fraction-time traces at the open and closed ends are presented in Figure 6.30. The void friction predicted using HRM is larger than the result of HEM. It is because the lower pressure and temperature correspond to the larger void fraction at the open end. While the effect of non-equilibrium is opposite at the closed end, and this is owing to the slightly higher temperature under the almost same pressure.

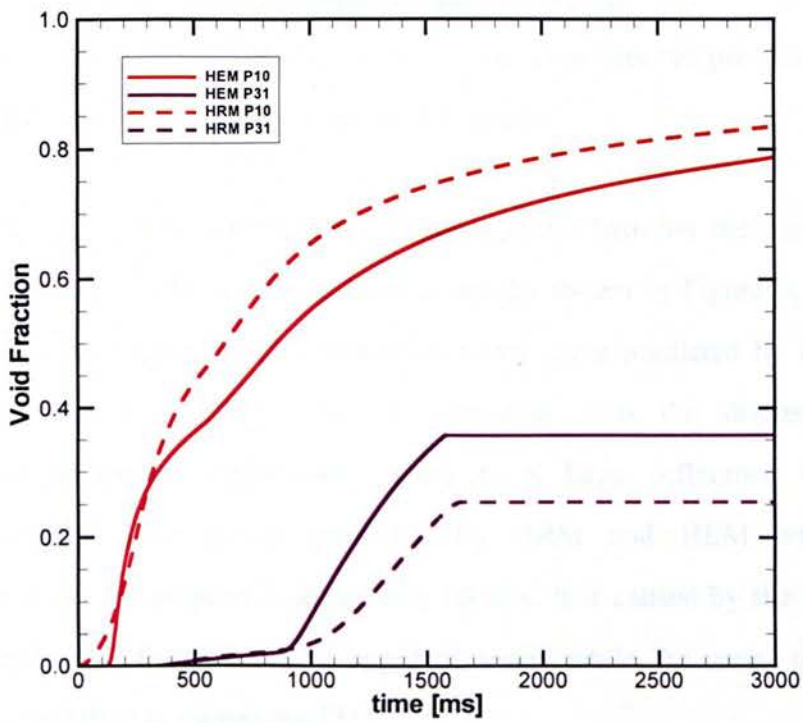

Figure 6.30 Comparison of void fraction-time traces between predictions with HEM and HRM at the open and closed ends for Test 19.

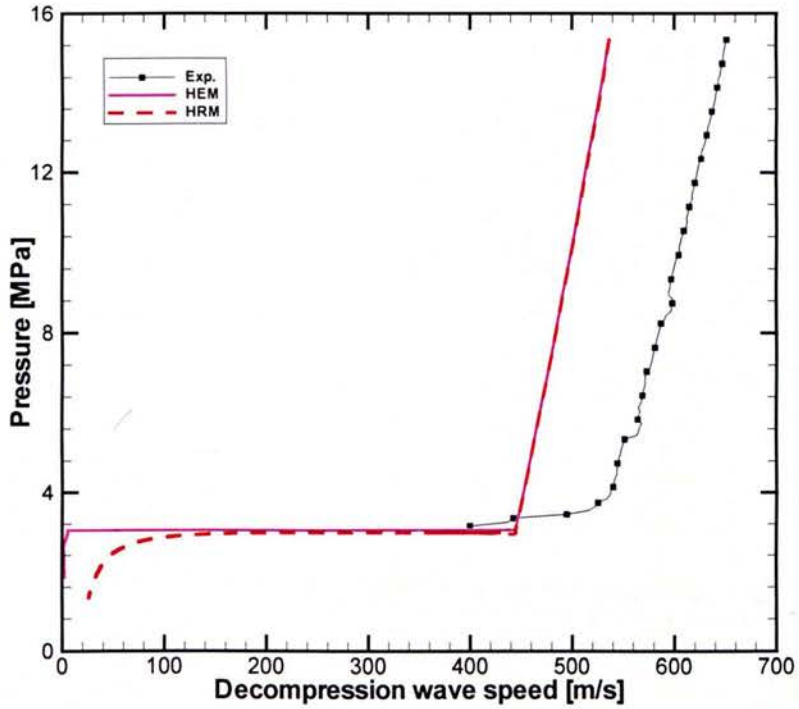

Figure 6.31 Comparison of decompression wave curve between predictions using HEM and HRM and measurement for Test 19.

The comparison of the decompression wave curve between the predictions using HEM and HRM and the measurement are shown in Figure 6.31. It is clearly that the plateau of decompression wave curve predicted by HRM is slightly lower than HEM. This is consistent with the discussion of pressure-time traces. Additionally, there is a large difference between decompression wave curves predicted by HRM and HEM when the decompression wave speed is lower than 100m/s. It is caused by the fact that HEM predicts a discontinuity of speed of sound while the speed of sound predicted by HRM is continuous [31].

6.4.2. Dense CO_2-rich Mixture

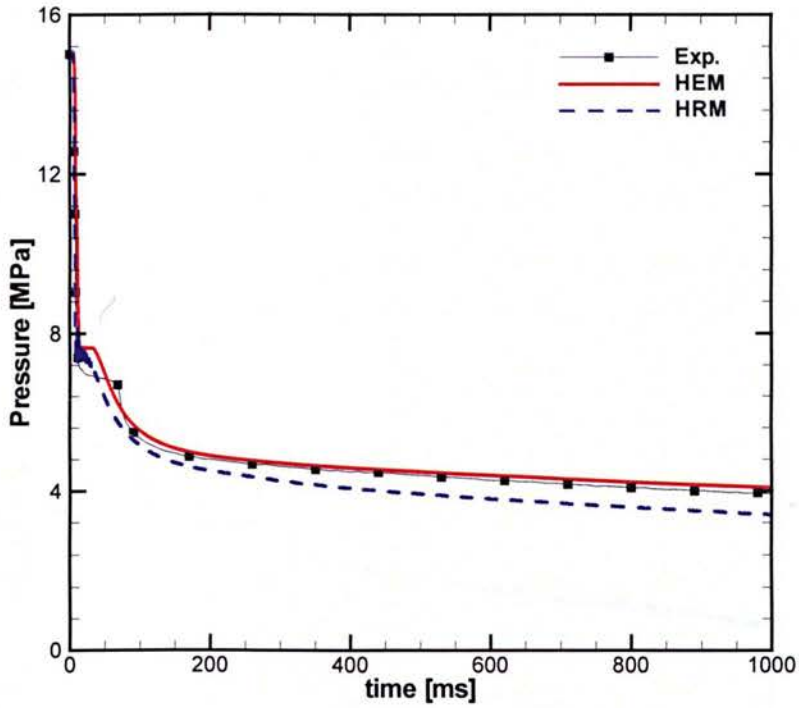

Figure 6.32 Comparison of pressure-time traces at P15 between predictions with HRM and HEM and measurement for Test 31.

Figure 6.32 displays the comparison of pressure-time traces at P15 between prediction with HRM and HEM and measurement. It is seen that the result of dense CO_2-rich mixture test is similar to the pure CO_2 test. The prediction at P15 with HRM agrees reasonably well with the experimental data. At the initial stage of entering the two-phase envelope, the pressure plateau predicted by HRM is lower than HEM.

Pressure-time and temperature-time traces predicted by HEM and HRM for Test 31 are shown in Figure 6.33 and Figure 6.34, respectively. The predictions at both the open and closed end are presented here. It is seen that the non-equilibrium phenomena causes the same effect on flow parameters as the dense pure test. The effect of non-equilibrium at the open end is larger than that at the closed end. Comparing with the results predicted by HEM, the

decompression rate is larger, and the decrease of temperature is more rapid. At the closed end, the pressure predicted by HRM is slightly lower than HEM at the initial decompression stage, then the difference decrease after 1000ms, and the plateaus at pressure-time and temperature-time traces are lower than HEM.

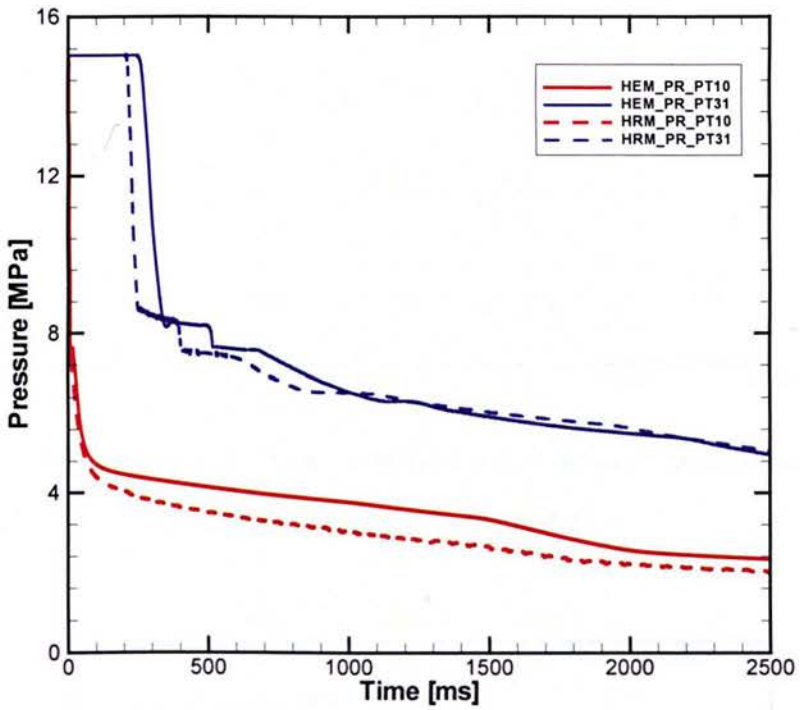

Figure 6.33 Comparison of pressure-time traces between predictions with HEM and HRM at the open and closed ends for Test 31.

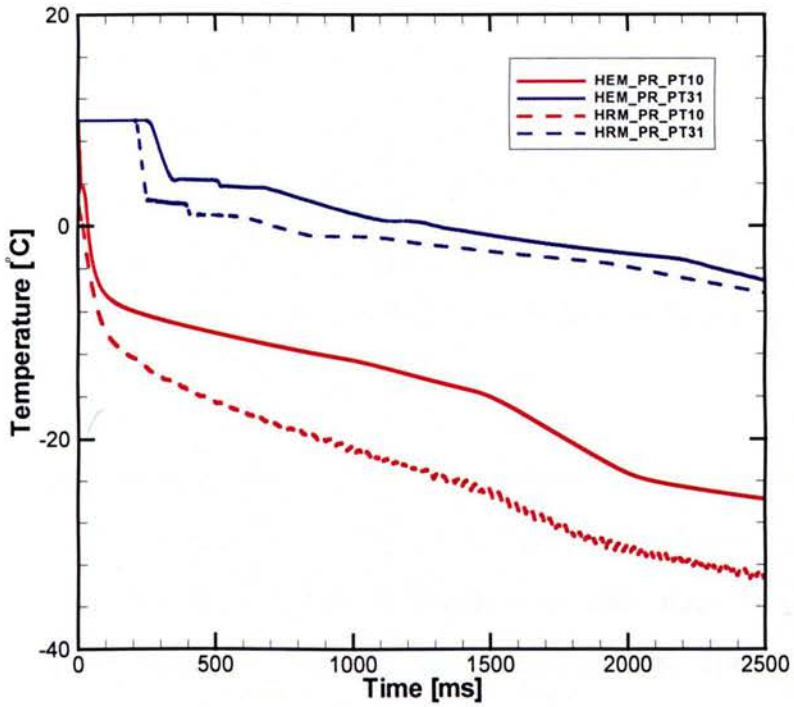

Figure 6.34 Comparison of temperature-time traces between predictions with HEM and HRM at the open and closed ends for Test 31.

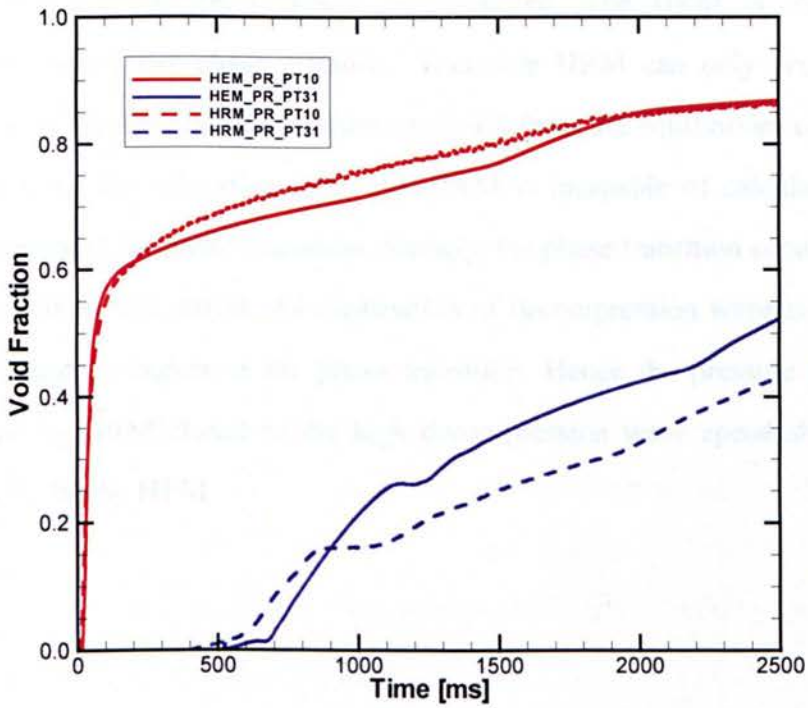

Figure 6.35 Comparison of void fraction-time traces between predictions with HEM and HRM at the open and closed ends for Test 31.

Figure 6.35 shows a comparison of void fraction-time traces between prediction with HEM and HRM at open and closed ends for Test 31. It is seen that the difference at the open end is smaller than that at the close end. This is owing to the fact that solution of HRM for mixture is totally different with pure fluid. On the pressure-temperature diagram, the two phase envelope of mixture covers a wide region, while only one single line (saturation line) is present for pure fluid.

The decompression wave curves predicted with HEM and HRM are displayed in Figure 6.36. The pressure plateau predicted with HRM is lower than HEM. This is consistent with the effect on the pressure-time trace. There is in reasonable good agreement between the prediction with HRM and the measurement. It is seen that the prediction from HRM may be not better than that from HEM, even the results show the pressure plateaus predicted by HRM get worse. This is inconsistent with the expectation which the decompression curve predicted by HRM should be improved. The HRM is inherently conducted under two-phase mixtures. Therefore HRM can only predict the deviation of local two-phase mixture condition from the equilibrium condition by employing the relaxation time. But HRM is incapable of calculating the actual threshold for phase transition. Namely, the phase transition occurs at the same condition with HEM. As explanation of decompression wave curve, the pressure plateau occurs at the phase transition. Hence the pressure plateaus predicted by HRM closed to the high decompression wave speed should be same with that by HEM.

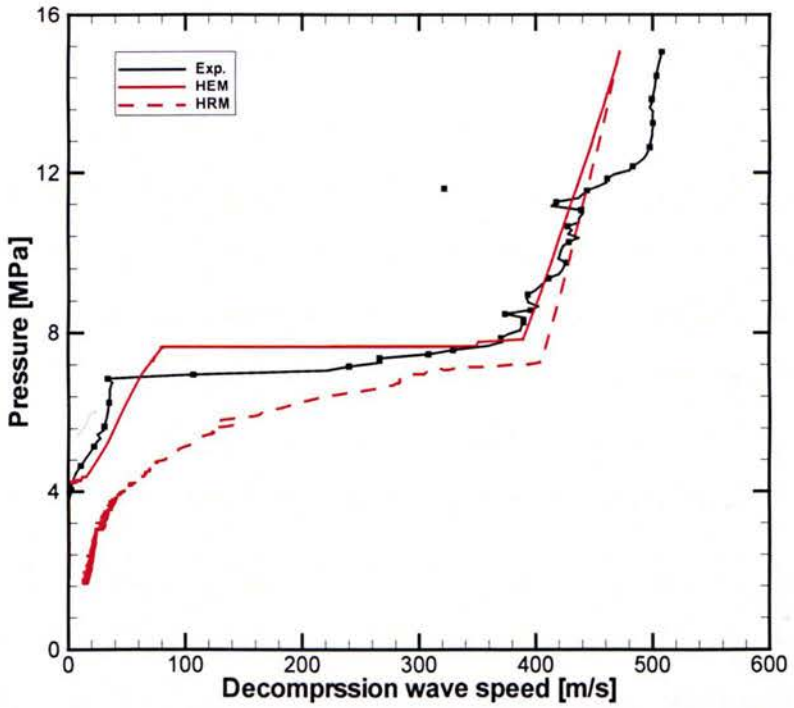

Figure 6.36 Comparison of decompression wave curve between predictions using HEM and HRM and measurement for Test 31.

6.4.3. Summary

Non-equilibrium effects on pure dense CO_2 and dense CO_2-rich mixture are examined by employing HRM. Two dense phase tests were predicted with HRM. Comparisons of flow parameters between predictions with HEM and HRM and measurement were carried out. The results showed that the non-equilibrium effect on the decompression rate is obvious at the open end. The predicted decay of pressure and temperature is slightly quicker than HEM at the open end. At the closed end, the effect of non-equilibrium is smaller as there is more time for the mixture to reach equilibrium. Additionally, the inclusion of the non-equilibrium effect results in a lower pressure plateau on the predicted decompression wave curve.

6.5. Concluding Remarks

Several CO_2 shock tube tests with dense phase pure CO_2 and CO_2-rich mixture were predicted using current model with HEM assumption. The predicted pressure-time traces and decompression wave curves were compared with the currently available experimental data. The decompression behaviours of dense CO_2 were investigated. The effect of impurities on the decompression behaviours was examined. Additionally, the effects of friction and heat transfer were also assessed for the dense tests. Finally, the non-equilibrium effect on the decompression behaviour was also evaluated.

Fourteen dense CO_2 tests were investigated using current model with HEM assumption to compare the experimental data. Totally, the predictions of decompression wave curves were in reasonably good agreement with the experimental data. Likewise, the predicted pressure plateaus are consistently higher than the measurements. The prediction of pressure-time traces agrees well with the experimental data. More detailed findings from the dense phase CO_2 study are summarized as below:

- For dense phase CO_2 decompression, the speed of sound is accurately predicted by the SW EOS and significantly under-predicted by PR and PRSV EOSs. The saturation pressure is also slightly under-predicted by PR and PRSV EOSs.

- The plateau on the decompression curve is also deserved. Likewise, it results from the discontinuity in the speed of sound across the phase boundary and the continuity in the escaping velocity. The width of plateau is larger than the gaseous case. The speed of sound of two-phase mixture is less than one tenth of that of dense phase during crossing the phase boundary.

- For dense phase CO_2 decompression, the decompression process is nearly isenthalpic at the early stages. During the late stage of the decompression, appreciable increases in enthalpy are observed due to wall heat transfer. An isentropic decompression process can be assumed for the early stage and slight increase in entropy is only observed during the later stage.

- Likewise, the fast decompression rate is predicted and the decompression wave is reflected back towards to the open end. Then the further decompression behind the reflected wave causes the occurrence of phase transition at the close end. And a fast growing void fraction at the closed end is caused.

- After the initial decompression caused by the decompression wave, the compressed CO_2 quickly depressurizes to a value above the saturation pressure (dense Test 19) due to the influence of friction which becomes relatively more profound with the increase of the initial pressure.

- For the dense phase cases, at least one or two plateaus exist for the pressure-time traces at all the monitoring points. The first plateau is caused by the decompression wave at a pressure higher than the saturation pressure (no phase transition) due to the wall friction. Upon the arrival of the deflected wave, the pressure drops to the second plateau from which phase transition starts to happen.

- For dense phase CO_2 decompression, increasing initial pressure will decrease the pressure of plateau at the decompression wave curve, and increasing initial temperature will increase the pressure of plateau at the decompression wave curve. The existence of impurities results in the obvious increase of the pressure plateau.

- The decompression wave curves predicted with GERG-2004 for dense phase CO_2-rich mixture did not always show better agreement than these predicted with PRSV EOS.
- The location of initial condition is close to the saturated line enhances the effect of non-equilibrium.
- Although pressure drops sharply behind the decompression wave, temperature only drops slightly for the dense phase release.
- The outer wall temperature also significantly lags behind the fluid temperature.

Secondly, the effects of friction and heat transfer were also investigated for the dense cases. Likewise, no significant influence on the pressure plateau of the decompression wave curve was observed. However, there is an obvious effect at the "tail" region of decompression wave curve and heat transfer and wall friction also produce the increase of decompression wave speed at the "tail" region. It was also found that heat transfer plays important role only during the later stage of the decompression. Compared with the gaseous CO_2 decompression, the larger effect of wall fraction is also observed at the location close to the open end. Totally, the effect of friction on dense phase decompression is smaller than the gaseous case due that the escaping velocity and the friction force are small.

Additionally, the comparison between prediction with 1D and 2D meshes was made. It was concluded that the 1D assumption is well reasonable for predicting the decompression flow inside the pipeline.

Finally, the non-equilibrium effect was examined for dense pure CO_2 and CO_2-rich mixture by employing the approach of HRM. Comparison between the predictions using HEM and HRM were carried out. When the

decompression initially enters the two-phase envelope, the non-equilibrium between two phases causes the lower local pressure at the open end. It was found that the non-equilibrium effect on the decompression rate is obvious at the open end. The decreasing of pressure and temperature is slightly quicker than HEM. At the closed end, the effect of non-equilibrium is smaller due to the enough time for equilibrium. Additionally, the non-equilibrium result in a lower pressure plateau on decompression wave curve.

Chapter 7 Conclusions and Suggestions for Future Work

7.1. Conclusions

The transient two-phase flow during the decompression of high pressure pipeline containing gaseous and dense CO_2 has been modelled theoretically and solved numerically. The main thrust of the study involved the development of modelling based on the CFD technique and the two-phase flow methods (Homogeneous Equilibrium Model and Homogeneous Relaxation Model) to simulate the two-phase flow for the high pressure pipeline decompression.

In the Chapter 2, the two-phase flow models were presented by employing a fully compressible flow solver which renders it to be more suitable for modelling the characteristics of fast transient decompression flow following the pressurized pipeline rupture. Firstly, the Homogeneous Equilibrium Model was described. The one-dimensional flow was assumed for the pipeline decompression flow. In the HEM approach, the two-phase mixture was treated as a pseudo-fluid, which can be handled as a single-phase flow and described by the conservation equations for single-phase flow. Additionally, HRM approach was also presented to account for the non-equilibrium effect. An analytical relaxation method was incorporated to represent the non-equilibrium mass transfer source by a simple linear approximation of the rate of quality change. Additionally, the thermodynamic properties of two-phase fluid were examined with the equation of state such as PR, PRSV, SW EOSs and GERG-2004. Finally, the boundary conditions were specified for pipeline decompression flow. Wall friction and heat transfer were carefully involved to take into account of the non-isentropic flow. The heat transfer between fluid

and pipeline wall were evaluated by a conjugate wall heat transfer model in which a separate heat transfer problem was simultaneously solved with the flow solver.

In the Chapter 3, Arbitrary Lagrangian-Eulerian method was employed to discretize the conservation equations. The solutions of these difference equations were performed in the Lagrangian and Eulerian phase respectively. In the Lagrangian phase, the source terms and diffusion terms of conservation equations were solved, and the iterative solution procedure was executed to solve the Lagrangian phase pressure. With the predicted results from the Lagrangian phase, the convective terms were calculated in the Eulerian phase. In addition, a quasi-second-order upwind scheme calculating the quantities on the cell face was applied here.

The proposed two-phase model was extensively validated against the available experimental data. The experiments cover a wide range which is from the conventional gas, rich gas to LPG, as well as dense phase CO_2. The predictions of decompression wave curve are similar to the predictions by the model DECAY, Exxon and GASDECOM. The similarity of the predictions is partly due to the fact that the homogeneous equilibrium assumption was adopted in all the models. The homogeneous equilibrium assumption and the employment of EOS are two significant factors to impact the accuracy of model for predicting the decompression wave curve. On the whole the predictions of decompression wave curve are in reasonably good agreement with the experimental data. Furthermore, the comparison was also made for the flow parameters such as pressure and temperature between the prediction and experimental data using British Gas shock tube experiments, Botros cases and Isle of Grain full-scale experiments. These cases include the fast decompressions as well as slow blowdown of a pipeline. The predictions of flow parameters such as temperature and pressure are in reasonably good agreement with the

measurements. The predicted pressure and temperature-time traces show better agreement than the predictions with DECAY and OLGA. The propagation speed of the fast moving decompression wave and the reflected wave were accurately predicted. In summary, the current model was verified to be capable to predict fast pipeline decompression as well as slow Blowdown of pipeline, and it can be employed for the decompression flow of high pressure CO_2 shock tube.

In the Chapter 5 and Chapter 6, several CO_2 shock tube tests with gaseous and dense phase pure CO_2 and CO_2-rich mixture were calculated using current model with HEM assumption to study the decompression of CO_2 shock tube. Predictions of pressure-time traces and decompression wave curves were compared with the currently available experimental data, and the results showed that there is in reasonably good agreement. The decompression of gaseous and dense CO_2 shock tube test was discussed in more detail.

For gaseous CO_2 decompression, as the decompression wave reaches the measurement points, the compressed CO_2 quickly depressurizes to the saturation pressure and its decompression rate decreases with increasing distance to the open end. The volume fraction of droplet at the closed end quickly increases and then turns around and mildly decreases. The changing trend of the local temperature follows that of pressure. The increases in the temperature were observed at the locations close to the open end due to wall heat transfer. The reflected wave was clearly predicted by current model. Additionally, the plateau of the decompression wave curve increases with an increase in the initial pressure and decreases with an increase in the initial temperature. The existence of impurities results in the decrease of the pressure plateau for gaseous CO_2. The decompression behaviour of gaseous CO_2 is similar to that of rich gas, while the plateau is shorter in the decompression curve for the gaseous CO_2.

For dense CO_2 decompression, it is similar to the gaseous test. The compressed CO_2 quickly depressurizes to a value above the saturation pressure, and then quickly drops to the saturation pressure, and finally the pressure decrease mildly. At the locations close to the open end, the void fraction rapidly increases when the decompression wave reach the monitoring points, and then mildly increases. At the locations close to the closed end, the void fraction increases and then keeps constant for a while, and continues to increase. Although pressure drops sharply behind the decompression wave, temperature only drops slightly for the dense phase release. The increasing initial pressure will decrease the pressure of plateau at the decompression wave curve, and increasing initial temperature will increase the pressure of plateau at the decompression wave curve. The existence of impurities results in the obvious increase of the pressure plateau.

Different equations of state were employed, such as PR, PRSV, SW EOSs and GERG-2004. SW EOS predicted the most accurate thermodynamic properties but only for pure CO_2. PRSV EOS was found to give a slightly more accurate prediction of the plateau pressure for gaseous phase CO_2. The predictions for gaseous phase CO_2 decompression were found to be less sensitive to the choice of EOS than that for the dense phase CO_2. For dense phase CO_2-rich mixture, the decompression wave curves predicted with GERG-2004 did not always show better agreement than these predicted with PRSV EOS. It is stated that the accurate equation of state is required for the dense phase CO_2-rich mixture.

Moreover, the effects of the wall friction and heat transfer on the decompression behaviours were examined for the gaseous and dense CO_2 tests. It was found that the heat transfer and wall friction do not have a significant influence on the pressure plateau of the decompression wave curve. However, there is a significant effect at the "tail" region of the decompression wave curves, particularly for the gaseous phase CO_2, and heat transfer and wall

friction produced the increase of decompression wave speed at the "tail" region. The effect of the wall friction was consistent with the study of Mahgerefteh et al [155]. The wall heat transfer plays an important role only during the later stage of the decompression. The effects of the wall heat transfer were more pronounced for gaseous CO_2 decompression in comparison with the dense phase tests due to the higher escaping velocity and the lower density.

Additionally, the comparison between prediction with 1D and 2D meshes was made. It was concluded that the 1D assumption is well reasonable for predicting the decompression flow inside the pipeline.

Finally, the non-equilibrium effect was examined for dense pure CO_2 and CO_2-rich mixture by employing the approach of HRM. The comparison between the predictions using HEM and HRM were carried out. When the decompression initially enters the two-phase envelope, the non-equilibrium between two phases causes the lower local pressure at the open end. It was found that the non-equilibrium effect on the decompression rate is obvious at the open end. The decreasing of pressure and temperature is slightly quicker than HEM. At the closed end, the effect of non-equilibrium is smaller due to the enough time for equilibrium, while there are large differences of flow parameters due to the accumulative effect of upstream. Additionally, the non-equilibrium results in a lower pressure plateau on the decompression wave curve.

Finally, the main contributions of current study are emphasized as follows:

1) The pipeline decompression model was developed with incorporating the EOSs to calculate the real fluid thermodynamic properties. It was widely validated using the available experimental data. Conclusively, it is suitable for fast decompression as well as slow blowdown.

2) The model employed the HEM and HRM to treat two-phase flow, and the HRM was extended to be capable to handle the relaxation for the mixture fluid.

3) Numerical method adopted the ALE method to discretize and solve the governing equations by dividing the solution procedure into two phases: Lagrangian phase and Eulerian phase. The calculation not only significantly simplifies the solution procedure but also improves the computational efficiency.

4) The validated model was employed to study the decompression behaviours of the high pressure gaseous and dense CO_2 pipelines. The key findings were presented to better understand the decompression characteristics. These are significant information for fracture control in the pipeline design and operation.

7.2. Suggestions for Future Work

Tuning of the constants in HRM

The mass transfer source term is determined from the analytical approach by employing the relaxation time to take into account of the non-equilibrium effect. The empirical correlation of relaxation time was proposed by Downar-Zapolsk et al. [31] based on water flashing. In order to adopt the correction for CO_2, the constant was corrected based on the study of Angielczyk et al [100] on CO_2 through converging–diverging nozzles for the ejector refrigeration cycle.

Therefore, the constants in the correlation of relaxation time are required to be tuned when the experimental data become available for the pipeline decompression of dense phase CO_2 and CO_2 mixture. The current framework allows for tuning of these constants when such data becomes available.

Transient flow in pipeline networks

The present work is limited to a simple pipeline without branching links. Nevertheless, it is possible to extend the current model and numerical method to more complicated establishment such as pipeline networks.

Incorporation of heterogeneous non-equilibrium

Despite the success of the CFD based model for predicting the decompression flow of high pressure pipelines, the technique is based on a homogeneous equilibrium model and homogeneous relaxation model. Both models assume that the constituent phases are in mechanical equilibrium. HRM takes account of the thermal non-equilibrium with the empirical correction. In practice, when the release happen from a small puncture for flashing liquids, the thermal and mechanical non-equilibrium will deteriorate the homogeneous equilibrium assumption.

A heterogeneous equilibrium model describing the separate conservation equations to each phase and accounting for phase change between two phases is expected to address the above limitation.

Reference

[1] J. O. Kadnar, *Experience in CO2 transportation via pipeline, in CCS Web Conference on CO2 Transport, Health and Safety Issues*. Paris: Internation Energy Agency, 2008.

[2] G. Koeijer, J. H. Borch, J. Jakobsen, and A. Hafner, "Construction of a CO2 pipeline test rig for R&D and operator training," in *Transmission of CO2, H2 and biogas: exploring new uses for natural gas pipelines conference, organized by Global pipeline Monthly and Clarion Technical Conferences, Amsterdam, Netherlands, May*, 2007.

[3] A. Zhao, "The Challenges of Carbon Capture and Storage (CCS) Development in China," *Int. J. Appl. Logist.*, vol. 3, no. 3, pp. 15–21, 2012.

[4] D. McDonald, M. Estopinal, and H. Mualim, "FutureGen 2.0: Where Are We Now?," in *Clearwater Clean Coal Conference Clearwater, Florida, U.S.A. June 3-7*, 2012.

[5] A. Hatta, R. Kuivalainen, T. Eriksson, M. Lupoin, V. Cortes, A. S.-B. Sacristan, J. M. Jubitero, and J. c. Ballesteros, "Development and demonstration of oxy-fuel CFB technology," *Joural South. African Inst. Min. Metall.*, vol. 112, pp. 431–436, 2012.

[6] X. Lai, Z. Ye, Z. Xu, M. Husar Holmes, and W. Henry Lambright, "Carbon capture and sequestration (CCS) technological innovation system in China: Structure, function evaluation and policy implication," *Energy Policy*, vol. 50, pp. 635–646, Nov. 2012.

[7] A. Cosham and R. Eiber, "Fracture control in carbon dioxide pipelines," *J. Pipeline Eng.*, vol. 6, pp. 147–158, 2007.

[8] J. Barrie, K. Brown, P. Hatcher, and H. Schellhase, "Carbon Dioxide Pipelines. A Preliminary review of design and risks," in *International Conference on Greenhouse Gas Technologies, volume 1, Vancouver, Canada. IEA Greenhouse Gas Programme, Cheltenham, UK*, 2004, pp. 315–320.

[9] B. N. Leis, X. K. Zhu, T. P. Forte, and E. B. Clark, "Modeling running fracture in pipelines-past, present, and plausible future directions," in *11th International conference on fracture. Turin, Italy.*, 2005.

[10] R. Doctor, A. Palmer, D. Coleman, J. Davison, C. Hendriks, O. Kaarstad, M. Ozaki, M. Austell, R. Pichs-Madruga, and S. Timashev, "Transport of CO2," in *IPCC Special Report on Carbon dioxide Capture and Storage*, 2005.

[11] J. Race, P. Seevam, and M. Downie, "Challenges for offshore transport of anthropogenic carbon dioxide," in *International Conference on Offshore Mechanics and Arctic Engineering*, 2007, pp. 1–14.

[12] W. A. Waxey, "Fracture initiation, propagation and arrest," in *Proceedings of the 5th symposium in Line Pressure Research. Houston*, 1974.

[13] A. Cosham, R. J. Eiber, and E. B. Clark, "GASDECOM: CARBON DIOXIDE AND OTHER COMPONENTS," in *Proceedings of the 8th International Pipeline Conference*, 2010, pp. 1–18.

[14] H. Mahgerefteh, S. Brown, and G. Denton, "Modelling the impact of stream impurities on ductile fractures in CO2 pipelines," *Chem. Eng. Sci.*, vol. 74, pp. 200–210, May 2012.

[15] GASDECOM, "Computer Code for the Calculation of Gas Decompression in 'Fracture Control Technology for Natural Gas Pipelines'," *R.Eiber, T.Bubenik W.A. Maxey, NG-18 Rep. 208, Am. Gas Assoc. Cat. N0. L51691*, 1993.

[16] E. Burlutskiy, "Numerical Analysis on Rapid Decompression in Conventional Dry Gases using One- Dimensional Mathematical Modeling," *World Acad. Sci. Eng. Technol.*, vol. 63, pp. 287–291, 2012.

[17] A. Haque, S. Richardson, G. Saville, and G. Chamberlain, "Rapid depressurization of pressure vessels," *J. loss Prev. Process Ind.*, vol. 3, no. 1, pp. 4–7, 1990.

[18] F. Eldevik, B. Graver, L. E. Torbergsen, and O. T. Saugerud, "Development of a Guideline for Safe, Reliable and Cost Efficient Transmission of CO2 in Pipelines," *Energy Procedia*, vol. 1, no. 1, pp. 1579–1585, Feb. 2009.

[19] F. Eldevik, "Safe Pipeline Transmission of CO2," *Pipeline Gas J.*, vol. 235, no. 11, pp. 76–77, 2008.

[20] G. B. Wallis, "One-dimensional two-phase flow," *J. Fluid Mech.*, vol. 42, no. 2, pp. 428–432, 1970.

[21] K. K. Botros, W. M. Jungowski, and M. H. Weiss, "Models and methods of simulating gas pipeline Blowdown," *Can. J. Chem. Eng.*, vol. 67, no. 4, pp. 529–539, 1989.

[22] T. K. Groves, P. R. Bishnoi, and J. M. E. Wallbridge, "Decompression wave velocities in natural gases in pipe lines," *Can. J. Chem. Eng.*, vol. 56, no. 6, pp. 664–668, Dec. 1978.

[23] G. G. King, "Decompression of Gas Pipelines During Longitudinal Ductile Fractures," *J. Energy Resour. Technol.*, vol. 101, no. 1, pp. 66–73, 1979.

[24] A. Vaish, N. Verma, and R. Chhabra, "Transient analysis of two-phase flow during blowdown of a pipeline carrying flashing liquids," *J. Chem. Eng. Japan*, vol. 35, no. 10, pp. 982–995, 2002.

[25] Y. V. Fairuzov, "Blowdown of pipelines carrying flashing liquids," *AIChE J.*, vol. 44, no. 2, pp. 245–254, Feb. 1998.

[26] H. Mahgerefteh, P. Saha, and I. Economou, "A study of the dynamic response of emergency shutdown valves following full bore rupture of gas pipelines," *Process Saf. Environ. Prot.*, vol. 75, no. 4, pp. 201–209, 1997.

[27] H. Mahgerefteh, P. Saha, and I. G. Economou, "Modeling fluid phase transition effects on dynamic behavior of ESDV," *AIChE J.*, vol. 46, no. 5, pp. 997–1006, May 2000.

[28] J. R. Chen, S. M. Richardson, and G. Saville, "Modelling of two-phase blowdown from pipelines—I. A hyperbolic model based on variational principles," *Chem. Eng. Sci.*, vol. 50, no. 4, pp. 695–713, Feb. 1995.

[29] J. Chen, S. Richardson, and G. Saville, "Modelling of two-phase blowdown from pipelines--II. A simplified numerical method for multi-component mixtures," *Chem. Eng. Sci.*, vol. 50, no. 13, pp. 2173–2187, 1995.

[30] K. H. Bendiksen, D. Maines, R. Moe, and S. Nuland, "The dynamic two-fluid model OLGA: Theory and application," *SPE Prod. Eng.*, vol. 6, no. 2, pp. 171–180, 1991.

[31] P. Downar-Zapolski, Z. Bilicki, L. Bolle, and J, "The non-equilibrium relaxation model for one-dimensional flashing liquid flow," *J. Multiph. Flow*, vol. 22, no. 3, pp. 473–483, 1996.

[32] V. H. Ransom, R. J. Wagner, J. A. Trapp, K. E. Carlson, D. M. Kiser, H. H. Kuo, H. Chow, R. A. Nelson, and S. W. James, "RELAP5/MOD1 code manual volume 1: System models and numerical methods," *NUREG/CR-1826-V1, EGG-2070*, 1982.

[33] G. Wallis, "Critical two-phase flow," *Int. J. Multiph. Flow*, vol. 6, no. 1–2, pp. 97–112, Feb. 1980.

[34] M. Ishii and T. Hibiki, *Thermo-fluid dynamics of two-phase flow*, 2nd ed. Springer, 2011.

[35] H. Mahgerefteh, P. Saha, and I. G. Economou, "Fast numerical simulation for full bore rupture of pressurized pipelines," *AIChE J.*, vol. 45, no. 6, pp. 1191–1201, Jun. 1999.

[36] R. E. Henry and H. K. Fauske, "The Two-Phase Critical Flow of One-Component Mixtures in Nozzles, Orifices, and Short Tubes," *J. Heat Transfer*, vol. 93, no. 2, pp. 179–187, 1971.

[37] H. Fauske, "Contribution to the theory of two-phase, one-component critical flow," 1962.

[38] H. Fauske, "Two-phase critical flow with application to liquid metal systems," *ANL-6779*, 1963.

[39] F. J. Moody, "Maximum Flow Rate of a Single Component, Two-Phase Mixture," *J. Heat Transfer*, vol. 87, no. 1, p. 134, 1965.

[40] G. B. Wallis and H. J. Richter, "Isentropic streamtube model for flashing two-phase vapor-liquid flow," *J. Heat Transf.*, vol. 100, no. 4, pp. 595–600, 1978.

[41] H. C. Simpson and R. S. Silver, "Theory of one-dimensional, two-phase homogeneous non-equilibrium flow," in *Proc. I. Mech. Engr. Syrup. on Two-Phase Flow*, 1962, pp. 45–56.

[42] P. G. Kroeger, "Application of a non-equilibrium drift flux model to two-phase blowdown experiments," in *Proc. of the CSNI Specialists Meeting on transient two-phase flow, Atomic Energy of Canada*, 1976, pp. 112–152.

[43] E. G. BAUER, G. R. HOUDAYER, and H. M. SUREAU, "A non-equilibrium axial flow model and application to loss-of-accident analysis," in *Proc. CSNI Specialists Meeting on transient two-phase flow, Atomic Energy of Canada*, 1976, pp. 429–457.

[44] Z. Bilicki and J. Kestin, "Physical aspects of the relaxation model in two-phase flow," *Proc. R. Soc. London. A. Math. Phys. Sci.*, vol. 428, no. 1875, pp. 379–397, 1990.

[45] M. Réocreux, "Experimental study of steam-water choked flow," *Spec. Meet Two-Phase Flow, At. energy Canada*, vol. 2, pp. 637–669, 1976.

[46] M. Réocreux, "Contribution to the study of critical flow rates in two-phase water-vapor flow," Universite Scientifique et Medicale de Grenoble, 1974.

[47] K. H. Ardron and M. C. Ackerman, "Studies of the critical flow of subcooled water in a pipe," *Proc. 2nd CSNI Spec. Meet. Transient Tow-Phase Flow*, pp. 517–543, 1978.

[48] V. N. Blinkov, O. C. Jones, and B. I. Nigmatulin, "Nucleation and flashing in nozzles—2. Comparison with experiments using a five-equation model for vapor void development," *Int. J. Multiph. Flow*, vol. 19, no. 6, pp. 965–986, 1993.

[49] A. Sudi, M. Aritomi, A. Murase, and K. Iwaki, "Relaxation process of thermal non-equilibrium in boiling two-phase flow. I: Experimental results," *J. Nucl. Sci. Technol.*, vol. 31, no. 11, pp. 1171–1183, 1994.

[50] K. H. Ardron, "A two-fluid model for critical vapour-liquid flow," *Int. J. Multiph. Flow*, vol. 4, no. 3, pp. 323–337, 1978.

[51] R. Dagan, E. Elias, E. Wacholder, and S. Olek, "A two-fluid model for critical flashing flows in pipes," *Int. J. Multiph. Flow*, vol. 19, no. 1, pp. 15–25, 1993.

[52] H. K. Forster and N. Zuber, "Growth of a vapor bubble in a superheated liquid," *J. Appl. Phys.*, vol. 25, no. 4, pp. 474–478, 1954.

[53] M. Ishii, *Thermo-fluid dynamic theory of two-phase flow*. Paris: Eyrolles, 1975.

[54] B. Wendroff, "Two-Fluid Models: A Critical Survey," *Los Alamos Sci. Lab. LA-UR-79-291*, 1979.

[55] C. F. Schwellnus and M. Shoukri, "A two-fluid model for non-equilibrium two-phase critical discharge," *Can. J. Chem. Eng.*, vol. 69, no. 1, pp. 188–197, 1991.

[56] J. A. Trapp and V. H. Ransom, "A choked-flow calculation criterion for nonhomogeneous, nonequilibrium, two-phase flows," *Int. J. Multiph. Flow*, vol. 8, no. 6, pp. 669–681, Dec. 1982.

[57] S. T. Munkejord, "Analysis of the two-fluid model and the drift-flux model for numerical calculation of two-phase flow," Norwegian University of Science and Technology, 2006.

[58] F. Franca and R. Laheyjr, "The use of drift-flux techniques for the analysis of horizontal two-phase flows," *Int. J. Multiph. Flow*, vol. 18, no. 6, pp. 787–801, Nov. 1992.

[59] D. Jones and D. Gough, "Rich Gas Decompression Behavior in Pipelines," *AGA-EPRG Linepipe Res. Semin. IV, Br. GAS*, 1981.

[60] G. Soave, "Equilibrium constants from a modified Redlich-Kwong equation of state," *Chemical Engineering Science*, vol. 27, no. 6. pp. 1197–1203, Jun-1972.

[61] G. Shoup, J. J. Xiao, and J. O. Romma, "Multiphase pipeline blowdown simulation and comparison to field data," in *BHR Group Conference Series Publication*, 1998, vol. 31, pp. 3–16.

[62] K. K. Botros, J. GEERLIGS, J. ZHOU, and A. GLOVER, "Measurements of flow parameters and decompression wave speed following rupture of rich gas pipelines, and comparison with GASDECOM," *Int. J. Press. Vessel. Pip.*, vol. 84, no. 6, pp. 358–367, Jun. 2007.

[63] K. K. Botros, J. Geerligs, and R. Given, "Decompression Response of High-Pressure Natural Gas Pipelines Under Rupture or Blowdown Conditions," *Pr. PR-261-03115*, 2004.

[64] J. R. Chen, S. M. Richardson, and G. Saville, "A simplified numerical method for transient two-phase pipe flow," *Chem. Eng. Res. Des.*, vol. 71, no. 3, pp. 304–306, 1993.

[65] M. A. Haque, S. M. Richardson, and G. Saville, "Blowdown of pressure vessels-I. Computer Model," *Process Saf. Environ. Prot.*, vol. 70, no. b, pp. 5–11, 1992.

[66] S. Richardson and G. Saville, "Blowdown of LPG Pipelines," *Process Saf. Environ. Prot.*, vol. 74, no. 4, pp. 235–244, Nov. 1996.

[67] S. Richardson, "Isle of Grain pipeline depressurisation tests, HSE OTH 94441," *OFFSHORE Technol. Rep.*, 1994.

[68] H. Mahgerefteh and S. M. A. Wong, "A numerical blowdown simulation incorporating cubic equations of state," *Comput. Chem. Eng.*, vol. 23, no. 9, pp. 1309–1317, Nov. 1999.

[69] D. Y. Peng and D. B. Robinson, "A New Two-Constant Equation of State," *Ind. Eng. Chem. Fundam.*, vol. 15, no. 1, pp. 59–64, Feb. 1976.

[70] M. A. Haque, S. M. Richardson, G. Saville, G. Chamberlain, and L. Shirvill, "Blowdown of pressure vessels. II. Experimental validation of computer model and case studies," *Trans IChemE Part B Process Saf. Environ. Prot.*, vol. 70, pp. 10–17, 1992.

[71] V. H. Y. Tam and L. T. Cowley, "Consequences of pressurised LPG releases: the Isle of Grain full scale experiments," in *Proceedings of GASTECH 88, 13th International LNG/LPG Conference, Kuala Lumpur, pp.2–25.*, 1988.

[72] G. Denton, "CFD simulation of highly transient flows," University College London, 2009.

[73] H. Mahgerefteh, a Oke, and Y. Rykov, "Efficient numerical solution for highly transient flows," *Chem. Eng. Sci.*, vol. 61, no. 15, pp. 5049–5056, Aug. 2006.

[74] H. Mahgerefteh, O. Atti, and G. Denton, "An Interpolation Technique for Rapid CFD Simulation of Turbulent Two-Phase Flows," *Process Saf. Environ. Prot.*, vol. 85, no. 1, pp. 45–50, 2007.

[75] H. Mahgerefteh, a Oke, and O. Atti, "Modelling outflow following rupture in pipeline networks," *Chem. Eng. Sci.*, vol. 61, no. 6, pp. 1811–1818, Mar. 2006.

[76] A. Oke, H. Mahgerefteh, I. Economou, and Y. Rykoc, "A transient outflow model for pipeline puncture," *Chem. Eng. Sci.*, vol. 58, no. 20, pp. 4591–4604, Oct. 2003.

[77] M. J. ZUCROW and J. D. HOFFMAN, "Gas dynamics, Vol 2." John Wiley & Sons Inc, New York, 1976.

[78] S. Vahedi, "Modelling the effects of inclination and pipeline enlargement on outflow following pipeline rupture," University College London, 2003.

[79] PipeTech, "PIPELINE RUPTURE COMPUTATIONAL FLUID DYNAMICS SIMULATOR." [Online]. Available: http://www.ucl.ac.uk/~ucecm01/pipetech.htm.

[80] R. . Eiber, T. Bubenik;, and W. Maxey., "Fracture control technology for natural gas pipelines, Final Report to Line Pipe Research Supervisory Committee of the Pipeline Research Committee of the American Gas Association, Project PR-3-9113, NG-18 Report No. 208," USA, 1993.

[81] R. J. EIBER and T. A. BUBENIK, "; Fracture Control Plan Methodology, Paper 8, Eighth Symposium on Line Pipe Research, Pipeline Research Committee of the American Gas Association, Catalogue No. L51680," Houston, Texas, USA, 1993.

[82] K. H. Kumar and K. E. Starling, "The most general density-cubic equation of state: application to pure nonpolar fluids," *Ind. Eng. Chem. Fundam.*, vol. 21, no. 3, pp. 255–262, Aug. 1982.

[83] J. Blazek, *Computational fluid dynamics: principles and applications*. Elsevier Science Ltd, 2005.

[84] R. Stryjek and J. H. Vera, "PRSV: An Improved Peng- Robinson Equation of State for Pure Compounds and Mixtures," *Can. J. Chem. Eng.*, vol. 64, pp. 323–333, 1986.

[85] S. M. Walas, *Phase equilibria in chemical engineering*, vol. 4. Boston: Butterworth, 1985.

[86] R. Span and W. Wagner, "A New Equation of State for Carbon Dioxide Covering the Fluid Region from the Triple-Point Temperature to 1100 K at Pressures up to 800 MPa," *J. Phys. Chem. Ref. data*, vol. 25, no. 6, pp. 1509–1596, 1996.

[87] Gas Processors Suppliers Association, *Engineering Data Book*, 9th ed. 1974.

[88] O. Kunz, R. Klimeck, W. Wagner, and M. Jaeschke, "The GERG-2004 wide-range equation of state for natural gases and other mixtures," *GERG Tech. Monogr. 15*, 2007.

[89] GERG-2004, "The GERG-2004 wide-range equation of state for natural gases and other mixtures." [Online]. Available: http://www.ruhr-uni-bochum.de/thermo/Software/Seiten/GERG_2004-eng.htm.

[90] H. Li and J. Yan, "Evaluating cubic equations of state for calculation of vapor–liquid equilibrium of CO2 and CO2-mixtures for CO2 capture and storage processes," *Appl. Energy*, vol. 86, no. 6, pp. 826–836, Jun. 2009.

[91] M. Trujillo, P. Rourke, and D. Torres, "Generalizing the Thermodynamics State Relationships in KIVA-3V," *Los Alamos Natl. Labortory Rep. LA-13981*, 2002.

[92] D. L. Nguyen, E. R. F. Winter, and M. Greiner, "Sonic velocity in two-phase systems," *Int. J. Multiph. Flow*, vol. 7, no. 3, pp. 311–320, 1981.

[93] M. Chung, "Sound speed criterion for two-phase critical flow," *J. Sound Vib.*, vol. 276, no. 1–2, pp. 13–26, Sep. 2004.

[94] D. Picard and P. Bishnoi, "Calculation of the thermodynamic sound velocity in two-phase multicomponent fluids," *Int. J. Multiph. Flow*, vol. 13, no. 3, pp. 295–308, 1987.

[95] W. Gregor and H. Rumpf, "Velocity of sound in two-phase media," *Int. J. Multiph. Flow*, vol. 1, pp. 753–769, 1975.

[96] Z. Bilicki and D. Kardas, "Relaxation models for wave phenomena in liquid-vapor bubble flow in channels," *J. Fluids Eng.*, vol. 120, pp. 369–377, 1998.

[97] O. C. JONES, "Closure Conditions for Computation of Thermal Nonequilibrium in Two-Phase Flows," *J. Nucl. Sci. Technol.*, vol. 26, no. 11, pp. 979–992, Nov. 1989.

[98] G. Pinhasi and A. Ullmann, "Modeling of flashing two-phase flow," *Rev. Chem. Eng.*, vol. 21, no. 3–4, pp. 133–264, 2005.

[99] Z. Bilicki, R. Kwidzinski, and S. A. Mohammadein, "Evaluation of the relaxation time of heat and mass exchange in the liquid-vapour bubble flow," *Int. J. Heat Mass Transf.*, vol. 39, no. 4, pp. 753–759, 1996.

[100] W. Angielczyk, Y. Bartosiewicz, D. Butrymowicz, and J.-M. Seynheave, "1-D Modeling Of Supersonic Carbon Dioxide Two-Phase Flow Through Ejector Motive Nozzle," in *International Refrigeration and Air Conditioning Conferenc at Purdue, July 12-15*, 2010.

[101] M. Nakagawa, M. S. Berana, and A. Kishine, "Supersonic two-phase flow of CO2 through converging–diverging nozzles for the ejector

refrigeration cycle," *Int. J. Refrig.*, vol. 32, no. 6, pp. 1195–1202, Sep. 2009.

[102] J. Lee, R. Madabhushi, C. Fotache, S. Gopalakrishnan, and D. Schmidt, "Flashing flow of superheated jet fuel," *Proc. Combust. Inst.*, vol. 32, no. 2, pp. 3215–3222, 2009.

[103] Y. V Fairuzov, "Modeling of Conjugate Two-Phase Heat Transfer During Depressurization of Pipelines," *J. Heat Transfer*, vol. 122, pp. 99–106, 2000.

[104] A. A. Amsden, P. J. O'Rourke, and T. D. Butler, "KIVA-II: A computer program for chemically reactive flows with sprays," *Tech. Rep. LA-11560-MS, Los Alamos Natl. Lab.*, Dec. 1989.

[105] B. S. Massey, *Mechanics of Fluids*, 5th ed. Wokingham, Berkshire, England: Van Nostrand Reinhold Co. Ltd., 1983.

[106] J. Chen, "Modelling of transient flow in pipeline blowdown problems," Imperial College, University of London, 1993.

[107] D. BEATTIE and P. WHALLEY, "A simple two-phase frictional pressure drop calculation method," *Int. J. Multiph. Flow*, vol. 8, no. 1, pp. 83–87, Feb. 1982.

[108] V. Vesovic, W. A. Wakeham, G. A. Olchowy, J. V. Sengers, J. T. R. Watson, and J.Millat, "The transport properties of carbon dioxide," *J. Phys. Chem. Ref. Data*, vol. 19, no. 3, pp. 763–808, Dec. 1990.

[109] A. Fenghour, W. A. Wakeham, and V. Vesovic, "The Viscosity of Carbon Dioxide," *J. Phys. Chem. Ref. Data*, vol. 27, no. 1, pp. 31–44, 1998.

[110] K. S. Pedersen, A. Fredenslund, P. L. Christensen, and P. Thomassen, "Viscosity of crude oils," *Chem. Eng. Sci.*, vol. 39, no. 6, pp. 1011–1016, Jan. 1984.

[111] J. a. Jossi, L. I. Stiel, and G. Thodos, "The viscosity of pure substances in the dense gaseous and liquid phases," *AIChE J.*, vol. 8, no. 1, pp. 59–63, Mar. 1962.

[112] V. Gnielinski, "New equations for heat and mass transfer in the turbulent flow in pipes and channels," *Int. Chem. Eng.*, vol. 16, pp. 359–368, 1976.

[113] W. M. Rohsenow and J. R. Hartnett, *Handbook of Heat Transfer*, 3rd ed. New York: McGraw-Hill, 1988.

[114] M. M. Shah, "A general correlation for heat transfer during film condensation inside pipes," *Int. J. Heat Mass Transf.*, vol. 22, no. 4, pp. 547–556, 1979.

[115] M. J. Assael, J. H. Dymond, M. Papadaki, and P. M. Patterson, "Correlation and prediction of dense fluid transport coefficients:: II. Simple molecular fluids," *Fluid Phase Equilib.*, vol. 75, pp. 245–255, 1992.

[116] M. J. Assael, J. H. Dymond, M. Papadaki, and P. M. Patterson, "Correlation and prediction of dense fluid transport coefficients. III. n-alkane mixtures," *Int. J. Thermophys.*, vol. 13, no. 4, pp. 659–669, Jul. 1992.

[117] Z. Liu and R. H. S. Winterton, "A general correlation for saturated and subcooled flow boiling in tubes and annuli, based on a nucleate pool boiling equation," *Int. J. Heat Mass Transf.*, vol. 34, no. 11, pp. 2759–2766, 1991.

[118] E. Gungor and R. H. S. Winterton, "A general correlation for flow and annuli boiling in tubes," *Int. J. Heat Mass Transf.*, vol. 29, no. 3, pp. 351–358, 1986.

[119] H. Mahgerefteh and O. Atti, "Modeling low-temperature–induced failure of pressurized pipelines," *AIChE J.*, vol. 52, no. 3, pp. 1248–1256, 2006.

[120] F. P. Incropera, T. L. Bergman, A. S. Lavine, and D. P. DeWitt, *Fundamentals of heat and mass transfer*, 6th ed. New York: Wiley, 2011.

[121] S. W. Churchill and M. Bernstein, "A correlating equation for forced convection from gases and liquids to a circular cylinder in crossflow," *J. Heat Transfer*, vol. 99, pp. 300–306, 1977.

[122] J. Donea, A. Huerta, J.-P. Ponthot, and A. Rodriguez-Ferran, "Arbitrary Lagrangian-Eulerian methods," *Encycl. Comput. Mech.*, pp. 1–38, 2004.

[123] L. E. Malvern, *Introduction to the Mechanics of a Continuous Medium*. New Jersey: Prentice-Hall, Inc., 1969.

[124] W. F. Noh, "CEL: A Time-Dependent, Two Space Dimensional, Coupled Eulerian–Lagrange Code," in *Methods in Computational Physics*, New York: Academic Press, 1964, pp. 117–179.

[125] R. Franck and R. Lazarus, "Mixed Eulerian-Lagrangian method," in *Methods in Computational Physics, Vol. 3: Fundamental methods in Hydrodynamics*, New York, 1964.

[126] J. Trulio, "Theory and structure of the AFTON codes," *Rep. AFWL-TR-66-19, Air Force Weapons Lab.*, 1966.

[127] C. HIRT, A. AMSDEN, and J. COOK, "An arbitrary Lagrangian-Eulerian computing method for all flow speeds," *J. Comput. Phys.*, vol. 14, no. 3, pp. 227–253, Mar. 1974.

[128] R. Courant, "Über die partiellen Differenzengleichungen der mathematischen Physik (in German)," *Math. Ann.*, vol. 100, no. 1, pp. 32–74, 1928.

[129] S. V Patankar, D. B. Spalding, and E. Road, "A calculation procedure for heat, mass and momentum transfer in three-dimensional parabolic flows," *J. Heat Mass Transf.*, vol. I, pp. 1787–1806, 1972.

[130] W. F. Ames, *Numerical Methods for Partial Differential Equations*, 3rd ed. New York: Academic Press, 1992.

[131] P. O'Rourke, "The KIVA computer program for multidimensional chemically reactive fluid flows with fuel sprays," *Lect. Notes Phys.*, vol. 241, pp. 74–89, 1985.

[132] D. J. Picard and P. R. Bishnoi, "The importance of real-fluid behavior and nonisentropic effects in modeling decompression characteristics of pipeline fluids for application in ductile fracture propagation analysis," *Can. J. Chem. Eng.*, vol. 66, no. 1, pp. 3–12, Feb. 1988.

[133] K. K. Botros, W. Studzinski, J. Geerligs, and A. Glover, "Determination of Decompression Wave Speed in Rich Gas Mixtures," *Can. J. Chem. Eng.*, vol. 82, no. 5, pp. 880–891, May 2004.

[134] K. K. Botros and J. Geerligs, "Decompression Wave Speed in Rich Gas Mixtures at High Pressures (37 MPa) and Implications on Fracture Control Toughness Requirements in Pipeline Design," *Proc. 8th Int. Pipeline Conference*, pp. 1–13, 2010.

[135] K. K. Botros, J. Geerligs, L. Fletcher, B. Rothwell, L. Carlson, and P. Venton, "Effects of Pipe Internal Surface Roughness on Decompression Wave Speed in Natural Gas Mixtures," in *Proceedings of the 8th International Pipeline Conference*, 2010, pp. 1–16.

[136] K. K. Botros, J. Geerligs, B. Rothwell, L. Carlson, L. Fletcher, and P. Venton, "Transferability of decompression wave speed measured by a small-diameter shock tube to full size pipelines and implications for determining required fracture propagation resistance," *Int. J. Press. Vessel. Pip.*, vol. 87, no. 12, pp. 681–695, Dec. 2010.

[137] K. K. Botros, "Measurements of Speed of Sound in Lean and Rich Natural Gas Mixtures at Pressures up to 37 MPa Using a Specialized Rupture Tube," *Int. J. Thermophys.*, vol. 31, no. 11–12, pp. 2086–2102, Dec. 2010.

[138] K. K. Botros, J. Geerligs, and R. J. Eiber, "Measurement of Decompression Wave Speed in Rich Gas Mixtures at High Pressures (370 bars) Using a Specialized Rupture Tube," *J. Press. Vessel Technol.*, vol. 132, no. 5, pp. 1–15, 2010.

[139] W. A. Maxey, F. A. Syler, and R. J. Eiber, "Fracture Propagation Experiments on 48 inch X 0.72 inch Line Pipe," *NEB Public Doc. NPD-137*, 1975.

[140] K. K. Botros, W. M. Jungowski, and M. H. Weiss, "Models and methods of simulating gas pipeline blowdown," *Can. J. Chem. Eng.*, vol. 67, no. 4, pp. 529–539, Aug. 1989.

[141] W. A. Maxey, "Long Shear Fractures in CO2 Lines Controlled by Regulating Saturation, Arrest Pressures," *Oil Gas J.*, vol. 84, no. 31, pp. 44–46, 1986.

[142] A. Cosham and R. Eiber, "Fracture propagation in CO2 pipelines," *J. Pipeline Eng.*, pp. 115–124, 2008.

[143] D. J. Hayes, P. R. Bishnoi, and M. M. E. Wallbridge, "Full Scale Crack Arrest Test and Arrester Device Performance for the FLACS Gas Line," in *64th Annual Fall Technical Conference, Soc. Of Pet. Eng. Las Vegas*, 1976.

[144] W. A. Maxey, *Final report on gas expansion studies: to American Gas Association,NG-18 Report No. 133.* Columbus, Ohio: Battelle Memorial Institute, 1983.

[145] SPT Group, "OLGA." [Online]. Available: http://www.sptgroup.com/en/products/olga/.

[146] J. Gale, "Transmission of CO2 - safety and economic considerations," *Energy*, vol. 29, no. 9–10, pp. 1319–1328, Jul. 2004.

[147] A. Cosham, D. Jones, K. Armstrong, D. Allason, and J. Barnett, "The decompression behaviour of CO2 in the gas phase," *Int. Forum Transp. CO2 by Pipeline, Hilt. Gateshead-Newcastle Hotel. Gateshead, UK,22-23 June 2011*, 2011.

[148] A. Cosham, D. G. Jones, K. Armstrong, D. Allason, and J. Barnett, "The Decompression Behaviour of Carbon Dioxide in the Dense Phase," in *Proceedings of the 9th International Pipeline Conference IPC2012 September 24-28, 2012, Calgary, Alberta, Canada*, 2012, pp. 1–18.

[149] R. Cooper, "CO2 pipeline transportation for CCS: an operator's perspective," *Proceeding Frist Int. Forum Transp. CO2 by Pipeline, Hilt. Gateshead-Newcastle Hotel. Gateshead, UK, 1-2 July*, 2010.

[150] R. Cooper, "National Grid's COOLTRANS research programme," *J. Pipeline Eng.*, vol. 11, no. 3, pp. 155–172, 2012.

[151] J. Barnett and D. G. Jones, "The Longannet CCS Project Shock Tube Tests," *Proc. Second Int. Forum Transp. CO2 by Pipeline, Newcastle upon Tyne, UK,, 22-23 June*, 2011.

[152] M. Mohitpour, H. Golshan, and M. Murray, *Pipeline design & construction: a practical approach*. New York: ASME Press, 2000.

[153] C. B. Farris, "Unusual design factors for supercritical CO2 pipelines," *Energy Prog.*, vol. 3, pp. 150–158, 1983.

[154] E. Elias and P. Chambré, "Flashing inception in water during rapid decompression," *J. Heat Transfer*, vol. 115, no. 1, pp. 231–238, 1993.

[155] H. Mahgerefteh, S. Brown, and S. Martynov, "A study of the effects of friction, heat transfer, and stream impurities on the decompression behavior in CO 2 pipelines," *Greenh. Gases Sci. Technol.*, vol. 2, no. 5, pp. 369–379, Oct. 2012.

[156] M. Mohitpour, P. Seevam, and K. K. Botros, *Pipeline Transportation of Carbon Dioxide Containing Impurities*. ASME International, 2012.

[157] B. McBride, M. Zehe, and S. Gordon, "NASA Glenn coefficients for calculating thermodynamic properties of individual species," in *NASA/TP-2002-211556*, 2002.

[158] G. M. Wilson, "A modified Redlich-Kwong equation of state, application to general physical data calculations," *65th Natl. AIChE Meet. Cleveland, OH*, 1969.

[159] Versteeg, H. K., & Malalasekera, W. *An Introduction to Computational Fluid Dynamics The Finite Volume Method*, 2nd ed. Essex: Pearson Education Limited. 2007.

List of Publications

Jie, H., Xu, B.,& Wen, J. X. "A Pipeline Depressurization Model for Fast Decompression and Slow Blowdown." *International Journal of Pressure Vessels and Piping.* (submitted to Int. J. Pres. Ves. Pip. Chapter2, 3 and part of Chapter 4)

Jie, H., Xu, B., Wen, J. X., Cooper, R., & Barnett, J. "Predicting the Decompression Characteristics of Carbon Dioxide Using Computational Fluid Dynamics." In *Proceedings of the 2012 9th International Pipeline Conference; IPC2012-90649,September 24-28, 2012, Calgary, Alberta, Canada* pp. 1–12, 2012. (Chapter 2, and Chapter 5)

Wen, J. X., **Jie, H.**, Xu, B., Cooper, R., & Barnett, J. "Numerical Study of Compressed CO_2 Pipeline Decompression Characteristics Using CFD-DECOM." In *HAZARDS XXII, IChemE, 11–14 April 2011, Liverpool, UK.* (Chapter 2, and part of Chapter 4)

J. X. Wen, **H.E. Jie**, B.P. Xu and V.H.Y. Tam, Development of CFD-DECOM for the Prediction of gaseous and dense phase CO_2 decompression behaviour, *13th International Symposium on Loss Prevention and Safety Promotion in the Process Industry, Bruges*, 2010.

B. Xu, **H. Jie**, J. X. Wen. Appendix 3: Kingston far field dispersion analysis of a vertical vent release. in: R. Cooper et al.(eds.), COOLTRANS integrated CO_2 dispersion studies, *International Forum on the Transportation of CO_2 by Pipeline, Hilton Gateshead- Newcastle Hotel, Gateshead, UK, 2011.*

J. Wen, A. Heidari, B. Xu, and **H. Jie**. Dispersion of carbon dioxide from vertical vent and horizontal releases - a numerical study, *Proceedings of the Institution of Mechanical Engineers, Part E, Journal of Process Mechanical Engineering,* Vol.227, no. 2, pp. 125-139, 2012.

A. Heidari, B. Xu, **H. Jie**, and J. Wen. Numerical simulation of carbon dioxide dispersion from vertical vent release, *Third International Forum on Transportation of CO2 by Pipeline; 20-21 June 2012, Newcastle, UK.*

Appendix A. Parameters of Pure Components

Table A.1 Critical Pressure, Critical Temperature, acentric factor and molar weight for components [87]

	CO_2	O_2	N_2	C_1	C_2	C_3	i-C_4	n-C_4	i-C_5	n-C_5	n-C_6
P_c [MPa]	7.3773	5.043	3.3978	4.599	4.872	4.248	3.796	3.796	3.37	3.37	3.025
T_c [K]	304.1282	154.59	126.19	190.56	305.32	369.83	425.12	425.12	469.7	469.7	507.6
ω	0.225	-0.184	0.037	0.011	0.099	0.152	0.2	0.2	0.252	0.252	0.3
w [g/mol]	44.095	31.9988	28.0134	16.04246	30.06904	44.09562	58.1222	58.1222	72.14878	72.14878	86.17536

Table A.2 Binary Interaction Parameters [87]

	CO_2	O_2	N_2	C_1	C_2	C_3	i-C_4	n-C_4	i-C_5	n-C_5	n-C_6
CO_2	0	0	-0.017	0.0919	0.1322	0.1241	0.12	0.1333	0.1219	0.1222	0.11
O_2	0	0	-0.0119	0	0	0	0	0	0	0	0
N_2	-0.017	-0.0119	0	0.0311	0.0515	0.0852	0.1033	0.08	0.0922	0.1	0.1496
C_1	0.0919	0	0.0311	0	-0.0026	0.014	0.0256	0.0133	-0.0056	0.023	0.0422
C_2	0.1322	0	0.0515	-0.0026	0	0.0011	-0.0067	0.0096	0	0.0078	-0.01
C_3	0.1241	0	0.0852	0.014	0.0011	0	-0.0078	0.0033	0.0111	0.0267	0.0007
i-C_4	0.12	0	0.1033	0.0256	-0.0067	-0.0078	0	-0.0004	0	0	0
n-C_4	0.1333	0	0.08	0.0133	0.0096	0.0033	-0.0004	0	0.0174	0	-0.0056
i-C_5	0.1219	0	0.0922	-0.0056	0	0.0111	0	0.0174	0	0.06	0
n-C_5	0.1222	0	0.1	0.023	0.0078	0.0267	0	0	0.06	0	0
n-C_6	0.11	0	0.1496	0.0422	-0.01	0.0007	0	-0.0056	0	0	0

Appendix B. Thermodynamic Properties Based on PR EOS

$$H - H^{IG} = RT(Z-1) + \frac{T\dfrac{\mathbf{d}a}{\mathbf{d}T} - a}{2\sqrt{2}b} \ln\left(\frac{\upsilon + \left(\sqrt{2}+1\right)b}{\upsilon - \left(\sqrt{2}-1\right)b}\right) \tag{B.1}$$

$$I - I^{IG} = RTZ + \frac{T\dfrac{\mathbf{d}a}{\mathbf{d}T} - a}{2\sqrt{2}b} \ln\left(\frac{\upsilon + \left(\sqrt{2}+1\right)b}{\upsilon - \left(\sqrt{2}-1\right)b}\right) - P\upsilon \tag{B.2}$$

$$S - S^{IG} = R\left(Z - \frac{bP}{RT}\right) + \frac{\dfrac{\mathbf{d}a}{\mathbf{d}T}}{2\sqrt{2}b} \ln\left(\frac{\upsilon + \left(\sqrt{2}+1\right)b}{\upsilon - \left(\sqrt{2}-1\right)b}\right) \tag{B.3}$$

$$C_v - C_v^{IG} = \frac{T\dfrac{\mathbf{d}^2a}{\mathbf{d}^2T}}{2\sqrt{2}b} \ln\left(\frac{\upsilon + \left(\sqrt{2}+1\right)b}{\upsilon - \left(\sqrt{2}-1\right)b}\right) \tag{B.4}$$

$$C_p = C_v + mT\frac{\left(\left.\dfrac{\partial P}{\partial T}\right|_\rho\right)^2}{\rho^2 \left.\dfrac{\partial P}{\partial \rho}\right|_T} \tag{B.5}$$

where

$$Z = \frac{P\upsilon}{RT} \tag{B.6}$$

$$\begin{aligned} H^{IG}/(RT) = &-a_1T^{-2} + a_2 \ln T/T + a_3 + a_4T/2 \\ &+ a_5T^2/3 + a_6T^3/4 + a_7T^4/5 + b_1/T \end{aligned} \tag{B.7}$$

$$I^{IG} = H^{IG} - RT \tag{B.8}$$

$$S^{IG}/(RT) = -a_1 T^{-2}/2 - a_2 T^{-1} + a_3 \ln T + a_4 T + a_5 T^2/2 + a_6 T^3/3 + a_7 T^4/4 + b_2 \tag{B.9}$$

$$C_p^{IG}/R = a_1 T^{-2} + a_2 T^{-1} + a_3 + a_4 T + a_5 T^2 + a_6 T^3 + a_7 T^4 \tag{B.10}$$

$$C_v^{IG} = C_p^{IG} - R \tag{B.11}$$

$$\frac{\mathbf{d}a}{\mathbf{d}T} = \sum_i \sum_j z_i z_j \frac{\mathbf{d}a_i}{\mathbf{d}T} \frac{a_j}{a_i}\left(1 - \delta_{ij}\right) \tag{B.12}$$

$$\frac{\mathbf{d}^2 a}{\mathbf{d}^2 T} = \sum_i \sum_j z_i z_j \left[-0.5\sqrt{a_i a_j}\left(\frac{\mathbf{d}a_i}{\mathbf{d}T}\frac{1}{a_i}\right)^2 + \sqrt{\frac{a_j}{a_i}}\frac{\mathbf{d}^2 a_i}{\mathbf{d}^2 T} + 0.5\frac{\mathbf{d}a_i}{\mathbf{d}T}\frac{\mathbf{d}a_j}{\mathbf{d}T}\frac{1}{\sqrt{a_i a_j}}\right]\left(1 - \delta_{ij}\right) \tag{B.13}$$

$$\frac{\mathbf{d}a_i}{\mathbf{d}T} = 0.45724\frac{R^2 T_{c,i}^{\ 2}}{P_{c,i}}\left(1 + \kappa_i\left(1 - \sqrt{\frac{T}{T_{c,i}}}\right)\right)\left[-\kappa_i \frac{1}{\sqrt{T T_{c,i}}}\right] \tag{B.14}$$

$$\frac{\mathbf{d}^2 a_i}{\mathbf{d}^2 T} = 0.45724\frac{R^2 T_{c,i}^{\ 2}}{P_{c,i}}\left[\left(1 + \kappa_i\left(1 - \sqrt{\frac{T}{T_{c,i}}}\right)\right)\frac{\kappa_i}{2T\sqrt{T T_{c,i}}} + \frac{\kappa_i^{\ 2}}{2T T_{c,i}}\right] \tag{B.15}$$

$$\left.\frac{\partial P}{\partial T}\right|_{\rho} = \left.\frac{\partial P}{\partial T}\right|_{\upsilon} = \frac{R}{\upsilon - b} - \frac{\mathbf{d}a}{\mathbf{d}T}\frac{1}{v(v+b) + b(v-b)} \tag{B.16}$$

$$\left.\frac{\partial P}{\partial \rho}\right|_{T} = -\frac{m}{\rho^2}\left.\frac{\partial P}{\partial \upsilon}\right|_{T} = \frac{m}{\rho^2}\left(\frac{RT}{(\upsilon - b)^2} - \frac{2a(v+b)}{\left(v(v+b) + b(v-b)\right)^2}\right) \tag{B.17}$$

Here, ρ is density, H is specific enthalpy per unit mole, I is specific internal energy per unit mole, S is specific entropy per unit mole, C_p, C_v is constant

pressure and volume specific heat capacity respectively, the superscript *IG* means the thermodynamic properties for ideal gas, Z is compressibility factor, z_i is mole fraction in the mixture. The coefficients a_1-a_7, b_1, b_2 in Eqs. (B.7), (B.9) and (B.10) can be found in [157].

Appendix C. Flash Calculation

1. Flash calculation

Two-phase flash calculation aims to obtain the component of mixture based on the equilibrium method. Commonly, it is conducted at isothermal and isobaric conditions. The set of equations required to formulate the isothermal-isobaric two-phase flash calculations are as follows:

Material Balance Equations:

$$L+V=1.0 \tag{C.1}$$

$$Lx_i+Vy_i=z_i \quad i=1,....,N_c \tag{C.2}$$

where L and V are liquid and vapour fractions respectively. x_i, y_i and z_i are liquid, vapour and feed mole fractions, respectively, of an individual component I, N_c is number of components.

Constraint Equations:

$$\sum_i (y_i-x_i)=0 \tag{C.3}$$

$$f_i^L=f_i^V \quad i=1,....,N_c \tag{C.4}$$

where f_i^L, f_i^V are the fugacity of component i in the liquid and vapour phase respectively and are calculated from Peng-Robinson Equation of State, see Eqs. (C.5) and (C.6).

$$\ln\left(\frac{f_i^L}{x_i P}\right)=\frac{b_i}{b}(Z-1)-\ln(Z-B)-\frac{A}{2\sqrt{2}B}\times \left(\frac{2\sum_j x_i a_{ij}}{a}-\frac{b_i}{b}\right)\ln\left(\frac{Z+(\sqrt{2}+1)B}{Z-(\sqrt{2}-1)B}\right) \tag{C.5}$$

$$\ln\left(\frac{f_i^V}{y_i P}\right)=\frac{b_i}{b}(Z-1)-\ln(Z-B)-\frac{A}{2\sqrt{2}B}\times \left(\frac{2\sum_j y_i a_{ij}}{a}-\frac{b_i}{b}\right)\ln\left(\frac{Z+(\sqrt{2}+1)B}{Z-(\sqrt{2}-1)B}\right) \tag{C.6}$$

where

$$A=\frac{aP}{R^2T^2} \tag{C.7}$$

$$B=\frac{bP}{RT} \tag{C.8}$$

Solution Method for Flash Calculation:

The mole fraction of liquid and vapour, x_i, y_i can be correlated by the following equation:

$$y_i = K_i x_i \quad i=1,....,N_c \tag{C.9}$$

where K_i is the equilibrium constant for component *i*. Combining Eqs. (C.3), (C.4) and (C.8), x_i, and y_i can be rewritten in the following forms:

$$x_i=\frac{z_i}{1+(K_i-1)V} \tag{C.10}$$

$$y_i=\frac{K_i z_i}{1+(K_i-1)V} \tag{C.11}$$

The sum of mole friction is equal 1, as following:

$$\sum_i \frac{K_i z_i}{1+(K_i-1)V} = 0 \tag{C.12}$$

$$K_i = e^{5.373(1+\omega_i)(1-T_{c,i}/T)} \frac{P_{c,i}}{P} \tag{C.13}$$

If a set of K_i are assumed from the Wilson equation [158], Eq. (C.12) becomes a function of V. Eq. (C.12) can express function as follows:

$$g(V) = \sum_i \frac{K_i z_i}{1+(K_i-1)V} = 0 \tag{C.14}$$

The Eq. (C.14) is a monotonically decreasing function of V and the root of V between zero and one is possible only if the following two conditions are satisfied:

$$\sum_i K_i z_i > 1 \tag{C.15}$$

$$\sum_i \frac{z_i}{K_i} > 1 \tag{C.16}$$

If the Eqs. (C.15) and (C.16) are satisfied by the set of assumed value of K_m, Eq. (C.14) can be solved for V by Newton's method. Using the value of V and the assumed set of K_i, X_i and Y_i are calculated from Eqs. (C.10) and (C.11), respectively. Subsequently, fugacities of the phases are calculated by using Eqs. (C.5) and (C.6). If the equilibrium condition defined by Eq. (C.4) is not satisfied, K_i are updated with the successive substitution and Newton's Method for the next iteration.

Briefly, the procedure of flash calculation based on pressure P, temperature T and component z_i, are carried out as follows:

1. Assume the equilibrium constant with Wilson's equation Eq. (C.13);

2. Evaluate the root condition of Eq. (C.14), if satiated root, vapour mole fraction V is found, then the mole fraction of liquid phase and vapour phase for component will be calculated using Eqs. (C.10) and (C.11); otherwise the feed phase is specified as single phase then go to step 4, Eq. (C.16) is not satisfied, the feed phase is vapour, Eq. (C.15) is not satisfied, the feed phase is liquid;

3. Calculate the fugacities of phases for components using Eqs. (C.6) and (C.7), if Eq. (C.5) is not satisfied, update the equilibrium constant with the successive substitution and Newton's Method, then go back step 2 until the Eq. (C.5) is satisfied, here the condition $\sum_i \left(1-\frac{f_i^L}{f_i^V}\right)^2 \Big/ N_c \le 10^{-12}$ is applied to replace the Eq. (C.5);

4. Calculate the compressibility factor, molar volume, density for each phase.

With the flash calculation, one can find the vapour and liquid phase fraction V and L, component for vapour and liquid phase y_i and x_i, and density ρ_L, ρ_V as well. For two-phase, the thermodynamic properties are calculated as follows:

$$(\mathbf{TP}) = V(\mathbf{TP})^V + L(\mathbf{TP})^L \tag{C.17}$$

where **(TP)** means thermodynamic properties per mole unit, such as mole enthalpy H, internal energy per unit mole I, specific entropy per unit mole S, constant pressure and volume specific heat capacity C_p and C_v. $(\mathbf{TP})^V$, $(\mathbf{TP})^L$ means the thermodynamic properties of vapour and liquid phase respectively. For multi-component two-phase mixtures, the thermodynamic properties for each phase are defined as follows:

$$(\mathbf{TP})^V = \sum_i y_i (\mathbf{TP})_i^V \tag{C.18}$$

$$(\mathbf{TP})^L = \sum_i x_i (\mathbf{TP})_i^L \tag{C.19}$$

$$S^V = \sum_i y_i \left[S_i^V - R \ln\left(\frac{y_i P}{P_{atm}} \right) \right] \tag{C.19}$$

$$S^L = \sum_i x_i \left[S_i^L - R \ln\left(\frac{x_i P}{P_{atm}} \right) \right] \tag{C.19}$$

Here, $\mathbf{TP}_i^V$, $\mathbf{TP}_i^L$ are the thermodynamic properties of component *i*, *H*, *I*, C_p, C_v, for vapour and liquid phase respectively; P_{atm} is the atmosphere pressure. The description of entropy for mixture is slightly different, showed as Eqs. (C.18) and (C.19).

The thermodynamic properties per unit mass are considered during the calculation, therefore the conversion are presented as follows:

$$(\mathbf{tp}) = \frac{(\mathbf{TP})}{w} \tag{C.20}$$

$$\rho = \frac{w}{\dfrac{(1-V)w^L}{\rho^L} + \dfrac{Vw^V}{\rho^V}} \tag{C.21}$$

where $(\mathbf{tp})$ is the thermodynamic properties per unit mass for mixture, w is the molar weight for mixture, $w = \sum_i z_i w_i$, w^L, w^V are the molar weight for liquid and vapour phase mixture, $w^L = \sum_i x_i w_i$, $w^V = \sum_i y_i w_i$.

For two-phase calculation, the fraction of vapour phase is calculated as follows:

void fraction α: $\alpha = \dfrac{\rho^L - \rho}{\rho^L - \rho^V}$ (C.22)

quality (mass fraction) x: $$x = \alpha \frac{\rho^V}{\rho} = \frac{\rho^L - \rho}{\rho^L - \rho^V} \cdot \frac{\rho^V}{\rho} \tag{C.23}$$

Normally, the Equation of State is chose to close the Navies-Stokes Equation during process of flow simulation. For two-phase multi-component flow, density and internal energy flash calculation is finally performed based on equation of state. The process of solution is described as follows:

1. Read the parameter density ρ , internal energy i, and component z_i, and initial estimated temperature T_{guess} and pressure P_{guess};
2. Carry out the Pressure-Temperature flash calculation to find the liquid x_i and vapour y_i component of individual component;
3. Calculate the internal energy i_{cal} and density ρ_{cal} using the Eqs. (C.22), (C.17) and (C.23), respectively, then evaluate them with the initial parameters, if the below Eq. (C.24) is satisfied, then calculation finished;

$$res = \left| \frac{i_{cal} - i}{i} \right| + \left| \frac{\rho_{cal} - \rho}{\rho} \right| \le 10^{-7} \tag{C.24}$$

4. Update the pressure P_{guess} and temperature T_{guess} using the Newton's method, go step 2.
5. Calculate and output the pressure, temperature, void fraction, quality, and component for liquid and vapour phases and so on.

The calculation of algorithm is showed in Figure C.1.

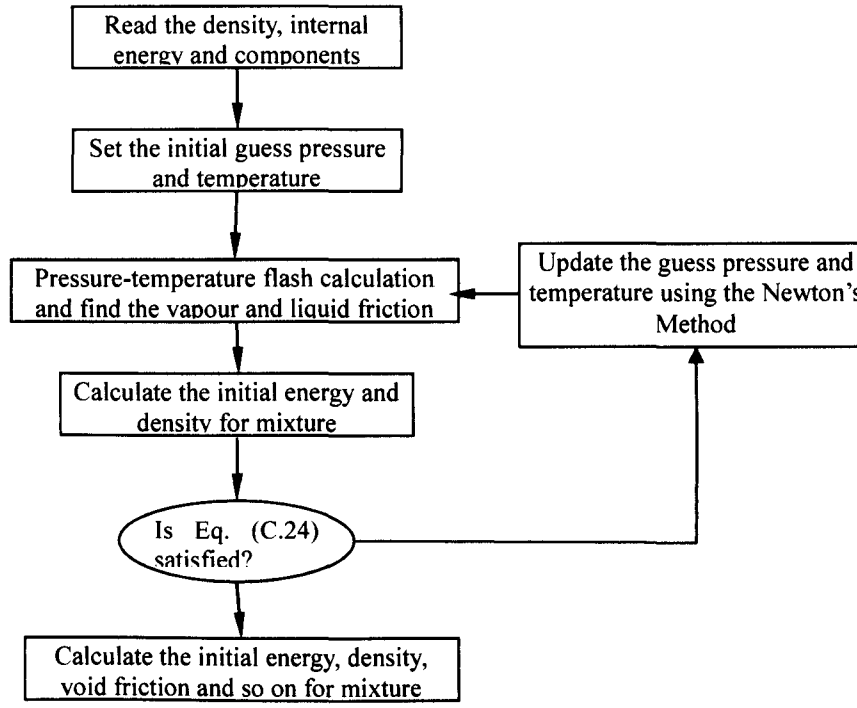

Figure C.1 Description of density and internal energy flash calculation